Principles of Small-Scale Hydraulic Systems for Human Assistive Machines

A Dissertation
SUBMITTED TO THE FACULITY OF
UNIVERSITY OF MINNESOTA
BY

Brett Cullen Neubauer

IN PARTIAL FULFILLMENT OF THE REQUIREMENTS
FOR THE DEGREE OF
DOCTOR OF PHILOSOPHY

Advisor:
William K. Durfee, PhD

March 2017

Acknowledgements

I would like to thank my parents Paul and Linda Neubauer in the continuous support of my academic pursuits. It is their guidance from a young age that led me to pursue my aspirations in education and of knowledge. I would also like to give thanks to my adviser Professor William Durfee at the University of Minnesota for sharing his expertise and guidance during my graduate education.

There are several individuals that need to be acknowledged for their efforts in this research. Jonathan Nath is a mechanical engineering student completing his master degree at the University of Minnesota, and he provided assistance in designing and building the electrohydraulic power supply for the hydraulic ankle-foot orthosis. He has also provided assistance and expertise in the design and construction of the ankle actuator assemblies of the pediatric hydraulic ankle-foot orthosis. Sangyoon Lee, a PhD candidate in the mechanical engineering program at the University of Minnesota, assisted in developing the axial piston pump performance model. Dr. Andre Ries is a PhD graduate working at Gillette Children's Hospital in St. Paul, MN, and he assisted with the collection of AFO stiffness data using the BRUCE measurement system. Dr. Ries also provided gait data collected with 3D motion capture for patients with cerebral palsy.

This work was supported the National Institutes of Health, grant number R21 EB 019390-02, and by the Center for Compact and Efficient Fluid Power, a National Science Foundation Engineering Research Center, EEC-0540834. In addition, I had the opportunity and privilege to be receive the National Science Foundation's Graduate Research Fellowship from 2012-2015 providing additional financial support for my graduate education.

Abstract

The high power and force density of hydraulic actuators, along with the ability to distribute system weight through the separation of the power supply and actuators makes hydraulic technology ideal for use in human assistive machines. However, hydraulic systems often operate inefficiently due to throttling losses in the control valves and have increased viscous losses in small-scale applications as bore size is decreased. The objective of this research is to address the limitations of small-scale hydraulics using validated modeling techniques to optimize performance and minimize system weight.

This research compares and contrasts the use of different hydraulic technology as well as develops detailed models of small-scale hydraulic components. These models are used to construct a software tool that optimizes the design of a hydraulic system using specified input requirements of actuation, conduit lengths, operating pressure, and runtime. A system-level energetics analysis provides estimates of efficiencies and weights, while a heat transfer analysis estimates the working fluid and component surface temperatures.

In addition, the dynamic performance of different small-scale pump and valve controlled hydraulic systems are simulated to compare the cycle efficiencies, rise times, and flow rate capabilities as a function of duty cycles. The use of an accumulator, unloading valves, variable displacement pumps, and proportional pressure control are explored to improve the efficiency of the system during intermittent operation. In addition a small-scale, digital, high frequency switching valve is designed and simulated to reduce the throttling losses of a traditional proportional control valve.

This body of knowledge is used to design, prototype, and performance test two hydraulic powered ankle-foot orthoses. The first orthosis is an untethered system that provides active gait assistance. Hydraulics allows the system to be separated into two parts as the actuator is secured to the ankle, and the portable electrohydraulic power supply is positioned on the lower back. The second orthosis emulates the dynamics of a passive ankle-foot orthosis providing torque assistance to bring the ankle to a neutral position. This device is specifically designed to reduce the time and resources in the clinical prescription of passive ankle-foot orthoses while providing more quantitative metrics.

Table of Contents

List of Figures

Appendix

List of Tables

Appendix

Chapter 1 Applications, Research Objectives, and Prior Art

1.1 Introduction

The objective of this thesis is to lay the engineering foundation for the use of small-scale hydraulic power in human assistance machines. This research is focused on small-scale applications with power requirements between 10 and 1000 W. Human assistive machines are defined as portable devices that directly interface or interact with the human body. The prior art described in section 1.2 provides several examples of hydraulic powered human assistive machines.

1.1.1 Applications

There exists a variety of applications for portable human assistive machines in the manufacturing, military, and medical industries. There are an estimated annual $45-54 billion of lost wages, compensation costs, and lost productivity due to musculoskeletal injuries and disorders occurring in the workplace with $13.4 billion specifically attributed to overexertion injuries like lifting, pushing, or carrying heavy objects [1]. Human assistive machines have the ability to reduce muscle strain and fatigue for repetitive motion tasks on the manufacturing floor and other work spaces. These devices augment human strength capabilities, making them useful for the manipulation of heavy and oblong objects. This technology is not meant to replace automated manufacturing, but to assist skilled laborers in areas where human decision making is required or in areas where automated machines are not easily accommodated. Some example applications are the manipulation of plywood, drywall sheets, or A-frames by a carpenter or the lifting of vehicle tires in auto repair shop.

The results of the research devised in this thesis can be used to develop human assistive devices in the emerging field of rehabilitation robotics by improving a variety of rehabilitation processes. These devices have the potential to not only decrease patient recovery time, but also reduce clinic costs as more of the rehabilitation process can be completed at home instead of in the clinic. This research lays the foundation for the use of hydraulic technology in powered orthoses, prostheses, and exoskeletons. Hydraulic power is capable of replicating the dynamics of muscle torque, assisting users to restore or regain normal limb functions. As researchers work to better

decipher the user intent and interfacing with nervous system, more complex exoskeletons will have the capability to restore multiple limb functions for paraplegic and quadriplegic users. Magnetic resonance imaging (MRI) is a popular and noninvasive method of collecting visual health metrics. A limitation of MRI is that electronics in the observation room may disrupt the imaging process. Small-scale hydraulic technology can be designed for use in electrically sensitive environments [2] like an MRI observation room, and as a result provides an alternative to typical electromechanical surgical tools.

1.1.2 Comparison of actuation methods with human muscle

The following section deciphers what type of actuation method should be used for use in human assistive machines, conventional actuation methods and smart materials are compared against human muscle tissue in table 1.1 [3, 4, 5]. Piezoelectric and magnetostrictive actuation are not considered in this analysis due to they can only stretch to strains up to 0.1% and 0.2%, whereas human muscle tissue can undergo up to 40% strain [5].

Table 1.1 Properties of Actuation Methods

Actuator	Power density (W/kg)	Bandwidth (Hz)	Stiffness (MPa)	Strain (%)
Muscle	50	30	50	40
Shape memory alloy	50000	10	80000	5
Hydraulic	3000	50	1300	Unlimited
Conductive polymers	1000	10	5	2
Electromagnetic	200	> 100	0.1	Unlimited
Pneumatic	300	50	0.1	Unlimited
Polyelectrolyte gel	5	10	0.1	40

Hydraulic actuators along with shape memory alloys (SMA) and conductive polymer can achieve high volumetric and weight power densities allowing the design of light-weight and compact devices [6, 7, 2, 8, 3, 9] . In addition, hydraulic and pneumatic actuators have high specific torques making them ideal for generating large moments in confined spaces [2, 3].

Shape memory alloys have mechanical efficiencies up to 3% [10], and this is limiting for portable devices that must carry their own energy. The efficiencies of hydraulic and pneumatic actuators increase with load, while electric motors operate efficiently only at high angular velocities, 70-

90% no-load speed, and low torque [11]. Hydraulic actuators can be operated continuously and efficiently at low velocity and high load conditions, while an electrical motor can only be operated intermittently near stall conditions [12].

The bandwidth listed in table 1.1 is a metric that compares the actuation response speed. Linear and rotary electrometrical systems demonstrate high bandwidth capabilities superseded only by piezo electric and magnetostrictive materials [13]. SMA fibers contract as they are heated causing a phase transition from martensite to austenite [14]. In order to get the fiber to return to the original length the fiber must be cooled. This transition time is dependent on the surrounding heat transfer environment with a lower limit of 100 ms. This bandwidth limitation makes SMAs unable to replicate muscle dynamics.

An essential element to providing control of human assistive machines is the ability to adjust the stiffness of the device. Humans are capable of adjusting the stiffness of their limbs by a factor of 5 by controlling the magnitude of the synapses on contracting antagonist muscle groups [5]. Hydraulic systems are capable of achieving much higher stiffness using less energy compared to other actuation methods [3, 6]. As a result of the high stiffness, hydraulic systems under loaded conditions have quicker response times and less positional error compared to pneumatic actuation [6, 15, 9]. The stiffness of hydraulic systems is easily adjusted through the use of various pressure regulation techniques; and therefore hydraulic systems can emulate low stiffness as well as high stiffness behavior.

Fluid power systems have a similar mechanical structure as a muscle-tendon [16, 9]. The myosin and actin filament fibers in myofilaments can be modeled as a contractile element in parallel with an elastic element representing extracellular connective tissue (Fig. 1.1). The tendon is modeled as a series elastic element connecting the muscle bone [17]. In hydraulic and pneumatic systems the contractile element is the actuator, while the series elastic element is the natural compliance of the system. The compliance is a result of the compressibility of the fluid and the elastic stretch of the conduit. When a hydraulic system is coupled with the body, the tissues will act like the parallel resistive element.

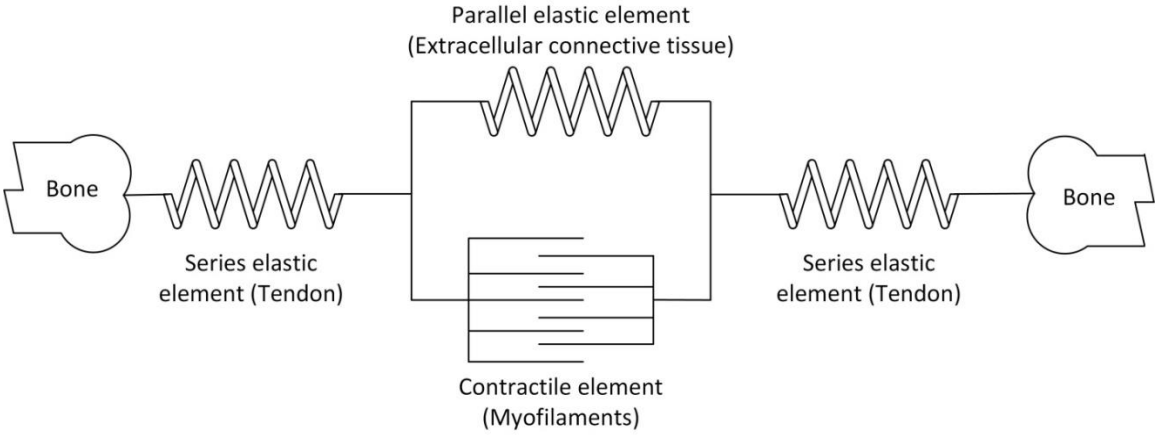

Figure 1.1 Mechanical structure of skeleton muscle tissue

The maximum sustained power capabilities of electromagnetic and fluid power systems are governed by balancing the heat generated due to inefficiencies with the heat dissipated from the system. Hydraulic systems have low thermal resistances as the circulating fluid distributes heat evenly throughout the system [6, 7]. This increases the surface area and the heat dissipated due to natural convection with the surroundings. The increased heat transfer allows a portable hydraulic device to operate at higher power levels compared to electromechanical, while maintaining safe exterior temperatures. In addition, the working fluid acts as a lubricant, decreasing wear of moving parts and increasing component lifetime [6].

It is essential for human assistive machines to position actuators based on anatomy for user comfort and ease of use. Hydraulic systems have the ability to separate the power generation and the actuators through the use of hoses [6, 8], while electromechanical systems need to incorporate heavy gear or pulley transmissions. This has two additional benefits in that the weight of the power supply can be positioned in an ideal location on the body or device, and it allows a single power supply to provide pressurized fluid to multiple actuators.

Hydraulic systems have no saturation limits, because force is always proportional to a pressure difference. Torque is proportional to current in electric motors, but is limited by magnetic

saturation [11]. In addition the ratio of force to velocity is easily adjusted within fixed power system by increasing or decreasing the acting surface area of the piston.

1.1.3 Limitations of small-scale hydraulic systems

The use of small-scale hydraulic technology for use in portable human assistive machines suffers a few limitations that this thesis addresses. Currently hydraulic technology is employed primarily in large power (> 10 kW) industrial applications undergoing large and continuous load like earth moving equipment. In these applications there exists high uncertainty in the magnitude and direction of the loading. These applications require high reliability with a low risk of fatigue failure. As a result these machines are heavy and bulky to accommodate these design requirements, whereas in human assistive machines the overall system weight and packaging are crucial requirements. Industrial influences have led to little research in modeling, designing, and manufacturing of small-scale portable hydraulic systems. In addition few commercial small-scale hydraulic components are available.

Hydraulic systems suffer from several mechanisms that reduce the overall system efficiency. The primary method of controlling hydraulic systems is through the use of proportional valves. A major drawback of proportional valves is they introduce large pressure drops throttling the flow [6], which results in hydraulic systems having lower efficiencies compared to the electromechanical systems [18]. There exists a need for innovative control valves and methods to improve hydraulic efficiency without compromising performance. In addition, as the diameter of hydraulic conduits are decreased, the viscous losses within the system increase [2, 6] resulting in lower efficiencies as hydraulic systems are scaled smaller. Finally, the proportion of seal friction losses to nominal power increase as hydraulic technology is scaled to smaller bore sizes [19].

Hydraulic power transmission equipment is typically expensive to manufacture compared to electromechanical systems due to tight machining tolerances to prevent leakages. Fluid passageways in the hydraulic manifolds often require multiple machining operations, and plugs are required to create bends within the conduit. Conduit bends typically are sharp 90° angles inducing small pressure drops that lower the overall efficiency of the system. There exists a

need to explore alternative manufacturing methods to reduce manufacturing cost and time, while producing a part whose quality meets or surpasses the current standards.

Hydraulic valve and pumps are highly susceptible to damage by contamination; therefore, the circulating fluid is flushed though systems of filters. In small two stage valves the orifice and mechanical feedback in the pilot stage can be damaged by particles as small as 10 um. These filtration systems often add addition weight and bulk to the hydraulic system, especially when scaled down to human assistive machines. If hydraulic technology is to be scaled down, there exists a need for future research on reducing the susceptibly of pumps and valves to particle damage.

The empirical laws that define fluid flow in hydraulic components are nonlinear, resulting in less accurate system models with higher uncertainties. This hampers the development of control methodologies resulting in hydraulic systems with smaller bandwidth compared to electromechanical systems at low power levels [7]. It is uncertain whether current empirical design guidelines for large scale systems are valid when scaled for low power applications. There exists a need for more accurate and validated methods of modeling small-scale hydraulic systems. These techniques will assist in the development of general design guidelines for hydraulic system and equipment to improve efficiency while reducing weight and size.

1.1.4 Research objectives

The purpose of this research is to design optimal hydraulic systems for small-scale human assistance machines that minimize over weight while maintain system performance. The following is a list of objectives that help to accomplish this task. One objective of this thesis is to model component-level (Chapter 2) and system-level performance (Chapter 3-7) of small-scale hydraulic systems by constructing validated models. The accuracy of models was validated by comparing the simulated results with measurements collected with physical hardware for both pump and valve controlled hydraulic systems. The validated models can then be used to quantify a variety of performance metrics for different methods of hydraulic control. This allows the different control methodologies to compared and contrasted across several metrics.

A second objective of this research is to predict the total hydraulic system weight for a desired application. Chapter 3 details the development of a computer design algorithm that can predict the weight and other metrics of a hydraulic system using the component models introduced in chapter 2. The design algorithm uses the application requirements to design a hydraulic system that is optimized for minimal weight. This allows the designer to gather a better understanding of their design space and how various requirements change the design. This design tool calculates ideal component parameters like cylinder and conduit bore sizes along with the various weights of components within the system. Finally the efficiencies of the components are mapped across all operating conditions.

The design algorithm and dynamic simulations were used to develop and simulate the performance of an adult and pediatric hydraulic powered ankle-foot orthosis in chapter 6 and 7. Both systems were prototyped to allow validation of the model with comparison of measured data, but also to illustrate how these tools can assist in the development of hydraulic powered human assistive machines. Chapter 7 explores the feasibility of using additive manufacturing to fabricate a hydraulic manifold for a pediatric-sized hydraulic ankle-foot orthosis. The additive manufacturing of hydraulic components can be used to reduce weight and manufacturing cost, while increasing hydraulic efficiency with the elimination of sharp bends, expansions, and contractions.

Another objective of this research is to determine methods of increasing the efficiency of small-scale hydraulic systems. The use of digital hydraulic technology is explored in chapter 5 in an effort to reduce valve throttling losses found in traditional proportional hydraulic systems. The flow rate of the system was controlled with a pulse width modulated (PWM) digital valve unloading to a reservoir. This analysis includes the detailed design and simulation of a small-scale digital valve.

1.2 Prior art on small-scale hydraulics in human assistive machines

Surgical tools are the smallest and most precise application of fluid power technology that highlights the compact force capabilities. In Peirs et al [20, 21], a miniature hydraulic actuated manipulator is attached to the end of a self-propelled endoscope. The 12 mm diameter endoscope manipulator uses three separate hydraulic pistons in a Stewart platform

configuration allowing a 10 mm stroke and tilts up to 35°. The manipulator is capable of generating up to 7 N with supplied pressures around 1 MPa. The hydraulic actuators are controlled with miniature piezoelectric valves that are integrated into the manipulator.

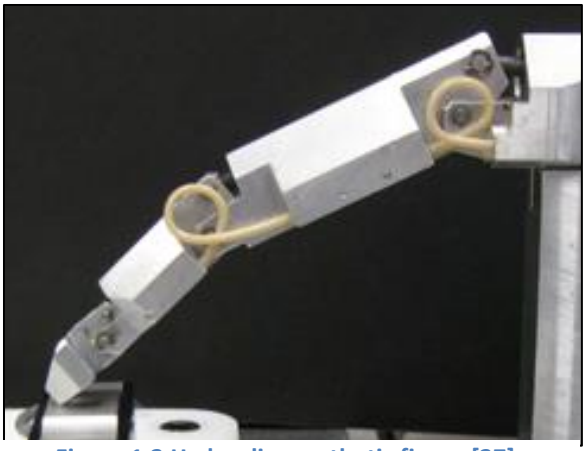

Figure 1.2 Hydraulic prosthetic finger [27]

A characteristic of hydraulic and pneumatic actuation methods are that they can be fabricated to be MRI compatible. Powered surgical tools that are MRI compatible assist in the development of better healthcare through less evasive surgeries. This is accomplished by improving positional accuracy through MRI feedback of endoscopes, ablators, and other surgical tools [22, 23, 24, 25, 26].

The power density and specific torque of hydraulic actuation systems are further demonstrated in the fabrication of a hydraulic prosthetic finger [27]. The prosthetic finger in fig. 1.2 weighs only 63 grams and uses two antagonistic 4 mm bore hydraulic cylinders at each joint with fluid pressures up to 13.8 MPa to generate 10 kg of clamping force. In Schulz et al [28], a hydraulic powered prosthetic hand is illustrated with a total of 15 degrees of freedom. The prosthetic hand demonstrated several key functional modalities that are important in everyday routines (Fig 1.3).

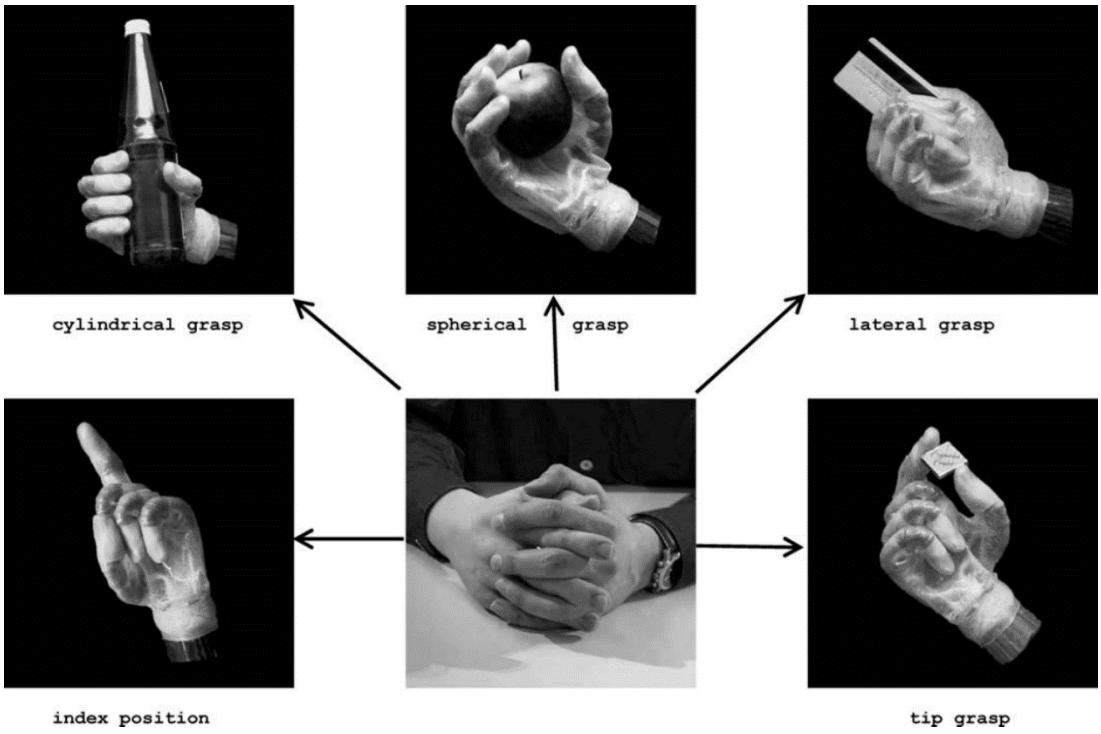

Figure 1.3 Functional modalities of hydraulic prosthetic hand [28]

The Berkeley Lower Extremity Exoskeleton (BLEEX) debuted in 2005 and was the first energetically autonomous, hydraulic, lower-limb exoskeleton, using 7 DOFs per leg with 3DOFs at the ankle, 1 at the knee, and 3 at the hip [29]. There are four joints actuated with bidirectional linear hydraulic cylinders: hip flexion/extension, hip abduction/adduction, knee flexion/extension, and ankle flexion/extension. The BLEEX used an onboard liquid-cooled, two stroke, opposed cylinder gasoline engine driving a hydraulic pump and a three phase brushless generator for powering the hydraulic actuators and control electronics [30]. The maximum efficiency of the power supply is 8.1% while producing 2.3 kW of hydraulic power (6.9 MPa and 20 LPM) with an additional 220 W of electrical power [31].

A second generation of hydraulic, lower-limb exoskeleton, the ExoHiker, weighed only 14 kg and was capable of distributing the weight of a 68 kg load to the ground requiring no additional effort from the operator [32] (Fig. 1.4). An 80 W-hr battery weighing 0.55 kg allowed the ExoHiker to carry its 68 kg load for 21 hours. The ExoClimber was specifically developed to allow the rapid ascent of stairs and steep inclines while carrying up to 68 kg load. A fully loaded

exoskeleton can ascend 600 stairs per pound of battery. The latest generation called the Human Universal Load Carrier (HULC), has a carrying capacity of 91 kg and demonstrated unloaded oxygen decrease of up to 12% when unloaded and up to 15% when fully loaded.

Figure 1.4 Left BLEEX [29] and right HULC [32]

In 2008 Raytheon Sacros unveiled their XOS2 exoskeleton that used hydraulic powered actuators to allow an operator to increase their lifting and carrying capacities at a ratio of 17:1 (Actual to perceived weight). The prototype in fig. 1.5 demonstrated walking at 1.6 m/s while carrying 91 kg distributed on the front and back of the suit [33]. A drawback of the current exoskeleton was that it can only run for 40 minutes untethered before the batteries need to be recharged [34]. The current work on the exoskeleton includes the development of an internal combustion power supply, an overall weight reduction, and the redesign of the servo valves to improve efficiency.

Figure 1.5 Raytheon Sacros's XOS2 [35]

Research conducted by Boston Dynamic illustrates the benefits of miniaturizing hydraulic systems for use in robotic system to accomplish human like function such as bipedal walk and running, in addition to lifting and manipulation of heavy objects (Fig. 1.6). Boston Dynamics has produced two continuously evolving untethered hydraulic robotic platforms, the humanoid robot “ATLAS”, and quadruped “BigDog” The latest generation of the ATLAS platform stands 175 cm tall (69 in) and weighs 82 kg (180 lb) with 28 hydraulic actuated degrees of freedom [36]. ATLAS takes advantage of additive manufacturing to reduce weight by incorporating lattices structures inside of large load bearing members. In addition, the hydraulic hoses were eliminated by directly routing the hydraulic conduits through the structure members with banjo style fittings at the joints [37]. Additive manufacturing has improved ATLAS’ strength to weight ratio allowing the robot to transverse a variety of terrains, and it also has the ability to stand up upon falling. All of these methods of improving the strength to weight ratio of the robotic platform can also be used in human assistive machines.

The quadruped robotic platform BigDog uses an internal combustion engine to directly drive a hydraulic power supply [38]. BigDog stands 76 cm tall and 92 cm long weighing 109 kg. The robotic platform is capable of running up to 4 mph across rubble, inclines up to 35°, and snow and water covered terrains. Internal combustion and hydraulic power have given BigDog the ability to carry loads up to 154 kg which is greater than the mass of the robotic platform. A fifth

arm was installed in the latest generation of BigDog, and it demonstrated an ability to throw 23 kg cinder blocks across the room [39]. This was accomplished by using synergistic motions of the legs and torso to supplement the powered motions of the arm. The use of synergistic movements should also be explored in multiple degree of freedom human assistive machines. The BigDog robot has evolved into two other hydraulic platforms the AlphaDog and the WildCat [40]. The AlphaDog aims to improve BigDog's loaded range capabilities from carrying a 57 kg load a distance of 19 km to 181 kg load a distance of 32 km while reducing the overall noise of the robot. WildCat is a platform designed for mobility and speed galloping up to 32 km/h.

Figure 1.6 Old gen. ATLAS, current gen. ATLAS, BigDog, WildCat, and AlphaDog (Left to right) [36]

Chapter 2 Comparisons, Models, and Properties of Small-Scale Hydraulic Components

2.1 Introduction

This chapter provides detailed and validated models techniques of small-scale hydraulic systems to compare and contrast system-level metrics. As a precursor to system-level modeling, component-level models must be defined or built from previous art. The objective of this chapter is to introduce empirical models and the crucial performance variables for the different components of a hydraulic system.

There are a variety of working fluids, accumulators, valves, and pumps that use different technology to perform similar function. The first step in optimizing a hydraulic system for use as a human assistive machine is the selection of the best hardware suited for the application. This requires comparing different types of hydraulic equipment against the requirements of human assistive machines, in order to select the best hydraulic technology for this application.

2.2 Working fluids

There are six types of working fluids used in hydraulic systems: mineral oils, HFA oil in water emulsions (5% oil & 95% water), HFB water in oil emulsions (60% oil and 40% water), HFC water in glycol emulsions (60% glycol & 40% water), HFD synthetic fluid containing no water, HFE synthetic fluid biodegradable fluid [2]. The main advantage of using a water based fluid is to reduce the thermal degradation and overall flammability of the working fluid [41]. As water based fluids are heated a layer of steam forms around the fluid preventing ignition. The viscosity of water is approximately two orders of magnitude lower compared to mineral oils. This is an attractive property, because it reduces viscous losses at the cost of being a poor lubricant for mating surface. The reduction is viscosity also increases leakage losses. Finally the bulk modulus of water is higher compared to mineral oil. This makes water based systems stiff and responsive for high frequency dynamics at the cost of introducing pressure shock referred to as water hammer [41]. Braking fluids require relatively high stiffness fluids, and therefore are typically HFC fluids. In colder climates the high water content percentages can lead to issues with freezing as a result HFD fluids are recommend for braking systems in this environment.

The use of water based working fluids has the disadvantage of requiring bacteria control with the use of additives [42]. It is essential that working fluids used within human assistive machines are nontoxic, and often the additives in water based fluids are toxic. In addition, the vapor pressure of water is three orders of magnitude lower than mineral oil at similar temperatures, so water based oils are more susceptible to cavitation [2]. Finally water is often a more chemically unstable working fluid, because of its wiliness to oxidize with metals. There has been significant research to overcome the disadvantages of using water as a working fluid by designing specialized motor/pumps [41, 43], valves [44, 45]

The six types of working fluids can be modeled as Newtonian fluids where fluid shear stress is proportional to the rate of change of the fluid velocity with respect to the distance from the surface (2.1). The material property relating shear stress to the velocity profile is dynamic viscosity. It is an essential parameter when modeling hydraulic systems, because nearly all of hydraulic energy losses are a function of the working fluid viscosity. The kinematic viscosity is the dynamic viscosity normalized by the fluid's density.

$$\tau = \mu \frac{dU}{dy} \quad (2.1) \qquad \nu = \frac{\mu}{\rho} \quad (2.2)$$

The most common method of defining the relationship between fluid viscosity and temperature is using Walther's equation which is entirely empirical [46]. It is common convention to use a based 10 measurement, so d is assumed to be 10.

$$\left(\upsilon + a\right) = bd^{1/T^c} \quad (2.3)$$

There is a strong nonlinear relationship between viscosity and temperature [2, 6]. As a result heat losses and temperatures of the working fluid must be considered when modeling and designing hydraulic systems for continuous operation. This is crucial in small-scale applications where there is little thermal capacity in the system allowing the component surfaces and working fluid to quickly heat up. Water has a significantly lower viscosity than mineral oil, so water based working fluids, especially HFA fluids, typically have viscosities lower than standard

mineral oil. There exists a trade-off controlled by fluid viscosity. As the working fluid viscosity is reduced, viscous losses decrease but leakages increase resulting in lower volumetric efficiencies. As a result Type HFA fluids are typically only used within pumps with high volumetric efficiencies like axial and radial piston pumps [2]. This trade-off is further explored within axial piston pumps in section 3.3.2.

Table 2.1 Fluid properties and variable definitions

Sym.	Description	Unit	Sym.	Description	Unit
a,b,c,d	Fluid dependent constants	-	V_G	Volume of gas	m^3
B	Effective bulk modulus	Pa	V	Total volume	m^3
B_L	Liquid bulk modulus	Pa	Y	Length from surface	m
n	Specific heat ratio of gas	-	α	Volumetric gas content at atmospheric pressure	-
P_a	Atmospheric pressure	Pa	ρ	Fluid density	kg/m^3
P	Fluid mixture pressure	Pa	τ	Fluid shear stress	N/m^2
T	Fluid temperature	K	μ	Dynamic viscosity	$N\ s/m^2$
U	Fluid velocity	m/s	ν	Kinematic viscosity	m^2/s
V_L	Volume of liquid	m^3			

The bulk modulus of a fluid is a measure of volumetric compressibility due to a pressure difference and is generally one of the largest sources of compliance in a hydraulic system [47].

$$B = -V\frac{dP}{dV} \quad (2.4)$$

The natural frequency of a pump and valve controlled systems are a function of the effective bulk modulus of fluid as shown in section 4.2.1, resulting in the dynamic performance being correlated to this fluid property. A decrease in the effective bulk modulus of the fluid has shown to cause additional compressibility losses, decrease response time, decrease the accuracy of positional control, and increase instability with a hydraulic system [2, 6, 47].

The effective bulk modulus decreases with the addition of air trapped in the working fluid through system cavitation [6]. Air has a bulk modulus that is three orders of magnitude lower than typical hydraulic fluids, so the addition of small amount of entrapped air can significantly lower the effective bulk modulus of the working fluid. As a result, small-scale hydraulic systems are especially susceptible to trapped air. If equal volumes of air are entrapped within equal length small bore and large bore rigid conduits, the effective bulk modulus of the smaller conduit will be exponentially lower than the large conduit. In addition, there is an increasing asymptotical relationship between pressure and bulk modulus of a fluid with entrapped air that is illustrated in figure 2.1.

$$B = B_L \frac{1 + \alpha\left(\frac{P_a}{P_a + P}\right)^{1/n}}{1 + \alpha \frac{P_a^{1/n}}{n(P_a + P)^{(n+1)/n}} B_L} \text{ where } \alpha = \frac{V_G}{V_L} \quad (2.5)$$

The red horizontal line in figure 2.1 represents the constant bulk modulus of the liquid with no entrapped air. Therefore, high accuracy hydraulic systems are often operated at high pressures to reduce compressibility uncertainty. In small-scale hydraulic systems where entrapped air has a significant effect on the effective bulk modulus, it is good practice to maintain higher operating pressure to increase the effective bulk modulus.

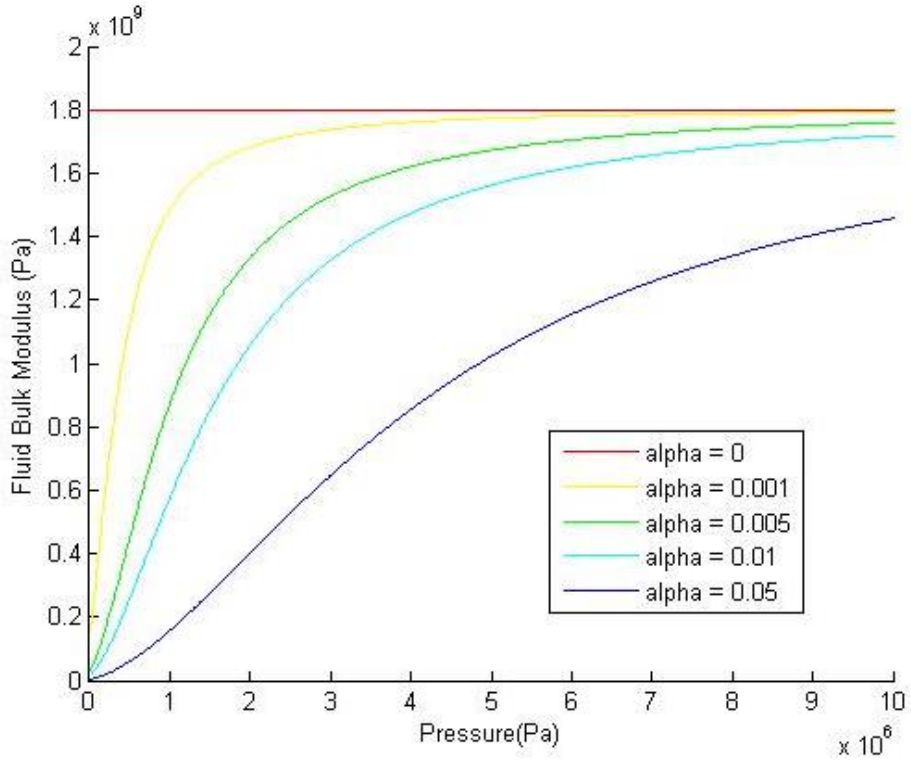

Figure 2.1 Effective bulk modulus as a function of pressure and entrapped air

The final property used to select a working fluid for a small-scale hydraulic system is density, because it can significantly impact the weight of them system. The densities of mineral oils are typically around 870 kg/m^{-3}, while the densities of water based fluids are higher ranging from HFB type fluids around 930 kg/m^3 to 1130 kg/m^3 for HFD phosphate ester.

Based on a comparison of chemical and physical properties, the preferred working fluid for use in human assistive hydraulic machines is mineral oil. Water based fluids are primarily used in applications with elevated working temperatures due to the risk of ignition. This is not the case for human assistive machines where the operating temperatures of the working fluid along with the surface temperatures of the machinery must remain low as it is directly interfaced with the body. In addition, mineral oils are non-toxic and can be safety ingested, whereas other fluids should not be in direct contact with the skin. The use of a toxic fluid would limit a user's ability to perform their own maintenance on the device without specialized personal protective equipment. There often exists an optimum fluid viscosity to achieve maximum system-level

efficiency. Mineral oils provide a large range of viscosities to select from. Finally mineral oils have a relatively high bulk modulus and low chemical reactivity. They also have to lowest density making the system weight lighter compared to using a water based working fluid.

2.3 Cylinders and Seals

Standard single and double rod cylinders with O-ring seals are used to convert the fluid power to linear mechanical power. O-ring seals are also used in the poppets and spools of the control valves. A variety of hydraulic seals have specifically designed geometries for specific pressure ranges and fluid viscosities; however, there is little quantitative modeling on leakage and friction. In addition, specialized rod seals are typically limited to 0.125" bore size, and would not be small enough for many applications.

O-rings represent a standardized seal within the industry with several leakage and friction models. O-ring seals also represent a worse-case friction scenario, as more complicated geometries are used to reduce friction while decreasing leakage. There exist other types of low friction cylinders including rolling diaphragm cylinders and clearance cylinders that do not incorporate seals**,** but neither are feasible for high pressure applications due to the high amount of leakage. The piston and rod inertia, fluid viscous damping, and compressibility of the fluid inside the cylinder are assumed negligible in steady state operation, while they are included in the dynamic models.

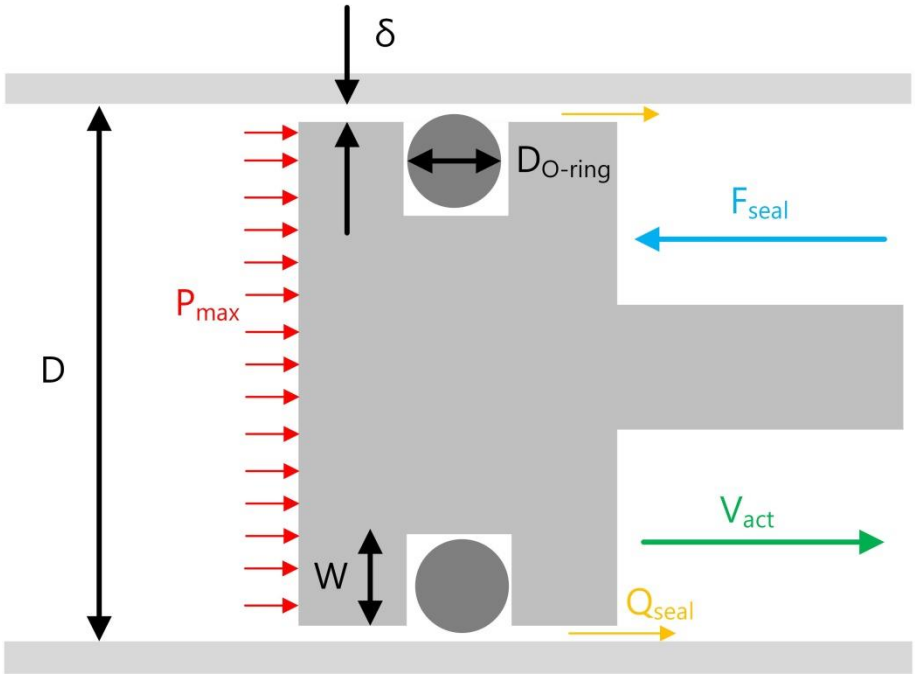

Figure 2.2 Seal cross-section

Table 2.2 Actuator and seal variable definitions

Symbol	Description	Unit	Symbol	Description	Unit
$D_{O\text{-}ring}$	O-ring cross-section diameter	m	T	O-ring deformation parameter	-
D	Diameter of piston/cable	m	V_{act}	Piston velocity	m/s
E_{seal}	Elastic modulus of seal mat.	Pa	W	Seal gland depth	m
F_{seal}	Seal friction force	N	δ	Piston clearance	m
P_{act}	Cylinder pressure	Pa	λ	Squeeze ratio	-
Q_{seal}	Seal leakage flowrate	m^3/s	μ_f	Seal coefficient of friction	-
S	O-ring contact width	m	σ_m	Maximum O-ring contact pressure	Pa

The experimentally validated O-ring friction empirical models are highly dependent on the seal squeeze ratio. The squeeze ratio is a measure of how much the seal is radially compressed between the gland diameter and matting surface. The current manufacturing standards

recommend a radial compression of between 8 and 16% for dynamic applications due to friction and wear considerations [48, 49].

$$\lambda = \frac{D_{O-ring} - 0.5 \cdot (W + \delta)}{D_{O-ring}} \quad (2.6)$$

A significant amount of research has been previously conducted in [49] to characterize the seal friction forces of specifically small O-rings.

$$F_{seal} = \pi \cdot \mu_f \cdot E_{seal} \cdot D_{piston/cable} \cdot D_{O-ring} \cdot \lambda \cdot \sqrt{2 \cdot \lambda - \lambda^2} \quad (2.7)$$

The selected material for the O-rings is nitrile rubber with a coefficient of friction μ_f = 0.3-0.5 for relatively smooth and lubricated surfaces and an elastic modulus E_{seal} of approx. 3.5 MPa. This empirical model has been validated for miniature piston and rod seals, and assumes that the seal friction force is independent from pressure. A second model of seal friction described in [48], is dependent on both seal compression and pressure but has only been experimentally validated for large-scale applications.

The seal friction force is highly dependent of the squeeze ratio; therefore the squeeze ratio should be determined based on the clearance and pressure of the particular application. In low pressure, applications the squeeze ratio can be lower to improve the efficiency, while still maintaining a leak free interface.

The Stribeck curve is an elastic-hydrodynamic lubrication model defining the coefficient of friction μ_f as a function of the lubricating fluid viscosity, interfacing materials, normal loads, and the velocity between the surfaces [50] (Fig. 2.3). The Stribeck model is separated into three regions that define lubrication dynamics: boundary, mixed, and fluid friction. In the boundary region there is a significant amount of surface contact between the mating surfaces with little fluid lubrication. As the lubrication parameter transitions to the fluid region, there is less surface contact and a thicker layer of lubrication.

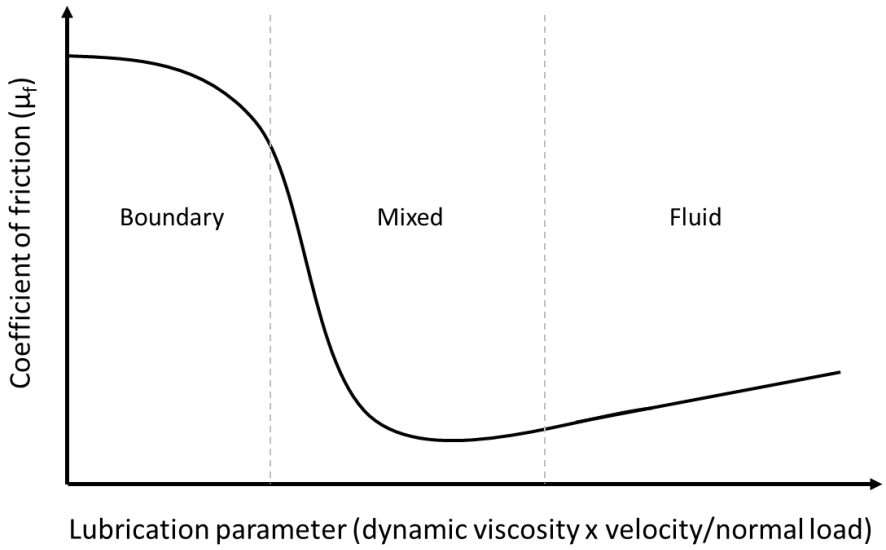

Figure 2.3 Stribeck elastic hydrodynamic lubrication model

The Stribeck model illustrates that there is a region where friction is minimized. Seals can be designed to operate within this region by selecting the appropriate fluid viscosity normal load. The normal load is primarily a function of squeeze ratio with pressure being negligible. The seal velocity is typically varied over a large range during operation. This model also illustrates that at low piston velocities, there is significantly higher amount of friction until the mixed region is reached.

The model for seal leakage is dependent on the velocity of the mating surface and the pressure [49]. The leakage across an O-ring seal using current industrial seals and dimensional recommendations is negligible compared to small-scale flow rates.

$$Q_{seal} = 1.495 \cdot \pi \cdot D_{piston/cable} \cdot \mu^{0.71} \cdot V_{act}^{1.71} \cdot \sigma_m^{-0.71} \cdot S^{0.29} \quad (2.8)$$

$$S = D_{O-ring} \cdot (2 \cdot \lambda + 0.13) + D_{O-ring} \cdot T \quad (2.9)$$

$$T = \left(\left(\frac{0.39}{1-\lambda} \right) - (\lambda + 0.065) \right) \cdot \left(1 - \exp\left(\frac{-4.6 P_{act}}{E_{seal}} \right) \right) \quad (2.10)$$

$$\sigma_m = E_{seal} \cdot (1.34 \cdot \lambda + 0.087) + 1.15 \cdot P_{act} \quad (2.11)$$

2.4 Hose, Tubing, and Viscous Losses

All hydraulic systems incorporate conduits to transfer the fluid power generated by a pump to the distal valves and actuators. Hydraulic conduits can be separated into two types: rigid fixed geometry like manifolds and bent metal tubes and flexible geometry like Teflon or other elastomer hoses. Hoses are manufactured with a variety of methods. The hose design commonly used for high pressure applications has a Teflon core with an external Kevlar braid. The Teflon functions to seal the fluid, while the Kevlar braid provides the necessary hoop strength for high pressures and protection from punctures. This hose design has a high ratio of hoop strength to weight compared to traditional rubber hoses while maintaining a high degree of flexibility. Bent tubing has a significantly higher ratio of hoop strength to weight compared to all hose designs. As a result, bent tubes should be used in all applications where a flexible conduit is not required to reduce the weight of the hydraulic system.

A significant source of pressure compliance within a hydraulic system results from the elastic stretch of the fluid conduit. The elasticity of the hydraulic conduit is typically negligible for small diameter metal cylinders and tubing. However, in systems with flexible hoses made of rubber or Teflon the elasticity effects of the conduit can be the dominant factor of compliance [2, 6]. The results of section 4.3.1 show that the elastic expansion of the hose as it is pressurized needs to be accurately characterized in order to accurately predict the response time of a small-scale hydraulic system.

Table 2.3 Conduit variable definitions

Symbol	Description	Unit	Symbol	Description	Unit
$D_{H/T}$	Inside diameter of conduit	m	Re	Reynolds number	-
f	Darcy friction factor	-	ΔP	Pressure drop	Pa
K_d	Bend or fitting loss factor	-	U	Average fluid velocity	m/s
K_s	Hydraulic diameter shape factor	-	ρ_f	Fluid density	Kg/m^3
$L_{H/T}$	Length of conduit	m	v_f	Fluid kinematic viscosity	m^2/s
Q	Fluid flow rate	m^3/s			

The viscous losses within the hydraulic conduit can be estimated using the Darcy Friction Factor for internal flow [51]. The Reynold's number of the internal flow can be calculated using:

$$\mathrm{Re} = \frac{4 \cdot Q}{\pi \cdot D_{H/T} \cdot \nu_{fluid}} \quad (2.12)$$

For an internal flow the critical Reynold's number marking the separation between laminar and transition/turbulent flow is 2300. The Darcy Friction Factor for laminar flow (Re < 2300) is estimated using (2.13) where K_s is a shape factor of the internal conduit. The shape factor for a circular profile is 64. There are several empirical formulas for estimating viscous losses of turbulent flow including Blasius [51], Swamee-Jain [52], and Haaland [53]. Since the surface roughness of the conduit is difficult to measure for flexible hoses, the assumption was made to consider the conduit smooth bore and use the Blasius correlation. The Blasius correlation is valid for smooth bore internal turbulent flow with Reynold's numbers between 2300 and 10^5 (2.14) [51].

$$f = \frac{\mathrm{Re}}{K_s} \quad (2.13) \qquad f = \frac{0.316}{\mathrm{Re}^{0.25}} \quad (2.14)$$

The fluid velocity profile across the conduit diameter is parabolic, but has an average velocity that can be approximated with:

$$\overline{U} = \frac{4 \cdot Q}{\pi \cdot D_{H/T}^2} \quad (2.15)$$

The pressure drop across the length of tube or hose is calculated with (2.14). The viscous losses for internal, smooth bore flow are illustrated in fig. 2.4 using mineral oil at 60°C and a viscosity of 16 cSt. The results illustrate that there is a steep increase in pressure drop as the fluid transitions into turbulent flow. The figure also shows that if the inside bore of the conduit is not sized appropriately with conduit flow rates, that the viscous losses within the conduit could be significant and pull the overall system efficiency down. The pressure drop across a bend or fitting is calculated with (2.16) where K_d is a dimensionless constant representing different

bends and fittings. A 45° and 90° bend in hose or tubing have K_d values of 16 and 30. A standard tee fitting has K_d values of 20 (thru) and 60 (branch) [51].

$$\Delta P_{H/T} = \frac{f \cdot \rho_f \cdot L_{H/T} \cdot \overline{U}^2}{2 \cdot D_{H/T}} \quad (2.16) \qquad \Delta P_{bend\ /\ fittings} = \frac{f \cdot \rho_f \cdot K_d \cdot \overline{U}^2}{2} \quad (2.17)$$

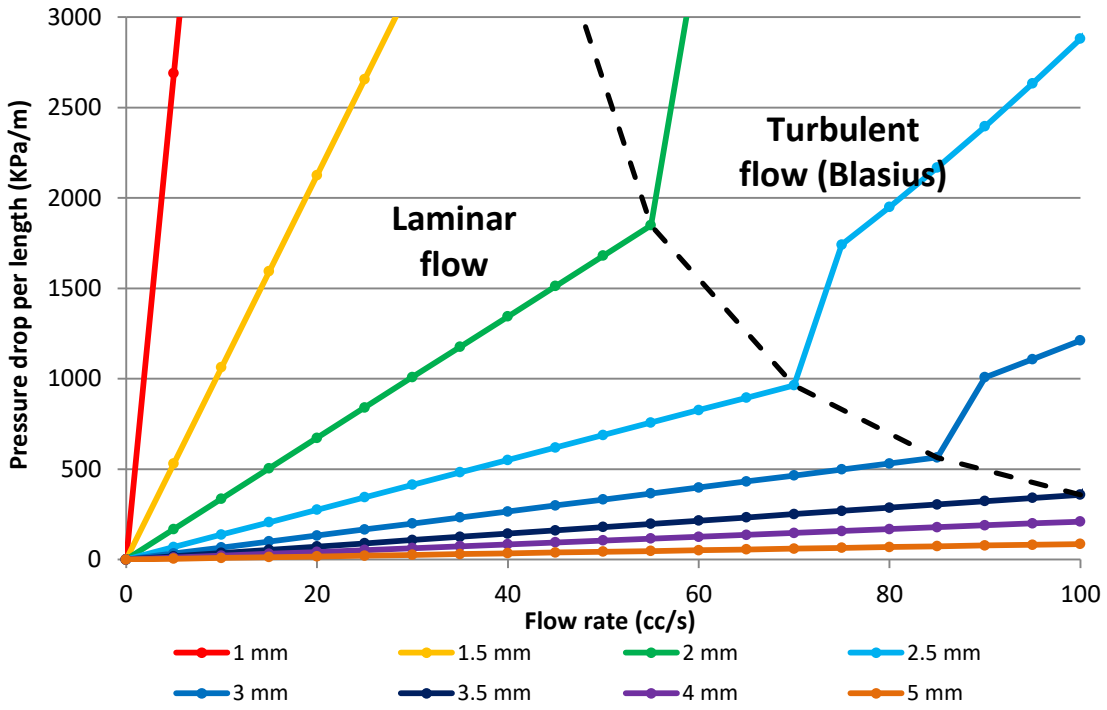

Figure 2.4 Pressure drop per length as a function of flow rate for internal smooth bore flow, at seven bore sizes

The viscous losses in conduits are highly dependent on the kinematic viscosity of the fluid. As a result of the fluid's kinematic viscosity varying exponentially with temperature according to eq. 2.3, the viscous losses within the system are highly dependent on temperature. It is common for many machines using fluid for lubrication or power transmission to require a warm-up period that increases the temperature of the circulating fluid and lowers fluid viscosity before the system is loaded.

Lowering fluid viscosity also results in higher Reynold's numbers, shifting the transition from laminar to turbulent flow to lower flow rates. The selection of the tubing and hoses for an

application has to consider the expected fluid working temperatures and flow rates to ensure flow within the conduits remain laminar and minimize viscous losses. Fig. 2.4 plots the pressure drop constant across the internal, laminar, smooth bore flow as a function of fluid temperature for three different hose sizes. The pressure drop constant represents the pressure drop per unit length per fluid flow rate. There are currently three high pressure Teflon hydraulic hoses sizes available for low flow rate hydraulic systems 2, 3.5, and 5 mm. Fig 2.5 can assist future engineers and designers in selecting hose and tubing for small-scale hydraulic systems.

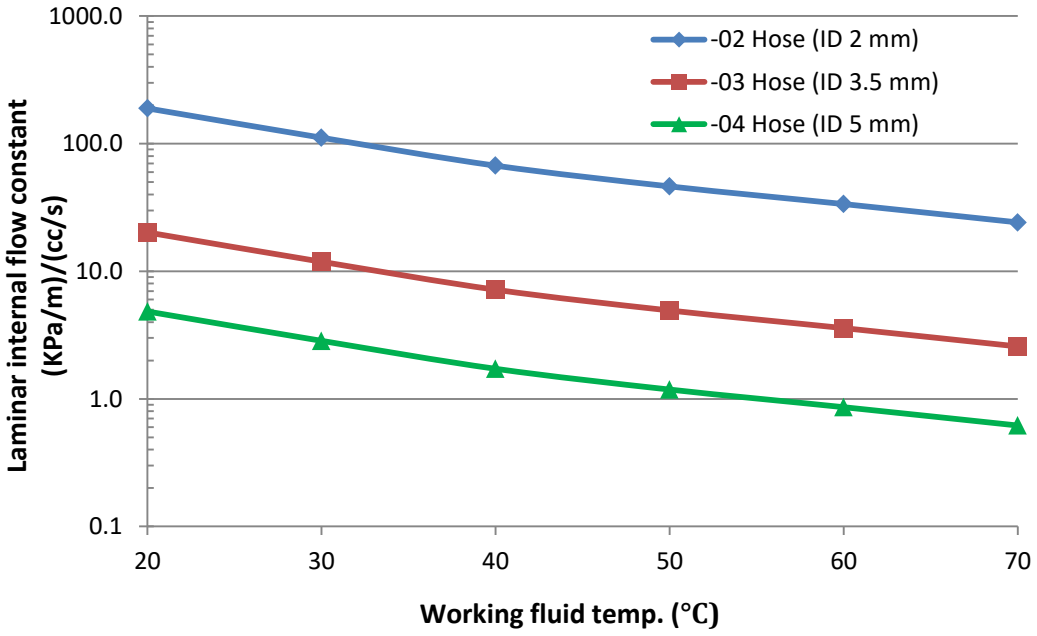

Figure 2.5 Pressure drop const. across the internal, laminar, smooth bore flow as a function of fluid temperature

2.5 Accumulators

An accumulator stores hydraulic energy in the form of a pressurized fluid and a mechanical elastic element. There are two types of accumulators that are feasible for small-scale hydraulic systems; compressed gas and spring loaded. In a compressed gas accumulator a pressure gradient forces fluid into a reservoir, a chemically inert gas like nitrogen is compressed on the opposite side of a diaphragm or inside a bladder. In a spring loaded accumulator pressurized fluid loads a spring on the opposite side of the piston as fluid is drawn into a reservoir. The

energy in the accumulators is stored within the pressurized inert gas or the springs. The force generated by a spring is proportional to the deflection distance, so the pressure increases linearly as the cylinder is charged. The pressure exerted by the compressed gas in the accumulator is generally modeled with the ideal gas dynamics. The use of compressed gas and spring loaded accumulators in small-scale portable hydraulic system are compared in a case study in section 2.5.1.

There exist three common functions of accumulators. Accumulators can be used to increase the maximum power capabilities of a system during intermittent operation by charging the accumulator when the system is at rest and discharging the accumulator to supplement the fluid power provided by the pump. In this application, the accumulator also saves energy as the pump is charging an accumulator instead to dissipating power over a relief valve. Accumulators make an inexpensive method of increasing the peak power and efficiency of system compared to the additional expense of a hydraulic power unit [6]. An accumulator also functions as a capacitive element that can be used to filter pressure fluctuations within a system making them ideal for dampening and shock absorption vehicle suspensions [6, 54]. A common industrial manufacturing function of accumulators is to maintain system pressure, suppling additional fluid for leakages during holding operations [54].

2.5.1 Comparison of compressed gas and spring loaded accumulators

The objective of this section is to compare the weight and volume of equivalent gas and spring accumulators, because these are important in constructing a lightweight and compact small-scale hydraulic system. The pressure and volume of enclosed ideal gases are governed by eq. 2.18. In a compressed gas accumulator the gradual charging of the accumulator can be modeled as an isothermal process (n = 1, Eq. 2.19). The discharging of the accumulator is modeled as a rapid adiabatic process (n > 1 in Eq. 2.20).

$$PV^n = const \quad (2.18) \qquad P_1V_1 = P_2V_2 \quad (2.19) \qquad P_2V_2^n = P_3V_3^n \quad (2.20)$$

The exponent can vary based on what gas is compressed and how fast the accumulator is discharged. Exponent values can be found in [2] for accumulator discharging.

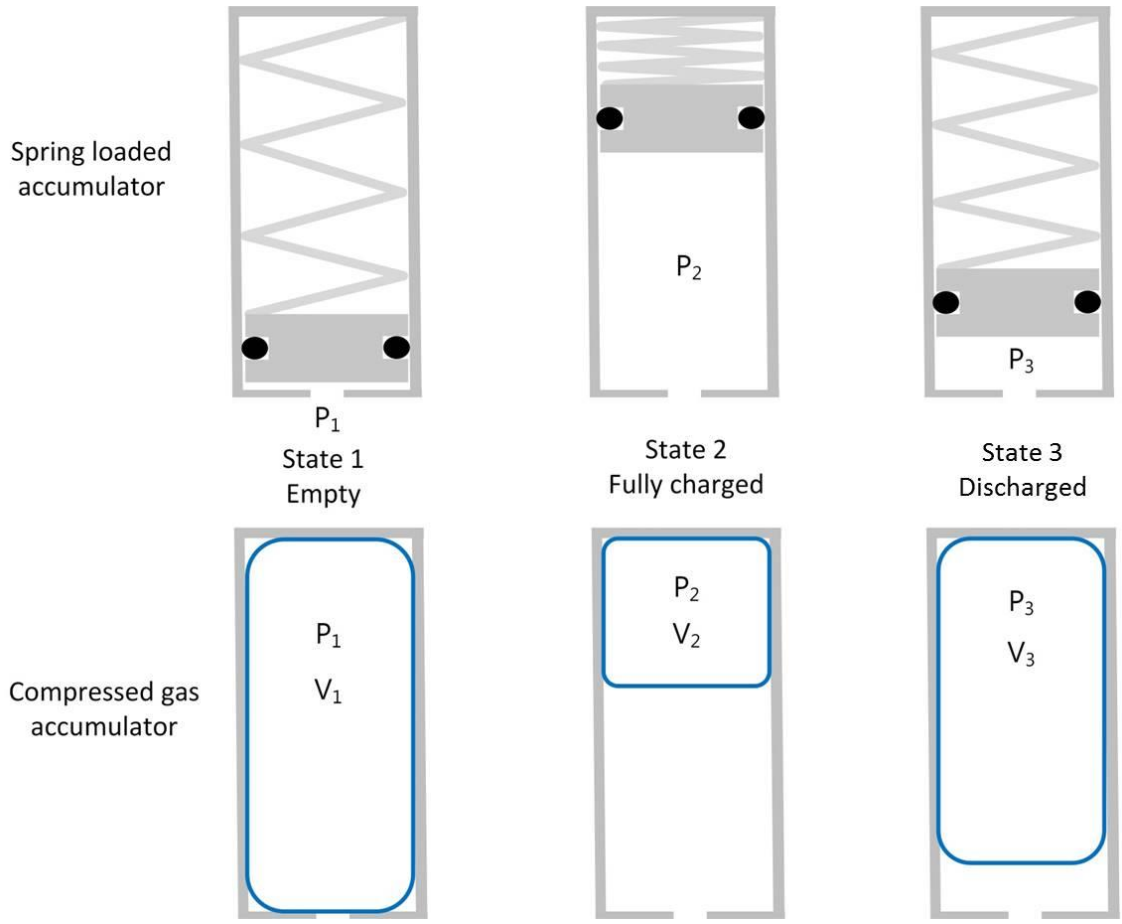

Figure 2.6 Comparison of spring and gas accumulators (Empty, Fully charged, Discharged)

The gas accumulator is modeled in three states in order to calculated unknown properties (Fig 2.6). State 1 is an empty preloaded state with no fluid in the accumulator, state 2 is the fully charged state after gradual isothermal compression, and state 3 is the discharged state after the rapid adiabatic expansion. Accumulators are typically preloaded to 90% the lowest operational pressure [2]. If the accumulator has equal acting areas of pressurized fluid and gas, the fluid pressure and gas pressure can assumed to be equal. This provides a pressure buffer where the accumulator maintains a small amount of fluid to assist in maintaining the lowest operational pressure. The pressures at preload P_1, maximum system pressure P_2 and minimum system pressure P_3 are all known. The difference between the gas volumes at states 2 and 3 is equal to the volume that the accumulator will discharge. If the system of equations are solved, it yields

preloaded gas volume V_1, a charged gas volume V_2, and end of actuation gas volume V_3. The size of the accumulator is approximately equal to the preloaded gas volume.

In designing a spring loaded accumulator a geometry parameter k specifies the ratio between the outside diameter D and total length of the accumulator L_T (Eq. 2.21). The preload spring force F_1 can be calculated with the pressure at preload P_1 and the accumulator piston area A_p (Eq. 2.22). The accumulator linear spring constant k_s can be calculated using a force balance on the piston comparing states 2 and 3 with the actuated fluid volume ΔV_{23} and the maximum and minimum system pressures P_2 and P_3 (Eq. 2.24). The total fluid volume of the accumulator ΔV_{12} can be calculated using a force balance of the piston comparing states 1 and 2 (Eq. 2.22).

$$k = \frac{L_T}{D} \quad (2.21) \qquad F_1 = P_1 A_p \quad (2.22) \qquad \frac{\Delta V_{23}}{A_p} k_S = A_p \left(P_2 - P_3\right) \quad (2.23)$$

$$\frac{\Delta V_{12}}{A_p} k_S = A_p \left(P_2 - P_1\right) \quad (2.24)$$

The maximum spring deflection including the preload force is calculated with force balance on the piston at state 2 (Eq. 2.25). High performance compression springs are capable of a maximum 50% deflection. The total volume of the spring loaded accumulator can be estimated by adding the total fluid and spring volume at the fully charged state of the accumulator (Eq. 2.26).

$$\Delta x_{\max} = \frac{P_2 A_p}{k} \quad (2.25) \qquad V_{tot} = \Delta x_{\max} A_p + \Delta V_{12} \quad (2.26)$$

Figure 2.7 illustrates the total volume of a compressed gas and spring loaded accumulators with a minimum and maximum operating pressures 13.7 and 20.7 MPa. If the minimum and maximum operating pressures are varied, the total accumulator volume demonstrates a similar trend where the compressed gas accumulator volume is approximately twice the volume of the spring loaded accumulator for the same fluid capacity.

It is crucial to understand that a significant portion of an accumulator volume is required for the storage of the gas and the deflected spring. When the accumulators are fully charged, only 50%

and 25% of the total volumes in spring loaded and compressed gas accumulators store pressurized fluid, while the remaining is designated for the spring or compressed gas storage.

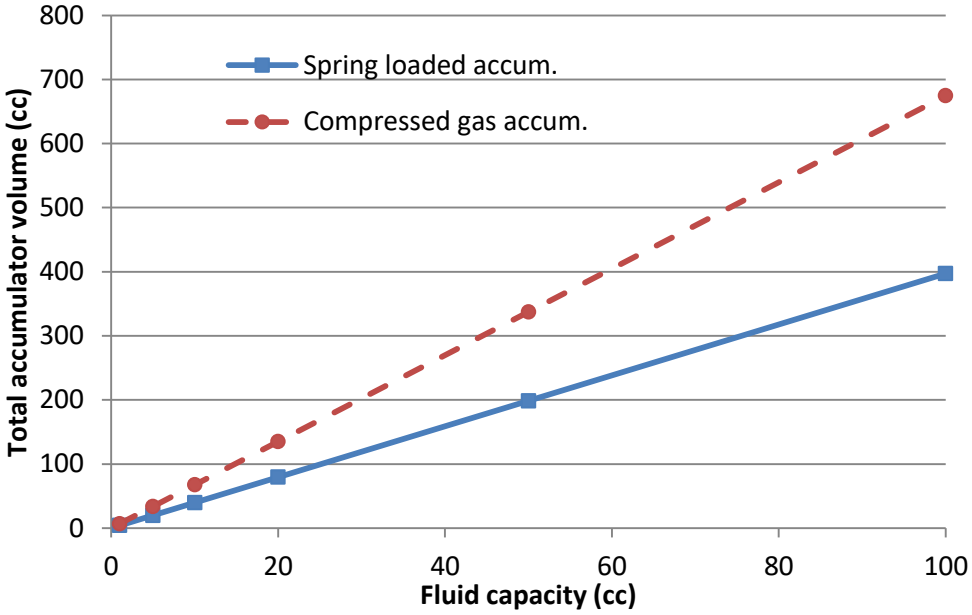

Figure 2.7 Case study: Accumulator size as a function of fluid capacity

The thicknesses side walls t_1 of the compressed gas and spring loaded accumulator cases were estimated using an approximation for thin walled pressure vessel (Eq. 2.27) [55]. The thickness of the accumulator end caps t_2 were approximated using thin plate formula (Eq. 2.28) [56]. These empirical strength formulas or pressure were also used in estimating the dimensions of cylinder and pumps cases.

$$t_1 = \frac{N_S P_2 D}{2\sigma_y} \quad (2.27) \qquad t_2 = \sqrt{\frac{3D^2 N_S P_2 (1+\upsilon)}{32\sigma_y}} \quad (2.28)$$

An average safety factor N_s for pressure vessels of 4.5 is used due to the fact that an accumulator failure is dangerous to the user of the device. The accumulators were designed such that the geometry parameter k is a constant between the types and sizes of accumulators. The material properties of tensile yield stress σ_y, Poisson's ratio ν, and density ρ are based on the accumulator being composed of a high strength to weight material, aluminum alloy 7075-T6.

The ratio of the outside spring diameter D_s to the diameter of the coiled d wire is defined as the spring index C (Eq. 2.29). Typical springs are designed to have index values from 4 to 12 with higher stiffness applications having low index valves [57]. The linear stiffness k_S of a helical compression spring can be calculated with eq. 2.30 [57], with N_C being the number of active coils. The spring is constructed of spring steel using the corresponding values of the material's shear modulus G and density ρ. For this case study it is assumed that the outside spring diameter D_S can be set equal to the outside accumulator diameter D. The spring index is selected to be 5 based on the high stiffness application, and there are assumed to be an un-active coil on each side of the spring to better distribute the force to the coincident surface. Using these relations and assumptions, the number of active spring coils N_C and the weight of the spring can be calculated.

$$C = \frac{D_S}{d} \quad (2.29) \qquad k_S = \frac{d^4 G}{8 D^3 N_C} \quad (2.30)$$

The geometries and material densities of the accumulator cases, springs, and fluid were used to estimate the weight of a fully charged accumulator as a function of the accumulator fluid capacity (Fig 2.8). In general, the spring loaded accumulators were 27% heavier compared to compressed gas accumulators for the same capacity. For this case study the weight of the spring was around 50% of the total weight of the accumulator. The relatively high minimum system pressure requires a large preload force and a stiff spring. This requires more spring material to absorb and store the elastic energy increasing the overall weight. The lower the spring index the heavier the overall spring will be for a given stiffness with a constant diameter. Therefore it is crucial to select the highest spring index possible within the spring design that will withstand the applications stresses and not fail due to fatigue.

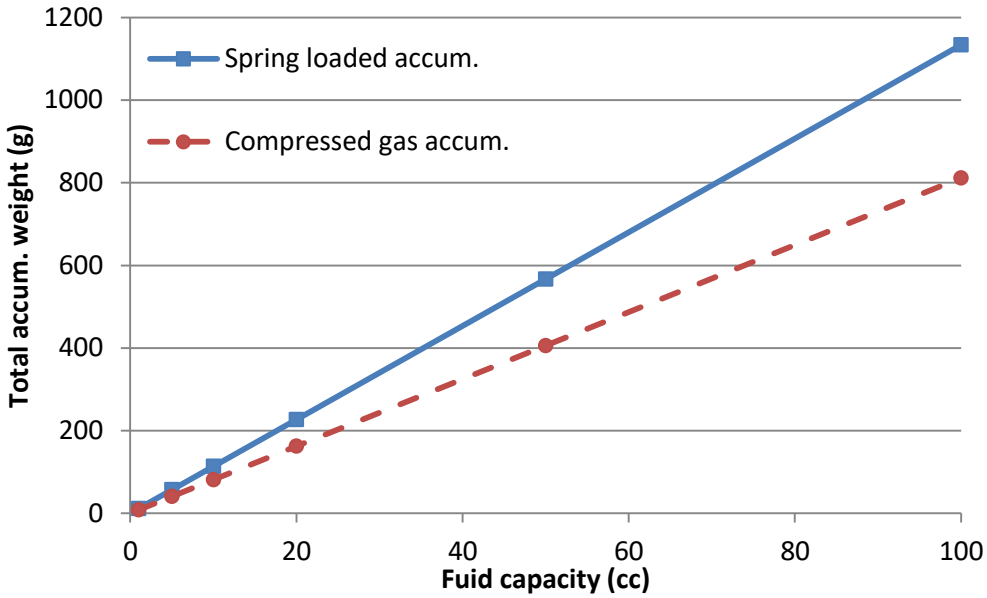

Figure 2.8 Case study: Accumulator weight as a function of fluid capacity

The recoverable energy stored within a compressed gas accumulator is equal to the total work W required to compress an ideal gas adiabatically (Eq. 2.31) [58]. The recoverable energy within a spring accumulator is approximately equal to the work required to compress a preloaded spring. (Eq. 2.32)

$$W = P_2 V_2^n \frac{V_3^{1-n} - V_2^{1-n}}{1-n} \quad (2.31)$$

$$W_S = \frac{1}{2} k_S \Delta x^2 + F_1 \Delta x = \frac{1}{2} k_S \left(\frac{\Delta V_{23}}{A_p} \right) + F_1 \left(\frac{\Delta V_{23}}{A_p} \right) \quad (2.32)$$

The volumetric and weight energy densities of the two types of accumulators scale linearly with fluid capacity (Table 2.4). In this case study, the volumetric energy density of a spring loaded accumulator is 59.7% higher compared to the compressed gas accumulator. In contrast, the mass energy density of the compressed gas accumulator is 35.0 % higher compared to the spring loaded accumulator. The results illustrate one type of accumulator does not offer an overall design advantage. If the hydraulic system is being optimized to be compact a spring loaded accumulator should be used; however, if weight is being minimized a compressed gas

accumulator will likely fit the application better. The use of spring loaded accumulators is rare within traditional high pressure, high flow hydraulics, because of the requirements of large, heavy, and stiff springs. However, when spring loaded accumulators are shrunk down to small-scale applications, the spring size is feasible with the additional bonus of spring load accumulators being more compact compared to gas counterparts.

The performance of a compressed gas accumulator is based on the gas dynamics, and since there is typically only one gas used for this application, the performance is fixed. In a spring load accumulator the spring can be switched out quickly for a spring with different stiffness, changing the charging dynamics. Both types of the accumulators have the ability to change the minimum charge pressure by setting a minimum spring compression or a precharge gas pressure.

Table 2.4 Accumulator comparison

	Compressed gas accumulator	Spring loaded accumulator
Volumetric energy density (J/cc)	2.51	4.01
Mass energy density (J/g)	1.89	1.40

The minimum, maximum system pressures, and the geometry parameters were the constants for this case study. Varying these input variables shifts the individual values but the general trends are still observed.

2.6 Valves

Hydraulic valves can be separated into two categories based on their output control method: digital and proportional. Digital hydraulic technology and valves are discussed in chapter 5. Proportional hydraulic valves use the concept of varying orifice area (throttling) to control the flow rate or pressure of a flowing fluid (Fig. 2.9).

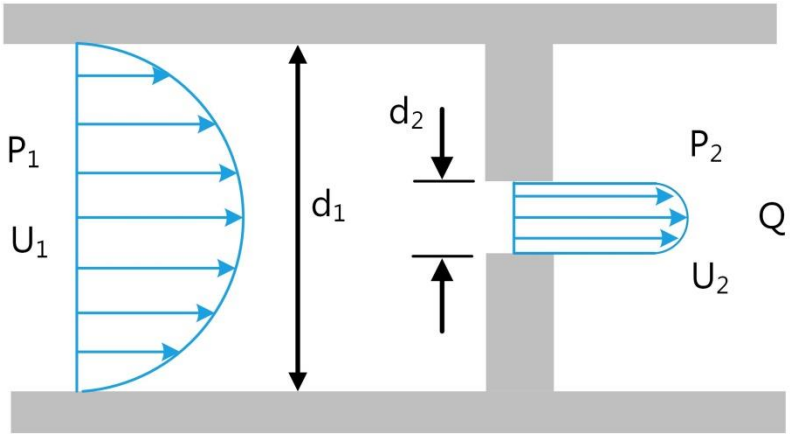

Figure 2.9 Orifice geometry and parameters

Table 2.5 Orifice parameters

Symbol	Description	Unit	Symbol	Description	Unit
A_2	Orifice area	m^2	Q	Flowrate	m^3/s
C_d	Discharge coefficient	-	U	Average fluid velocity	m/s
P	Pressure	Pa	ρ	Fluid density	kg/m^3

According to Bernoulli's equation, if the cross-sectional area of an internal flow is reduced, the fluid velocity increases and the pressure decreases. In hydraulic valves the change in potential energy of a fluid can be assumed negligible, and Bernoulli's equation can be reduced to eq. 2.33. If assuming a steady state and incompressible flow, Bernoulli's equation through a standard orifice can be rearranged to eq. 2.34.

$$P_1 - P_2 = \frac{\rho}{2}\left(U_2^2 - U_1^2\right) \quad (2.33) \qquad Q = C_d \sqrt{\frac{1}{1-\left(d_2/d_1\right)^4}} A_2 \sqrt{\frac{2\left(P_1 - P_2\right)}{\rho}} \quad (2.34)$$

The discharge coefficient takes into consideration the viscous losses as energy within the flowing pressurized fluid is converted to thermal energy. The value of the discharge coefficient is determined by the orifice geometry.

All hydraulic valves have three essential components: a control element, an actuation mechanism, and a housing. The flow control element actuates within the housing to vary orifice area. The two most common control element geometries are poppet and spool, but there exists

a variety of control geometries that are variations of the two listed [6]. The second component of a hydraulic valve is an actuation mechanism to position and hold in place the control element. Fluid pressure, fluid momentum, and seal friction exert forces of the control member and a high force, low displacement actuation methods are required to vary the orifice area. The main actuation mechanisms employed in hydraulic valves are springs, solenoids, torque motors, and hydraulic pressure amplification.

2.6.1 Valve function

The function of a valve can be separated into three main categories: pressure control and flow or directional control [6, 59]. In the orifice equation there is one control variable, orifice area, and two other variables. If the desired function of the valve is to control flow rate, the pressure supplied to the valve is held constant, while flow rate is controlled by varying orifice area. In pressure control, the flow rate supplied to the valve is held constant, while the pressure is controlled by varying the orifice area. However, it is often difficult and inefficient to hold one variable either pressure or flow rate constant, and alternative methods are explored within this research. The following sections describe more specific valve functions in detail.

The operation of a large proportion of valves is controlled directly from the supply port or from a pilot line. A pilot operated valve uses an auxiliary hydraulic line to define the function of the valve. In addition, valves can include pilot stages where often a smaller pilot valve directly controls a larger valve using hydraulic amplification. Pilot stages can be used to improve efficiency as larger orifices can be used at the cost of longer response times. The forces on the valve control member can become large in high pressure applications, and pilot stages with hydraulic amplification might be necessary to adequately position the main control member within the valve.

Relief valve

A type of valve commonly used within hydraulic circuits to protect the pump and other pressure sensitive components from pressure fluctuations is a pressure relief valve [6]. As the force generated from the pressure differential across the control element equals the spring preload force, the control element moves to allow fluid flow to a low pressure or reservoir port. This

pressure differential is defined as the relief valve cracking pressure. The spring preload force can often be varied with the use of a screw adjustment, allowing the cracking pressure to be varied.

Check and shuttle valves

A check valve is a two port valve allowing fluid flow in only one direction. A pilot-operated check valve is three port valve with unidirectional flow when the pilot line differential pressure is below the cracking pressure. As the pilot line pressure differential surpasses the valve cracking pressure, flow is allowed in both directions. A shuttle valve is a three port directional valve that uses the comparison between the valve cracking pressure and pressure differential between the two inlet ports to control which inlet port is connect to the outlet port. In a traditional shuttle valve the inlet port with the higher cracking pressure is connected with the outlet port; however, in an inverse shuttle valve the lower pressure port is connected with the outlet port.

2.6.2 Electromechanical Valves

In order to obtain high accuracy with fast rise times, hydraulic systems have incorporated electrically controlled valves including electrohydraulic proportional solenoid valves (EHPSV) and servo valves. An EHPSV uses a proportional solenoid to allow a continuous range of spool positions. A servo valve uses a torque motor and a pilot stage hydraulic amplifier to allow a continuous range of spool positions. In both proportional solenoid and servo valves the continuous range of spool positions allows an infinite range of output flow rates or pressures.

In general there are several differences in design that allow servo valves to be used in applications where rise time and valve weight are critical, while EHPSV are used in applications where efficiency is critical. First, servo valves use internal mechanical feedback increasing the accuracy of the spool position. This internal feedback assists in maintaining the linear relationship between current supplied to the torque motor and flow rate [54]. The spool within a servo valve is designed to be critically centered having no overlap and decreasing the deadband [6, 60]. A limitation of a critically centered spool is that when power to the valve is lost, there is little assurance that there is no flow through the valve. The clearances and tolerances with servo valves are often tighter compared to EHPSVs allowing improved accuracy, hysteresis, and less spool leakage at the cost of being more expensive to manufacturer [59].

EHPSV often require the use of large and heavy solenoids to generate sufficient force to actuate the spool. The high inductance coils require large actuation currents. A servo valve uses hydraulic amplification and a pilot stage which are often much lighter than the direct drive solenoid. However, a servo valve pilot stage requires a small continuous flow to operate properly. Therefore, servo valves constantly dissipate energy through the pilot stage even when the spool is in the null position.

In order to improve the controllability and accuracy of EHPSVs, the solenoid plunger is connected with a linear variable differential transformer (LVDT) that measures position and provides closed loop feedback [59]. An additional advantage of EHPSV is that they are less susceptible to contamination damage, because there is no pilot stage with small orifices and tiny mechanical parts. This is especially true when the valves are scaled down for small-scale hydraulic systems where damage can result from particles as small as 10 microns [54].

There are two common methods for hydraulically amplifying the force of a torque motor in a servo valve to position the spool valve using a flapper nozzle (fig. 2.10) or a flexjet (fig. 2.11). In a flapper nozzle system the torque motor positions a flapper against one of two pilot nozzles. The actuation angle of the flapper is less than 3° in most valves [6]. As the flapper obstructs the pilot nozzle flow by creating a ring orifice, the pressure inside the pilot conduit increases [6]. The pilot lines are connected to the sides of the spool. In fig. 2.10 if the left pilot line pressure P_{n1} increases while P_{n2} maintains a constant pressure, the spool is pushed to the right as the force generated from the pressure differential equals the force generated by the centering springs. A feedback spring is connected between the spool and the armature to provide a positional feedback force that adjusts the flapper to the correct position. As the spool shifts to the right the orifice between the supply line and the output A port opens as does the orifice between output port B and the return line.

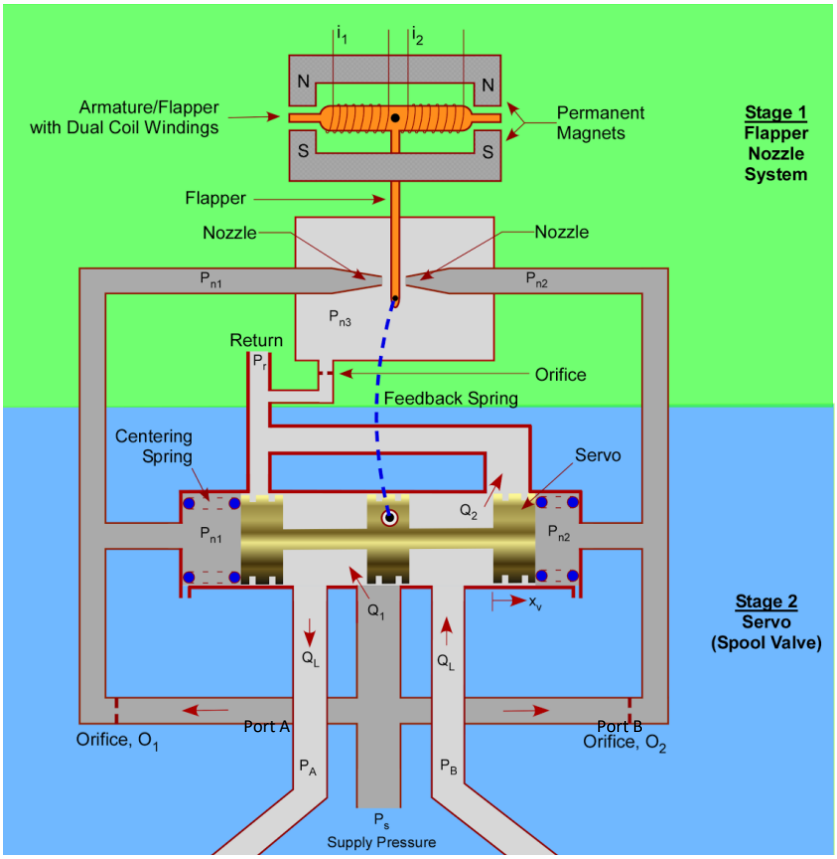

Figure 2.10 Cross section of flapper nozzle servo valve [61]

In a flexjet system, the pilot flow is forced through a jet pipe that is directly connected to the torque motor arm. The torque motor positions the end of the jet pipe over two orifices that are connected to the ends of the spool. If the torque motor positions the pipe to the left orifice in fig. 2.11, pressure P_{s1} increases due to increase in the kinetic energy of the fluid. The spool shifts right until the pressure differential between P_{s1} and P_{s2} is balanced by the centering springs.

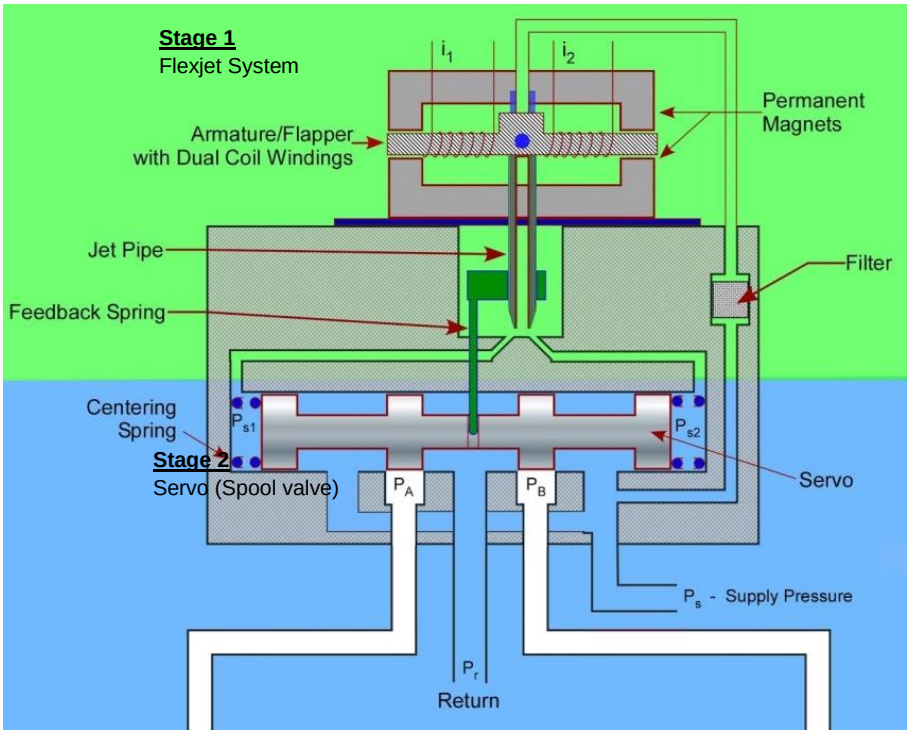

Figure 2.11 Cross-section of flexjet system [61]

It is impractical to determine what type of valve should be used for small-scale hydraulics without knowing the application or specific design of the valve. There exists trade-offs between system response dynamics and valve efficiency that need to be matched to the specific application. In general, EHPSVs are ideal for applications with prolonged periods of inactivity due to the fact they can be designed to require no energy to hold the spool in the specified position, while servo valves always dissipate a pilot flow. Both EHPSV and servo valves use orifice metering to control fluid flow. This introduces a pressure drop and significantly lowers system-level efficiency. Chapter 5 introduces the digital high frequency switching valve that reduces metering losses and eliminates pilot flow losses while maintaining a fast system response. Therefore, small-scale hydraulics systems exclusively use positive displacement pumps.

2.7 Motors and Pumps Technology

The heart of every hydraulic system is a pump that supplies the pressurized fluid that is dispersed throughout a system of valves and actuators. There are two main categories of

pumps: hydrostatic otherwise known as positive displacement and hydrodynamic. In a hydrostatic pump fluid is drawn into an expanding cavity and then forced out as the cavity contracts and compresses the fluid. A hydrodynamic pump uses a rotor to accelerate the fluid, and then converts the kinetic motion of the fluid into pressure. Hydrodynamic pumps have the benefit of not being susceptible to pressure damage but the drawback of not being able to generate significant pressure with limited radial fluid momentum [6]. Hydrodynamic pumps are typically limited to fluid transport system where the system experiences minimal pressure.

There are seven types of positive displacement pumps in use and are listed in order of increasing cost, efficiency, and pressure capabilities: spur gear, internal gear, gerotor, balanced vane, radial piston, axial piston, and screw [6, 8]. In spur gear, internal gear, and gerotor pumps the expansions and contraction takes place in the space where the gears or rotors meshes. Internal gear and gerotor pumps use a rotating internal gear that mates with a ring gear on offset axes. A limitation that all three designs share is that the drive shaft experiences significant side loading due to unbalanced pressure forces [8]. This means that gears can only be of limited width and displacement for a certain pressure rating. In addition, the geometry of meshing gears has a large amount of dead volume resulting in a lower volumetric efficiency. The unique aspect of a gerotor pump is the mating surface has a crescent moon geometry that provides more displacement and reduces dead volume compared to the gear pumps [6].

Balanced vane pumps consist of a circular rotor with evenly spaced protruding vanes circulating with a double eccentric cam ring with two inlet ports and two outlet ports. The vanes extend and retract to maintain a seal with the inner diameter of the ring. As a result of the mirrored ports, the pressure on the main drive shaft is balanced, increasing the reliability and lifetime of the bearings. In addition, the fluid flow generated by the rotating vanes is uniform and generates little noise even at high power levels [8].

In radial and axial piston pumps the expansion and contraction of the fluid takes place in a cylinder with an actuating piston. The major benefit of this design is the cylinder and piston geometry has a longer sealing surface resulting in higher volumetric efficiencies and allowing pressure generation upwards of 5000 psi. However, the increased complexity results in higher manufacturing costs along with increased weight and size. Axial piston pumps typically have

volumetric efficiencies above 95% and overall maximum efficiencies around 85% resulting in significant energy savings at high power levels [8]. The majority of the energy loss within piston pumps is in the form of seal friction and viscous losses that is converted to heat and dissipated through the case and working fluid. The high volumetric efficiency capabilities of piston pumps allow the use of lower viscosity working fluids [8]. The displacement of the axial piston pump can be adjusted by altering the angle of the swash plate that controls the position of the pistons.

A notable feature of the radial piston design is that it provides protection from high pressure damage and has the ability to be a variable displacement pump. This is accomplished by pressurizing the back side of the piston in the stroke control cavity. This alters the position of the piston connected to the stroke control spring. A slight variation of a traditional inline axial piston pump is a bent axis axial piston pump where the barrel and piston rotate on an inclined axis, and the pistons are secured to the drive shaft with ball joints, thus eliminating the swash plate. The angle of the bent axis can be up to 40°, and this increases the displacement compared to an inline axial piston pump.

The purpose of this research is to design optimal hydraulic systems for small-scale human assistance machines that minimize overall weight while maintain system performance. This application requires a highly efficient pump that has high weight and volumetric power densities. In large-scale hydraulic applications gear pumps are typically employed in applications where high weight and volumetric powered densities are required, whereas axial piston pumps typically demonstrate the highest efficiencies. In order to select a pump type for this application, small-scale axial piston and gear pumps are compared quantitatively in the next section.

2.7.1 Comparison gear and axial piston pumps

This section compares performance of axial piston pumps with gear pumps using data collected on commercially available pumps. The methods and performance parameters used to compare different pump technologies depend on whether the system uses a tethered electrical power source or a portable battery. When using a tethered electrical source, the electrical energy is assumed to be plentiful and electrical energy has no cost in added weight. In this scenario one should select a pump that results in the highest pump power density. Figure 2.12 uses table 2.6

and eq. 2.35 to compare the energy densities of commercial axial piston pumps produced by Takako Industries with gear pumps produced by Marzocchi Pompe.

Table 2.6 Pump comparison metrics and parameters

Symbol	Description	Unit	Symbol	Description	Unit
D_p	Pump Displacement	cc/rev	η_m	Pump mechanical efficiency	-
E_{hyd}	Hydraulic energy capacity	W·hr	η_{motor}	Motor efficiency	-
m	Mass	kg	η_{vol}	Pump volumetric efficiency	-
P_{max}	Maximum pump pressure	MPa	γ	Energy density	W·hr/kg
ε	Power density	W/kg	ω	Pump shaft angular velocity	rpm

$$\varepsilon_{pump} = \frac{P_{\max}\omega_{\max}D_p\eta_v}{60 \cdot m_{pump}} \quad (2.35)$$

The commercial availability of hydraulic pumps below 500 W is limited, so the commercial data is limited to pumps produced by these two companies. The commercial catalog data shows that gear pumps are capable of reaching higher power densities, around 5 kW/kg, while axial piston pumps are lower. The results illustrate that for a tethered hydraulic power supply a gear pump should be used to minimize weight of the system.

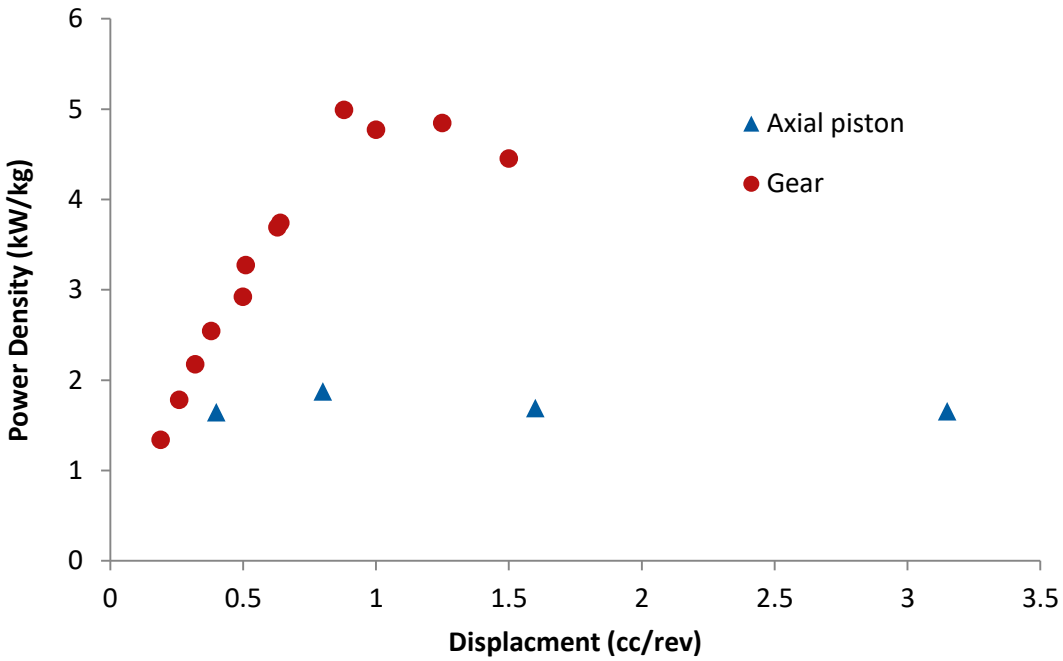

Figure 2.12 Commercial pump comparison: Power density as a function of pump displacement

If the hydraulic power supply is untethered and designed to use a battery, additional electrical energy requires a larger battery, adding additional weight to the system. The metric used to compare battery powered hydraulic power supplies is total energy density of the pump and battery.

$$\gamma_{pump\&batt} = \frac{E_{hyd}}{m_{pump} + m_{battery}} = \frac{E_{hyd}}{m_{pump} + \frac{E_{hyd}}{\eta_n \eta_v \eta_{motor} \gamma_{battery}}} \quad (2.36)$$

The weights of the electric motors and conduits in the power supply are excluded, because they are assumed to be similar with the use of different pump types of equal power. The efficiency of the electric motor is assumed to be 70%, and the energy density of current lithium polymer battery technology is assumed to be 151 W·hr/kg [62]. Figure 2.13 compares the energy densities of axial piston and gear pump types while varying the hydraulic energy capacity. The hydraulic energy capacity is the amount of hydraulic energy a power supply can generate on a

single charge of the battery. Catalog data is acquired from Takako Industries and Marzocchi Pompe.

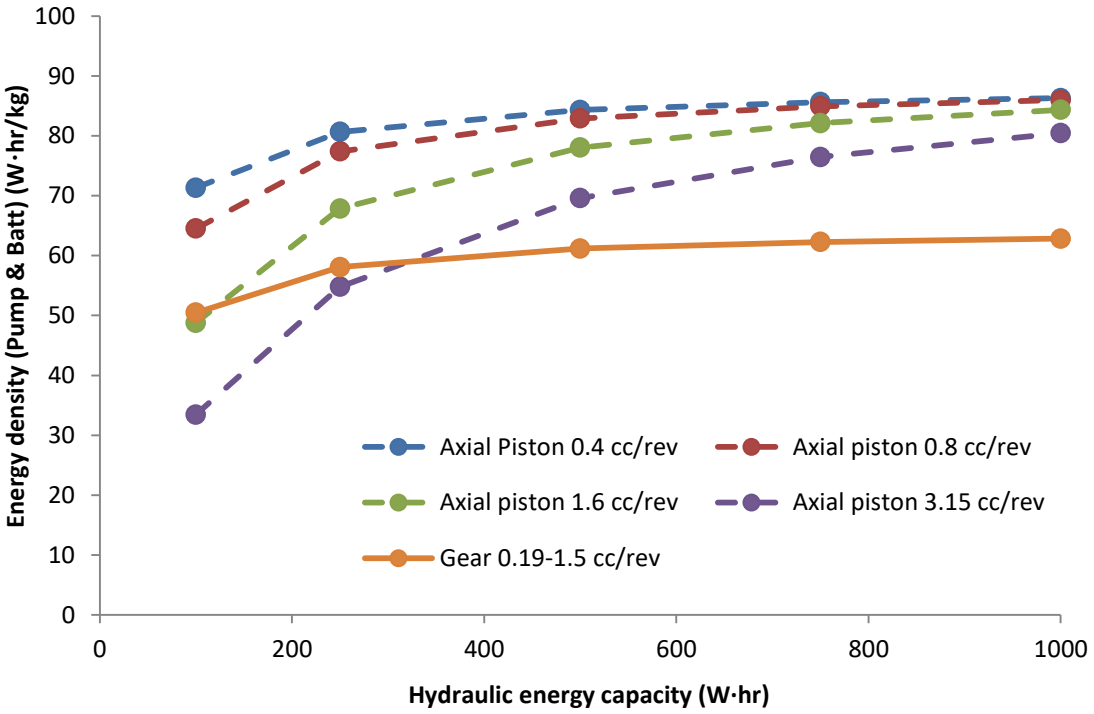

Figure 2.13 Commercial pump comparison: Energy density as a function of hydraulic energy capacity

The results illustrate that if the required hydraulic energy capacity of the portable hydraulic power supply is above 300 W·hr, the use of an axial piston pump will result in an overall lighter system. The shift in pump types can be attributed to the increased influence of pump efficiency and battery weight as the runtime increases. The volumetric efficiencies of the pumps are comparable, but commercial data suggests that axial piston pumps typically have 10 to 15% higher mechanical efficiencies than gear pumps for small displacement pumps. The only scenario when a gear pump should be used for a portable hydraulic power is if a large displacement, high flow pump is required for a short period of time. In this situation the high power density of the pump outweighs the difference in mechanical efficiency.

2.7.2 Model of hydraulic axial piston pump

The pump is the heart of a hydraulic system and is one of the main sources of losses in pump and valve controlled systems. This section develops an empirical model of the losses within an

axial piston pump that is based a modeling foundation established in the literature. This model is also used for modeling the losses within a hydraulic motor. In the past two decades there has been a significant amount of work done modeling axial piston pumps. This began with Ziegler et al in [63, 64] modeling the forces on the swash plate from the piston and slipper assemblies. This 11th order axial piston pump model was simplified and validated to a 2nd order model by Manring et al [65, 66]. The axial piston pump model in Bergada et al [67, 68] focuses on dynamics between the port plate and barrel modeling leakages as well as the torque distribution.

The cross-section of the axial piston pump geometry is illustrated in fig. 2.14. The relative position of the piston (X_p) with reference to the barrel is modeled with the sinusoidal function as the barrel is rotated, and the slippers maintain contact with the swash plate (Eq. 2.37). The fluid flowrate generated by an individual piston Q_p is modeled with (Eq. 2.38).

$$L_X(t) = R\tan(\alpha)(1+\cos(\theta(t))) \quad (2.37)$$

$$Q_P(t) = A_P \frac{dX_p}{d\theta}\frac{d\theta}{dt} = A_P R\tan(\alpha)\sin(\theta(t))\omega(t) \quad (2.38)$$

The sign convention is fluid leaving the piston is negative and entering is positive. As the barrel rotates from 0 to π, the piston actuates from top dead center (TDC) to bottom dead center (BDC) drawing fluid into the piston. As the barrel continues to rotate from π to 2π, the piston actuates from BDC to TDC pushing and compressing fluid out of the piston.

Table 2.7 Axial piston pump parameters

Symbol	Description	Units	Symbol	Description	Units
A_p	Piston area	m^2	r_p	Piston radius	m
h_0	Axial barrel and port plate separation	m	α	Swash plate angle	rad
L_X	Piston position	m	θ	Angle of barrel rotation	rad
N	Number of pistons	-	ω	Angular velocity of barrel	rad/s
Q_p	Piston flowrate	m^3/s	Ω	Tilt angle between barrel and port plate	rad
R	Piston radial distance	m			

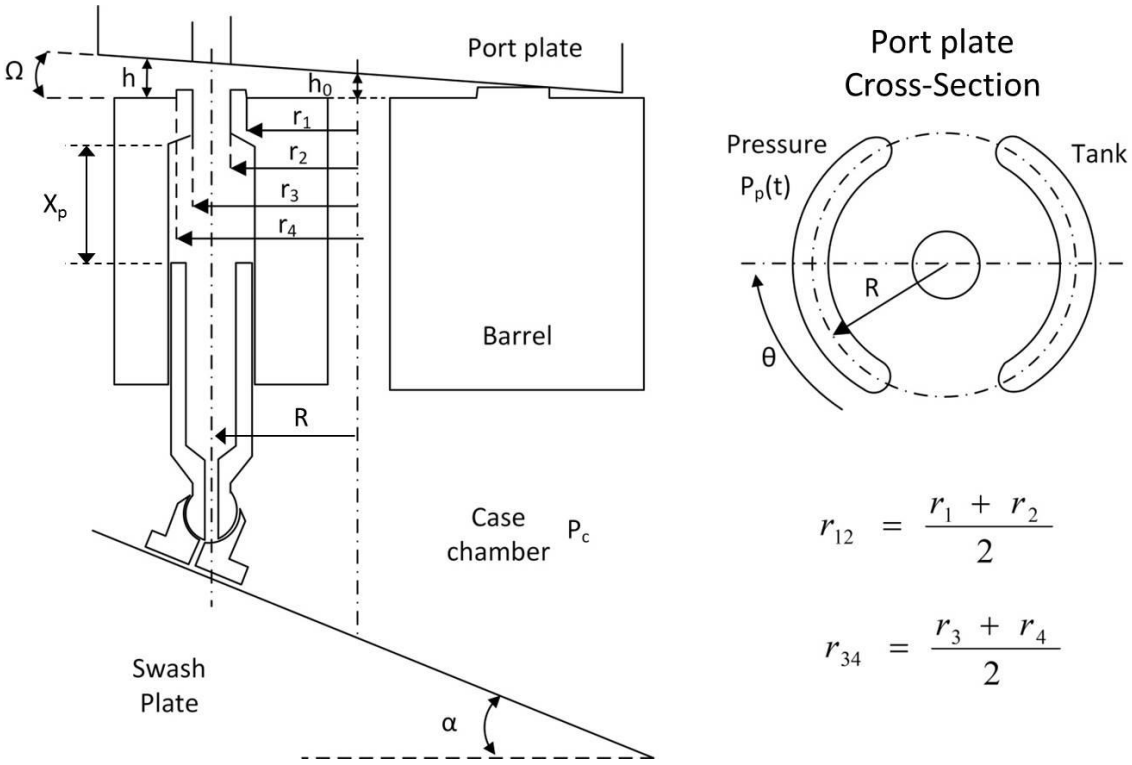

Figure 2.14 Axial piston pump model and geometry

Fluid leakage within an Axial Piston Pump

There are two significant locations of leakage within an axial piston pump. The first is the spacing between the piston and the barrel housing allowing fluid to flow into the pump case. The second is the interface between the valve plate and piston barrel where fluid again flows into the pump case.

The pistons inside of an axial piston motor/pump do not use traditional O-ring or cup rubber seals between the piston and the housing. Instead, they use simple clearance seals and dissimilar materials to reduce the coefficient of friction between them. It is unrealistic to assume that the piston is perfectly centered within the casing, because the pressure distribution around the piston would need to be radially uniform (Fig. 2.15). This scenario represents an unstable equilibrium point that can only be maintained if the fluid flow is perfectly radially uniform. Instead, an eccentricity piston model is used that assumes the piston is pressed against the casing making contact at one radial point. The gap between the piston and barrel piston housing h_1 is a function of the clearance between piston housing and the piston c, the eccentricity distance e, and the piston cross-sectional angle ϕ.

$$h_1 = c + e \cdot \cos(\varphi) \quad \text{where} \quad c = r_0 - r_p \quad (2.39)$$

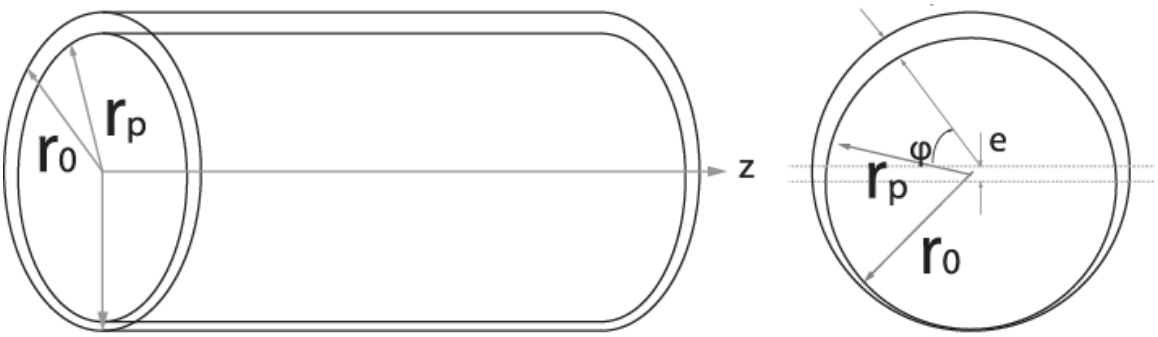

Figure 2.15 Eccentricity piston model

The fluid leakage between the piston and barrel housing at a given time can be calculated with:

$$Q_{L,P}(t) = \frac{\pi \cdot r_p \cdot c^3\left(1 + 1.5e^2\right)}{6\mu_f L_L(t)}\left(P_P(t) - P_c\right) \quad (2.40)\ [7] \qquad L_L(t) = L_0 + L_x(t) \quad (2.41)$$

In order to determine the leakage for an entire revolution of the barrel, the leakage must be integrated with respect to time as the piston pressure and leakage length vary.

Table 2.8 Axial piston parameters

Symbol	Description	Units	Symbol	Description	Units
c	Piston chamber clearance	m	P_c	Case pressure	Pa
e	Eccentricity	m	P_P	Piston pressure	Pa
L_0	Initial leakage length	m	$Q_{L,P}$	Piston leakage flowrate	m^3/s
L_L	Piston leakage length	m	μ_f	Fluid dynamic viscosity	Pa·s

The interface between the barrel piston housing and the valve plate is designed to be parallel; however, there exists a large radial pressure distribution that causes the interface between the port plate and barrel to tilt. As the barrel rotates, the pistons on one side experience high pressures as the fluid is pressurized and pushed out of the barrel, and on the opposite side of the barrel, the pistons experience low pressures as fluid is being drawn in. In order to accurately model the leakage and torque loss due to friction at the barrel and valve plate interface, the offset must be incorporated into the model. The pressure distribution over the exterior and interior radial lands at this interface can be calculated using the equations (2.42 & 2.43) from [67, 68].

$$P_{ext\_land} = P_{\text{int}}\left(1+\frac{\ln(r/r_3)}{\ln(r_3/r_4)}\right)+P_{ext}\frac{\ln(r_3/r)}{\ln(r_3/r_4)}+\frac{3\mu\cdot\omega\cdot\alpha\cdot r_{34}\sin(\theta)}{2(h_0+\alpha\cdot r_{34}\cos(\theta))^3}\left(\left(r_3^2-r^2\right)+\frac{\left(r_4^2-r_3^2\right)\ln(r_3/r)}{\ln(r_3/r_4)}\right) \quad (2.42)$$

$$P_{\text{int}\_land} = P_{\text{int}}\left(1+\frac{\ln(r/r_2)}{\ln(r_2/r_1)}\right)+P_{ext}\frac{\ln(r_2/r)}{\ln(r_2/r_1)}+\frac{3\mu\cdot\omega\cdot\alpha\cdot r_{12}\sin(\theta)}{2(h_0+\alpha\cdot r_{12}\cos(\theta))^3}\left(\left(r_2^2-r^2\right)+\frac{\left(r_1^2-r_2^2\right)\ln(r_2/r)}{\ln(r_2/r_1)}\right) \quad (2.43)$$

The fluid velocities over the exterior and interior lands $V_{ext/int}$ are defined with (Eq. 2.44) and an interface height $h_{ext/int}$ of (Eq. 2.45).

$$V_{ext/\text{int}} = \frac{dP}{dr}\frac{y}{2\mu}\left(y - h_{ext/\text{int}}\right) \quad (2.44) \qquad h_{ext/\text{int}} = h_0 + \Omega \cdot r_{mext/\min t}\cos(\theta) \quad (2.45)$$

The leakage flowrate of the piston barrel and valve plate interface $Q_{L,I}$ is determined by integrating the fluid velocity across the area dy ·dθ (Eq. 2.46) [67, 68].

$$Q_{L,I} = \int_{-\theta_i}^{\theta_j}\int_{0}^{h} V_{ext}\, r \cdot dy \cdot d\theta + \int_{-\theta_i}^{\theta_j}\int_{0}^{h} V_{ext}\, r \cdot dy \cdot d\theta =$$

$$\frac{\left(P_{ext} - P_{\text{int}}\right)}{12\mu\ln\left(r_{ext}/r_{ext\,2}\right)}\left(\begin{array}{l} h_0^3\left[\theta\right]_{-\theta_i}^{\theta_j} + 3h_0^2\alpha \cdot r_{mext}\left[\sin(\theta)\right]_{-\theta_i}^{\theta_j} + 3h_0^2\alpha^2 \cdot r_{mext}^2\left[\frac{1}{4}\sin(2\theta) + \frac{\theta}{2}\right]_{-\theta_i}^{\theta_j} + \\ \alpha^3 \cdot r_{mext}^3\left[\frac{1}{12}\sin(3\theta) + \frac{3}{4}\sin(\theta)\right]_{-\theta_i}^{\theta_j} \end{array}\right) -$$

$$\frac{\left(P_{ext} - P_{\text{int}}\right)}{12\mu\ln\left(r_{\text{int}}/r_{\text{int}\,2}\right)}\left(\begin{array}{l} h_0^3\left[\theta\right]_{-\theta_i}^{\theta_j} + 3h_0^2\alpha \cdot r_{\min t}\left[\sin(\theta)\right]_{-\theta_i}^{\theta_j} + 3h_0^2\alpha^2 \cdot r_{\min t}^2\left[\frac{1}{4}\sin(2\theta) + \frac{\theta}{2}\right]_{-\theta_i}^{\theta_j} + \\ \alpha^3 \cdot r_{\min t}^3\left[\frac{1}{12}\sin(3\theta) + \frac{3}{4}\sin(\theta)\right]_{-\theta_i}^{\theta_j} \end{array}\right)$$

(2.46)

Frictional losses within an axial piston pump

The ideal torque T_P generated by an individual piston is given by (Eq. 2.47). Within this model, a positive torque represents torque generated during motoring, while a negative torque represents a torque requirement during pumping.

$$T_P(t) = A_P R\tan(\alpha)\sin(\theta(t))P_P(t) \quad (2.47)$$

Torque losses that are included into the model occur in three locations: friction between the piston shoe and the swash plate, viscous friction losses between the piston and the piston barrel housing, and viscous friction losses between the valve plate and barrel. The model used to represent the torque loss $T_{P,S}$ due to friction between the piston shoe and the swash plate is a hydrostatic sliding bearing with a fixed coefficient μ (Eq. 2.46). The shoe surface is thoroughly lubricated with hydraulic fluid being forced through a small orifice on the shoe interface surface that is connected to the high pressure in the piston. In addition this channel lubricates the ball

joint that a piston shoe rotates on. In order to further decrease friction, the shoe and swash plate are composed of dissimilar materials that lower the coefficient of friction. The coefficient of friction is experimentally determined to be approximately $\mu = 0.025$.

$$T_{P,S}(t) = \mu \cdot A_P R \cos(\alpha) P_P(t) \quad (2.48)$$

There are two sources of fluid movement within the piston, drag induced (Couette) flow and pressure gradient induced (Pouiseuille) flow. The piston and barrel housing geometries are assumed to be two infinite parallel plates with one plate at velocity of the piston V_P. The velocity of the piston is estimated from the ideal piston flowrate Q_P (Eq. 2.49) The Couette fluid velocity V_y scales linearly with the distance from the stationary surface y (Eq. 2.50) [51]. The fluid shear stress τ_C due to fluid movement induced by viscous drag is Eq. 2.51.

$$V_P = \frac{Q_P}{A_P} \quad (2.49) \qquad V_{FC} = V_P \frac{y}{h_1} \quad (2.50) \qquad \tau_C = \mu_f \frac{dV_{FC}}{dy} = \mu_f \frac{V_P}{h_1} \quad (2.51)$$

The Pouiseuille fluid velocity takes into consideration the pressure gradient dP_p/dz across the length of the piston L_p (Eq. 2.52) [51]. The fluid shear stress τ_P due to fluid movement induced by a pressure gradient across the piston is Eq. 2.53.

$$V_{FP} = -\frac{1}{2\mu_f}(h_1 - y) y \frac{dP_P}{dz} \quad (2.52) \qquad \tau_P = \mu_f \frac{dV_{FP}}{dy} = \frac{P_P}{2 \cdot L_P}(c + e \cdot \cos(\varphi) - 2y) \quad (2.53)$$

The force on a piston due to viscous drag F_{PV} is the shear stress integrated over the angular and length dimensions of the piston (Eq. 2.54). The torque loss due to viscous friction force losses $T_{P,V}$ between the piston and housing as a function of time is Eq. 2.55.

$$F_{P,V}(t) = \int_0^{2\pi} \int_0^{L_P} \left(\mu_f \frac{V_P \cdot r_p}{c + e \cdot \cos(\varphi)} + \frac{P_P \cdot r_p}{2 \cdot L_P}(c + e \cdot \cos(\varphi) - 2y) \right) d\varphi \cdot dz = \pi \cdot r_p \left(\frac{2 \cdot \mu_f L_P V_P(t)}{\sqrt{c^2 - e^2}} + P_P(t) \right) \quad (2.54)$$

$$T_{P,V}(t) = F_{PV}(t) R \tan(\alpha) \sin(\theta(t)) \quad (2.55)$$

The viscous friction losses between the valve plate and the barrel are a function of their gap distance h (Eq. 2.56). The fluid shear stress τ_B due to fluid movement induced by viscous drag is Eq. 2.57. The total shear friction force T_v is the fluid shear stress integrated across the radial and angular dimensions (Eq. 2.58).

$$h = h_0 + R\tan(\delta)\cos(\theta + \psi) \quad (2.56) \qquad \tau_B = \mu_f \frac{r\omega}{h_2} \quad (2.56)$$

$$T_V = 2\mu\omega \int_{r_1}^{r_2} \int_0^{2\pi} \frac{r^2}{h_m + r \cdot \tan(\delta)\cos(\theta + \psi)} d\theta \cdot dr \quad (2.57)$$

The total torque loss T_{Loss} due to piston shoe friction, viscous fluid losses between piston and housing, and the viscous fluid losses between the valve plate and barrel is:

$$T_{Loss}(t) = T_V(t) + \sum_{P=1}^{N} \left(T_{P,S}(t) + T_{P,V}(t)\right) \quad (2.58)$$

Model Validation

The model was validated by comparing the measured performance of the Takako Industries 0.8 cc/rev axial piston pump with the modeling equations using the measured pump geometry. This axial piston pump is a lightweight, high efficiency pump uses 7 pistons to generate up to 21 MPa and 40 cc/s (Fig. 2.16).

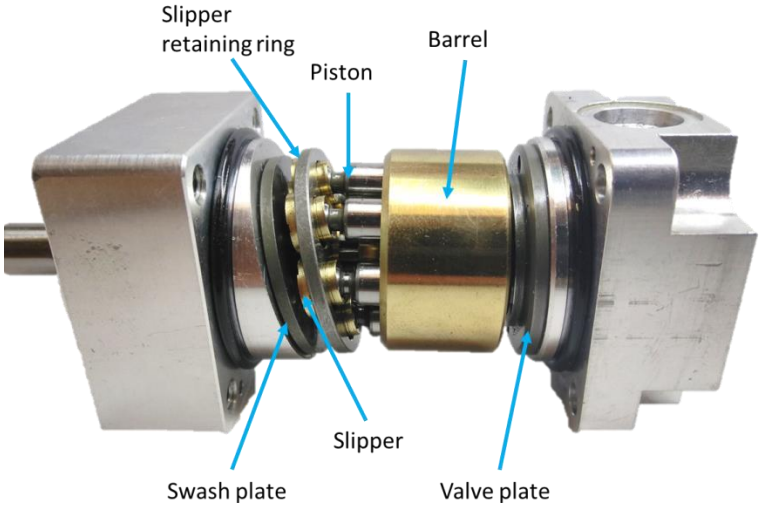

Figure 2.16 Takako 0.8 cc/rev axial piston pump

The axel, pistons, slipper retaining ring, swash plate, and valve plate are composed of stainless steel, while the barrel and slippers are composed of brass to reduce the friction with dissimilar materials. The slipper retaining ring severs the purpose of constraining radial forces generated by the angled swash plate. This allows the piston barrel to be made of a soft material like brass. The bearings for the pump shaft are housed in two aluminum manifolds. The pump dimensions summarized in table 2.9 were measured with a standard micrometer and caliper with accuracies of ±0.05 mm.

Table 2.9 Takako 0.4 cc/rev axial piston dimensions

Symbol	Description	Value	Units
D_p	Piston diameter	5.95	mm
N	Number of pistons	7.0	-
R	Radial pitch	13.0	mm
Xp	Piston stroke length	5.3	mm
θ	Swash plate angle	11.5	deg

The experimental setup for measuring pump volumetric and mechanical efficiency is described in further detail in section 4.2. The flow rate was measured by collecting a fluid volume over a sample time period, while the pump angular velocity was held constant. The desired flow rate was calculated by multiplying the pump displacement by the angular velocity of the pump shaft measured with an encoder. The pump displacement was calculated with using the measured dimensions of the pump.

$$D_p = A_p N \tan(\theta) R \quad (2.59)$$

The fluid pressure at the pump outlet was measured with a pressure transducer. It was assumed that the torque on the pump/motor shaft is proportional to the current supplied to the motor. Therefore, the pump inlet torque was calculated by measuring the motor current and multiplying it by the torque constant given by the motor manufacturer's specifications.

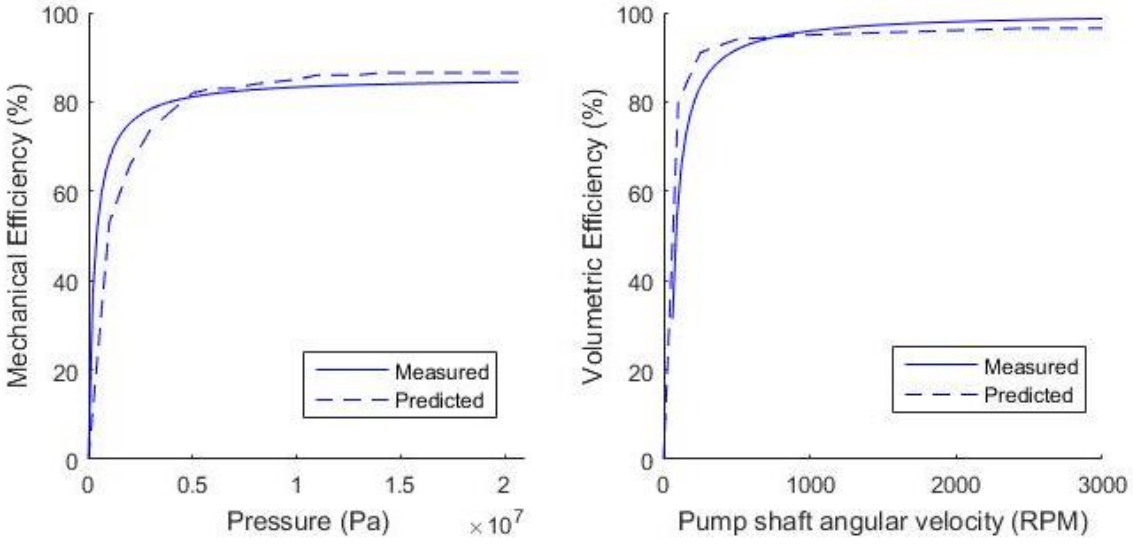

Figure 2.17 Comparison of axial piston model and catalog data

The validation results are shown in fig. 2.17. The comparison of the simulation and the performance data illustrate that the model provides an accurate depiction of the pump performance. The highest percentage error was illustrated at low pressures as the measured performance was 12.2% higher than the simulation predicted. This could be due a poor estimation of the coefficient of friction or discrepancies between the simulated and actual pump dimensions.

Chapter 3 Steady State Modeling and Optimal Design of Small-Scale Hydraulic Systems

3.1 Objective

The objective of this chapter is to use the component models introduced in chapter 2 to create an algorithm that optimizes the design of small-scale pump and valve controlled hydraulic actuations systems. This optimization functions by taking user specified actuation requirements and working backwards to design an actuation cylinder, control valve, conduit, and pump, as well as selecting an appropriate sized brushless direct current (BLDC) motor, reservoir, and battery. The purpose of creating this design tool is to provide design engineers assistance in selecting the right hardware to build more efficient and lighter small-scaled hydraulic systems for human assistive machines. The assistance this tool provides is demonstrated in section 3.3.1 where a case study of a child's sized ankle-foot orthosis is conducted. The design algorithm serves a second purpose of exploring general design guidelines that should be considered when developing small-scale hydraulic systems. A heat transfer analysis is also included to determine if the proposed system design would have adequate heat transfer to maintain safe working fluid temperatures. It will also allow an engineer to explore methods of increasing heat transfer such as increasing conduit length, the size of the reservoir, or the velocity of the ambient air with the addition of a cooling fan.

The two parameters selected to guide the design optimization are weight and efficiency. The majority of hydraulic hardware suffers from a competing balance of efficiency and weight. As hydraulic hardware is shrunk to smaller displacements and bore sizes, the weight of the hydraulic hardware diminishes at the expense of increasing viscous losses and a higher ratio of internal leakages to nominal flow rate capabilities. As bore sizes and displacements of hydraulic hardware is scaled larger, component efficiencies improve along with an increase in weight. The existence of two optimization parameters requires a method of combining the metrics to simplify the optimization. The user defined actuation requirements including a desired system run time along with the calculated hydraulic hardware efficiencies are used to estimate battery weight. This translates the efficiency into a weight metric, and a single variable optimization can be performed on the overall system weight.

3.1.1 Pump and Valve controlled actuation

Two types of hydraulic control circuits that can be used in small-scale hydraulic systems: pump control and valve control. In pump controlled hydraulic circuits the pump shaft displacement is directly coupled to the actuator displacement allowing two control inputs: the pump shaft angular velocity and the position of control member adjusting pump displacement for variable displacement pumps. In pump controlled systems there exists an auxiliary pump or valve system to replenish the main lines with fluid in the case of leakages. Pump control systems are typically much slower response due to large volumes of fluid between the pump and actuator that take time to pressurize [2]. Pump controlled systems are often more efficient since the pressure and flow are generally a function of load requirements, and because there are no throttling valves.

In a valve controlled circuit, the actuator is controlled with a valve that varies flowrate by controlling orifice area. Valve controlled systems allow fast response with small control volumes and constant supply pressure. However, the generation of a constant supply pressure means the systems have poor efficiencies when the actuator is at rest. Also the throttling of the valve introduces large pressure drops further decreasing efficiency. With a large portion of the fluids kinetic energy being transferred into heat, valve systems operate at high oil temperatures and require heat exchanges [7]. Valve systems allow the control of many independent actuators with a central power supply.

3.1.2 Prior art in the design of small-scale hydraulic systems

The efficiencies and weights of small-scale hydraulic and electromechanical actuation systems are analytically compared in [69] for systems generating between 10 and 100 W. The electromechanical system was composed of an electric motor driving a ball screw for linear actuation, whereas the hydraulic system used a hydraulic conduit connected to a traditional hydraulic cylinder. The results concluded that the weight of a hydraulic actuation system will be less compared to electromechanical if it is run above 500 psi.

A limitation of this analysis is that the weight of electrical and fluid power generation was not included in the analysis. In most applications, it can be assumed that the actuation system will require a portable source of hydraulic power and therefore a pump model needs to be incorporated. There also needs to be a source of energy storage. The weights and efficiencies of

valves, pumps, motors, and batteries must be considered to better optimize the design for portable human assistive machines. The algorithm also takes heat transfer into consideration during the process of optimizing the system design, because the sizing, performance, and weight of a system are often limited by how much heat can be dissipated.

3.2 Methods

The hydraulic schematic of the pump and valve controlled circuits are illustrated in figure 3.1. The pump controlled circuit is capable of bidirectional operation with the addition of an inverse shuttle valve connected to the reservoir. This valve functions to supply the low pressure line with additional fluid in case of leakages. Both pump and valve controlled circuits include pressure relief valves, so it can be assumed that the system pressure does not surpass the desired operating pressure. This is necessary to protect pressure sensitive components from dangerous pressure spikes. The optimization is completed at continuous steady-state operation at a specified operating point. At this operating point, it is assumed that the hydraulic power supply for the valve control system is continuously operating at full-scale conditions.

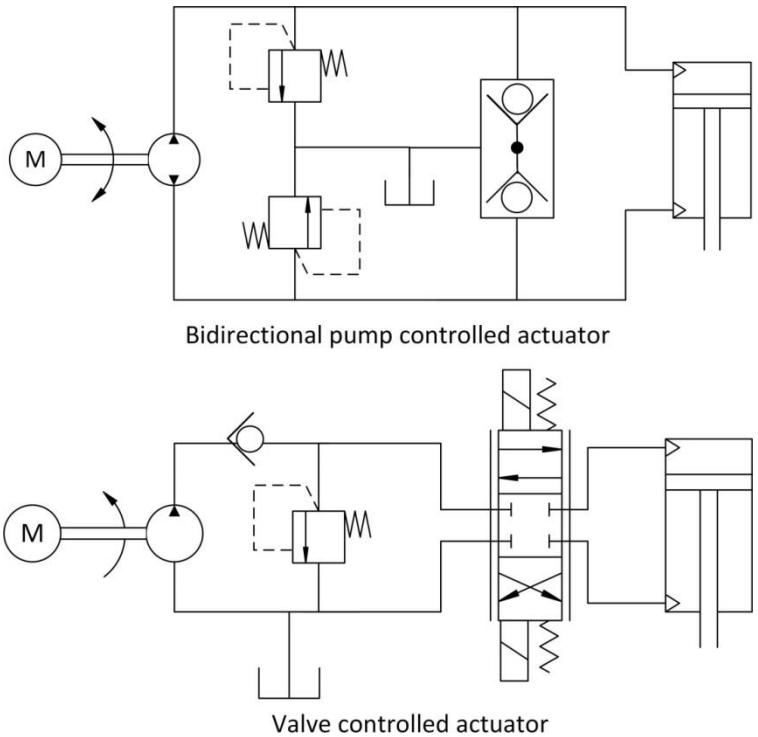

Figure 3.1 Pump and valve controlled hydraulic actuation systems

The following design script works in the same fashion as a design engineer, specifying actuation requirements and using these to work backwards to design a small-scale hydraulic system. The script is split into five separate parts that design a custom hydraulic cylinder, conduit, solenoid valve, axial piston pump with reservoir, and size a brushed DC motor and battery based on run time. Several of the component scripts use iteration to find an optimal solution. In addition, each of the component scripts communicates with one another to iterate through possible system level solutions.

3.2.1 Cylinder Design

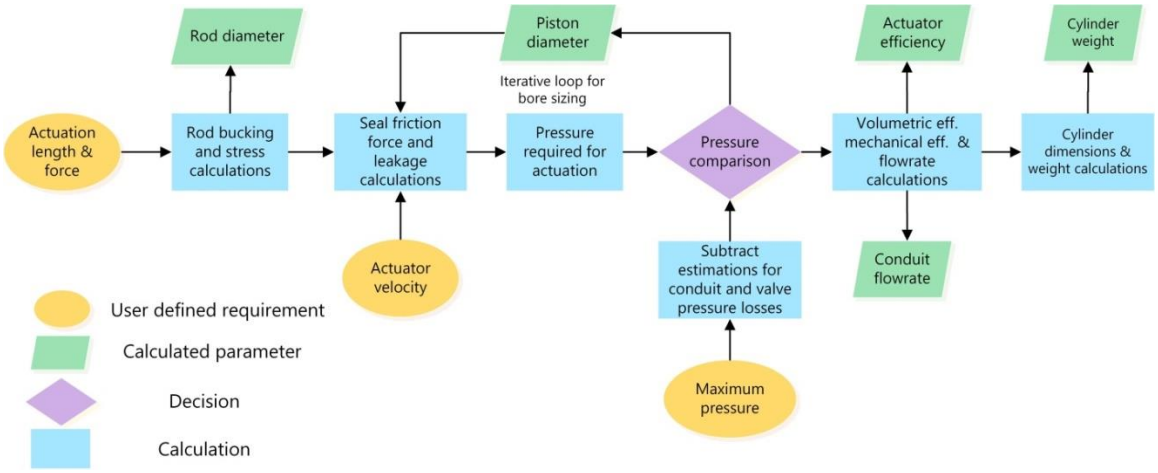

Figure 3.2 Cylinder design flowchart

Figure 3.2 illustrates the design process for the single ended hydraulic cylinder that uses traditional O-rings for sealing around the piston and rod. Figure 3.3 is a cross-section of the hydraulic actuator with labeled dimensions and variables. The first calculation in the optimization procedure is to determine an adequate rod diameter based on comparing bucking criteria (3.1) and material tensile strength (3.2) using the defined inputs of actuation length and force requirements [70]. The larger of the two calculated rod diameters is selected as the final rod diameter. The material selected for this application is 7075-T6 aluminum due to the high strength to weight ratio, availability, relative low cost, and chemical stability.

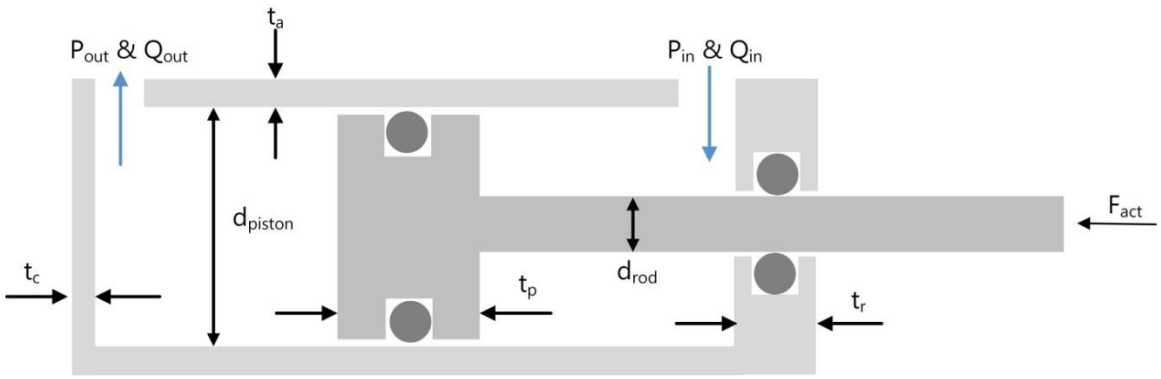

Figure 3.3 Actuator cross-section and dimensions

Table 3.1 Cylinder variable definitions

Symbol	Description	Unit	Symbol	Description	Unit
E	Elastic modulus	Pa	ΔP_{cond}	Pressure drop across conduit	Pa
F_{act}	Actuator force	N	ΔP_{valve}	Pressure drop across valve	Pa
F_{seal}	Seal friction force	N	Q_{in}	Actuator inlet flowrate	m^3/s
L_{act}	Length of actuation	m	Q_{leak}	Seal leakage flowrate	m^3/s
N_{mech}	Mechanical safety factor	-	Q_{out}	Actuator outlet flowrate	m^3/s
N_{hyd}	Hydraulic safety factor	-	V_{act}	Actuator velocity	m/s
P_{act}	Actuator inlet pressure	Pa	σ_s	Yield stress	Pa
P_{max}	Maximum system pressure	Pa	σ_{sy}	Shear yield stress	Pa
P_{out}	Actuator outlet pressure	Pa			

$$d_{rod} = \left(\frac{16 N_{mech} L_{act}^2 F_{act}}{\pi^3 E} \right)^{1/4} \quad (3.1) \qquad d_{rod} = \left(\frac{4 F_{act} N_{mech}}{\pi \sigma_y} \right)^{1/2} \quad (3.2)$$

The minimum piston diameter is selected with an iterative loop that compares the actuator pressure requirements with the estimates of the system pressure capabilities.

$$\frac{F_{seal} + F_{act}}{\pi\left(d_{piston}{}^2 - d_{rod}^2\right)} = P_{\max} - 2\Delta P_{cond} - \Delta P_{valve} = P_{act} \quad (3.3)$$

This process begins by initializing the piston diameter equal to the rod diameter. The total seal friction force is calculated using eq. 2.4 and 2.5. The required actuation pressure is defined as the summation of the actuation and seal friction forces. An estimate of the maximum pressure obtainable at the inlet port of the actuator is calculated by subtracting estimates of the pressure drop across the valve and conduit from the defined maximum system pressure. If the required pressure is larger than the estimate of maximum actuation pressure, the bore size is increased and calculations are repeated until they are equal. The actuation flowrate requirements and efficiency are estimated using:

$$Q_{in} = \frac{\pi}{4}\left(d_{piston}^2 - d_{rod}^2\right)V_{act} + Q_{leak} \quad (3.4) \qquad \eta_{act} = \frac{F_{act}V_{act}}{Q_{in}\left(P_{act} - P_{out}\left(\frac{d_{piston}^2}{d_{piston}^2 - d_{rod}^2}\right)\right)} \quad (3.5)$$

The limiting stresses in the circumferential wall of the hydraulic cylinder are the circumferential tensile stress (3.6) and an out of plane shear stress orientated at 45° (3.7).

$$t_A = \frac{N_{hyd} \cdot P_{\max} \cdot d_{piston}}{2 \cdot \sigma_y} \quad (3.6) \qquad t_A = \frac{N_{hyd} \cdot P_{\max} \cdot d_{piston}}{4 \cdot \sigma_{sy}} \quad (3.7)$$

The required thickness of the circumferential wall is determined by solving for the larger of the circumferential thicknesses. The factor of safety used for pressure vessel applications is traditionally elevated to ensure there is no potential for hazardous eruption. The industrial standard for pressure vessel safety factors range between 3 and 6. The design script uses a safety factor of 5 for components loaded by circumferential pressure and a safety factor of 2.5 for mechanical loadings. The remaining thicknesses of the piston t_p, cap and piston end walls t_c & t_r are calculated using design specifications from [71] (Appendix A.3.1). The weight of the individual components is calculated using the material density and the calculated geometry parameters.

3.2.2 Conduit Design

One of the benefits of hydraulic power is the ability to use various types of hydraulic conduits to transport fluid power through irregular paths to locations where weight or size might be limiting factors. Hydraulic systems unlike mechanical systems do not need to use complex and heavy gear transmissions in power transmission, division, or amplification. In order to design a lightweight and portable hydraulic system, the hydraulic conduit must be properly designed to find the optimal balance between weight and efficiency. The algorithm in fig. 3.4 is implemented for each conduit within the system to determine the optimum inner diameter.

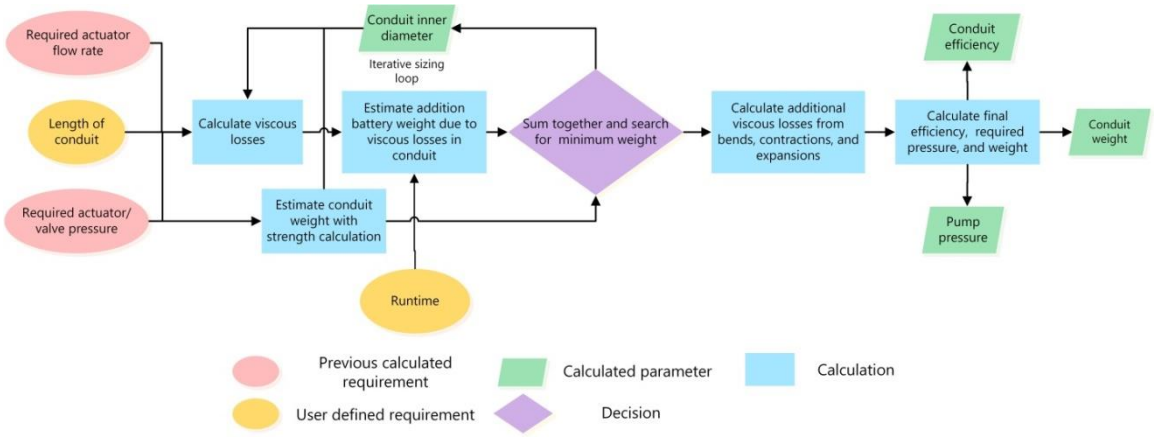

Figure 3.4 Conduit design flowchart

There are three variable input parameters that control the design of the hydraulic conduit: length of conduit being sized, the system runtime, and information on additional losses including bends, contractions and expansions. Since the pressure drop across a conduit is primarily a function of flow rate, it is important to consider the pressure losses across the return conduit from the low pressure side of the actuator to the tank. In addition, due to their lower hoop strength to weight ratio, hoses should only be used to transport fluid in applications where the body of the actuator experiences movement or the hydraulic conduit experiences signification vibrations or stresses.

The inner diameter of the conduit is selected by using an iterative loop to locate a minimal system weight. The first step is to initialize the inner diameter and calculate the viscous losses with the methods discussed in section 2.3. Using the energy density of current battery

technologies along with estimates of other component efficiencies, the additional battery weight required to compensate for the viscous losses can be calculated. The thickness and weight of the hydraulic conduit can be estimated using hoop strength calculations similar to Eq. 3.5A-B. The fluid weight is also taken into consideration using hose geometry and fluid density. The battery compensation weight due to viscous losses and conduit weight are summed, and this process is repeated for a range of inner conduit diameters. Since this design space represents a balance between system weight and efficiency, there exists an optimum conduit diameter to minimize system weight

Table 3.2 Conduit design input conditions

Description	Valve	Description	Value
Actuator flow rate	47.2 cc/s	Reservoir size	0.25 L
Actuator and Valve pressure	21.7 MPa	Run time	2 hours
Hose length	0.5 m	Tube length	0.5 m
Number of 90° bends	4		

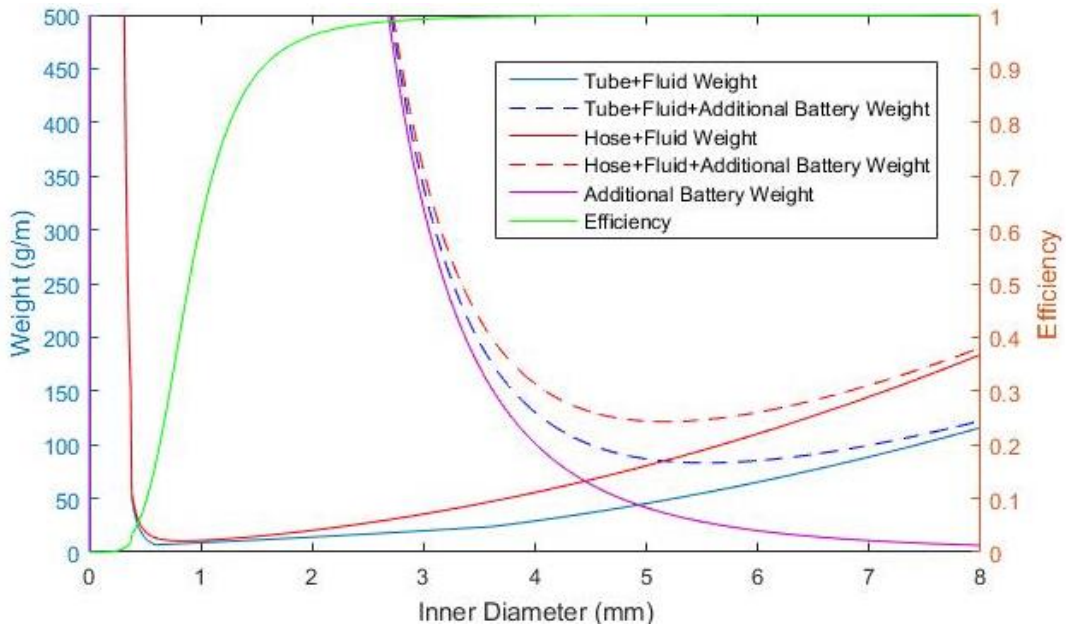

Figure 3.5 Conduit design space

Figure 3.5 illustrates an example design space for a tube and hose conduit with the input conditions in table 3.2. The conduit efficiency decreases rapidly as the inner diameter decreases below 3 mm. The additional battery weight increases exponentially to compensate for the decreased efficiency. The dashed lines represent the summed conduit and battery compensation weight. The optimal inner diameters of the hose and tube for this application are 5.2 and 5.5 mm. If the conduit flow rates and lengths are equal like the input conditions, the hose should have a smaller diameter compared to the tube. The tube has a ratio of higher hoop strength to weight that shifts the optimum inner diameters to larger, more efficient conduits compared to the hose.

Figure 3.5 illustrates an iterative search for an optimal solution of conduit size using the weight of the battery and conduit. These results do not take into consideration the weight and sizing of other components, while the system level design process does take into consideration all components not just the conduit and battery. An example of this iterative process is selecting a smaller conduit will result in a larger pressure drop across the conduit. The bore size of the cylinder will increase to stay with the specified maximum pressure. This results in increased flow rate requirements and a larger pump, motor, and battery.

3.2.3 Valve Design

This section describes the process and assumptions taken in the design of the control valve. Valve design is discussed more in depth in chapter 5 as feasibility and design of a digital high frequency switching are considered. The valve design starts by using the calculated conduit flow rate and user defined nominal pressure drop to calculate the cross-sectional area of the orifice using eq. 2.32

There are a variety of valve body styles for different applications, but the one most commonly employed for directional control valves is spool geometry. The spool geometry can be used to construct multiple way valves with the precise control of multiple orifices with a single spool [6]. The spool is a series of cylindrical drums called lands that are connected on a shaft.

There exist two main geometries used for the valve body. In applications where high flow is required with minimal spool displacement, a rectangular slot orifice is used. A rectangular slot orifice is formed by machining grooves into the bore of the valve. As the spool is translated and

the lands and grooves are offset, a cylindrical ring orifice is formed. The bore grooves serve the purpose of reducing radial pressure forces on the spool and minimizing the Coulomb friction between the spool and the bore [6]. However, this geometry requires high precision machining to prevent leakages across the spool. A more common geometry due to relative ease of manufacturing is where the holes are drilled directly into the bore at a 90° angle creating a circular section as the lands of the spool are translated across the holes. Figure 3.6 illustrates the two orifice geometries and formulas used to calculate orifice area A.

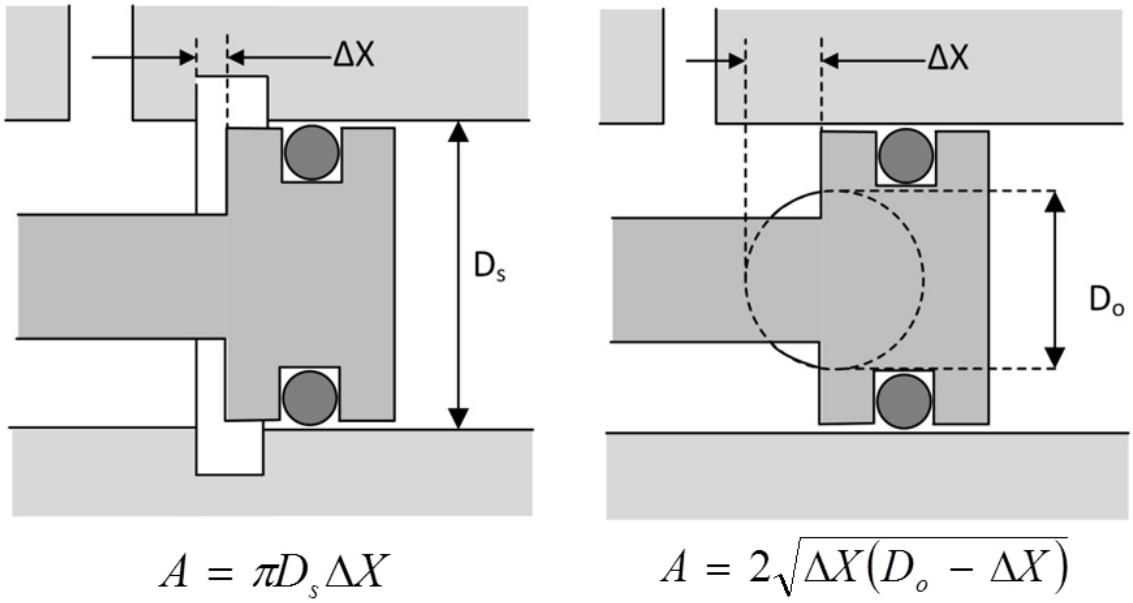

Figure 3.6 Rectangle slot orifice (left) and circular section orifice (right)

The diameter of the orifice can be calculated by assuming that the calculated cross-sectional orifice area is represented by a fully open annular orifice. The spool is set to be the same diameter as the orifice with a minimum of a 2 mm diameter. This limitation is due to manufacturing capabilities, and also decreases the susceptibility to contamination damage. An analysis of the forces on the spool is conducted in section 5.2.3. In this analysis, the spool is assumed to have two control orifices as fluid is metered from the pump to actuator and from the actuator to the reservoir. This allows the actuator position to be locked in a constant position as both orifices are closed. If an application does not require the actuator to be locked when not in use, a single orifice valve between the pump and actuator can be used. This will allow the actuator to relax in a single direction as fluid flows from the actuator to tank.

The spool translation is controlled with a solenoid that is sized using the summation of forces on the spool. A solenoid controlled valve is used rather than a traditional servo valve to increase efficiency of the system. Servo valves require a pilot stage where small amount of high pressure flow passes continuously through the valve. This continuously consumes energy and is not desirable for high efficiency applications. Valve design for small-scale hydraulic system is further discussed in section 5.2. The design algorithm provides estimates of valve geometry, weight, efficiency, and energy consumption for an opening/closing cycle.

3.2.4 Axial piston pump design

The model developed in section 2.7.2 is used to predict the efficiency of the axial piston pump. The design of the axial piston pump starts with an initialized 7 piston geometry and a fixed swash plate angle. The number of pistons was selected due to geometric constraints and general design principle to use an odd number of pistons. This principle is physically explained by the fact that pumps with an even number of pistons can instantaneously and simultaneously have pistons at top and bottom dead center. This creates a situation where two pistons are simultaneously not contributing to flow, resulting in more fluctuations of the output flow rate in even number pumps, otherwise referred to as flow ripple. A flow ripple analysis in Manring [72] of 7, 8, and 9 piston axial piston pumps concluded that quantitatively even number pumps did produce more flow ripple but not an appreciable amount compared to odd number piston pumps when leakages and compressibility were considered. Even number axial piston pumps are not optimal, but feasible considering flow ripple.

The pump design uses a brass barrel and piston slippers with hardened stainless steel pistons, swash plate, and valve plate. The dissimilar materials decrease friction at the four wearing interfaces; valve plate/ barrel, barrel/piston, piston/slipper ball socket, and the slipper/swash plate. The swash and valve plate are separate parts with the pump case, sealed bearing housing, and valve port block being aluminum. This decreases the overall weight of the pump, while still maintaining good wear surfaces. Figure 3.7 is a line drawing of the pump model labeling the parts considered in the performance and weight analysis.

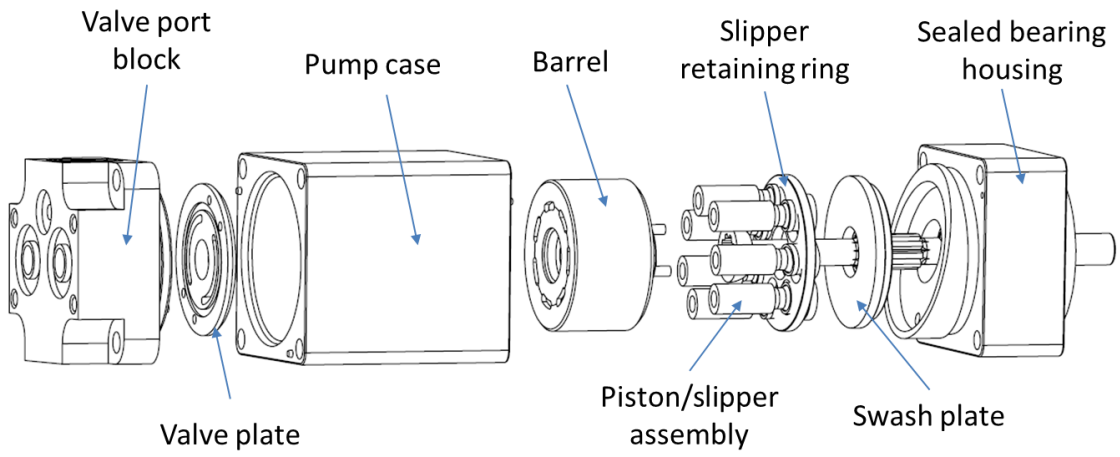

Figure 3.7 Line drawing of pump model labeling parts considered in weight and performance analysis

The initial pump geometry is scaled to accommodate larger or smaller flow rates. The scaling factor is based on the comparison of the required system flow rate and the calculated theoretical flow rate of the pump.

In order to validate that the model of the fixed displacement axial piston pump is scaling appropriately, the model was compared to three commercial axial piston pumps from Takako Industries. The flow rate requirements entered into the pump design were set equal to each of manufacturer's flow rate specifications. The important geometry scaling parameters are illustrated in figure 3.8 for the pump design algorithm and the Takako axial piston pumps. The results verify that the pump geometry is scaling accurately compared to the commercial design of an axial piston pump as the displacement is varied.

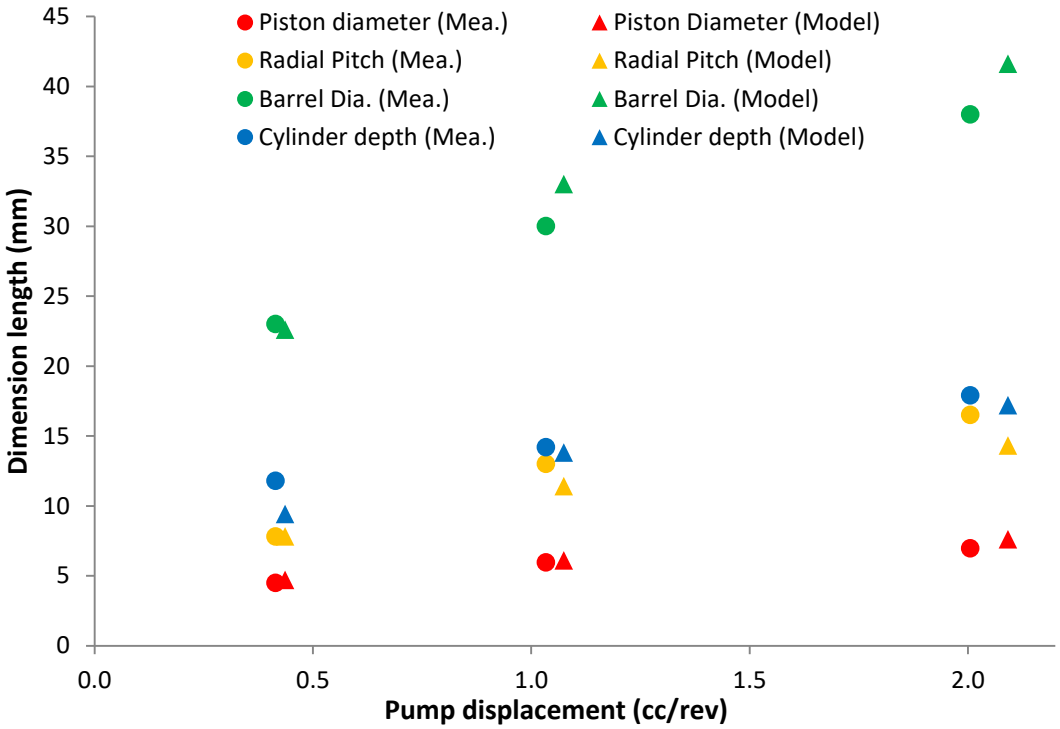

Figure 3.8 Comparison of optimized and commercial axial piston design

The dimensions and weights of the components within the pump are calculated by comparing yield stresses of the selected materials with the estimated internal forces with an additional factor of safety. Figure 3.9 shows the calculated optimal pump weight compared with the measured weights of the commercial pumps. For the two smaller pumps the weights match well; however, the larger pump the model predicts a significantly lower weight than the commercial pump. In an effort to better understand this discrepancy, the weights of the individual components within the pump are compared in appendix A.3.2. The component weight comparison illustrates that the bulk of the total weight discrepancy is caused by a difference between the weight of the sealed bearings in the commercial and modeled designs. This is likely the cause of using two different types or designs of sealed bearings. In addition, the predicted weight of the pump case is much lower than the measured weight. This is likely because the modeled case design is a minimal shell-like geometry, whereas the commercial pump includes attachment points to secure the pump to a manifold. The commercial pump case

also includes additional space for a case drain port that is necessary in some hydraulic applications.

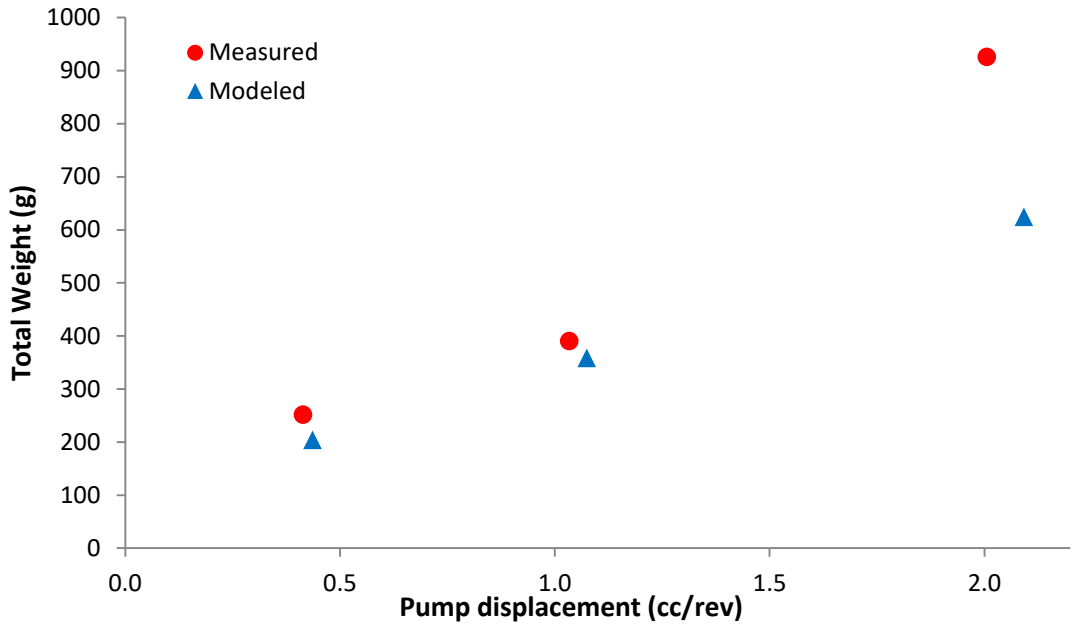

Figure 3.9 Comparison of optimal and commercial axial piston pump weight

3.2.5 Motor and battery modeling

The focus of this research is on the modeling and design for small-scale hydraulic systems; however, to get a more accurate depiction of overall system weight, the efficiency and properties of electric motors and batteries were estimated using commercial data.

It was assumed that the pump is directly driven with a direct current (DC) motor. The use of direct current allows the use of a battery without additional losses from an inverter to convert to alternating current (AC). In addition, a brushless motor is used instead of a brushed motor due to their higher nominal power densities [73]. Since the specific operating conditions are unknown, the motor is sized by matching the maximum pump inlet power with the nominal power of the DC brushless motor. This allows the hydraulic power supply to be operated continuously at the maximum operating conditions without overheating the motor.

In appendix A.3.3 nominal motor power is compared with the motor weight and the maximum operating efficiencies using commercial data provide by three separate manufacturers of

brushless DC motors. The data is used to develop fitted equations that provide estimates of motor weight and nominal efficiency using the required nominal power of the motor. If specific operating conditions/duty cycle were assumed, a more precise motor efficiency could be calculated using the internal electrical resistance of the motor and estimated bearing friction.

The ideal battery to provide energy storage for portable small-scale hydraulic systems is light-weight, compact, and rechargeable while providing the large amount of electrical energy for hundreds of cycles. The primary metrics used to compare battery technologies for portable systems are the volumetric and weight energy densities. The weights, volumes, and energy capacities of several battery types are compared in appendix A.3.4. The volumetric and weight energy densities of the several battery technologies are compared in table 3.3 were determined by fitting a best-fit line to the data in figures A.3.5 and A.3.6 and from [62] [74] [75].

Table 3.3 Weight and volumetric energy densities of different battery technologies

Battery Chemistry	Nominal voltage (V)	Cycle life	Weight energy density (Wh/kg)	Volumetric energy density (Wh/cc)
Lead-acid	2.0	750	33-42	(0.06-0.11)
NiMH	1.2	500	66.3	0.161
$LiFePO_4$	3.3	1000-2000	90-120	0.118
$LiMnO_2$	3.3	500	224	0.145
$LiCoO_2$	3.6	500-1000	150-200	NL
$LiNiMnCoO_2$	3.7	1000-2000	150-220	NL
$LiNiCoAlO_2$	3.6	500	200-260	NL
$LiSOCl_2$	3.5	Non-rechargeable	568	0.260

The data illustrates the lithium-thionyl chloride ($LiSOCl_2$) batteries provide superior weight energy density; however, this is a non-rechargeable technology. This technology is commonly employed in low temperature, long life, military and industrial applications. In addition, these batteries are high cost and hazardous to use. There are several lithium cobalt battery

technologies with high energy densities that are also rechargeable. Lithium nickel cobalt aluminum oxide ($LiNiCoAlO_2$) and Lithium nickel manganese cobalt oxide ($LiNiMnCoO_2$) are common batteries employed in medical devices and electric powertrains for bikes and vehicles. The $LiNiCoAlO_2$ battery is susceptible to decreasing battery life if discharged quickly, while the $LiNiMnCoO_2$ is susceptible to decreased battery life with fast charging. Hydraulic machines are often used for applications where the operation is highly intermittent requiring short bursts of high power and fast discharge from the battery making $LiNiCoAlO_2$ battery technology a poor choice for hydraulic systems. Based on the high weight energy density, high discharge capabilities, and high cycle life, $LiNiMnCoO_2$ is the ideal battery technology for use in small-scale hydraulic systems with energy densities of 3 to 5 times greater than nickel metal hydride and lead acid batteries. An energy density of 200 Wh/L for $LiNiMnCoO_2$ battery technology is used in this algorithm to estimate the energy capacity, size, and weight of the overall system.

3.2.6 Heat Transfer

Hydraulic systems often operate at low efficiencies with significant amount of fluid power being transferred into heat [76, 7]. The heat transfer must be modeled to ensure that the system maintains safe exterior surface temperatures, as human assistive machines are can in contact with the operator's skin. In addition, the working fluid temperature must stay within the manufacture's specified operating range to ensure reliable operation. The maximum operating temperature of mineral oil is 150 °C. If a hydraulic system does not have the necessary heat dissipation, a larger reservoir, longer conduits, or heat exchanger will have to be incorporated, and this will add additional weight to the system.

This heat transfer analysis aims to determine a worst-case scenario for when the maximum amount of heat will be generated. For a traditional pump controlled system, the operating conditions that generate the largest amount of heat is when the pump is driven at the maximum angular velocity suppling torque equal to the maximum system pressure. For a valve controlled hydraulic system, the maximum heat generation occurs when the control valve is fully closed and the full-scale flow rate is being dissipated across a relief valve set at the maximum system pressure. Since the fluid is not circulating through the majority of the conduit or the actuator, the overall surface area for heat convection to the surroundings is decreased. The combined

effects of increased thermal resistance and increased heat generation makes this an especially thermally hazardous operating condition.

In order to model the worst-case scenario, steady state heat transfer can be assumed and transient effects ignored. This assumption allows the thermal capacitance of the fluid and other components to be neglected, and the heat transfer modeled as thermal resistances (Fig. 3.10). A limitation of the model is that it only models thermal dynamics for low and high actuation duty cycles. For intermittent actuator operation, thermal capacitance needs to be considered as the system goes through cycles of heating and cooling.

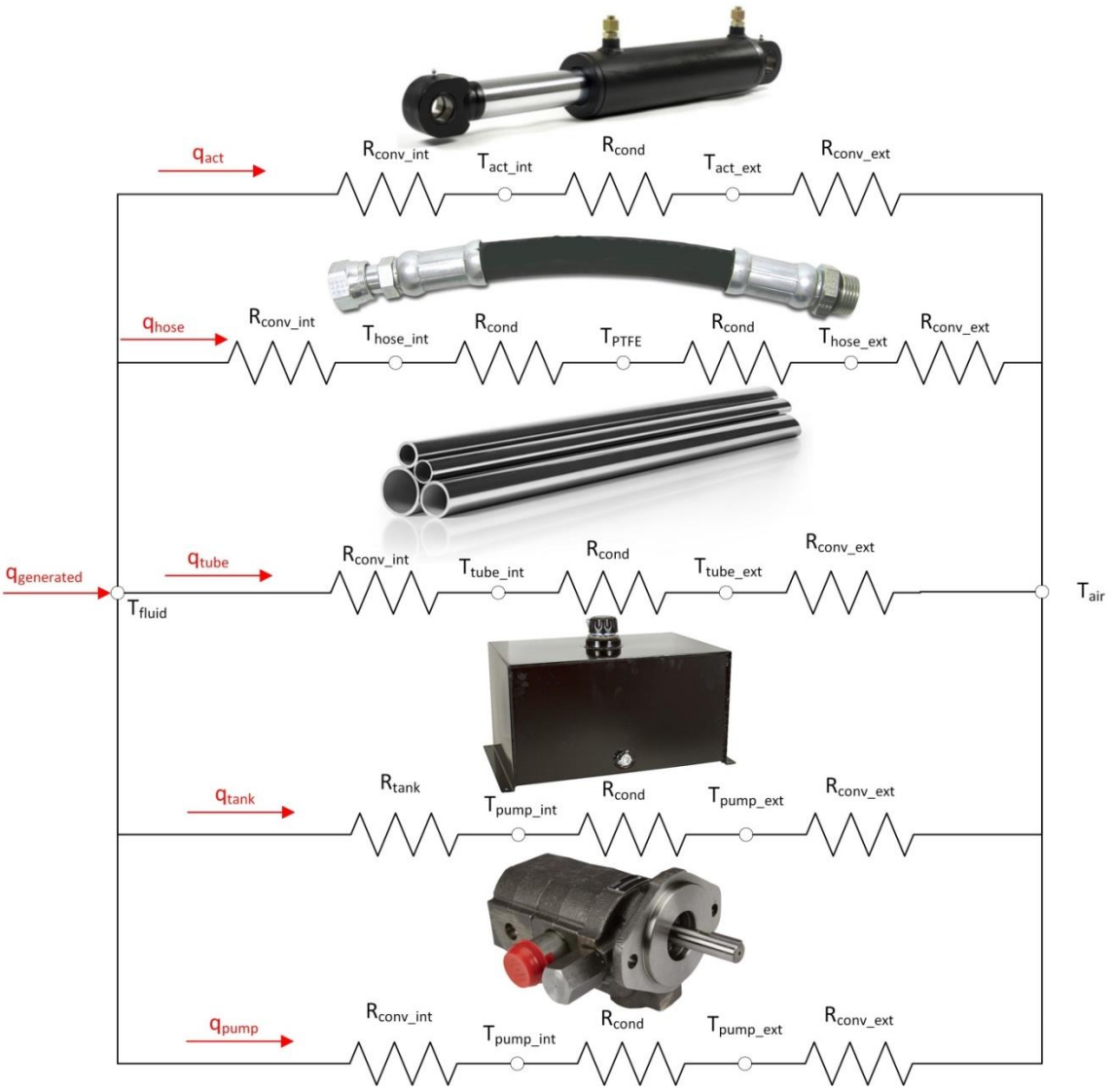

Figure 3.10 Hydraulic system thermal resistance network

It is assumed that all friction and viscous losses in the actuator, valves, conduits, and pump are converted into heat that collects in the fluid. This assumption models a worst-case scenario as all the heat is transferred immediately to the working fluid, where in reality it is likely that a small portion is lost to the environment through convection off the surface of the component. A second assumption is that the working fluid is a uniform temperature due to high flow rates and mixing. This assumption is not valid for cases where large reservoirs are used, as radial temperature gradients can develop due to heat convection on the outside of the tank. In addition, large reservoirs have areas of stagnant fluid that depend on the placement of the ports. However, for a system to be portable enough for human assistive machines, the reservoirs have to be as small as possible to limit weight and allow compact packaging.

Heat is dissipated through one of the five parallel branches representing the actuator, hose, tubing, pump, and tank exterior surfaces. The valve bodies are assumed to negligible surface area resulting in only minor heat loss. Within each branch, the different modes of heat transfer from the working fluid to the surrounding air are modeled by three or more thermal resistances in series. The first thermal resistance represents heat convection from the working fluid to the interior surface of the component (3.6). The second resistance is the heat conduction through the component case wall (3.7). The exterior wall of a hose uses two materials, so the thermal resistances are calculated separately. The final thermal resistance models the heat convection from the exterior surface to the surrounding air (3.6). The temperature of the working fluid and exterior surface temperatures are calculated using eq. 3.8 and the summed resistances. The interior and exterior convection coefficients for the different hydraulic components were determined by empirical methods shown in [77].

$$R_{cond} = \frac{\ln\left(r_o / r_i\right)}{2\pi kL} \quad (3.6) \qquad R_{conv} = \frac{1}{2\pi rhL} \quad (3.7) \qquad q_{total} = \frac{T_{flluid} - T_{air}}{R_{total}} \quad (3.8)$$

3.3 Results

3.3.1 Ankle-Foot Orthosis Case Study

The objective of this case study is to illustrate how the outlined computer design optimization can be used to design and optimize a small-scale hydraulic system. In this case study, the input

requirements in table 3.4 represent a child-sized powered ankle-foot orthosis (AFO) that is discussed in chapter 7. It is important to minimize the weight while maximizing the performance of prostheses and orthoses, because it has been shown increased weight can have negative effects on the user [78]. In Lenzi et al [79], a similar design optimization was performed matching the power requirements of a lower-limb motorized prosthesis with a person's body weight. Their design optimization allowed the design of lighter prostheses that better benefitted the patients using them.

Table 3.4 AFO Case study: Input conditions

Description	Valve	Description	Value
Actuator force	2333 N	Tube length	0.5 m
Actuator velocity	0.131 m/s	Number of 90° bends	4
Length of actuation	0.0367 m	Maximum system pressure	21 MPa
Valve nominal pressure drop	3.5 MPa	Run time	30 minutes
Hose length	1.5 m	Reservoir size	0.5 liter

The design parameters and estimated performance for a pump and valve controlled hydraulic powered children's AFO are summarized in table 3.5. The proposed design incorporates a 3 cm ankle pulley to transmit the linear cylinder force into assistive ankle torque.

Table 3.5 AFO case study: Optimized design results

Parameter	Pump controlled system	Valve controlled system
Total system weight (kg)	3.67	4.43
Hydraulic output power density (W/kg)	327	307
System output energy density (kJ/kg)	150	124
Full-scale efficiency (%)	65.4	53.3
Pump displacement (cc/rev)	0.32	0.40
Actuator bore (mm)	13.0	14.4
Control valve orifice area (mm^2)	-	0.30
Hose/Tube ID (mm)	3.5/3.8	3.8/4.1

Figure 3.11 illustrates the distribution of losses within the valve controlled system for two separate operating conditions. The left pie chart represents the system with the actuator operating at full velocity and force. At this operating condition the leakage across the relief valve is negligible. The second operating condition represents an application where the actuator is traveling at half velocity against half of the total force requirements. The total flow is divided, so half travels across the control valve and the other half across the relief valve. At both operating conditions the leakage across the seals in the control valve and actuator are negligible. However the seal friction leads to about 1% of the total losses. The conduit losses are limited to approximately 1% due to the balancing of conduit weight and efficiency. The areas of the hydraulic actuation system where efficiency needs further improvement are the control valve, pump, and the electric motor.

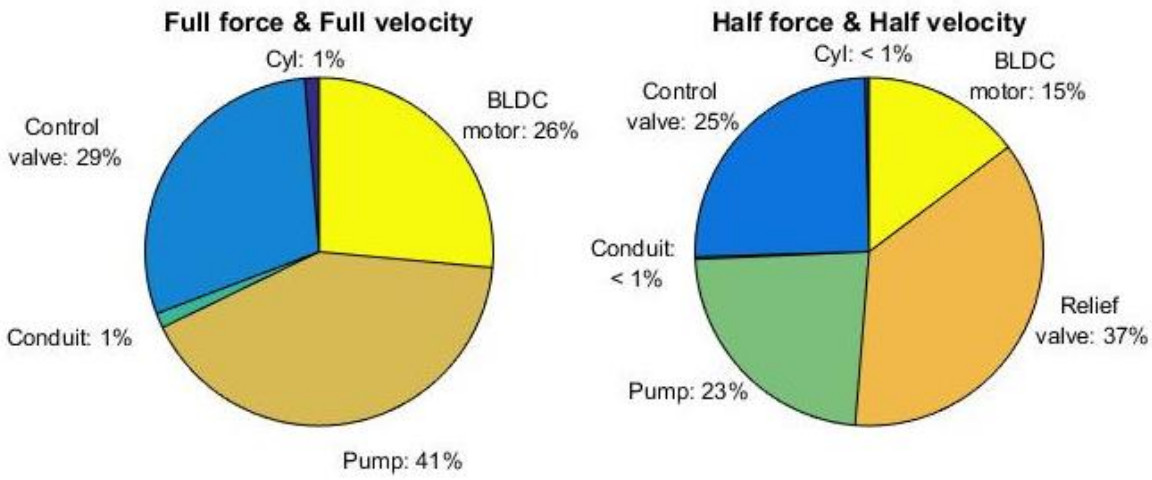

Figure 3.11 Distribution of losses of a valve controlled system for a powered ankle-foot orthosis

The weight distribution for human assistive machines is critical for making the device easy to use and maneuver. The proposed weight distribution for a pump controlled system is illustrated in figure 3.12 using the input conditions in table 3.4. An estimate of the total actuator and conduit weight positioned at the ankle is approximately 217 g, and the auxiliary power supply is estimated to weigh 3.45 kg. The estimated total system weight for a pump controlled system is 3.67 kg.

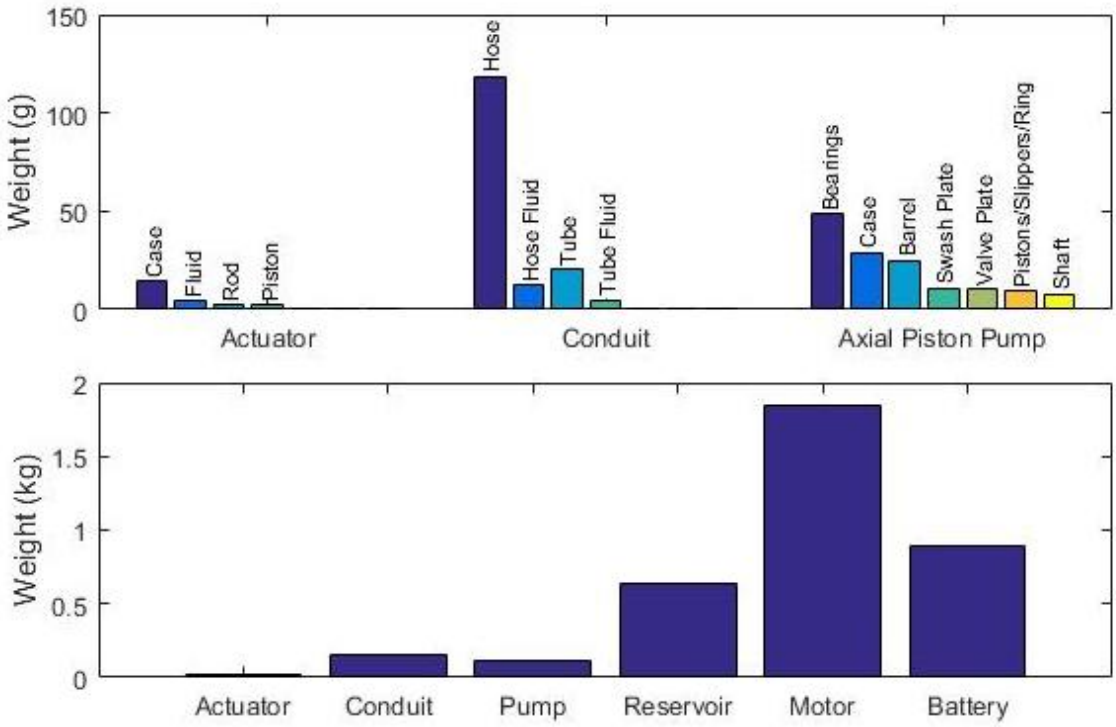

Figure 3.12 Weight distribution of a pump controlled powered ankle-foot orthosis

Hydraulic actuators controlled with proportional valves require a pressure drop over the control valve at nominal flow rates that does not occur in pump controlled systems. The addition of a control valve pressure drop requires a larger bore cylinder for the same maximum operating pressure. As a result of the larger bore, the flow rate and pump size increase to maintain the same actuator velocity. This resulted in the valve controlled system having a lower full-scale efficiency, a higher weight, and a lower power output density compared to a pump controlled system.

Table 3.6 illustrates the results from the heat transfer analysis assuming surrounding air temperature of 25°C and velocity of 1 m/s. The heat transfer analysis for the pump controller system was done at full-scale conditions as the actuator was cycled back and forth at maximum velocity and force. The heat transfer analysis for the proportional valve controlled system represents the actuator at rest as all of the fluid power is dissipated over the relief valve.

Table 3.6 AFO case study: Heat transfer analysis results

Parameter	Pump controlled system at full-scale	Valve controlled system at rest
Total hydraulic heat generated (W)	99.1	502
Total heat generated (W)	162	576
Fluid temperature (°C)	93.8	1920

The heat transfer results illustrated that it is hazardous to let the valve controlled design run continuously when the actuator is at rest, as the working temperature of the fluid and the exterior surface temperatures of the hardware would far surpass safe working limits. The working fluid parameters are based on mineral oil which has a maximum manufacturer operating temperature of 160°C. The proposed pump control design has adequate cooling to stay within the safe working temperatures of the fluid and to maintain safe exterior temperatures under continuous operation.

Figure 3.13 illustrates the worst-case heat generation and loss for the pump and valve controlled systems. The hazardous heat buildup in the valve controlled system is due to the fact all the hydraulic power needs to be dissipated through convection to the surroundings on the cases of the pump and a small reservoir. When the actuator is at rest in a pump controlled system there is no heat generated. When it is operated continuously at full-scale, the bulk of the heat is generated as frictional losses at the pump. The majority of the heat loss is spread between the hose, tubing and reservoir surfaces.

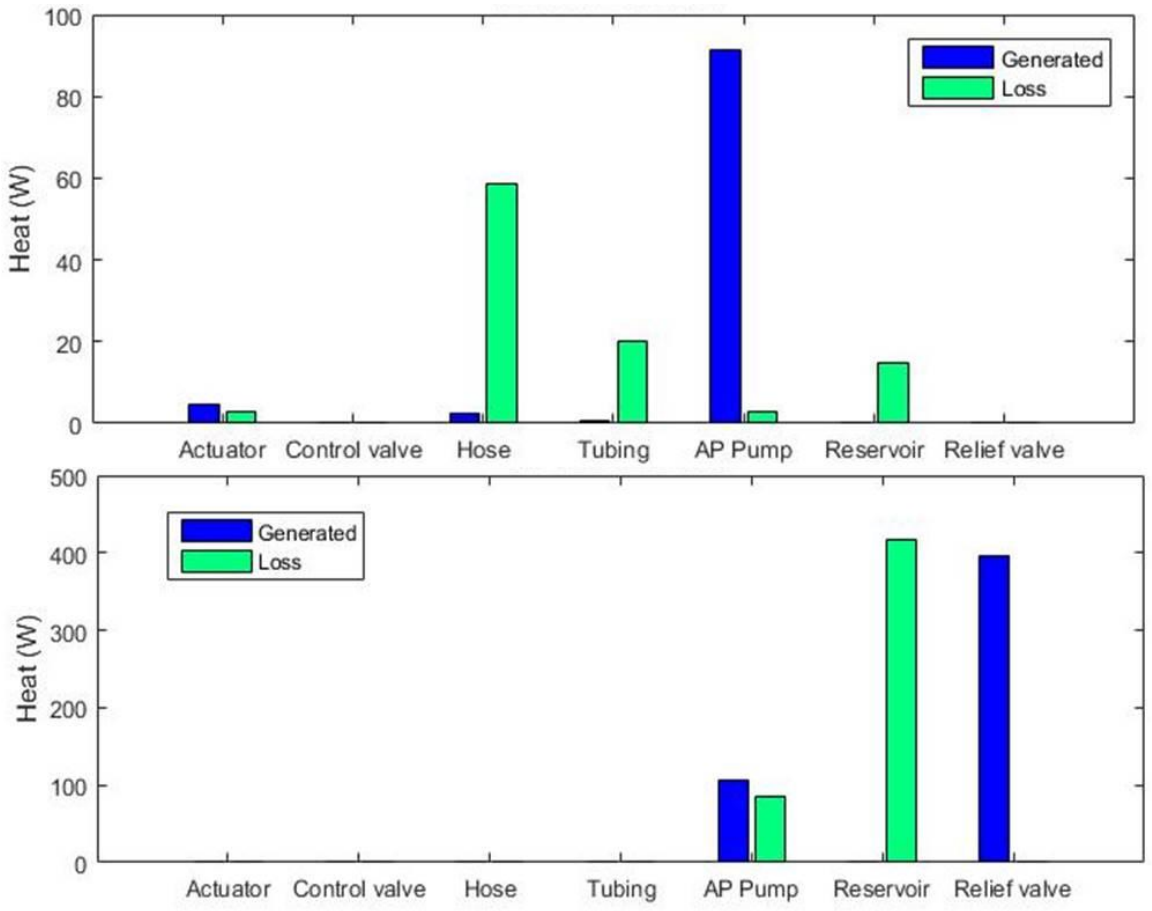

Figure 3.13 Heat distribution comparing pump and valve control operation

The operation of a powered ankle-foot orthosis is intermittent with small duty cycles. The results illustrate that a valve controlled system would require the addition of or a combination of longer conduits, a larger reservoir, or a heat exchanger to operate within safe temperatures. Other methods for limiting the energy dissipated when the actuator is at rest in a valve controlled system include the use of by-pass valves or proportional pressure control discussed in chapter 4.

3.3.2 Design Guidelines for Small-Scale Hydraulic Systems

The objective of this section is to use the described design optimization tool to develop design guidelines for small-scale hydraulic systems. These guidelines focus on increasing the power density and efficiency. The first variable of interest is operating pressure. In order to compare operating pressure, all the input variables in the design algorithm are held constant according to

table 3.7 as the operating pressure is varied. The only exception is the nominal pressure of the valve is always set to be 15% of the operating pressure. With the actuation force and velocity requirements held constant, all compared systems have identical output power.

Table 3.7 Design guidelines: Input conditions

Description	Valve	Description	Value
Actuator force	1000 N	Tube length	0.5 m
Actuator velocity	0.5 m/s	Number of 90° bends	4
Length of actuation	0.2 m	Maximum system pressure	21 MPa
Valve nominal pressure drop	15% OP	Run time	0.5 hr
Hose length	0.5 m	Reservoir size	0.25 liter

The ratio of seal friction force to actuation force increases as pressures decreases, because the seal friction is constant with respect to pressure. This results in seal friction becoming a significant loss at low pressures. The same is true for viscous and bearing friction within the axial piston pump. These losses cause the actuator efficiency and mechanical pump efficiency to decrease rapidly for operating pressures below 2 MPa (Fig. 3.14).

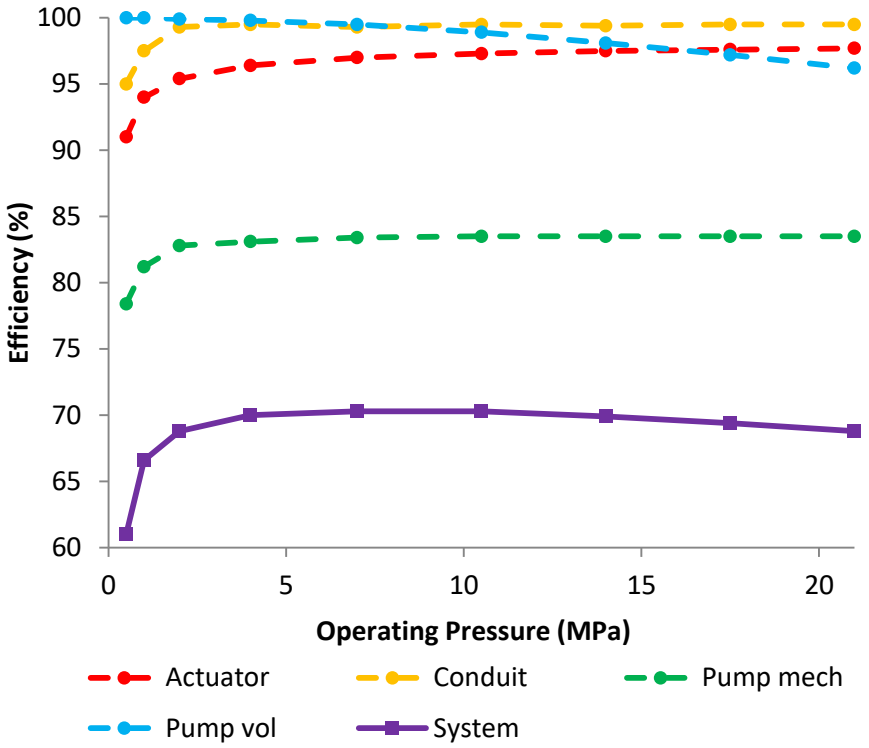

Figure 3.14 Efficiency as a function of operating pressure

The expectation is that the conduit efficiency should decrease significantly as the system operating pressure is decreased, resulting in a higher flow rate and viscous losses for a system with constant output power. However, the algorithm optimizes the size of the conduit inner diameter to mitigate losses by balancing conduit weight with battery weight. Only at low pressures does this balance shift to efficiencies below 98%. The pump volumetric efficiency decreases as the operating pressure is increased due to increased pressure gradient for leakages. If a control valve was included, the valve efficiency is constant due to the assumption that the nominal pressure drop is 15% of the operating pressure. The data illustrates at an operating pressure of 8.3 MPa the overall full-scale efficiency of the system is at a maximum.

The hydraulic power density as a function of operating pressure is illustrated in figure 3.13 for pump and valve controlled systems. The hydraulic power density is defined as the power output of the hydraulic actuator divided by the total weight of the hydraulic components. This metric

excludes the weight of the battery and BLDC motor, in order to only compare the difference in the power densities of the hydraulic components.

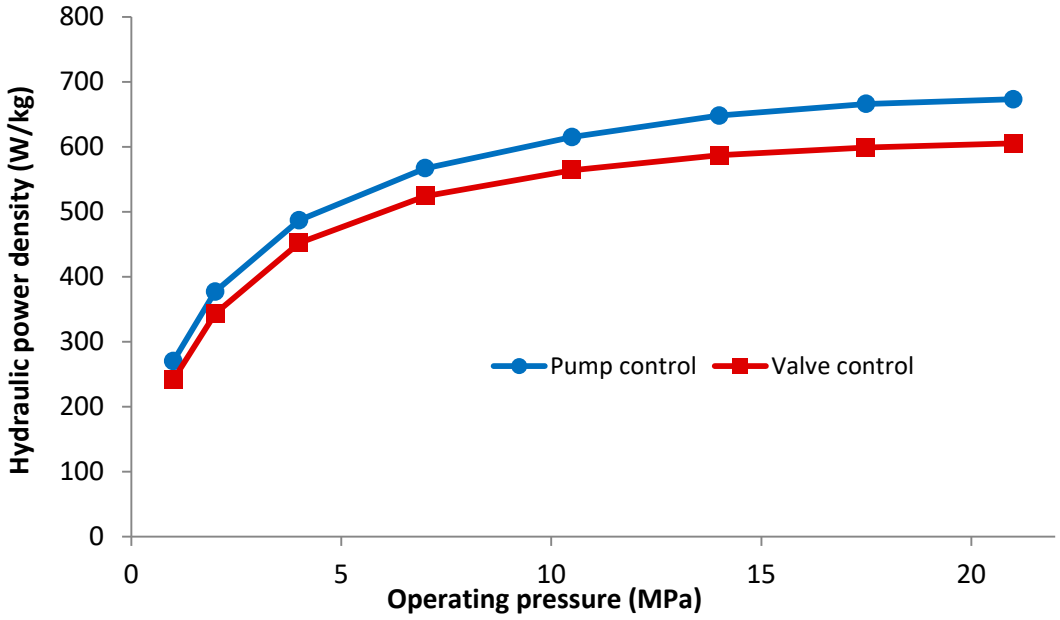

Figure 3.15 Hydraulic power density as a function of operating pressure

The values of hydraulic power density in fig. 3.15 are specific to the design requirements; however, the general trends hold for a wide range of hydraulic systems. The hydraulic power density decreases with a decrease in operating pressure with steep decline under 4 MPa. This steep decline at low pressures is the result of a decreased efficiency in the actuator, conduits, and pump. The design algorithm compensates for the decreased efficiency by increasing the cylinder bore and the pump displacement making the system heavier. In addition, the conduit optimization includes a minimal wall thickness that is based on manufacturing capabilities. At low pressures, the manufacturing limitations will force the conduit to be significantly thicker than pressure stress calculations require, adding unutilized weight.

The metric used to quantify how well the system utilizes the portable chemical energy of the battery is system energy density. System energy density is defined as the total hydraulic energy produced at the actuator divided by the total weight of the system (fig. 3.16). It is assumed that the system is being continuously cycled at the operating pressure for a specific run time.

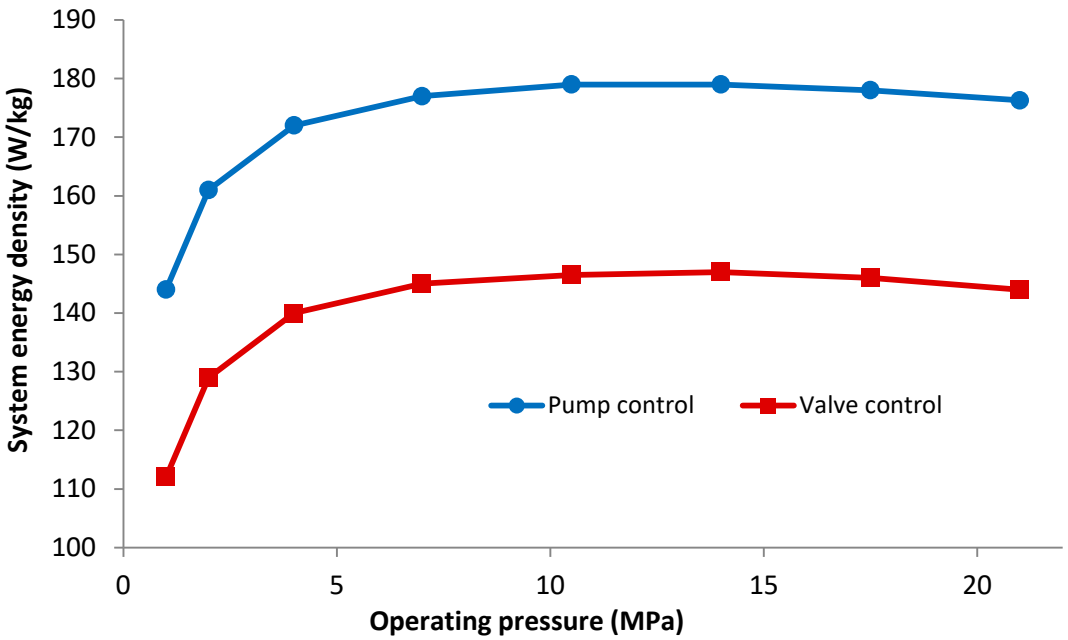

Figure 3.16 System energy density as a function of operating pressure

The system energy density illustrates that there is an operating pressure where the battery energy is being utilized to generate a maximum amount of hydraulic output energy. The reason why the system energy densities decline for higher pressures is that the pump volumetric efficiency declines. Another general trend is the hydraulic power and system energy densities of pump controlled systems are greater than valve controlled systems. The efficiency of valve controlled system is lower due to the additional metering losses across the control valve.

In the following results, the working fluid was varied to analyze how viscosity affects the efficiency of the system. The design of the system was held constant with the input conditions in table 3.7, so the only variables were fluid properties.

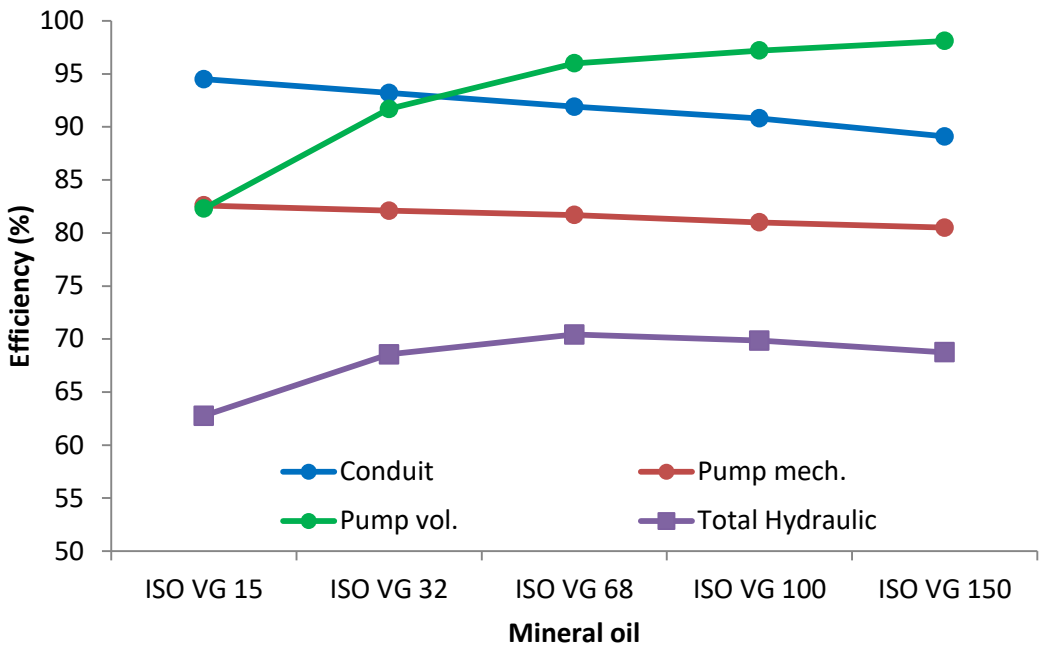

Figure 3.17 System efficiency as a function of mineral oil selection

Figure 3.17 illustrates that there exists an optimum fluid to maximize the efficiency of the system. The location and value of this maximum are based on the input conditions, but the general trends can be extended to other hydraulic systems. In figure 3.17 the X-axis is a list of different mineral oils that increase in kinematic viscosity from left to right. The kinematic viscosity is measured with International Standards Organization Viscosity Grade (ISO VG) classification techniques at 40°C. The low viscosity fluids significantly increased leakages in the pump, decreasing the volumetric efficiency. As the viscosity of the fluid is increased, the viscous losses in the conduit and pump increase.

Figure 3.18 illustrates how the hydraulic power density of the system increases with the system power. The system power is defined as the actuator power requirement multiplying the force and velocity requirements. As the hydraulic system power is varied, the ratio between the actuator force (kN) over velocity (m/s) is held at constant at 2. The rate at which hydraulic power density increases, decreases with increasing system power. However, this is unlikely to plateau until manufacturing large-scale size limitations are reached. Larger cylinders, pumps and

electrical motors have higher power densities as material within the design is better utilized for power transmission compared to small-scale systems.

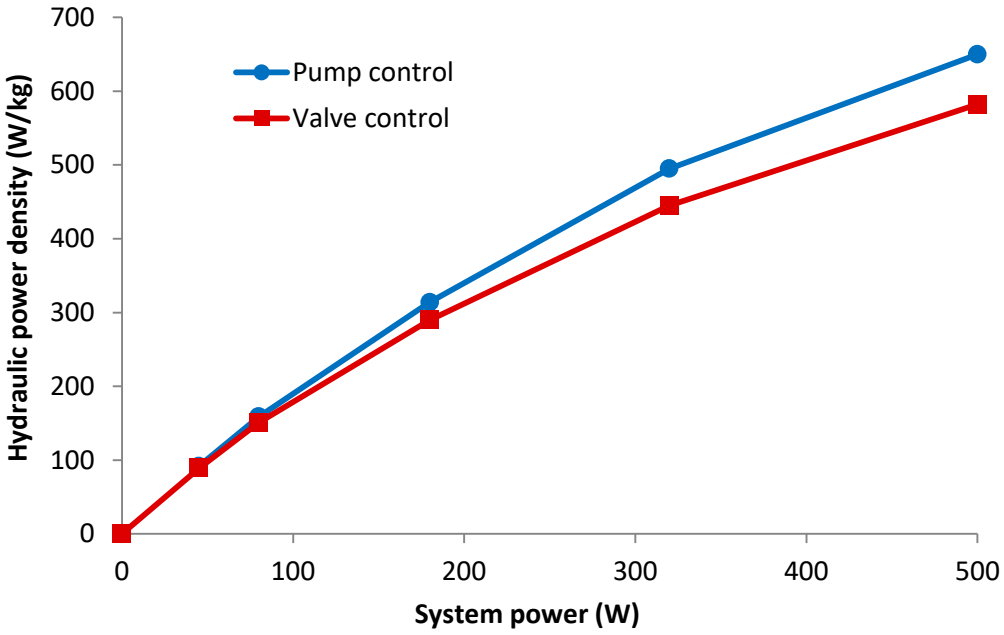

Figure 3.18 Hydraulic power density as a function of system output power

As a hydraulic system power is decreased, the efficiencies of all the hydraulic components decreases due to increased proportions of viscous, seal, and bearing losses. There are also higher proportions of leakage losses to nominal flow rates. The viscous pressure losses within the conduit increase as the inner diameters are decreased. This leads to a decrease in conduit efficiency as the hydraulic system power level is scaled down. As low system power levels are reached, there exist many manufacturing limitations that add additional weight to all of the components. Several parts incorporate minimal thickness limitations due to the fact that material defects can become a significant threat to part failure. The thickness limitations reduce the ability of cracks to form and propagate within thin material.

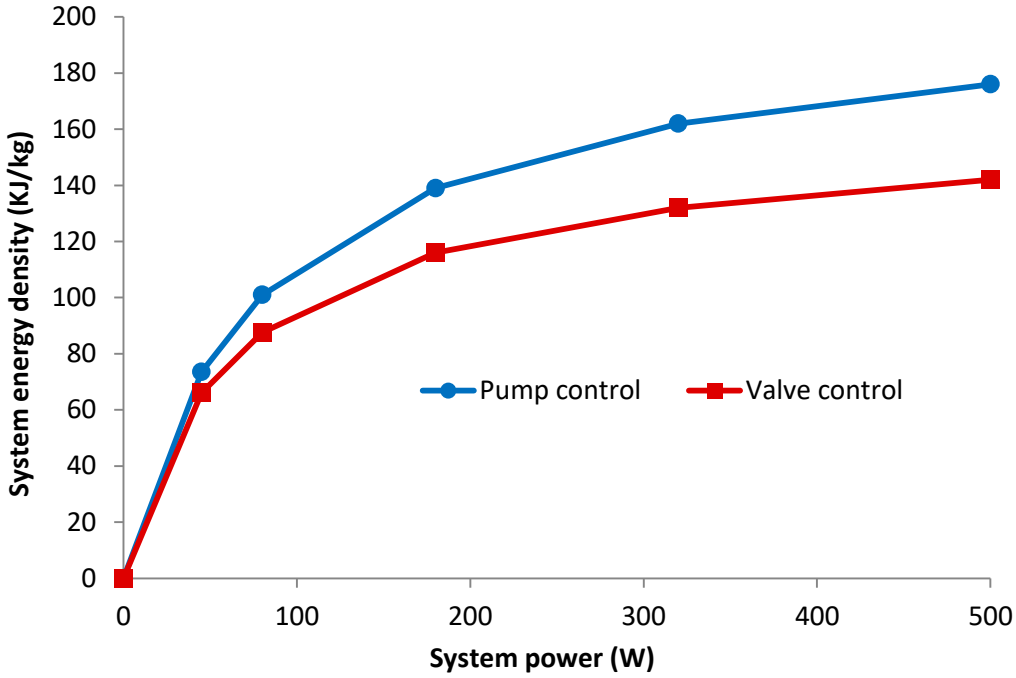

Figure 3.19 System energy density as a function of system output power

The system energy density tends to decline rapidly for systems under 50W (Fig. 3.19). This is a result of system efficiency dropping off. As the system power level is increased, the efficiency begins to plateau causing system energy density to slow its rate of incline. The results illustrate that portable hydraulic systems below 100 W utilize battery energy poorly to produce actuator work.

3.4 Discussion

3.4.1 Summary of results & design guidelines

The system-level design optimization script is composed of individual component models that have all been separately validated. This research tool takes a novel approach to optimizing the design of small-scale hydraulic systems by performing the optimization at a system-level as opposed to focusing on individual component design. This provides a solution for the lightest weight possible system that meets the defined user's actuation requirements.

The results show that for small-scale hydraulic system efficiency, power and energy densities quickly drop with operating pressures below 4 MPa. As operating pressure is increased, there

reaches an operating point where maximum system efficiency is reached. As the operating pressure is further increased, leakage flow within the pump increases resulting in a drop in overall system efficiency. For systems that require portable energy storage of a battery, the operating pressure should be set near this maximum point of efficiency.

In large-scale high flow rate pumps, the volumetric efficiency of the pump is negligible in comparison to flow rate capabilities of the pump. In small-scale applications the volumetric efficiency of the pump provides the upper limit to the pressure capabilities of the system. By further researching and improving the volumetric efficiencies of the pump, the power and energy densities of hydraulic actuation system could be improved with higher operating pressures.

The results illustrate the selection of the appropriate fluid can improve the performance of the system. The fluid property that is most significant for optimizing the steady-state performance is viscosity. In the case study, the system efficiency was increased by 7% by selecting the best fluid. System efficiency can be maximized with a quantitative comparison of leakages and viscous losses.

In comparing the steady state performance of pump and valve controlled systems, pump controlled systems have superior efficiency, power density, and energy density. Another conclusion to be drawn from the results is that small-scale valve controlled systems will likely have inadequate heat loss and require the addition of heat exchanger. This is especially true for intermittent operation, as fluid only circulates though the relief valve, reservoir and pump, building heat quickly within the system.

The case study of the hydraulic powered AFO illustrated that such a system should be pump controlled to minimize weight while keeping the component surface and working fluid temperatures within safes limits. A valve controlled system will be heavier and require additional heat exchanges. The current pump design operates most efficiently at around 14 MPa (2000 psi) with a fluid viscosity around 50-70 mm^2/s. When the pump controlled hydraulic system is operated under these conditions, the maximum theoretical efficiency of the system is 65%. However, the ankle duty cycle is highly intermittent in force and velocity requiring the hydraulic system to be operated at lower pressures and flow rates for the majority of the duty

cycle. As a result, the average efficiency of the system will be significantly lower, because it is not being operated constantly at full-scale conditions.

3.4.2 Limitations of the design guidelines

The component models have all been validated either in this research or in prior art; however, system-level validation was not performed. This validation will require building custom actuators, hoses, pumps, and a BLDC motor to confirm the predicted performance and weight matches the hardware. In addition, extensive temperature measurements will need to be taken to validate the assumptions taken in modeling the system-level heat transfer.

A large percentage of the losses for a hydraulic system exist in the hydraulic power supply; therefore, it is essential to optimize the efficiency of pairing the pump and BLDC motor. This study assumed that the winding within the BLDC electric motor could be designed to match the angular velocity and torque requirements of the axial piston pump. In reality the limited commercial availability of low flow rate, high pressure pumps leads to a scarcity of sizes. The pairing of a BLDC motor often requires a gearbox to ensure that the BLDC motor is operating at a torque and angular performance where the efficiency is maximized. A gearbox may lead to a reduction in efficiency and will add significant weight to the overall design. Future research should include an in depth model of the losses and design of the windings within the electric DC motors. Other possible variables of interest that could further improve system efficiency and minimize weight are swash plate angle, piston diameter, and winding geometry.

The design of the hydraulic actuation system is based on continuous operation; whereas in reality most hydraulic systems are in intermittent applications. In these applications, the addition of an accumulator can significantly increase the efficiency of the system. The use of an accumulator to improve the efficiency of the systems with low duty cycles is explored in chapter 4. In addition, the use of motor control algorithms is explored to minimize the flow dumped across the relief valve when actuators on valve control systems are not operating at full-scale velocity.

The current research is focused on single degree of freedom actuation. However, one of the main benefits of hydraulic valve technology is that multiple actuators can be powered by a single pump. Future research should address the question, under what conditions should

multiple control valves be used with a single hydraulic power supply, and when should the system be separated into individual pump controlled actuation systems? This is likely to depend on the placement of actuators, valves and pump, as conduit length will be a determining variable.

Chapter 4 Dynamic Modeling of Small-Scale Pump and Servo Valve Controlled Hydraulic Systems

4.1 Introduction

The objective of this chapter is to develop a dynamic model of pump and valve controlled hydraulic systems. The accuracy of the model was validated as the simulation results were compared with measurements from physical hardware. The validated models were used to simulate step and frequency responses and to predict dynamic performance metrics like bandwidth, rise time, and settling time. The results of this research can be used to determine when a pump or valve control hydraulic system should be used based on the design requirements. These models also provide designers with insight into how varying system parameters change the dynamic performance of the system.

In addition this chapter uses simulations to explore methods of decreasing energy consumption for intermittent operation. An accumulator and unloading valve are used to increase the flow rate capabilities for low duty cycle operation. The accumulator acts as a means of energy storage for valve controlled actuation systems as the actuator is at rest, providing a significant increase in cycle efficiency. In a valve controlled systems the control input is the orifice area of the control valve, while motor voltage is held constant. The concept of proportional pressure control is to monitor and maintain an operational pressure by varying the motor voltage. This principle is explored to further reduce energy consumption during intermittent operation.

4.2 Methods

4.2.1 Linearized algebraic models of hydraulic actuation

Modeling dynamic hydraulic performance is complex due to the presence of nonlinearities within the state equations [6, 80, 2]. In system level design it is common to linearize the differential equations around a particular operating point, so that the dynamics of the system can be simplified into a transfer function that is capable of being analyzed with classic control principles [6, 2]. This provides general information of how to improve the rise time and decrease sources of instability by adjusting different parameters within the system.

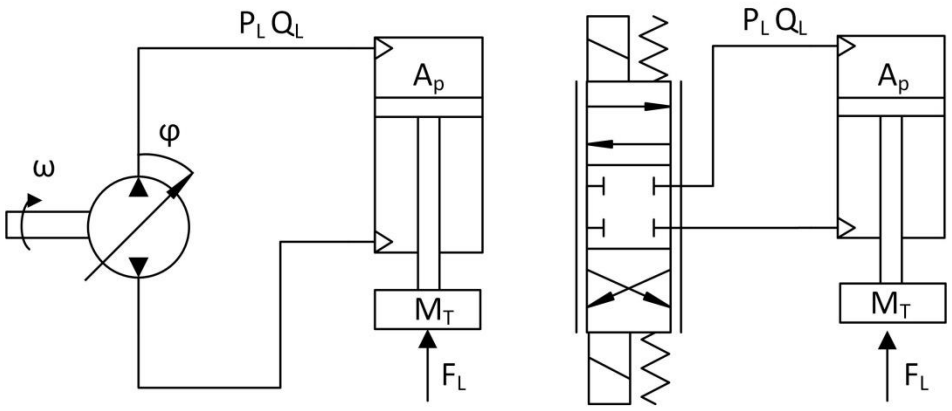

Figure 4.1 Linearized models of pump (right) and valve (left) controlled hydraulic actuation

Table 4.1 Hydraulic system linearization: Variable definitions

Symbol	Description	Units	Symbol	Description	Units
A_p	Area of piston	m^2	P_f	Forward chamber pressure	Pa
B_e	Effective bulk modulus	Pa	P_L	Load Pressure (Pa)	Pa
B_p	Piston dampening	N·s/m	P_r	Replenishing chamber pressure	Pa
C_{IT}	Total internal leakage coefficient for pump & piston	$m^3/s/Pa$	Q_L	Load flowrate	m^3/s
C_T	Total leakage coefficient for pump & piston	$m^3/s/Pa$	x_p	Actuator piston position	m
C_{TP}	Total leakage coefficient of actuator piston	$m^3/s/Pa$	x_v	Valve spool position	m
F_L	Load force	N	V_T	Total volume of forward and return chambers	m^3
G_p	Pump displacement gradient	$m^3/rev/rad$	V_f	Average volume of forward chamber	m^3
K	Piston load spring	N/m	δ	Dampening ratio	-
K_q	Valve flow gain	$m^3/s/m$	φ	Swash plate angle	rad
K_{TP}	Total flow-pressure coefficient	$m^3/s/Pa$	ω	Pump shaft angular velocity	rev/s
K_{VP}	Valve flow-pressure coefficient	$m^3/s/Pa$	ω_n	Undamped natural frequency	rad/s
M_T	Total mass of piston and load	kg	ω	Pump shaft angular velocity	rev/s

Valve controlled

In the valve controlled model, the fluid dynamics between the pump and valve are assumed negligible (Fig. 4.1) .It is assumed that the valve is supplied with a flow greater than Q_L. The orifice equation can be linearized with eq. 4.1 where flow gain defines load flow rate as a function of valve spool position and valve flow-pressure coefficient defines load flow rate as a function of change in load pressure [80].

$$\Delta Q_L = \left.\frac{\partial Q_L}{\partial x_v}\right|_1 \Delta x_v + \left.\frac{\partial Q_L}{\partial P_L}\right|_1 \Delta P_L = K_q \Delta x_v - K_{VP} \Delta P_L \quad (4.1)$$

Equation 4.2 is a summation of forces form between the pressure applied to the piston and mass, damper, spring, and loading applied to the rod. The linearized model is written in Laplace domain to reduce the complexity of manipulating higher order derivatives. Fluid flow rate into and out of the system is balanced in the volumetric continuity equation (4.3).

$$A_p P_L = M_t s^2 x_p + B_p s x_p + K x_p + F_L \quad (4.2) \qquad Q_L = A_p s x_p + C_{TP} P_L + \frac{V_T}{4B_e} s P_L \quad (4.3)$$

The piston position as a function of valve spool position and load force (4.4) is a result of combining eqs. 4.1 thru 4.3 [80].The first term in the numerator is the no load speed, while the second term in the numerator defines the velocity gradient as a function of load.

$$x_p = \frac{\frac{K_q}{A_p} x_v - \frac{K_{TP}}{A_p^2}\left(1 + \frac{V_T}{4B_e K_{TP}} s\right) F_L}{\frac{V_T M_T}{4B_e A_p^2} s^3 + \left(\frac{K_{TP} M_T}{A_p^2} + \frac{B_p V_T}{4B_e A_p^2}\right) s^2 + \left(1 + \frac{B_p K_{TP}}{A_p^2} + \frac{K V_T}{4B_e A_p^2}\right) s + \frac{K_{TP} K}{A_p^2}} \quad (4.4)$$

This relation can to simplified by assuming that spring loads are absent (K = 0) and $B_p K_{PT}/A_p^2 \ll 1$. (4.5)

$$x_p = \frac{\frac{K_q}{A_p} x_v - \frac{K_{TP}}{A_p^2}\left(1 + \frac{V_T}{4B_e K_{TP}} s\right) F_L}{s\left(\frac{s^2}{\omega_n^2} + \frac{2\delta}{\omega_n} s + 1\right)} \text{ where } \omega_n = \sqrt{\frac{4B_e A_p^2}{V_T M_T}} \text{ and}$$

$$\delta = \frac{K_{TP}}{A_p}\sqrt{\frac{B_e M_T}{V_T}} + \frac{B_p}{4A_p}\sqrt{\frac{V_T}{B_e M_T}} \quad (4.5)$$

Pump controlled

In a pump controlled circuit the flowrate of the pump can be altered by varying displacement or the angular velocity of the pump shaft. In the case of a pump controlled actuator the volumetric continuity balance is eq. 4.6.

$$G_p \omega_p \phi = A_p s x_p + \frac{V_f}{B_e} s P_1 + C_T P_f - C_{IT} P_r \quad (4.6)$$

The equation for piston position as a function of pump shaft speed, swash plate angle, and load force (4.7) is a combination of the force balance in (4.2) and the volumetric continuity equation (4.6). This equation assumes that one side of the pump controlled actuator drains to atmospheric pressure.

$$x_p = \frac{\frac{G_P}{A_p}\omega\phi - \frac{C_T}{A_p^2}\left(1 + \frac{V_f}{B_e C_T} s\right) F_L}{\frac{V_f M_T}{B_e A_p^2} s^3 + \left(\frac{C_T M_T}{A_p^2} + \frac{B_p V_f}{B_e A_p^2}\right) s^2 + \left(1 + \frac{B_p C_T}{A_p^2} + \frac{K V_f}{B_e A_p^2}\right) s + \frac{C_T K}{A_p^2}} \quad (4.7)$$

This relation can to simplified by assuming that spring loads are absent (K = 0) and there is a relatively low about of dampening ($B_P C_T / A_p^2 << 1$) (4.8).

$$x_p = \frac{\frac{G_p}{A_p}\phi\omega - \frac{C_T}{A_p^2}\left(1 + \frac{V_f}{B_e C_T}s\right)F_L}{s\left(\frac{s^2}{\omega_n^2} + \frac{2\delta}{\omega_n}s + 1\right)} \quad (4.8) \text{ where } \omega_n = \sqrt{\frac{B_e A_p^2}{V_f M_T}} \text{ and}$$

$$\delta = \frac{C_T}{2A_p}\sqrt{\frac{B_e M_T}{V_f}} + \frac{B_p}{2A_p}\sqrt{\frac{V_f}{B_e M_T}}$$

The linear system analysis above shows that the undamped natural frequency of a valve controlled system is larger by a factor of 2 compared to a pump controlled system. The undamped natural frequency is a function of the hydraulic oil springs and the fluid inertia. Valve controlled systems include two trapped areas of pressurized oil, creating two springs in parallel that add together to create the factor of 2 (Fig. 4.2). Systems are capable of achieving faster and more accurate responses with improved stability the higher the natural frequency [80]. Therefore, valve controlled systems will achieve faster rise times and higher frequency bandwidths.

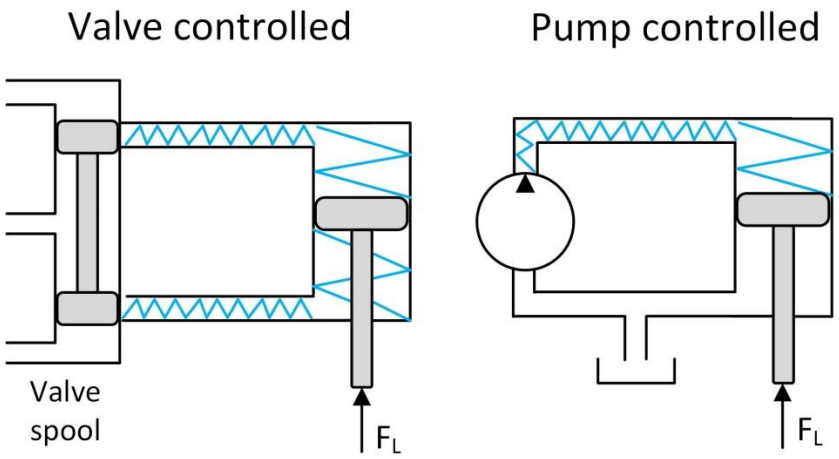

Figure 4.2 Comparison of valve and pump controlled hydraulic springs

The undamped natural frequency of the pump controlled system is a function of forward fluid volume, whereas it is a function of the total volume in a valve controlled system. This is due to a control valve using an inlet and exit orifice causing the hydraulic conduits to and from the actuator to be pressurized. In contrast, a pump controlled system is assumed to only have one

pressurized conduit, and the other drains to a reservoir at atmospheric pressure. Valve controlled systems have the ability to place the control valve as close as possible to the actuator, decreasing the total volume of the forward and return chambers [80]. The placement of the control valve as close as possible to the actuator can result in a significant increase of the undamped natural frequency.

In pump and valve controlled systems, the undamped natural frequency is also a function of the piston area squared. This means that undamped natural frequencies of small-scale hydraulic systems are significantly lower as a result of small bore cylinders. This is an additional control challenge applying to only small-scale hydraulic systems and not to larger systems.

The above linear models lacked several key dynamics that should be considered when estimating the overall system response. In order to get an accurate depiction of dynamic pump control performance, the dynamics of the electric motor must be included. Also the compliance of the system is dependent on the elastic properties of the conduit. It is common to use long and small bore hoses in small-scale hydraulic machines, and these hoses suffer significant expansion at high pressure greatly increasing overall system compliance.

The linear models assume linear dynamics and losses around a specified operating point. The model becomes invalid as the operating point shifts away from the point of linearization due to the presence of nonlinearities within the system. These nonlinearities include viscous losses, leakages, and seal friction. In order to get an accurate depiction of rise time and bandwidth, the system would need to be linearized around several transitioning operating points. This modeling process becomes time consuming and provides low accuracy. Instead, the section 4.2.2 describes the development of a higher order computer model that includes all the nonlinear dynamics as well as modeling of the conduit and motor dynamics.

4.2.2 Experimental Validation

One of the objectives of this thesis is to predict the performance of small-scale hydraulic systems through simulation. The nonlinear simulations were verified by the collection and comparison of experimental data to ensure that the simulate dynamics match the real physical dynamics.

The three hydraulic circuits used in the simulation validation were an axial piston pump loaded with a needle valve (circuit 1A), a pump controlled cylinder (circuit 2A), and a servo valve controlled cylinder (circuit 3A) (Fig. 4.3). The purpose of simulating circuit 1A was to simplify the hydraulic dynamics to a pump, conduit, and needle valve and eliminate more complicated dynamics introduced by electromechanical valves and actuators. Circuits 2A and 3A illustrated the two types of hydraulic circuits under examination, pump and valve controlled hydraulic actuation systems.

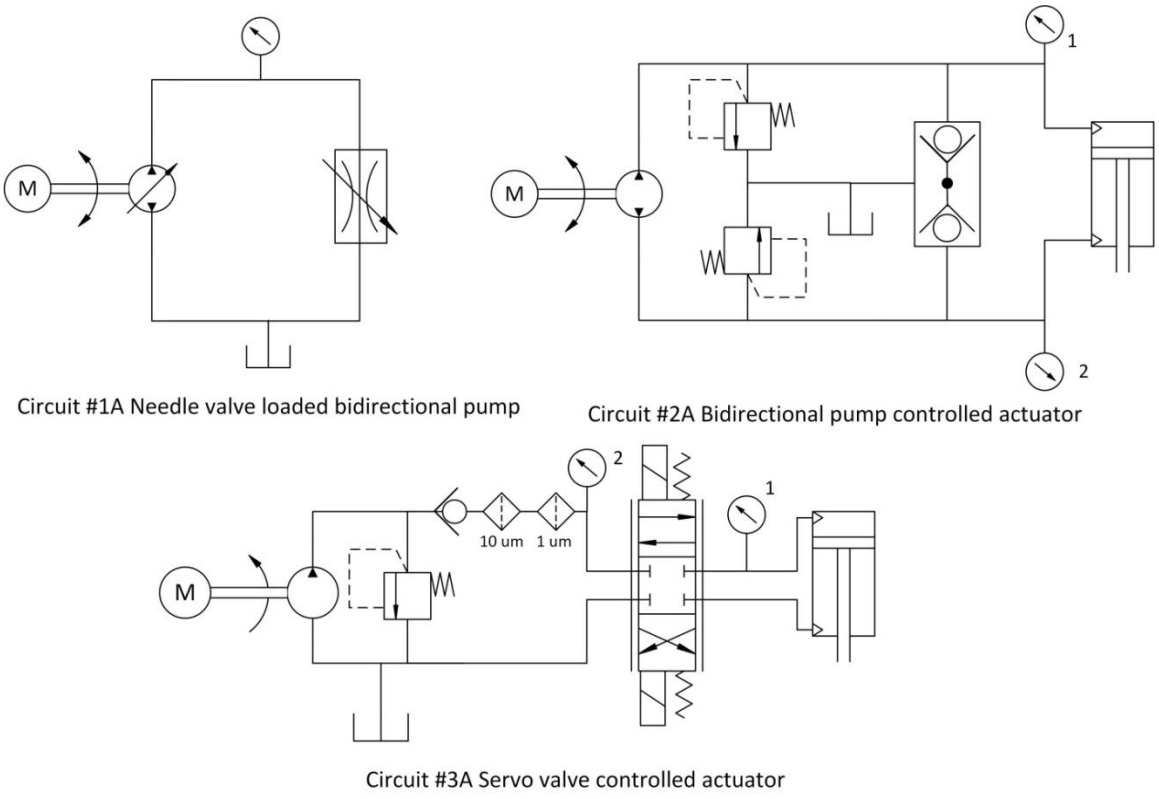

Figure 4.3 Hydraulic circuits used for simulation validation

4.2.3 Apparatus Description

Three separate hydraulic power supplies were used in the experiment validation to illustrate the simulations were valid for different styles of pumps and motors. In addition, the hydraulic power supplies were designed for different applications with two systems illustrating portability and the third tethered to a conventional electrical outlet. The portable hydraulic power supplies

used in circuits 1A and 2A were operated at intermittent conditions to prevent the motor from overheating, while the tethered hydraulic power supply in circuit 3A is operated continuously.

The portable hydraulic power supplies in circuits 1A and 2A used identical pumps and motors; however, the pump assembly in circuit 2A incorporated two pressure relief valves and an inverse shuttle valve allowing the pump to be reversible and directly control an actuator (Fig 4.4). The fixed displacement 0.8 cc/rev axial piston pump (PN: TFH-080-U-SV, Takako Industries) has a maximum operating flowrate and pressure of 40 cc/s and 21 MPa. The experimental validation used an axial piston pump due to comparison in section 2.7.1 showing that the high volumetric and mechanical efficiencies of this pump type are optimal for producing portable hydraulic systems with the highest possible energy densities.

The pump assembly in circuit 2A also included an inverse shuttle valve that allowed the tank to be connected to the low pressure port. The inverse shuttle valve allows the pump to directly control the actuator by serving two main functions. A standard hydraulic cylinder has unequal areas on the opposing sides of the piston creating two different flowrates into and out of the cylinder fluid chambers. The inverse shuttle valve allows fluid to be drawn from or flow into the reservoir to compensate for the unequal cylinder flowrates. The inverse shuttle valve also serves the purpose of replenishing the circuit with additional hydraulic fluid in the advent of leakages. The pump assembly also included two pressure relief valves that limit the maximum pressure of both ports to 24 MPa and an 80 cc reservoir.

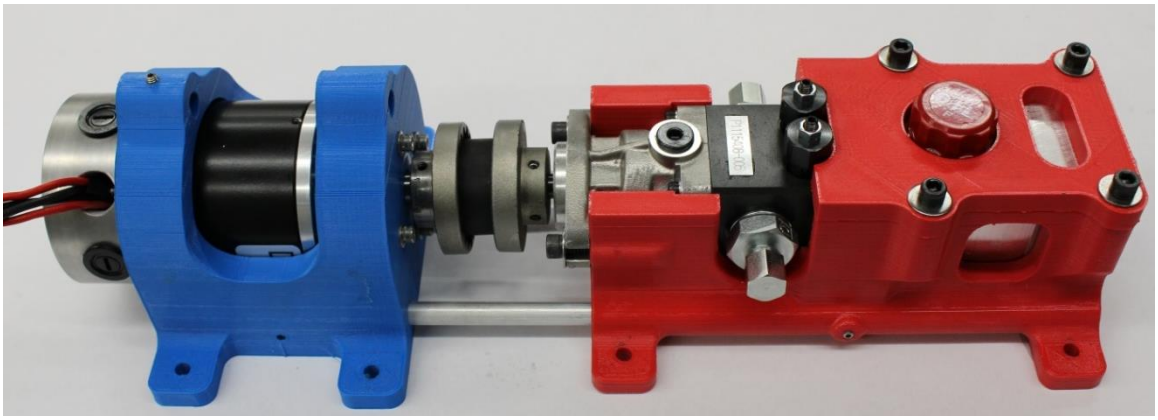

Figure 4.4 Hydraulic power supply for circuit 2A

The pump assembly in circuit 2A was coupled with a brushed DC motor (A28-150, AmpFlow) capable of producing up to 3 hp intermittently. The voltage controlled motor driver (Vyper, Robot Power) used a H-bridge to supply the motor with up to 120 A at 36V. The output voltage of the motor driver was controlled by a 0-5V input that was generated by a 12 bit digital to analog converter (DAC), while a microcontroller (Arduino Uno) communicated with the DAC using serial peripheral interface (SPI). The electrical power for the system was provided by a 3300 mAh, 8 cell lithium polymer battery (TP3300-8SPP25, Thunder Power) operated at 29.6 V. The angular position of the motor shaft was monitored with an optical encoder (E2-1000-375-IE-D-G-2, US Digital) with a resolution of 1000 cycles per revolution. The encoder quadrature output signal was translated with a 32-bit quadrature counter (LSR7366R, LSI Computer System INC.) with SPI communication to the microcontroller. The position data was integrated with respect to time to monitor motor shaft angular velocity.

The tethered hydraulic power supply in circuit 3A used a gear pump (G2206E2A330N00, Concentric) with a 1.59 cc/rev displacement to generate 78.8 cc/s. Although gears pumps typically have lower efficiencies, the relative simplicity and low cost of their construction makes them commercially popular. Gear pumps also exhibit higher power densities compared to axial piston pumps, making them ideal for portable applications with tethered electrical power like corded power tools. The hydraulic power supply was unidirectional with an adjustable pressure relief valve limiting the pressure of the pump port between 14 to 21 MPa. The electric AC motor was capable of producing 1 hp continuously while operating off a 230V electrical outlet.

Pressure transducer 1 (PX309-3KG5V, Omega) had a 21 MPa capacity and was used to monitor the upstream needle valve pressure in circuit 1A, the actuator cap pressures in circuits 2A and 3A. Pressure transducer 2 (MLH05KPSP06C, Honeywell) had a 35 MPa capacity, and was used to monitor the cylinder rod pressure in circuit 2A and the servo valve supply pressure in circuit 3. The hydraulic conduits between the pressure sensors and other hydraulic components were stainless steel braided Teflon hose with an inner diameter of 5 mm.

An important variable to characterize in the simulation is the radial stretch of the flexible hose. This was estimated by measuring the change in outside of hose as a function of pressure. A hose was plugged with a fitting at one end. A pressure transducer, hand pump, and a shutoff needle

valve were connected in series with the hose. The change in the outside diameter of the hose was measured with a caliper as the pressure was gradually increased with the hand pump. The measured conduit compliance was approx. $2.5\times10^{-4} \pm 0.5\times10^{-4}$ mm/MPa.

The single rod aluminum hydraulic cylinder in the experiment setup was custom machined with a 12.7 mm bore, 4.8 mm rod outer diameter, and stroke length of 102 mm (Fig. 4.5). There were two neoprene O-rings on the piston that serve the purpose of sealing the two fluid chambers and also balancing forces in the axial direction eliminating rubbing between the piston cylinder housing. The rod and piston neoprene O-ring seals had a compression ratio of 12-15% with the specified tolerances. The position of the piston within the cylinder was measured with a 10 KΩ linear potentiometer (LCP12Y-100-10K, ETI Systems). The position data was integrated with respect to time in order to estimate the piston velocity. The cylinders were assumed to have no measurable leakage, so the areas of the piston can be used to calculate the volumetric flow rate into and out of the cylinder. The static and dynamic seal friction forces of the cylinders were measured with the assistance of a strain gauge. The viscous drag on the piston is calculated with the empirical relations (2.47-2.51).

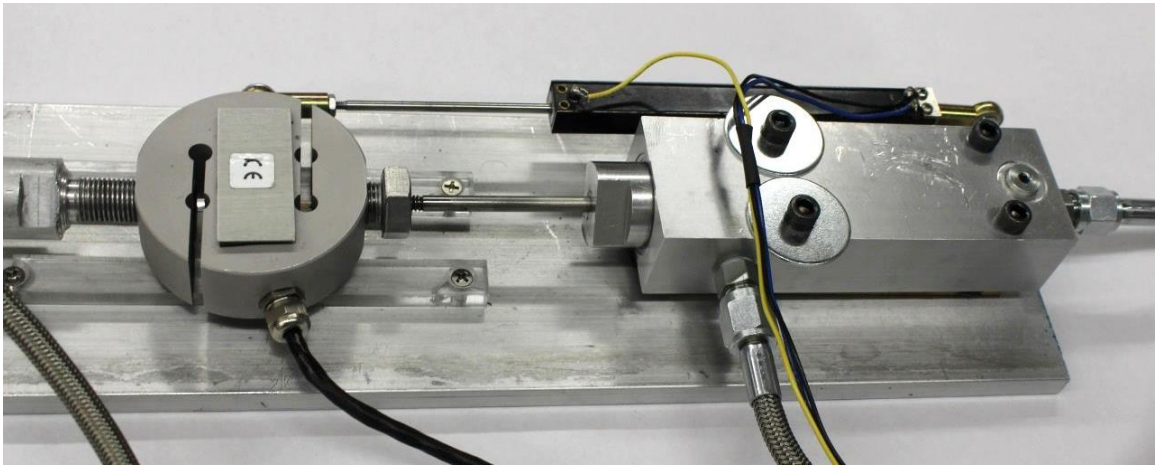

Figure 4.5 Custom hydraulic cylinder with load cell and potentiometer

The flow control servo valve (E024-Q38H21YGA15VAR2Y, Moog) in circuit 3A had a maximum rated flow of 63.3 cc/s. The supply pressure of the valve must be maintained between 14 and 28 MPa for the pilot stage to properly control the position of the spool. The servo valve control input was the torque motor current ranging between -10 mA to 10 mA. The current regulator,

operational amplifier, and DAC that control the current supplied to the servo valve torque motor are illustrated in appendix A.4.1. The microcontroller used SPI communication to vary the voltage output of the DAC. The servo valve pilot stage is susceptible to particle damage, so a 10 micron (9052V-10, Arrow Pneumatics) and 1 micron (421AT-1MP, Norman Filter Company) were put in series with the servo valve supply line. The filters are larger enough to cause small pressure drops in comparison to pressure drop along the conduit and valve. The filter dynamics are assumed to be negligible in the simulations.

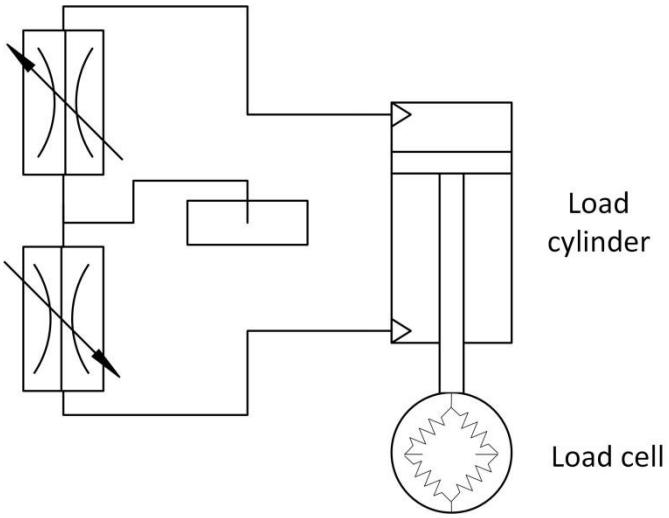

Figure 4.6 Needle valve loading fixture

A passive needle valve loading fixture in fig. 4.6 was constructed to generate 500 to 2500 N loading conditions. The loading fixture used two adjustable unidirectional poppet style needle valves (PN: EN10S, Deltrol Fluid Products) that introduced a large pressure drop across an orifice dissipating hydraulic power in the form of heat. The passive load cylinder (25KCHMIUW14M14M1001122, Parker) had a bore of 25 mm and stroke length of 100 mm. The rod of the passive load cylinder are connected through a 4450 N capacity S-beam load cell (LCR-1K, Omega) to the rod of the driven custom cylinder. The load cell output signal was amplified by a factor of 100 to have a resolution of 326.8 lb/V by the circuit illustrated in appendix A.4.1. The loading provided by this fixture is velocity dependent, so the needle valve orifice dynamics were incorporated into the simulations.

The output voltage of pressure traducers, linear potentiometer, and load cell amplifier are a connected to a data acquisition module (NI USB-6002, National Instruments). The microcontroller interprets the motor encoder position and relays the corresponding motor angular velocity to a DAC connected to the data acquisition module. All five signals are sampled at a rate of 2000 Hz. Finally the working fluid used was food grade white mineral oil that has a viscosity of 12.3 cST at 40°C.

4.2.3 Dynamic Simulations

This section describes how the Matlab and Simulink software with the additional SimHydraulics toolbox were used to construct simulations for small-scale hydraulic circuits. The simulation and data acquisition frequencies were 2000 Hz for all simulations except during servo valve frequency response testing when the frequencies were increased to 10000 Hz. The increased simulation and data acquisition frequencies were necessary to get an accurate depiction of a sinusoid output when the input signal frequencies are faster than 20 Hz.

The simulations were composed of an ideal voltage or current source powering an electromechanical converter representing the dynamics and properties of an electric motor. Several of the simulations incorporated a constant mechanical efficiency gearbox coupling the mechanical and fluid power converters. The rotary mechanical power was delivered to a hydro-mechanical converter that simulate the dynamics and properties of the pump. Inertial, capacitive, and resistive elements were added in several places within the electrical, mechanical, and fluid power systems to simulate a more accurate representation of the dynamics.

The pump was modeled as an conversion of torque to pressure and of angular velocity to flow rate. If the pump being modeled is an axial piston type the displacement, mechanical, and volumetric efficiencies were all calculated with the empirical models described in section 2.7.2. These calculations are performed outside of the simulation to decrease calculations and runtime within the simulation. The data is entered as 2-dimensional performance look-up table that used the current pressure and flow rate to determine the corresponding mechanical and volumetric efficiencies of the axial piston pump. When simulating commercial pumps other than axial piston, the standard SimHydraulics bidirectional pump model was used with parameters taken from the pump datasheet.

The conduits of the hydraulic circuit were simulated with the pipeline model in SimHydraulics. The pipeline model was composed of a hydraulic chamber nested between two hydraulic resistive tubes. The expansion of the hydraulic hose under pressure was modeled as a first order system with gain defined as the static pressure-diameter coefficient and a viscoelastic time constant. An analysis of these hose parameters and consideration of whether the hydraulic conduit should be modeled as a rigid pipeline or expandable viscoelastic volume is in section 4.3.1

The simulated fluid was mineral oil at 40°C with density of 0.83 g/cc, kinematic viscosity of 15 cSt, and a bulk modulus 1.9 GPa. The simulation did not take into consideration the varying fluid temperature; therefore, all the fluid properties remain constant and uniform throughout the hydraulic circuit. The relative amount of trapped air in the simulation is a parameter that is unknown and is not easily measured.

The hydraulic cylinders were assumed to have no leakage in the simulations. This assumption is supported based on the empirical O-ring seal model (2.6), where the leakage is less than 0.1% of the full-rated flow. This assumption is further supported with O-ring seal testing performed with the manufacturer suggested compression ratios resulting in no measureable leakage.

Custom models were created for electric motors, inverse shuttle valve, and spring loaded accumulators. These models and assumptions are described in appendix A.4.2.

Servo valve model

This section describes the model used for the two stage, pilot controlled servo valve. The valve models within SimHydraulics did not take into consideration the continuous fluid flow through the pilot stage. Pilot flow is one of the largest losses of power within servo valve actuation, especially for intermittent operation. The electrical and pilot dynamics were modeled as a first order system with a gain and magnitude based on the manufacturer's specifications. A servo valve was modeled as a four way valve with one fixed orifice and four variable controlled orifices. The fixed orifice represents the constant pilot flow from the supply port to the tank port. The fixed orifice area was calculated from the rated pilot flow on the manufacturer's specification sheets. The four variable orifices represent flow controlled by the actuation of the main spool. In a servo valve the flow passes through a set of two orifices controlled by the

position of the main spool, so there is a pressure drop as the flow travels from the supply port to either port A or B and as the flow returns from port A or B traveling to the tank port.

The spool shifting to the left from the neutral positive in fig. 4.7 represents a positive input signal that opens orifices P-A and B-T in the model structure diagram of fig. 4.7. A negative input signal represents the spool shifting to the right opening orifices P-B and A-T. The maximum area of these variable control orifices are calculated based on the full-scale pressure drop listed on the servo valve specification sheets and the empirical orifice model (2.32). All the variable orifices have an initial negative control height to represent the deadband. The deadband is caused by overlap on the spool between the edges of ports and spool. This overlap prevents leakage when the spool is in the neutral position, but also adds a delay to the response of the valve.

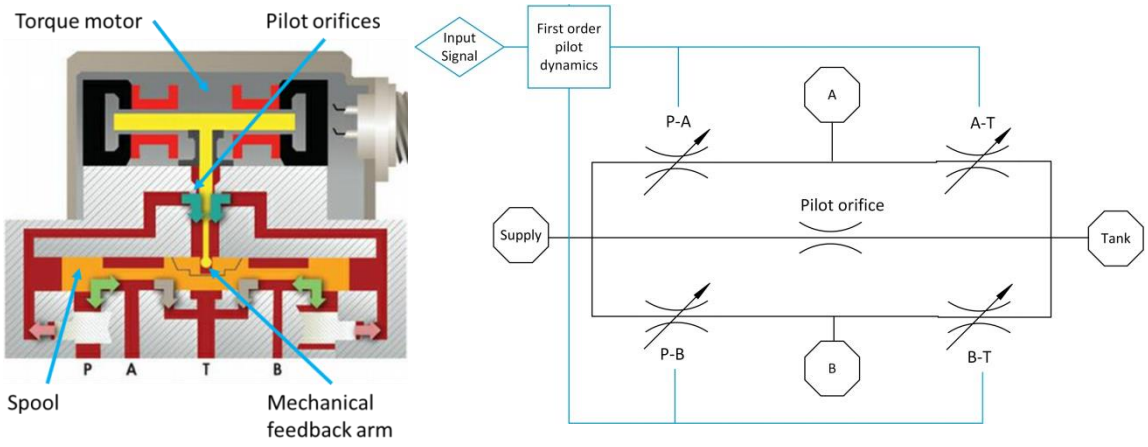

Figure 4.7 Cross-section of two stage servo valve (left) [81] and modeling structure diagram (right)

Figure 4.8 illustrates the pilot flow rate for the modeled servo valve as a function of the total pressure drop across the valve. The power loss due to pilot flow when the valve is operating at 20 MPa is 90 W. Most human assistive machines operate below 500W, and pilot flow power loss represents a significant proportion of the total system power. Fig. 4.8 also illustrates the flow rate supplied by the modeled servo valve as a function of the pressure drop across the orifices and the spool position.

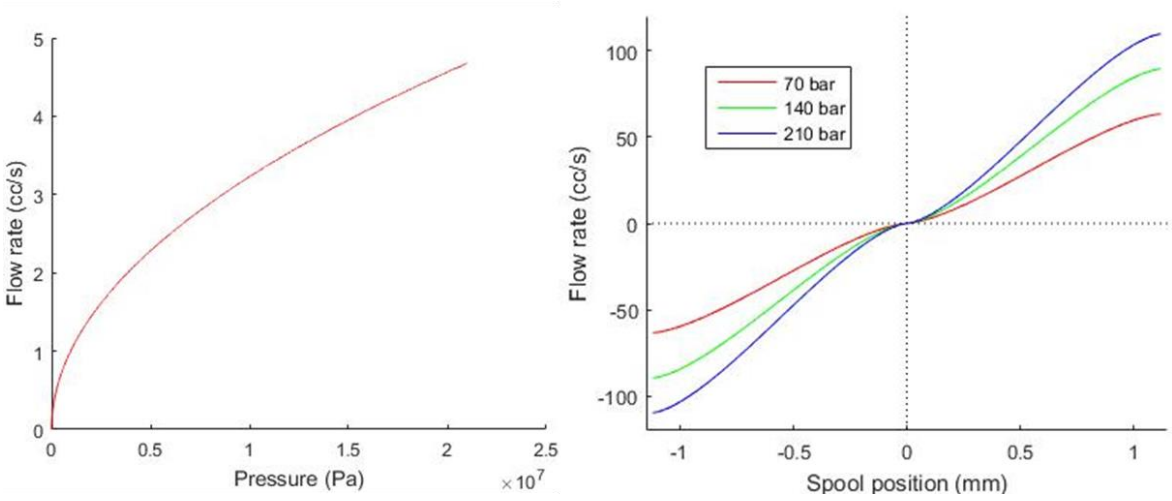

Figure 4.8 Servo valve pilot flow as a function of pressure drop (right) servo valve flow rate as a function of spool position (left)

4.2.4 Validation Criteria

There are two validation criteria that the comparison of the measured and simulated results must meet in order for the simulation to be considered a valid representation of the pump and valve controlled hydraulic actuation systems. The first validation condition is that the simulation results must stay within a 10% error on all measured metrics. With step inputs there may be a brief delay between the responses of the simulated and measured systems causing large errors. The delay is a result of the time it takes pressure within the system to overcome static friction. In this case, the rise time of the simulated and measured systems must be with 10 ms of each other.

The measured metrics that are compared between the experiments and simulations are the cap, rod, and system pressures, the cylinder piston velocities, the pump shaft angular velocities, and motor currents. The cylinder piston velocity was used to estimate flow rate due to the assumption that the cylinder seals have no leakage. The control variables are the electric motor voltage, the servo valve current, and the cylinder load.

4.3 Results

4.3.1 Needle valve loaded bidirectional pump validation

The main purpose of simulating a pump loaded with a needle valve is to ensure that the motor, pump, and conduit dynamics match the physical measurements using the essential hydraulic components. The inputs to both systems were voltage steps of 8.3V, 12.6, and 14.7V, which correspond to unloaded motor angular velocities of 2000, 3000, and 3500 RPM. The needle valve setting was constant during the simulation and data collection. The results of the 8.3V simulation and measured data are in fig. 4.8, with additional plots are included in appendix A.4.3.

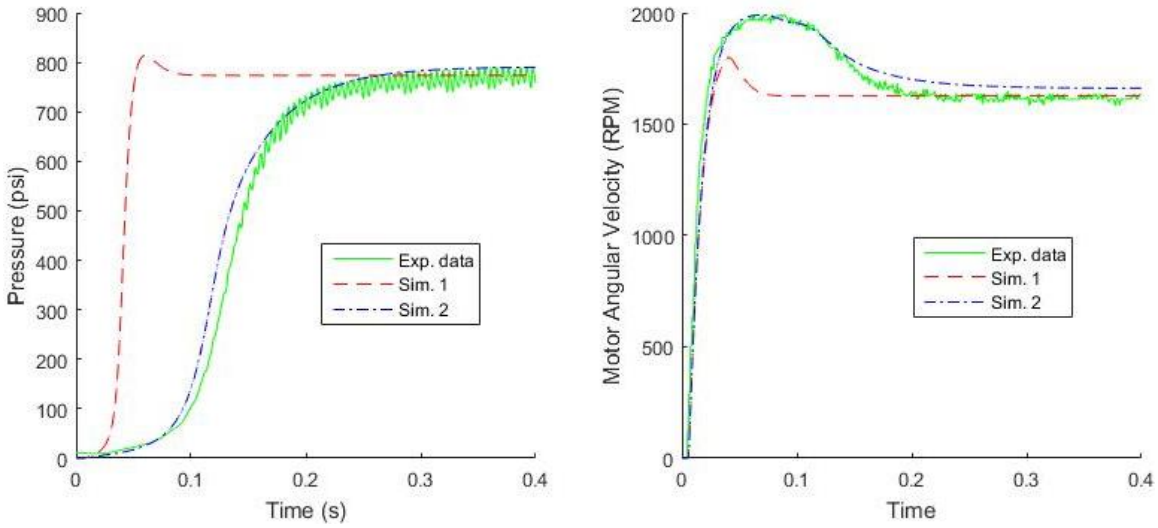

Figure 4.9 Simulation validation: Pump loaded with a need valve

In fig. 4.9 simulation 1 illustrates the system neglecting hose compliance and fluid inertia, while simulation 2 takes these parameters into consideration. The standard formula for fluid inertia within a pipe relates the derivative of flow rate with respect to time dq/dt, system pressure P, conduit diameter d, and fluid density ρ (4.9). The derivative of flow rate with respect to time is a variable that defines the rate of system response. The equation illustrates that the derivative of flow rate and the rise time will decrease exponentially for small diameter conduits. Based on the experiment results and the empirical relation for fluid inertia, the fluid inertia is an influential dynamic to include when simulating small-scale hydraulic systems. In addition, simulation 2

illustrates an accurate representation being within the 10% validation criteria of the measured hydraulic circuit dynamics.

$$\frac{dq}{dt} = \frac{\pi P d^2}{4\rho L} \quad (4.9)$$

The data also illustrates that a significant amount of time and energy are required to pressurize the fluid, and this energy will be lost as the fluid is depressurized. This energy required to pressurize the system is estimated by the time between when the pump shaft angular velocity reaches 90% steady state valve and when the system pressure reaches 90% steady state valve. The work required to pressurize a fluid can be estimated by (4.10), where ΔP is the pressure difference, V is the volume of fluid, and B_e is the effective bulk modulus of the fluid. Pump controlled systems will generally have larger amounts of fluid that cycle through large pressure ranges, and therefore suffer more compressibility losses.

$$W = \frac{\Delta p^2 V}{B_e} \quad (4.10)$$

4.3.2 Pump controlled validation

In an effort to better understand pump controlled cylinder dynamics and to validate the accuracy of the simulations, a loaded step response was conducted using the needle valve loading fixture. The input to the motor was a voltage step of 14.7V equivalent to approx. 3500 RPM unloaded motor velocity. The needle valve loading fixture is adjusted to simulate a 400 lb loading at the steady state velocity in Fig. 4.10. Additional results and simulations were collected varying the input magnitude and load force to ensure the simulation results are valid.

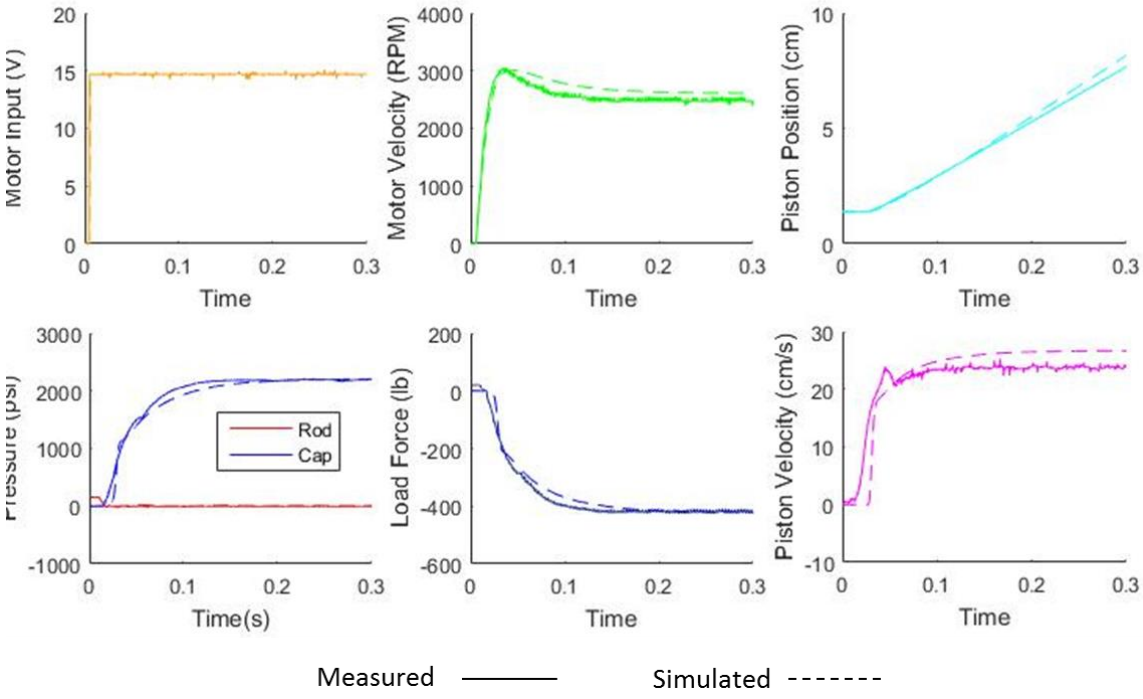

Figure 4.10 Simulation validation results: Pump controlled loaded step response

Overall the difference between the measured and simulated system variables stays with 5% error, except when comparing the simulated and measured steady state piston velocities. There is a 9.4% steady state velocity error that can be attributed to inaccuracies of the electrical motor resistance and the pump efficiency mapping compared to experimental conditions. As an electric motor heats up, its internal resistance increases leading to a decrease in the overall efficiency. Thermal dynamics like this are not considered within the simulation. The pump efficiency mappings are created using constant fluid properties and measured pump geometries. If the temperature of the fluid increases as heat is dissipated by friction and absorbed by the circulating fluid, the fluid viscosity decreases. A lower fluid viscosity results in more internal leakages within the pump and an overall lower volumetric efficiency.

The measured and simulated rise times of the loaded system step responses are approximately 75 and 95 ms. The difference in rise times is primarily from a difference in acceleration. With the other metrics matching well, the difference in acceleration could be the simulated system having too much fluid mechanical inertia. There is also a small peak of piston velocity and dip in

load force at time 0.06 seconds not seen in the simulation. This is likely attributed to an air pocket passing through the needle valve in the loading fixture.

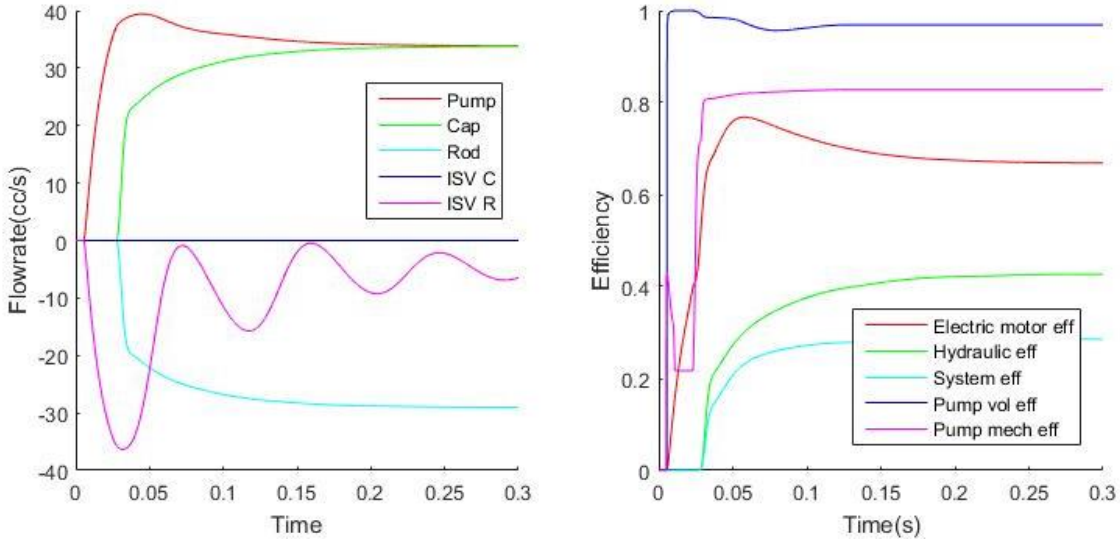

Figure 4.11 Simulate flow rate and component efficiencies of a pump controlled actuator

One of the benefits of constructing a validated simulation of a system is to observe the variables that are difficult or require multiple expensive sensors to measure. Figure 4.11 contains the simulated flow rates and efficiencies within the system. The data illustrates that the flowrate supplied by the pump and the flow rate entering the cap side of the actuator are different under dynamic conditions. Only a small amount of fluid will flow into the hydraulic cylinder until the pressure is sufficient to overcome the static seal friction force. As the pressure builds, the hydraulic conduit elastically stretches and the fluid compresses. The pump initially draws fluid from the reservoir through the inverse shuttle valve on the rod side port, instead of drawing fluid from the rod port on the cylinder. When the piston is stationary inside the cylinder, the pump would have to draw a vacuum on the rod cylinder port to draw fluid, but instead initially draws all the fluid from the reservoir. The flow rate drawn from the shuttle valve appears to have a under dampened response gradually oscillating until it reaches a steady state value that is the flow rate required to compensate for the area difference on the cylinder piston.

The volumetric efficiency of the pump stays well within 95% as the system is accelerating. The mechanical efficiency of the hydraulic pump is initially low. As pressure builds within the system,

the mechanical efficiency of the pump climbs to approximately 83% and stabilizes. The electric motor efficiency peaks at 77% at 53 ms and then decreases to a steady state value of 67%. This pattern of motor efficiency is explained by observing the load the electric motor experiences. The motor torque peaks at 4.2 Nm, around 3 ms after the beginning of the step input. The motor torque then continues to decrease before increasing slightly to a steady state value of 2.4 Nm. Initially the majority of the motor loading is a result of the winding, shaft, pump, fluid, and piston inertias accelerating. As the system reaches steady state velocity the inertia load decreases while the load from the cylinder rod force is still increasing. When the motor is heavily loaded, the motor suffers lowered efficiencies as the voltage across the internal resistance increases.

Pump controlled actuation circuits are often used due to their higher efficiency compared to other types of hydraulic circuits [80]. The steady state overall hydraulic and system efficiencies are 43% and 29% under these operating conditions. The overall hydraulic and system efficiencies both experience 24 ms delay until the actuator piston starts accelerating. The delay is primarily a function of the combined cylinder seal friction forces, the hose compliance, the fluid inertia and fluid bulk modulus. The system remains at rest until the pressure in the cylinder is greater than the combined seal friction within the custom and load cylinders. The main system parameters that define how pressure builds within the system are the volumetric percentage of entrapped air and the elastic properties of the hose. As the pressure within the system builds, the hose expands radially. This slows the pressure ascent as more fluid is required from the pump to build pressure compared to a rigid conduit. In addition, the higher the percentage of air entrapped in the fluid, the more it compresses. Again additional fluid is required to generate the same pressure compared to a fluid void of air.

In figure 4.12, a sinusoid voltage with an amplitude of 8.25V was supplied to the electric motor, and the magnitude and phase of the hydraulic actuators were measured as a function of frequency. The measured and simulated frequency responses illustrate similar trends with approximate cut-off frequencies of 13.5 and 10.9 Hz. The difference between the measured and motor frequency responses illustrate dynamics that are introduced by the hydraulic components. There is an erratic behavior in the magnitude and phase of the experimental system beyond 16 Hz that is the result of hydraulic dynamics. This irregularity could be the result

of inconsistencies within hydraulic fluid, including air bubbles or particulate passing through an orifice constriction within the system. The irregularity could also be a caused by reciprocating pressure waves.

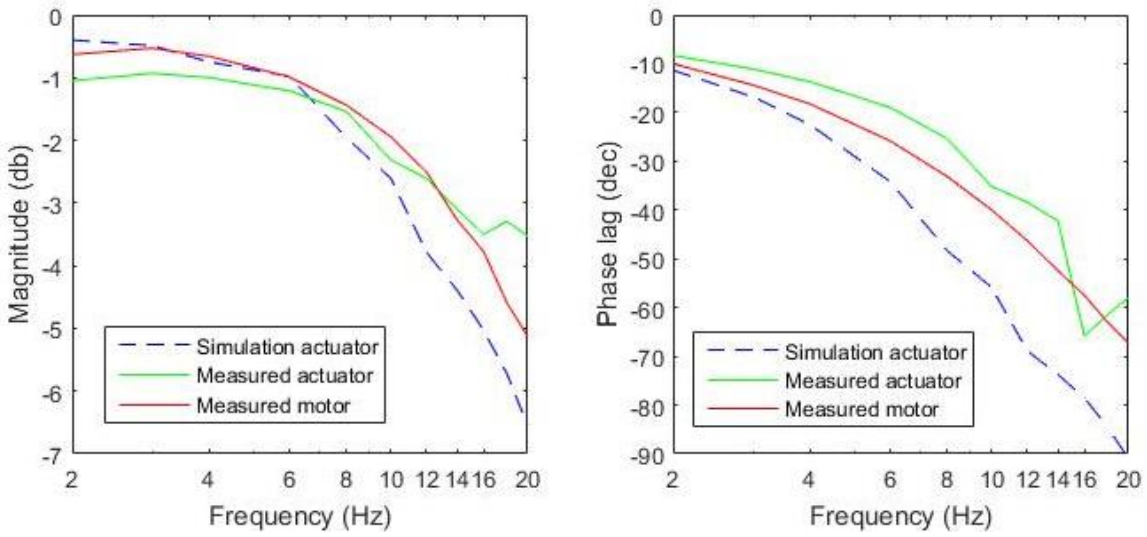

Figure 4.12 Simulation validation: Frequency response of pump controlled actuation systems

4.3.3 Servo-valve controlled validation

The third simulation used for validation broadens the scope to include hydraulic proportional valves as the measured unloaded step response of a servo valve controlled actuator is compared to simulation results (Fig. 4.13). The servo valve was calibrated by fitting the input valve current to the measured flow. The repeatability of this calibration showed flow rate fluctuations to be within ±1.6 cc/s which is 2.8% of the nominal flow rate. In the simulation and validation, the servo valve was supplied with a gear pump that generated 67 cc/s and was limited to 19 MPa with a relief valve.

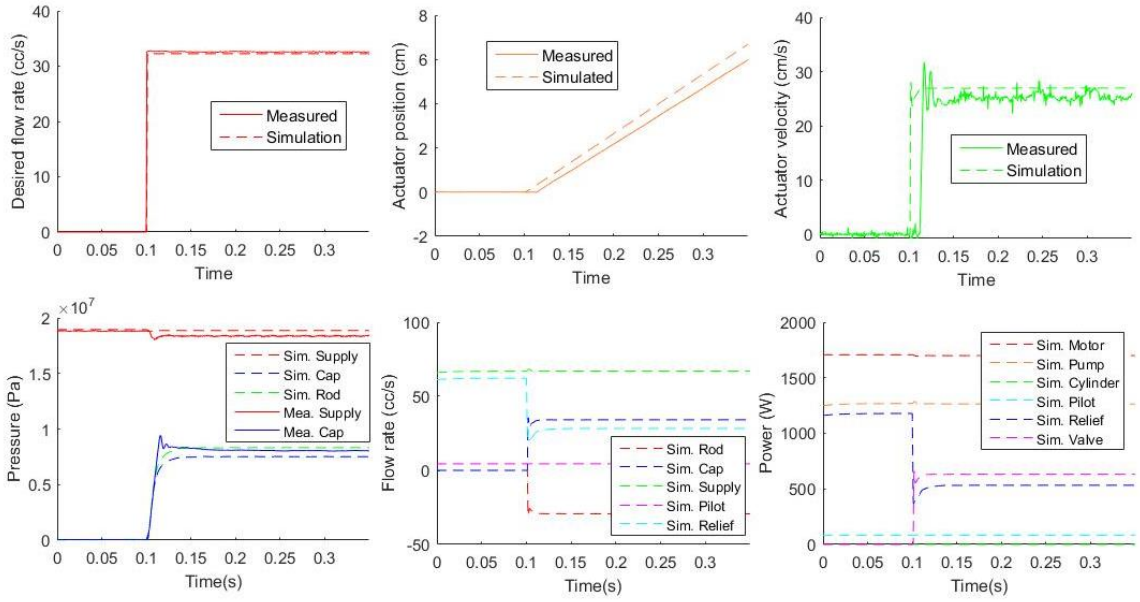

Figure 4.13 Simulated validation: Servo valve controlled unloaded step response

The simulated steady state actuator velocity demonstrates a 4.8% error compared to the measured, which is within the repeatability of the servo valve flow rate control. The measured actuator velocity also experiences an 11 ms longer delay compared to the simulation. This is likely due to a higher percentage of air trapped within the fluid at the actuator. The fluid supplied to the servo valve passes continuously through a reservoir at atmospheric pressure allowing air bubbles to escape; however, fluid between the valve and actuator is stagnate and air is trapped. The trapped air significantly reduces the bulk modulus of the fluid, increasing the compressibility and rise time of the system. Overall the simulation is an accurate representation of the physical hardware staying within the validation criteria of less than 10% steady state error.

This hydraulic circuit represents a typical servo valve controlled actuator with poor efficiencies. In order to actuate the unloaded cylinder, the system is using 1700 W of electrical power with 37% dissipated across the servo valve spool, 31% dumped across the relief valve, 5% to maintain servo valve pilot flow, and the remaining 27% lost on motor, pump, conduit, and actuator inefficiencies. The energy lost across the relief valve is due to a mismatch between the power supplied by the motor, and the required actuation power. The following section addresses

methods of better aligning the supplied and required power of the system to improve performance metrics. Chapter 5 addresses methods of reducing throttling and pilot losses using digital hydraulic technology.

4.3.4 Simulated performance comparison of small-scale pump and valve controlled hydraulic circuits

The objective of this section is to compare the dynamic performance of the pump and valve controlled hydraulic circuits in fig. 4.14. The performance metrics are the system rise time, the average full-scale flow rate during actuation, and the average efficiency over an actuation cycle.

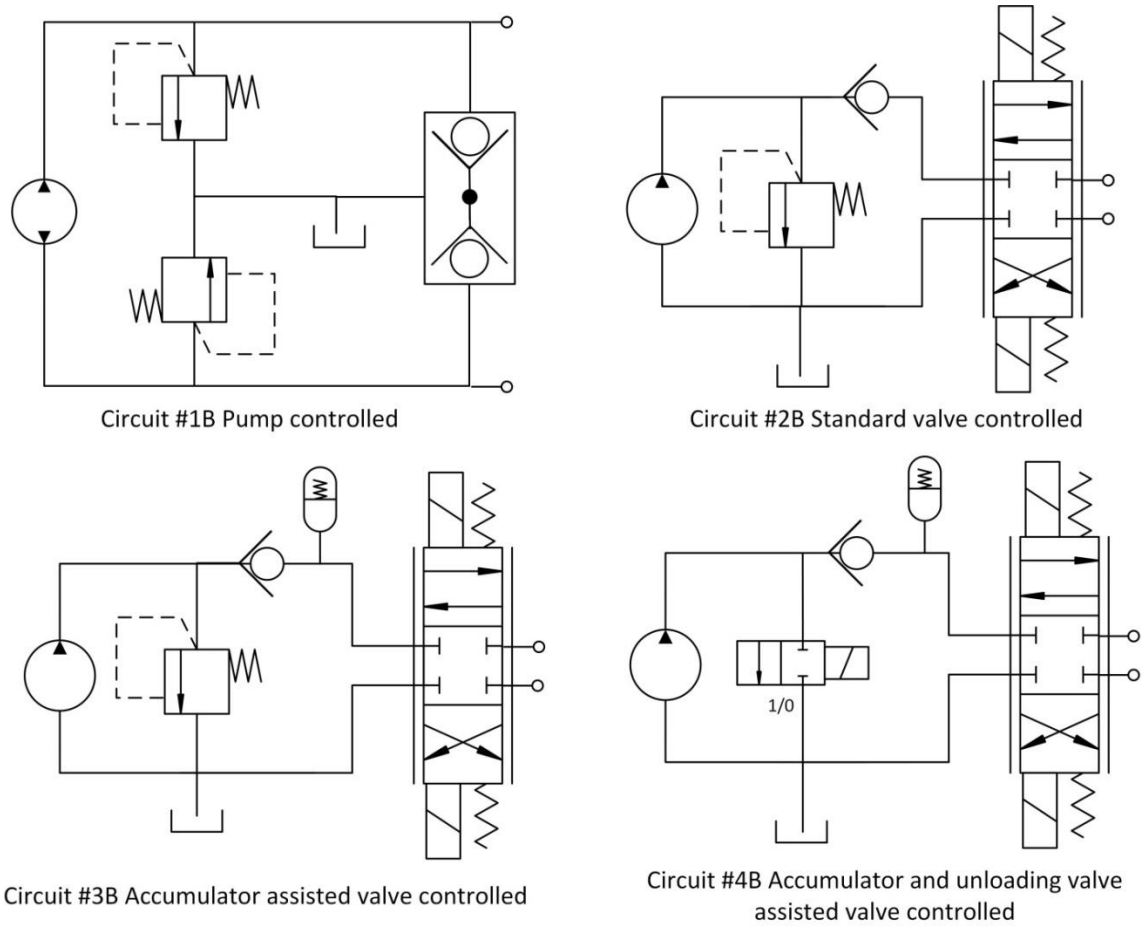

Figure 4.14 Pump and servo valve hydraulic circuits

Hydraulic circuits 1B and 2B are identical to circuits 2A and 3A from section 4.2.2. Circuit 3B positions an accumulator between the pump and supply port of the servo valve to store energy

during intermittent operation. This energy is then recovered to increase the full-scale flow rate capabilities of the system. Circuit 4B utilizes a digital unloading valve to replace the traditional control and relief valves, and is paired with an accumulator to increase the efficiency of valve controlled circuits during intermittent operation.

Circuit 1B is simulated with a variable displacement (VD) pump to illustrate the performance trade-offs of varying the angle of the swash plate compared to shaft angular velocity. There currently are no commercially available small-scale variable displacement axial piston pumps, so the swash plate dynamics correspond to a custom hydraulically actuated swash plate axial piston pump. The energy consumed by the swash plate actuator is incorporated in the performance metrics and is estimated based on the swash plate actuation distance and a force balance between the actuator and the pressurized pistons.

In an effort to decrease the energy for intermittent operations, circuits 2B, 3B, and 4B are simulated using a proportional pressure control (PPC) algorithm controlling the motor voltage. The algorithm monitors the system pressure and compares it against a preset regulation pressure. This pressure error signal is multiplied by a proportional constant and used to control the motor voltage. In instances where only servo valve pilot flow is required, the voltage and the corresponding motor angular velocity is decreased. This saves energy during low duty cycles.

Accumulator analysis

The accumulator in this case study was sized using the methods in section 2.5.1 on sizing an accumulator. A compressed gas and a spring loaded accumulator are compared below to observe the trade-offs within the case study. The application of the accumulator is to store hydraulic energy for the internment actuation of a 12.7 mm bore cylinder a distance of 8 cm against a 1000N force.

The volume of fluid required to actuate the cylinder based on the piston cap side area and assuming incompressible flow is approx. 10 cc. The minimum system pressure is set at 13.8 MPa based on the minimum operational pressure of the Moog flow control servo valve. The maximum system pressure is 20.7 MPa based on the maximum operational pressure of the Takako 0.8 cc/rev axial piston pump.

Based on these design parameters the calculated total volume of the compressed gas accumulator for this application is 67.5 cc, while the total volume of the spring loaded accumulator is 39.7 cc. The preloaded gas pressure is 12.4 MPa, and the preloaded spring force is 2,980 N with a linear spring constant of 37,800 N/m. The estimated weight of the compressed gas and spring loaded accumulators are 89.5 g and 114 g.

The results illustrate the trade-off between volume and weight for the two types of accumulators. In this application the advantages of a light-weight and compact design are equally weighted, so the spring loaded accumulator is favorable for this application. In addition, the mechanical failure of a compressed gas accumulator can be hazardous to operators in close proximity, as a rupture would allow the compressed gas to dangerously accelerate the accumulator along with possible shrapnel [2, 54]. An additional benefit of spring loaded accumulators is that the spring can be easily replaced, changing the gain between displaced volume and pressure. This dynamic is fixed to the inert gas properties and dynamics in a compressed gas accumulator. Spring loaded accumulators can also be easily built without the use of custom machines to form bladders or diaphragms. The spring loaded accumulator does suffer a limitation in that the piston and seals inside create friction and inertia resulting in slower response compared to a compressed gas cylinder. Spring loaded accumulators are also limited to low power applications, because large piston areas at high pressures would require forces that are impractical for springs [54].

The size and inertia of the piston in the spring loaded accumulator was estimated using the design guidelines for a hydraulic cylinder in appendix A.3.1. It was assumed that the accumulator piston uses a traditional O-ring for sealing between the spring and fluid chambers, so eqs 2.6 and 2.7 were used to estimated friction force within the accumulator.

The performance of the spring loaded accumulator in using the calculated parameters (circuit 3B) is compared against the same hydraulic circuit without an accumulator (circuit 2B) in figure 4.15. In the simulation the portable hydraulic power supply is used with an input voltage of 14.7V, and the servo valve is actuated to fully open and closed positions at times 0.5 and 0.7 sec.

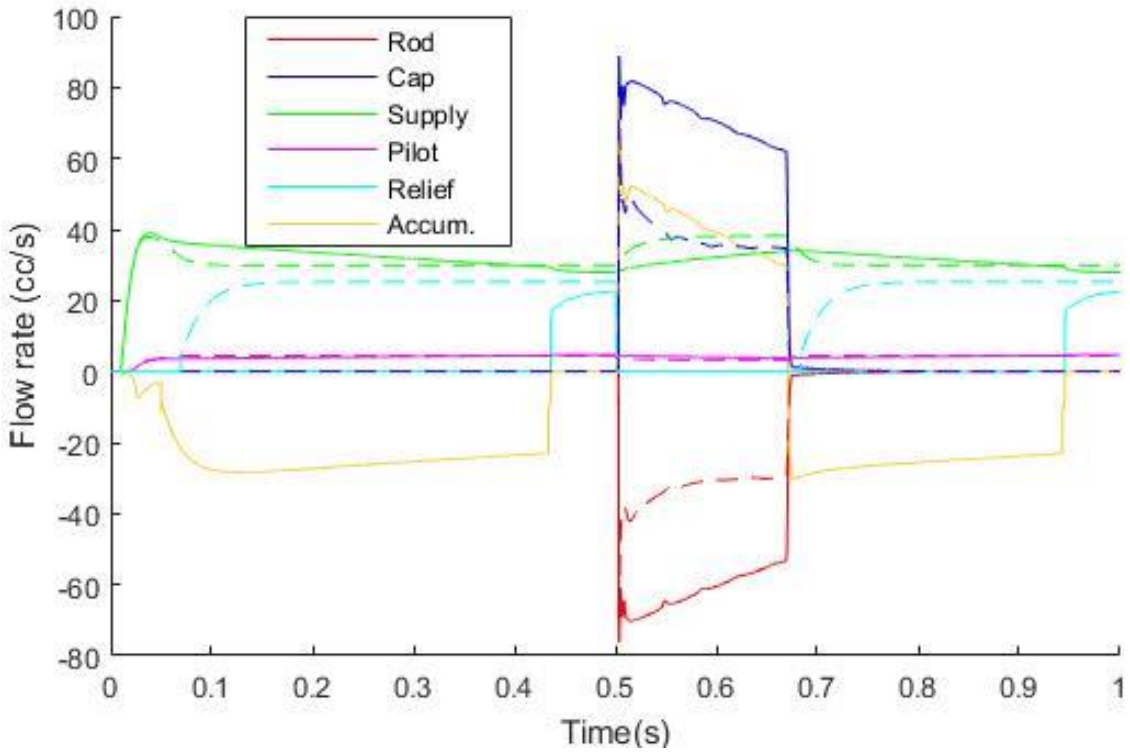

Figure 4.15 Accumulator assisted actuation during intermittent operation

Circuit 2B (no accumulator) is dashed lines, Circuit 3B (accumulator) is solid lines

This simulation illustrates that the flow rate supplied to the cap side of the cylinder is 67% higher with the accumulator assistance compared to without. The accumulator provides a peak power of 1220 W which increases the supplied hydraulic power by an additional 45% compared to maximum hydraulic power provided by just the pump. On the accumulator assisted hydraulic circuit, an average of 56.7% of the power supplied to the actuator is from the accumulator, while 43.4% was provided by the pump. The addition of an accumulator allows circuit 3B to move the load faster compared to without in circuit 2B.

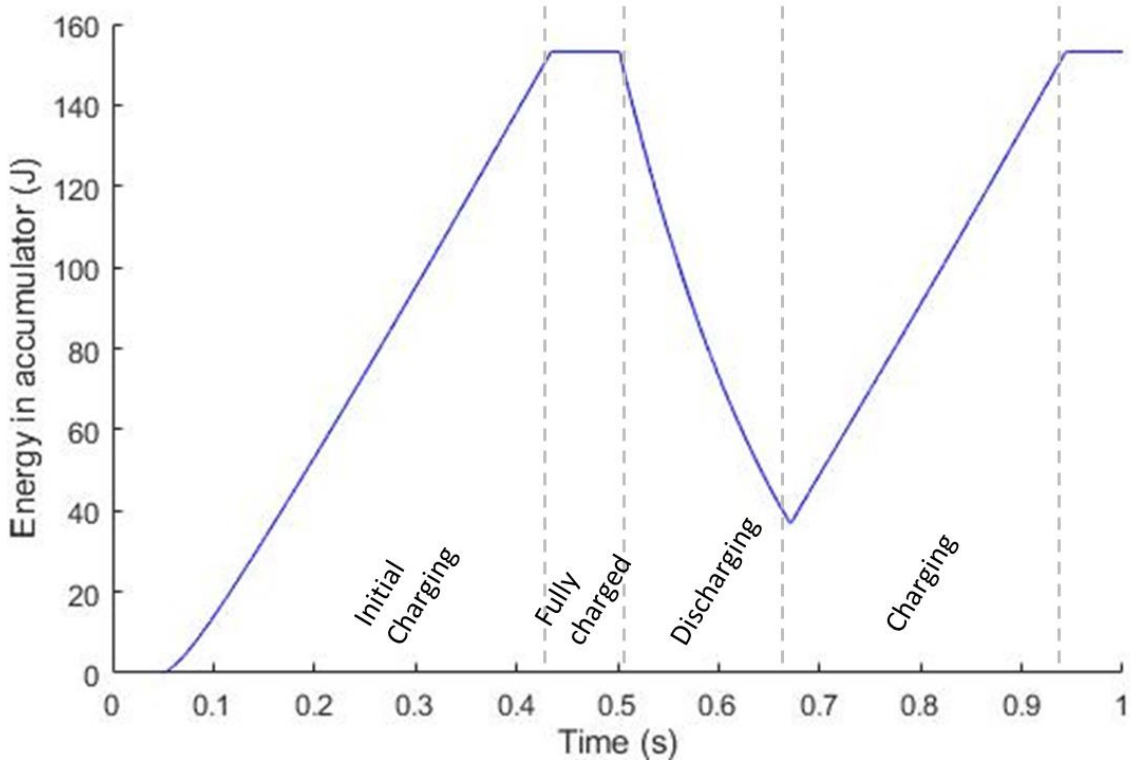

Figure 4.16 Charging and discharging of accumulator during duty cycle

The accumulator takes about 0.44 seconds to completely charge as 154 J of potential energy is stored in the mechanical compression of the spring (Fig.4.16). The accumulator supplies 117 J to assist the cylinder to actuate, depleting 76.0% of the total stored energy. The energy supplied by the pump is relatively constant and identical between circuits 2B and 3B.

Unloading valve

An unloading valve in circuit 4B is composed of a pilot operated relief valve and a check valve (Fig. 4.17). An unloading valve coupled with an accumulator allows a system to maintain high resting pressures while allowing the pump to operate at low pressures. The check valve traps backwards flow while the accumulator maintains a high resting pressure to the control valve. Once the system pressure rises above the cracking pressure of the pilot operated relief valve, the flow is diverted across the relief valve directly to the low pressure reservoir decreasing the load on the pump. This is useful in saving energy when the system is at rest, while not

compromising the response speed of the system as high pressure is maintained at the control valve.

In addition, this combination of unloading valve and accumulator are ideal at maintaining high actuator clamping forces. Clamping applications require maintaining a high actuator force under static conditions. An unloading valve and accumulator can maintain a clamping force with only the energy stored in the accumulator while the pump is completely unloaded. Without an accumulator, the cylinder would need to be constantly supplied flow to offset leakages. Finally an unloading valve can be useful in system startup, allowing a pump to ramp up at low pressures until it has reached operating speeds [2].

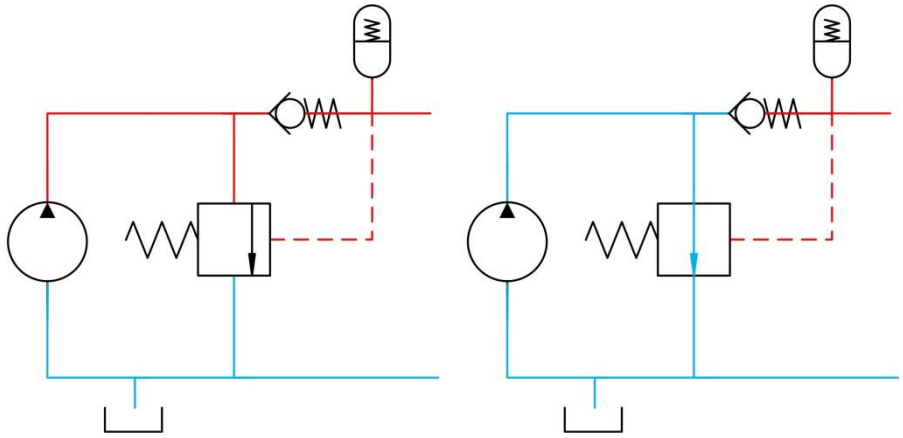

Figure 4.17 Operation of a unloading valve and accumulator in circuit 4B

In the event there is a pilot flow required during resting operations, a traditional relief valve will not function properly in this application. The pressure of the accumulator will oscillate around the cracking pressure of the relief valve due to the relief valve constantly opening and closing. In this application an electronically controlled digital valve can be used to customize and improve the performance. The algorithm controlling the digital unloading valve will allow a window of operational pressures. The algorithm used to control the digital unloading valve in the simulations fully charges the accumulator to 20.7 MPa and allows the pressure to gradually decrease to 14.1 MPa to stay within the operational range of the servo valve. In addition, whenever the servo valve is opened, the digital unloading valve immediately closes to supplement pump flow.

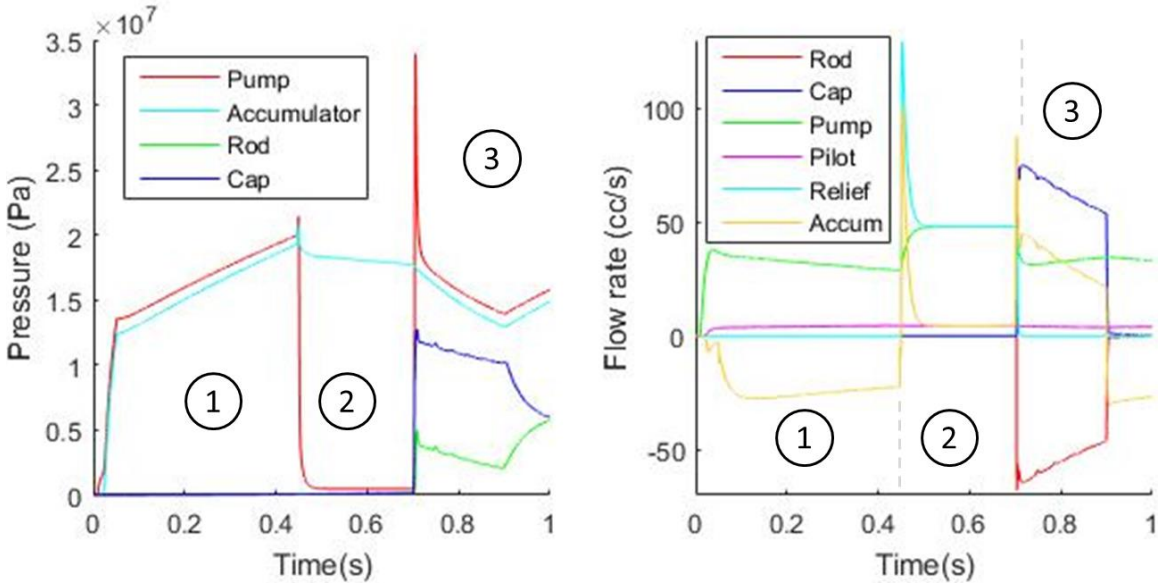

Figure 4.18 Simulated operation of the unloading valve

(1) Accumulator charging, (2) Resting state, (3) Cylinder actuation

Figure 4.18 illustrates the benefits of using an unloading valve coupled with an accumulator for intermittent operations. Initially in charging state (1) the accumulator is empty and reaches its fully charged state at 0.45 sec. With the system at rest and the accumulator fully charged, the digital unloading valve opens, dropping the pump pressure to 0.49 MPa, while high pressure is still maintained at the servo valve supply port due to the check valve and accumulator. In this unloaded state (2) the electrical power supplied to the motor is 125W, a 90.2% reduction compared to a system at rest using a standard relief valve with a 3000 psi cracking pressure. Finally in actuation state (3) the servo valve is fully opened, suppling the cap side of the cylinder with fluid power generated by the accumulator and pump.

The servo valve is not an ideal closed center valve due to the continuous pilot flow. This results in the accumulator slowly discharging in the unloaded state (2). In this simulation it takes 1.52 seconds for the accumulator to drain until the system pressure is 14.1 MPa, and the digital unloading valve closes to recharge the accumulator. The performance of this hydraulic circuit could be improved as the pilot flow rate is decreased with a different model of servo valve. In

addition, valves types that do not require a pilot flow like single stage valves with the spool directly positioned with a linear motor or solenoid are ideal in this circuit configuration, because the accumulator charge would last for long periods of time when the system is at rest. However, these valves typically require additional electrical energy to actuate, and this must be compared against pilot flow when deciphering the more efficient system.

Proportional Pressure Control (PPC)

Proportional pressure control (PPC) measures the system or accumulator pressure and compares that against a preset regulation pressure. The objective of PPC is to minimize the energy dissipated by the relief valve by slowing the electric motor. The preset regulation pressure should be slightly lower than the maximum operating pressure of the system that is typically governed by a relief valve. If the regulation pressure is set higher than the maximum operating pressure, the motor will consume unnecessary energy attempting to maintain a pressure it cannot reach. If the regulation pressure is too low, the accumulator might not be fully charged when the system is at rest. The regulation pressure used in simulation is 20 MPa with the maximum operation pressure 20.7 MPa. The control frequency needs to be an order of magnitude faster than the fastest system dynamics. The controller frequency in the simulation is 1 kHz. The error signal between the measured and preset regulation pressures is multiplied by a constant and used to control the motor input voltage. The value of this constant depends on the properties of the motor and the condition of the pressure error signal. The PPC can be tuned using the various methods in [82] to be a critically dampened system. Large pressure errors can results in erratic motor function, so a proportional pressure control functions best with an accumulator and/or a relief valve to filter pressure fluctuations.

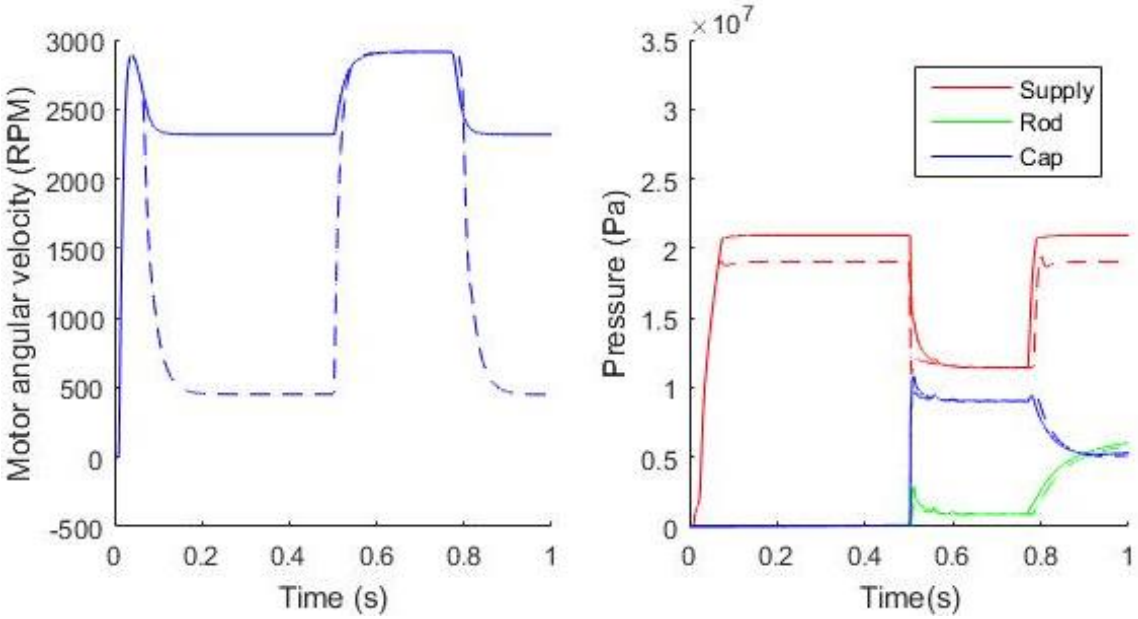

Figure 4.19 Simulation of proportional pressure control,

With PPC is dashed line and constant motor voltage is solid line

Figure 4.19 illustrates the operation of circuit 2B with and without PPC. In the first 0.1 seconds the motor and pump are accelerating the system up to operational pressure. From 0.1 to 0.5 seconds the servo valve is in the null position, and it opens full at 0.5 seconds to supply flow to the cap side of the cylinder. The operational pressure without using PPC is higher, because the pressure relief valve is regulating the pressure instead of the motor. The cracking pressure of the relief valve is 20.7 MPa, while the PPC regulation pressure is slightly lower at 20 MPa.

The PPC decreases the motor voltage from 14.7 to 6.76V slowing the angular motor velocity from a 2320 RPM to 452 RPM when the actuator is not in use. The motor and pump using PPC only provides enough fluid power to supply the servo valve pilot stage and maintain the regulation pressure.

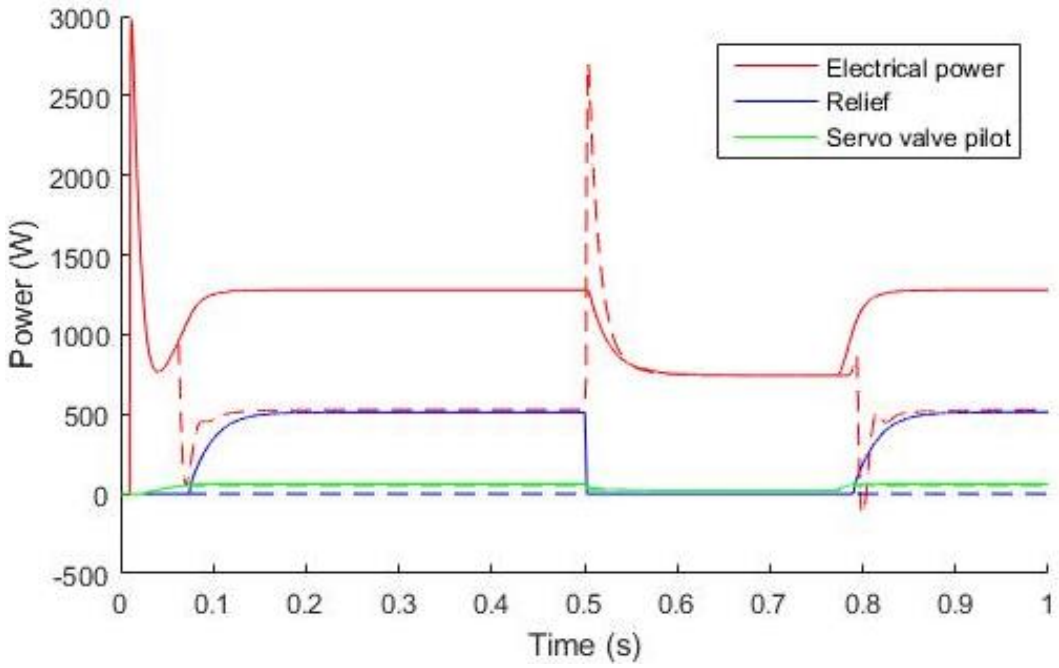

Figure 4.20 Electrical power consumption and relief valve power dissipation using PPC

With PPC is dashed line and constant motor voltage is solid line

Fig. 4.20 illustrates the electrical power that the DC motor draws and the power dissipated across the relief valve and pilot stage of the valve. As the servo valve is in the neutral position, the system without the PPC is dissipating 512 W of fluid power across the relief valve with the remainder of the flow going through the servo valve pilot stage. The system using PPC control wastes no power across the relief valve as the servo valve is in the null position. This results in a total power savings of 58.7% compared to a constant motor input voltage when the servo valve is in the null position.

A drawback of using PPC is that the rotational inertia of the pump shaft has to be continuously accelerated and decelerated. The pump shaft is accelerated at time 0.5 sec. causing a spike in electrical power supplied to the motor. This consumes additional energy compared using a constant motor voltage, but only for a brief time period. However, over the entire cycle PPC saved 480 J resulting in a 43.1% energy reduction.

Performance metric comparison

The objective of this analysis is to compare the performance of the four circuits in fig. 4.13 using different energy reducing strategies while varying the duty cycle. In these simulations, all the hydraulic components were identical in order to observe performance differences caused by the different control strategies.

In these simulations, the systems were operated in full-scale on/off operation. In full-scale on/off operation the control variables; motor voltage, swash plate actuator position, or servo valve spool position were triggered to full-scale output at the beginning of the load cycle, and switch off as the actuator displacement reaches 8 cm. The use of full-scale operation minimized valve throttling losses, so the measures of efficiency are a best case scenario. In all configurations the work output per the extension and retraction of the cylinder is an identical 160 J as the rod actuates against a constant 1000 N force.

The first performance metric of the system is the average full-scale flow rate at the actuator (Fig 4.21). This metric observes whether the accumulator is augmenting hydraulic performance. This is useful in systems that required large intermittent flow rates. The dependent variable is duty cycle and is defined as the actuation time over total time of the cycle.

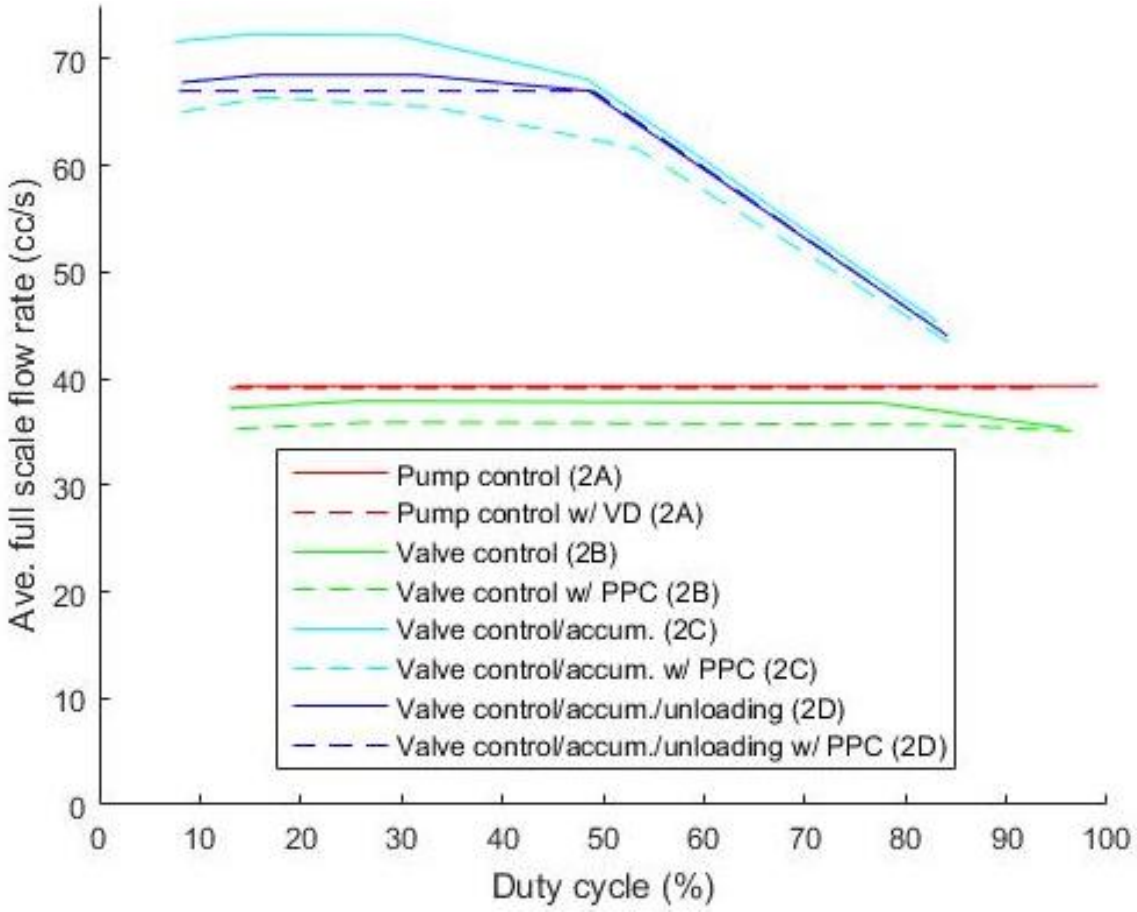

Figure 4.21 Full-scale flow rate as a function of duty cycle

The full-scale flow rate of pump controlled circuits is equal to the maximum flow rate of the pump, and it not dependent on duty cycle. The full-scale flow rate of valve controlled circuits without accumulators has little dependence on duty cycle with the flow rate capacity being the subtraction of the valve pilot flow from the flow supplied by the pump. At low duty cycles the addition of an accumulator augments the flow rate capabilities of the pump between 65 and 80%. As the duty cycles increases above 50%, the accumulator flow rate augmentation decreases due to the fact that the accumulator does not have time to fully charge. As the duty cycle increases to 100% the full-scale flow rate of the valve controlled configurations with and without the accumulator are equal, because there is no time for the accumulator to charge. The addition of the unloading valve allows the accumulator to cycle between a fully charge and

partially discharge state. On average this results in the accumulator storing slightly less energy, and reducing flow rate capabilities compared to the configuration without an unloading valve.

The second performance metric used to compare these systems is rise time. The rise time is defined as the time it takes the system to accelerate to 90% the steady state full-scale velocity. The rise time of the system defines how quickly a system accelerates and it also correlates to the systems cut-of-frequency. The smaller the rise time the higher the cut-off frequency will be.

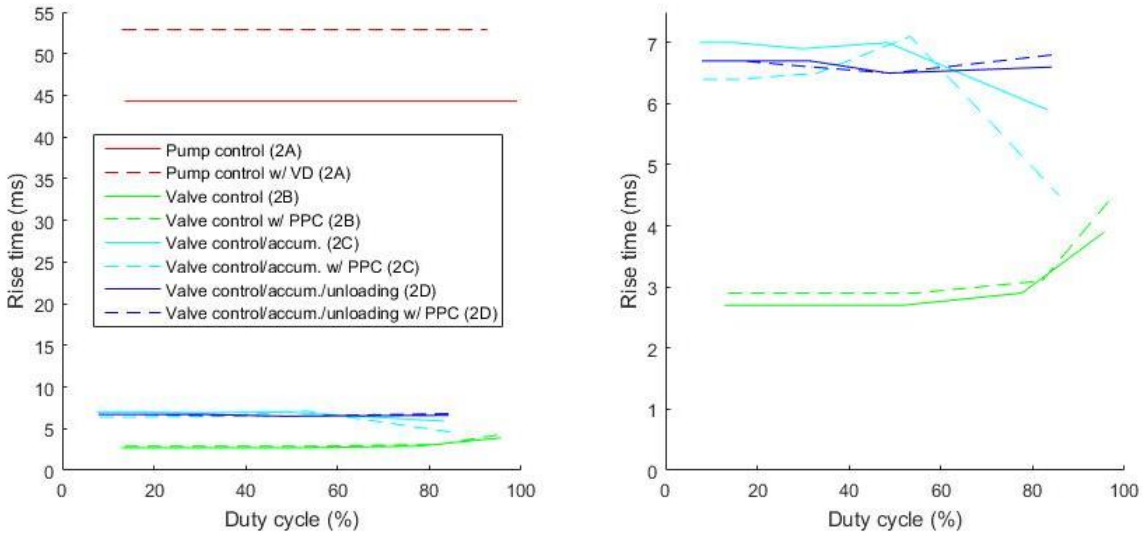

Figure 4.22 Rise time as a function of duty cycle

Figure 4.22 illustrates that the pump controlled circuits have slower rise times by almost an order of magnitude. The standard pump controlled circuit starts the loading cycle with the entire system completely at rest. It takes time to accelerate the mechanical rotary inertia of the motor winding and pump barrel encasing the pistons. The variable displacement pump controlled circuit has the motor and pump barrel rotating at full angular velocity during operation, but it takes approx. 35 ms just to actuate the swash plate to the full displacement position. This is highly dependent on the design of the swash plate actuator in addition to the sizing of charge pump. In all of the valve controlled configurations, the motor winding and pump barrel/pistons are always rotating, storing kinetic energy in the rotating inertia and circulating fluid. This energy can be immediately used to actuate the cylinders resulting in faster rise times.

The proportional pressure control (PPC) slows the motor to a lower angular velocity when the servo valve is in the central position, but motor and pump barrel are still rotating.

A second reason for why the valve controlled circuits have faster rise times is that they store more hydraulic potential energy in the pressurized conduits and accumulators when the valves are in the central position compared to the pump controlled configurations. As the pump controlled systems are at rest, all the pressures within the system are approximately equal to the reservoir pressure; therefore there is no hydraulic potential energy stored within the system. In valve controlled configurations, the supply pressure is always maintained above 14 MPa when the servo valve is in the neutral position. The time constant of the servo valve is 2.8 ms, so the hydraulic energy stored in the hydraulic conduit or accumulator is delivered to the actuator within this time.

Finally the results of section 4.2.1 illustrate that valve controlled systems have a higher stiffness, because there is pressurized fluid on both sides of the actuator in valve controlled systems compared to one side in pump controlled systems. The stiffer system allows more rapid accelerations and faster responses.

Figure 4.22 also illustrates that slower rise times for configurations using an accumulator. The steady state full-scale velocity of configurations using an accumulator is faster at lower duty cycles, so it takes more time for the system to accelerate to the faster velocity. If the rise time is normalized by the full-scale velocities, the normalized rise times with and without accumulators are within 25% of each other. In addition, accumulators are hydraulic capacitive elements that have the ability to store energy from pressure surges [83]. If the accumulator is not designed properly to the application, they can significantly increase the rise time of the system as hydraulic energy from the pump can be stored in the accumulator when it should be delivered to the actuator.

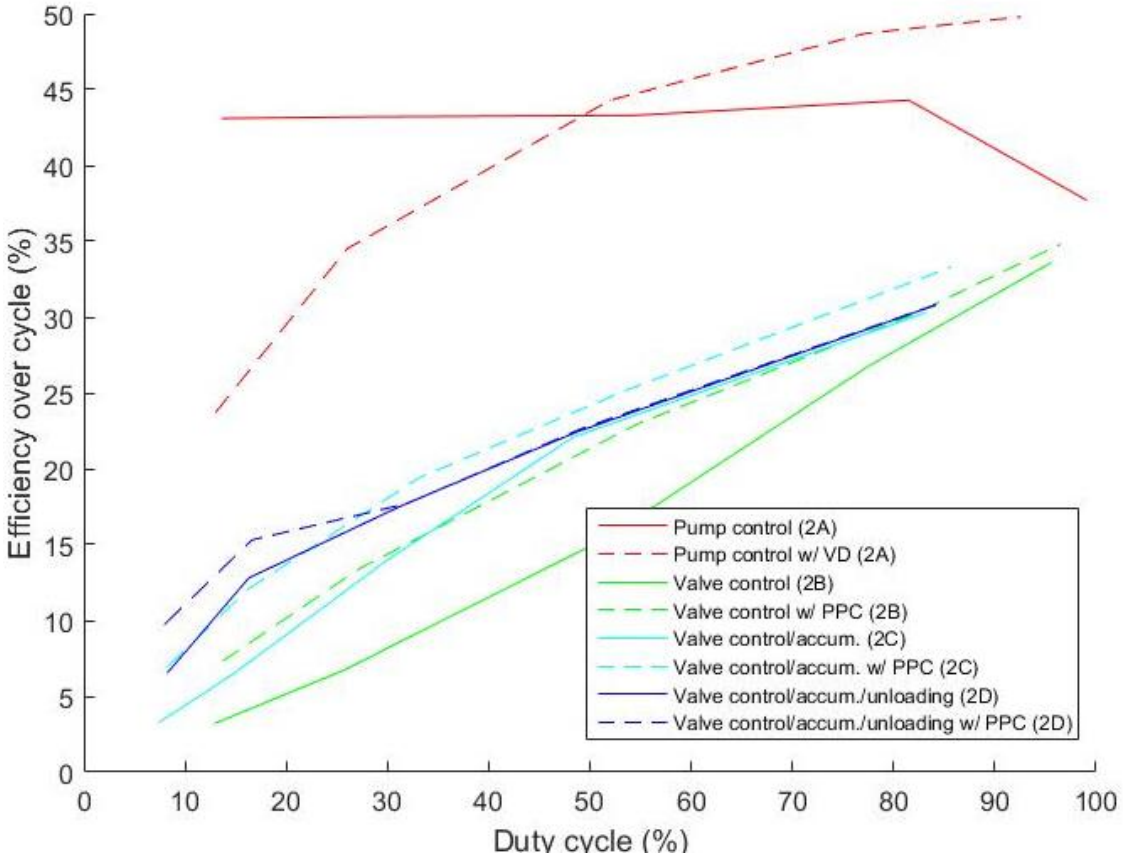

Figure 4.23 Average cycle efficiency as a function of duty cycle

The third comparison metric is the overall efficiency of the actuation cycle shown in fig. 4.23. The use of a fixed displacement pump control has the highest cycle efficiency at low duty cycles due to the fact no energy is used while the system is at rest. This also results in the cycle efficiency being relatively constant across lower duty cycles at 43%, but decreases at high duty cycles as there is an increase in the portion of the energy required to accelerate the system inertia. The variable displacement pump control has a higher cycle efficiency compared to the fixed displacement pump control at high duty cycles, because the energy required to accelerate the mechanical rotary inertia of the system is greater than the energy required to actuate the swash plate.

In general the cycle efficiencies of the pump controlled circuits are higher compared to valve controlled circuits across all duty cycles. Even when the valve is fully open there is still a pressure drop across the two spool orifices dissipating energy. In addition, both fixed and

variable displacement pump control do not produce any hydraulic power when the system is at rest, reducing the wasted energy at lower duty cycles.

All of the valve controlled circuits are expending energy to maintain a supply pressure and pilot flow when the valve is in the central position and the system is at rest. This results in a proportional trend of increasing efficiency with increasing duty cycle. The cycle efficiency can be improved by storing hydraulic energy in the accumulator for use during actuation; therefore, the circuits without an accumulator demonstrate the lowest cycle efficiency. The addition of an unloading demonstrated energy savings for low duty cycles when the system has enough time to fully charge the accumulator and unload the pump.

The addition of proportional pressure control (PPC) illustrates an energy savings that increases as duty cycle decreases. The valve control configurations with and without PPC converge to the same cycle efficiency of 35% at 100% duty cycle, because the additions of accumulators, unloading valves, and PPC all save energy as the system is at rest. There is a 128% increase in cycle efficiency on a standard servo valve circuit at a 13% duty cycle with implementing PPC. This represents a significant energy savings that can be implemented without the addition of hardware.

4.4 Discussion

4.4.1 Conclusions

The validation results illustrates that the described process for modeling small-scale pump and valve controlled actuation systems is valid according to the 10% error condition. The validation and modeling were completed using high pressure and low flow rate hydraulic systems; therefore, the design guidelines discussed are specific to these systems and further testing is required to extend them to other systems.

The validation results illustrate several sources of compliance in small-scale hydraulic actuation systems that significantly impact dynamic performance. A measure of system compliance is the time between the input signal and when the system starts accelerating from rest, in figs. 4.8, 4.9, and 4.12. The most important of these factors are the entrapped air in the fluid and the elastic stretch of the conduit. The additional volume of fluid required to compensate for the

stretch of the conduit and the compressibility of the working fluid is defined as the compliance volume. The ratio of compliance volume to flow capacity is higher for small-scale hydraulic systems compared to larger systems. In addition, the small-scale systems have a relatively high amount of fluid inertia to accelerate with small bore long conduits. If the design of a small-scale hydraulic actuation system requires fast and precise movement, precautions will have to be taken to reduce sources of compliance and inertia at rest from the system.

The results of the case study illustrate that the addition of an accumulator can significantly increase full-scale flow rate and efficiency for duty cycles less than 70%. In the case study, an accumulator led to a 75% increase in flow rate capacity for duty cycles below 50%. The results illustrate when developing a small-scale valve controlled system for applications with low duty cycles (< 50%), the addition of an accumulator allows the designer to reduce the flow rate capacity of the hydraulic power supply by approx. 40% while improving the overall system efficiency. Finally accumulators can have the added benefit of suppressing pressure fluctuations resulting in decreased wear and noise [83].

The rise time of valve controlled systems are typically an order of magnitude faster than pump controlled systems. This is a result of pump controlled systems have more fluid and mechanical inertia to accelerate compared to valve controlled systems. On a constant displacement pump controlled system, the motor windings, pump barrel and piston, main and auxiliary fluid lines, the actuator piston, and load all need to accelerate from rest; whereas on a valve controlled system it is just the load, actuator and the fluid in the auxiliary lines. In addition, valve controlled systems store potential hydraulic energy in the flow of pressurized fluid in the conduits and accumulator that can be quickly utilized by the actuator.

In this case study, the variable displacement pump control demonstrated a longer rise time compared to the fixed displacement pump. The angle of the swash plate was adjusted with a small hydraulic cylinder controlled with a proportional solenoid valve and supplied power with a charge pump that is 1/6 the displacement of the main pump. The rise time of the variable displacement pump is highly dependent on the design of the actuator controlling swash plate angle and the sizing of the charge pump. The position control of the swash plate typically requires the use of hydraulic actuation in conjunction with a dampening spring to actuate

against the large forces [84, 85]; however, in small-scale applications these forces decrease, allowing the use of other actuation methods. Future research should be conducted to explore the use of electrical actuation methods to improve the rise time of variable displacement pumps while increasing system efficiency through the elimination of a charge pump.

The case study results illustrate that for duty cycles below 50% the highest system efficiency is achieved by using an a constant displacement pump control, and for higher duty cycles using a variable displacement pump is more efficient. Variable displacement pump control is more efficient when the system is constantly accelerating and deccelating for high duty cycles whereas constant displacement pump control is more efficient when there are longer periods of rest between actuation cycles. Proportional pressure control (PPC) was capable of doubling the efficiency of valve controlled systems while adding little to no hardware. A downside of this control method is that it forces the electric motor to run at inefficient low speeds and high torque. Special precautions should be taken to ensure that the motor does not overheat while using PPC.

In comparing the static and dynamic performance results of both pump and valve controlled hydraulic actuation system, the rise time is the requirement that determines what type of hydraulic circuit should be used. If the actuation system requires a rise time less than 40 ms or a bandwidth greater than 25Hz, a valve control hydraulic actuation system will need to be used. For all other single DOF applications, a pump controlled actuation system should be used to maintain better system efficiency and weight.

4.4.2 Limitations of research

The results show that the percentage of air entrapped in the fluid can have a significant impact on the rise time and high frequency dynamics of the system. This is especially true for small-scale systems. In order to improve the accuracy of the modeling process there needs to be a method of quantifying the percentage air entrapped in the fluid. In addition, special precautions should be taken to eliminate as much air from the working fluid as possible before operation to increase response speed, decrease compressibility losses, and increase system stability. There are several methods of degassing a hydraulic system in Wang et al [47]. These degassing methods include using a pressurized reservoir to increase the solubility of the gas in oil. In

addition, a vacuum degassing apparatus was described and demonstrated the ability to increase the effective bulk modulus of the fluid. The process of bleeding the auxiliary lines at the actuator can also significantly reduce entrapped air.

The model of the control valve was assumed to be a first order system with a specified time constant. The value of this time constant was estimated using the manufactures rise time data. This provides a good estimation of the control valve delay at the operating conditions listed on the manufacturer's specification sheets, but is a poor representation of the valve dynamics at other operating conditions. In order to further improve the accuracy of the modeling process, the fluid and torque motor/solenoid dynamics inside the control valve should be incorporated. In addition, the current servo valve model assumes the switching power of the torque motor or solenoid is negligible, and the accuracy of the system efficiency could be improved by incorporating it.

Chapter 5 Small-Scale Digital Hydraulics

5.1 Introduction

One of the objectives of this dissertation is to explore alternative technology to improve the efficiency of small-scale hydraulic systems. This chapter introduces and analyzes the feasibility of using digital hydraulic technology in small-scale hydraulic systems to improve efficiency through the reduction of metering losses. This chapter includes the detailed conceptual design of a high frequency switching digital solenoid valve. The performance of the valve is simulated to quantify the improvements in efficiency and full-scale performance.

5.1.1 Review of digital hydraulics

A developing field of digital hydraulics utilizes on/off operation instead of traditional proportional valves. Digital hydraulic technology has several benefits including improved efficiency [86, 87], increased performance, and a robust fault tolerance [88, 89] compared to proportional hydraulic systems. Digital hydraulic technology can be separated into two branches, parallel connection systems and switch technologies [90, 91]. In parallel systems there are several discrete hydraulic elements in parallel that can create a discrete number of flow outputs. Digital switching technologies actuate a digital valve at high frequencies with a series of capacitive elements to provide variable flow outputs. The flow rate is adjusted by using different pulse width modulation (PWM) control techniques.

Parallel digital hydraulics

An assembly of digital valves in parallel is commonly referred to as a digital flow control unit (DFCU). The flow capacities of the individual valves within a DFCU may be an increasing series like binary (1, 2, 4, 8), Fibonacci (1, 1, 2, 3, 5) or constant (1, 1, 1, 1). In Linjama et al [87], two DFCUs were used to implement separate meter-in and separate meter-out control (SMISMO) to increase the efficiency of a system by a simulated 37% compared to a traditional proportional valve system. In a DFCU there is no switching required to maintain the discrete valve outputs, so there is little energy used to control the position of the valve members. DFCUs exhibit a tradeoff between flow resolution and the amount of hardware. Hydraulic systems requiring high resolution will require a large number of valves [92]. Valve fault tolerance is more pertinent for small-scale applications, where particles can be more damaging to the fluid flow control

elements on the pilot stages of valves [93]. An additional advantage of using a DFCU is that there is an increased fault tolerance as the failure of a single valve only inhibits the use of a few flow settings [88, 89, 92].

There exist two analogous forms of parallel digital cylinders and pumps. The first version is the parallel coupling of several fixed displacement actuators or pumps with digital control valves that select which components are connected to the system or routed to the tank (Fig 5.1A, C). A second version of a digital pump is where the individual pistons are controlled with on/off operation (Fig. 5.1B) [94]. The analogous actuator form is a cylinder that contains multiple chambers to allow the generation of several discrete force magnitudes from a constant pressure source (Fig. 5.1D). The different forms of a digital pump allow a better pairing of system flow rate and pressure requirements with the supplied motor angular velocity and torque to improve the efficiency of the overall system. In a digital actuator, the force and velocity requirements are better paired to the pressure and flow rate generated by the system.

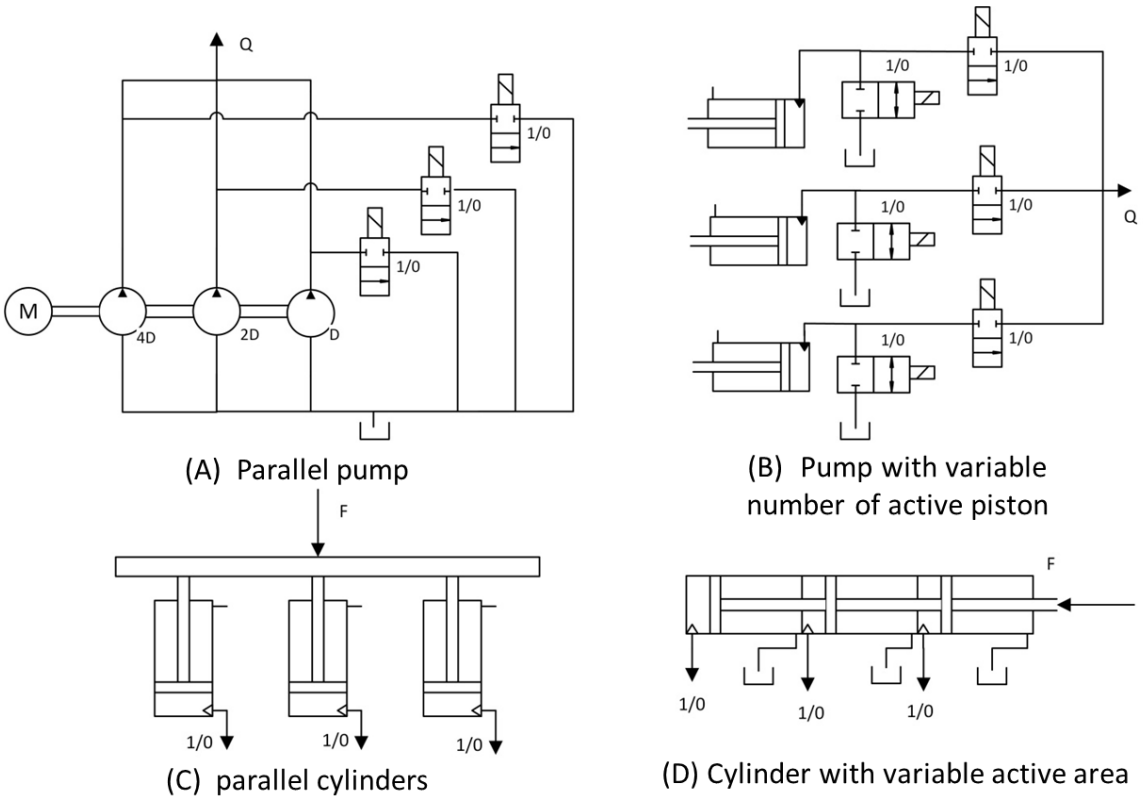

Figure 5.1 Digital cylinder and pump configurations

Digital Switching technologies

A common use of high frequency, digital valves are in pump unloading circuits illustrated in fig. 5.2 [95]. When the valve is open, it allows fluid to bypass the system and be ported to the tank at a low pressure and when the valve is closed, fluid is delivered to the supply line at high pressure. This reduces metering losses. The flow rate delivered to the system can be altered by adjusting the time when the valve is open or closed through PWM techniques. Digital switching circuits must include a large amount of capacitance past the check valve in the form of an accumulator or elastic hoses to smooth out the flow rate supplied to the system [90]. The capacitance before the unloading valve should be minimized to allow the pump to become unloaded as quickly as possible after the unloading valve is opened.

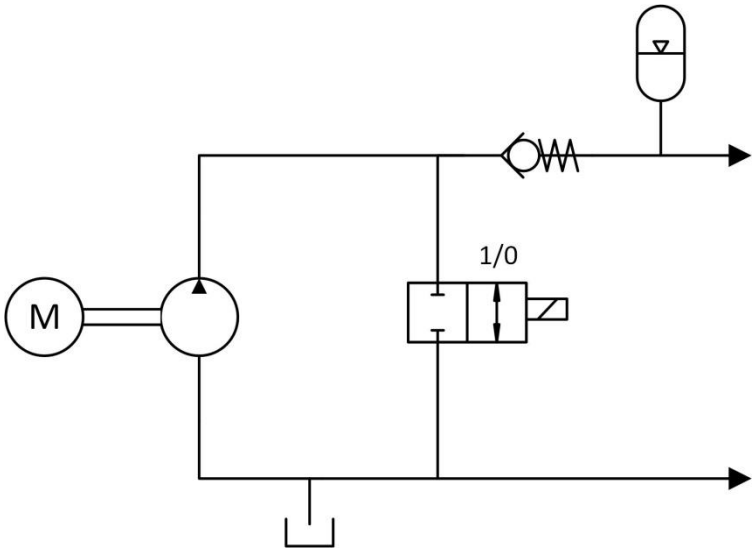

Figure 5.2 High frequency digital unloading valve

The main advantage of using this type of hydraulic circuit is it better matches system hydraulic power requirements with hydraulic power generated at the pump [95]. In traditional proportional hydraulic systems, additional power generated by the pump is dissipated across a relief valve through throttling losses. When the digital valve is open in fig. 5.2, the pump becomes unloaded as fluid is allowed to flow directly into the tank without throttling losses. In addition, the flow rate is adjusted by valve metering with conventional hydraulics requiring a large portion of energy dissipated through throttling losses [95, 96]. In a digital system the fluid supplied to the system does not suffer from significant throttling losses, because the fluid only

passes through a fully opened or is completely blocked passageway. The digital hydraulic configuration provides more hydraulic power to the actuator compared to a proportional valve system using the same pump with the reduction of throttling losses. These conclusions are supported by Manring [96] where load sensing, digital switching, pressure compensating and traditional relief valve hydraulic power units are compared through simulation. All of the results of the study show tradition relief valve systems are the most inefficient. Load sensing and digital systems were found to be the most efficient followed by pressure compensating systems. The research also concluded the efficiency savings from digital valve systems drop at low load flow rates.

A drawback of digital switching valves is the creation of pressure pulsations within the system that could result in jerky system movement [90, 76]. This can be reduced by increasing the switching frequency, system inertia, or system dampening [90]. The use of high frequency switching valves has shown to increase compressibility losses within the system [76]. In addition, a valve that is continuously switching at 50 Hz will cycle 1.6 billion times a year, which is a high amount of wear, increasing the likelihood of component failure. This can be decreased if switches are put in parallel, decreasing wear on a single valve and also making the system more robust as a single valve failure would not cripple the hydraulic system [92].

5.1.2 Prior art in digital and high frequency switching valves

There exists trade-offs in the design of hydraulic valves between switching response times, the actuation energy, and flow rate capabilities. The design of digital, high frequency switching valves require response times below 1 ms for a wide range of flow rates while minimizing actuation energy. Recent technological advances aimed at accomplishing this include the integration of Horbiger plate geometry, piezo electric technologies, and bistable actuation.

The Horbiger plate geometry (fig. 5.3) utilizes multiple metering surfaces to control high flow rates with small linear poppet/spool displacements. A drawback of the Horbiger plate is there is no sealing element. The plates require micrometer tolerances to prevent high leakage rates. In Winkler [97] the Horbiger plate geometry is used in the main stage, while the plate displacement is actuated with a solenoid controlled pilot stage. The two stage valve has a nominal flow of 100 l/min with a 0.5 MPa pressure drop and a switching response time of 2-3

ms. A second valve uses a solenoid to directly position a spool with a nominal flow rate of 10 l/min with a 0.5 MPa pressure drop and a switching response time of 1-2 ms [98].

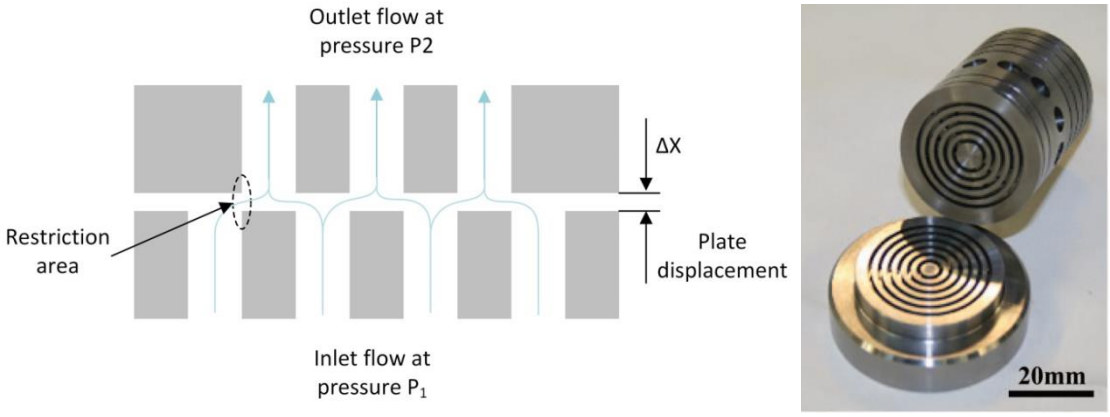

Figure 5.3 Horbiger plate valve cross-section (left) and prototype [99] (right)

Current piezo electric actuation technologies demonstrate high bandwidth (>1 KHz) and force generation (up to 30 kN) capabilities making it ideal for use in hydraulic valve actuation. A limitation of this technology is that the materials only allow strains up to 0.1%. The actuation distances are limited to micrometers, so they are often mechanically amplified to actuate within 0.01 to 1 mm. This allows piezo electric actuators to control valve pilot stages improving bandwidth and response time [100, 101, 102, 103, 104]. However, the addition of a pilot stage limits response time due to the compressibility of the fluid, and the pilot flow dissipates energy. In Branson et al [99], the Horbiger plate geometry is utilized to decrease the actuation distance to allow the plate to be directly actuated with a piezo electric stack (Fig 5.3). The nominal flow rate of the valve is 65 l/min with a 2 MPa pressure and a switching response time of 1.5 ms.

In an effort to further reduce the energy consumption for digital valve actuation, bistable actuation systems allow a poppet or spool to maintain two stable positions where no energy is consumed by the actuator [105, 106, 107] (Fig5.4). The actuator only consumes energy to switch between stable positions. A permanent magnetic is used to hold poppet/spool in the fully open and closed positions, while an electromagnetic force generated by a solenoid coil provides the required dynamic force to move the poppet/spool between the two stable positions. The balancing of electromagnetic, friction, fluid, and magnetic forces can reduce valve actuating energy and coil size.

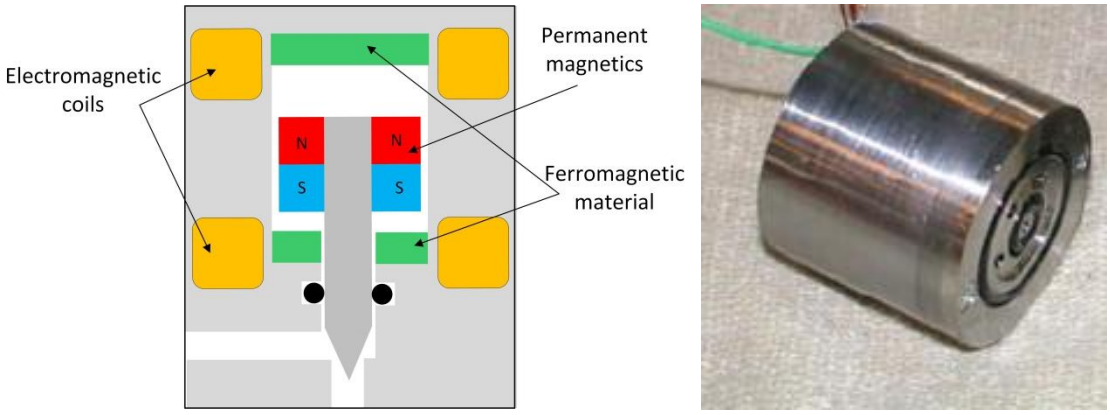

Figure 5.4 Electromagnetic bistable valve cross-section (left) and prototype [105] (right)

In an effort to further reduce the valve actuation energy, rotary valve geometries have been explored [108, 109] (Fig. 5.5). The governing principle of the valve is that the spool is designed to be self-spinning by harnessing throttling energy and fluid momentum. The turbine blades are composed of helical lands on the spinning spool directing flow to the tank or the system. The duty cycle is varied by axial translating the rotating spool with respect to the inlets. A valve prototype has demonstrated 65% efficiency at 50% displacement and 15 Hz, but predictive models for optimized valve geometries illustrate efficiencies of up to 85% at 50% displacement and 15 Hz.

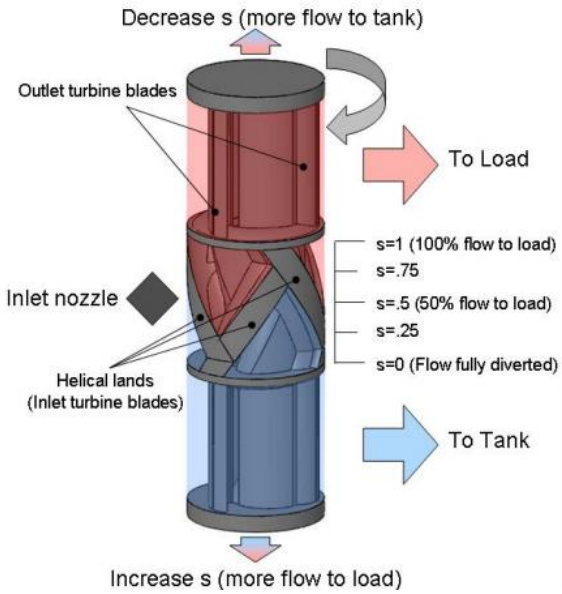

Figure 5.5 Rotary PWM valve spool [109]

The research in digital, high frequency switching valves is focused on increasing the flow rate capacities while decreasing response time and actuation energy. Current digital switching valves are designed for applications where the nominal flow rate is 10 to 100 L/min, while small-scale hydraulic typically stays below 3L/min (50 cc/s). In the current valve designs, little priority is given to making the valve lightweight and compact, which are essential attributes in human assistive machine design. In addition, the immaturity of digital hydraulic technology combined with industrial demand for large-scale hydraulic systems has resulted in the absence of commercially available digital switching valves. There exists a need for lightweight and compact digital hydraulic switching valves for small-scale hydraulic systems that are robust for human assistive applications. In order to assess the performance of small-scale digital hydraulic systems for use in human assistive devices, a digital high frequency switching valve is designed in section 5.2.2.

5.2 Methods

5.2.1 Analysis of high frequency digital solenoid valve energetics

This section is an analysis of valve energetics to determine why and how to design a high frequency digital switching valve that minimizes the amount of energy to actuate the valve control member against the pressure gradient, seal friction, and fluid momentum forces. Figure 5.9 illustrates the geometry of a poppet valve with orifice diameter of D. It is assumed that the poppet actuating distance is proportional to orifice diameter (5.1). The poppet actuation distance where the orifice area becomes saturated is calculated with eq. 5.2. The orifice area and corresponding nominal flow rate of the valve can be calculated with eq. 5.3 & 5.4, with the fluid density based on the properties of mineral oil. In this energetics analysis, the forces on the poppet due to the pressure gradient (5.5), seal friction (2.4), and fluid momentum (5.6) are assumed constant across the valve actuation distance. The O-ring material properties, cross-sectional diameter and squeeze ratio are adjusted appropriately to industrial standards as the orifice diameter is varied.

Table 5.1 Valve variable definitions

Sym.	Description	Value	Unit	Sym.	Description	Value	Unit
A	Orifice area	-	m^2	P_{out}	Outlet pressure	0	Pa
C_d	Discharge coefficient	0.7	-	Q	Valve nominal flow rate	-	m^3/s
D	Orifice diameter	-	m	W_C	Ave. closing power	-	W
f	Valve act. frequency	100	Hz	W_N	Nom. valve power	-	W
F_F	Fluid momentum force	-	N	ΔX	Poppet actuation distance	-	m
F_P	Poppet pressure force	-	N	ΔX_{sat}	Saturated poppet act. distance	-	m
F_S	Seal friction force	-	N	α	Poppet angle	π/4	rad
k	Geometry parameter	0.25	-	θ	Momentum vector angle	π/2	rad
P_{in}	Inlet pressure	$0.5x10^6$	Pa	ρ	Fluid density	830	kg/m^3

$$\Delta X = kD \quad (5.1) \qquad \Delta X_{sat} = D\frac{1-\sqrt{1-\cos(\alpha)}}{\sin(2\alpha)} \quad (5.2)$$

$$A = \begin{cases} \pi\Delta X \sin(\alpha)\left(D - \frac{\Delta X}{2}\sin(2\alpha)\right) \rightarrow 0 \le \Delta X \le \Delta X_{sat} \\ \frac{\pi}{4}D^2 \rightarrow \Delta X > X_{sat} \end{cases} \quad (5.3)$$

$$Q = \pi C_d k \sin(\alpha)\left(1 - \frac{k}{2}\sin(2\alpha)\right)\sqrt{\frac{2(P_{in}-P_{out})}{\rho}D^2} \quad (5.4)$$

$$F_p = \frac{\pi}{4}(P_{in} - P_{out})D^2 \quad (5.5) \qquad F_F = \frac{\rho Q^2}{A}\cos(\theta) \quad (5.6)$$

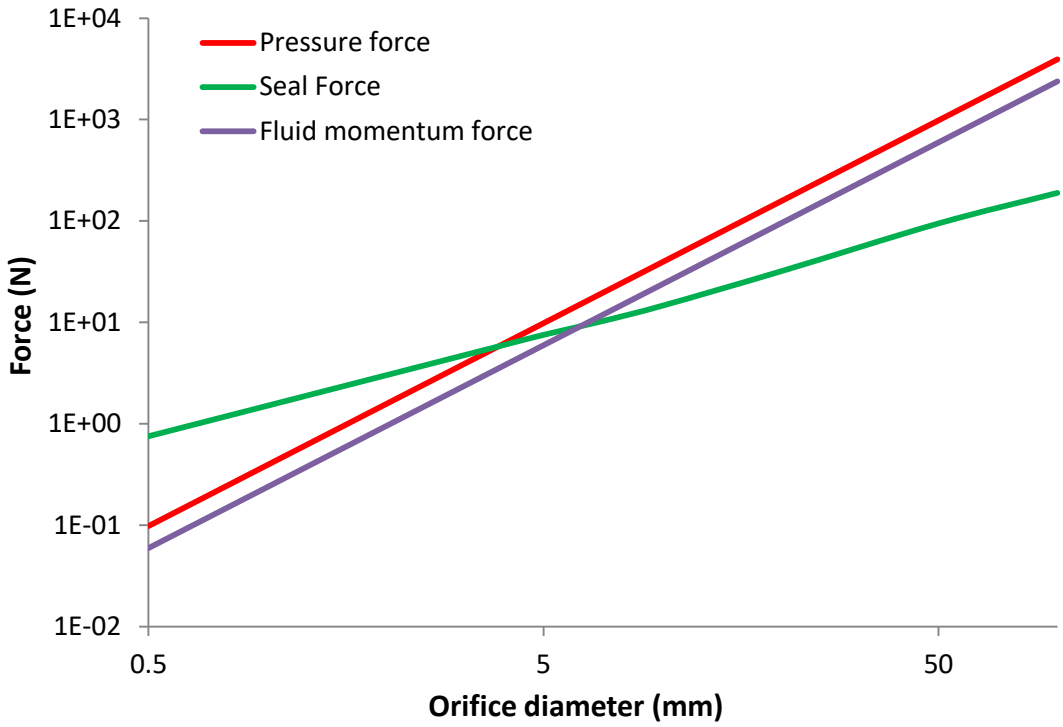

Figure 5.6 Poppet force as a function of orifice diameter

The pressure, seal, and fluid momentum forces on the poppet in the fully open position as a function of orifice diameters are illustrated in fig. 5.6. The algebraic relation for the valve poppet pressure force and fluid momentum force are functions of the orifice diameter squared, while the seal friction force is proportional to orifice diameter. As bore size is decreased below 4 mm, seal friction force becomes larger than pressure and fluid momentum forces. There is a larger portion of the valve actuation power devoted to working against seal friction forces for small valves compared to larger valves where pressure and fluid momentum forces are more influential. The average power required to close the valve and nominal valve power are calculated with eq. 5.7 & 5.8 assuming a constant switching frequency of 100 Hz.

$$W_C = f\left(F_P + F_F + 2F_S\right)\Delta X = f\left(F_P + F_F + F_S\right)kD \quad (5.7) \qquad W_N = Q\left(P_{in} - P_{out}\right) \quad (5.8)$$

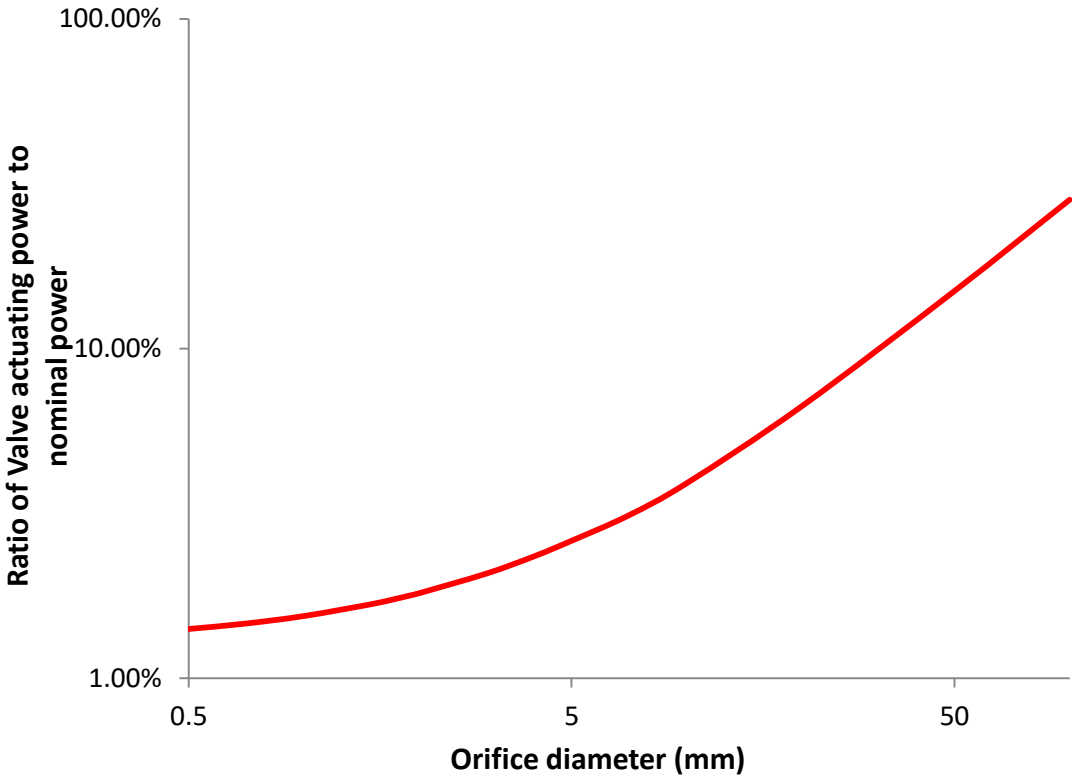

Figure 5.7 Ratio of actuation to nominal valve power as a function of orifice diameter

Fig. 5.7 illustrates that ratio of actuating power to nominal power of a poppet valve increases as orifice diameter increases. The trend supports the conclusion that small valves are more efficient when considering opening and closing work. This conclusion has also been illustrated in the design of optimized digital switching valves using spool geometry [91]. The algebraic relation for the valve nominal flow rate and nominal power are functions of the orifice diameter squared. The power required to actuate the valve against the pressure and momentum forces is proportional to the cube of the orifice diameter, while work against seal friction forces is proportional to orifice diameter squared. As the orifice diameter is scaled smaller and the nominal pressure remains constant, the ratio between the power to actuate the valve and the hydraulic power flowing through the valve decreases. This conclusion means that it is more efficient to use multiple small orifice valves compared to one large orifice valve for the same flow rate requirements. In Fikru et al [110], a micro electro mechanical sensor (MEMS) based pneumatic valve uses an array of orifices with individual piezoelectric control members. The

MEMS pneumatic valve uses less actuation energy compared to a valve with a single orifice or equal orifice area, in addition the MEMS valve has a higher fault tolerance.

In a second analysis orifice diameter is held constant while the geometry parameter is varied to determine what values minimizes the ratio of valve actuation power to nominal power. The geometry parameter is the ratio of actuation distance to orifice diameter. The rated valve power saturates above a certain geometry parameter due to the saturated poppet actuation distance. A poppet angle of $\pi/4$ rad. or 45° leads to saturated rated valve power at k = 0.46. Fig. 5.8 illustrates that in addition to minimizing the orifice size, the geometry parameter should also be minimized. Digital switching valve design should use small orifices coupled with small actuation distances. If large flow rate are required, use multiple small orifices.

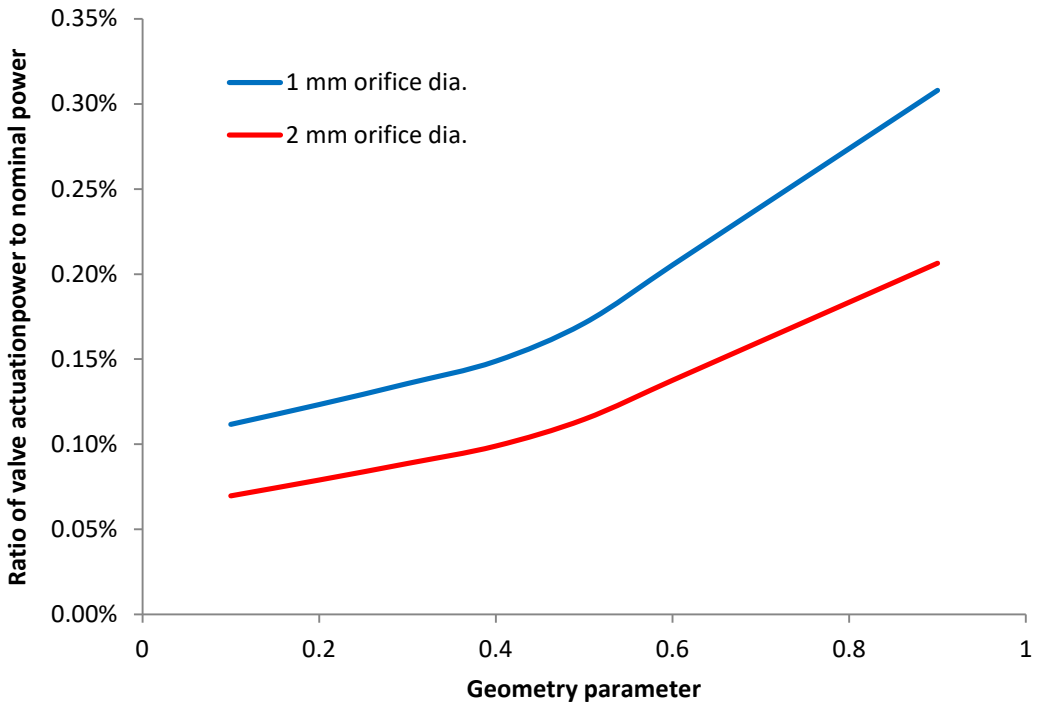

Figure 5.8 Ratio of actuation to nominal valve power as a function of geometry

5.2.2 Design Requirements of High Frequency Digital Valves

Two crucial parameters in optimizing the performance of a digital valve are the opening time and the switching frequency. The valve switching time is defined as the time for a valve member

to travel the maximum displacement from the fully closed position to fully open. The required switching time T_S is a function of the switching period τ and the minimum duty cycle D_{min} used for control (5.9).

$$T_S = D_{\min}\tau \quad (5.9)$$

There exists a trade-off within digital hydraulic systems of controllability and efficiency as a function of switching frequencies. Lower switching frequencies can exhibit higher efficiencies with decreased controllability compared to higher switching frequencies [90]. In addition, lower switching frequencies often required larger accumulators to filter the pressure fluctuations for systems with similar rated flow rates. Digital valve switching frequencies range between 50-100Hz requiring the switching times of 1 to 2 ms for a minimum duty cycle of 10%.

The digital switching valve described in this research is designed for use with a small-scale commercial axial piston pump (TFH-080, Takako Industries, Hutchinson, USA) that can provide 40 cc/s and a maximum operating pressure of 21 MPa. The proposed circuit is illustrated in fig. 5.15B. Since the flow rate is controlled using the PWM and varying duty cycle, the nominal pressure drop across the valve orifice should be minimized. However, a larger orifice area requires a larger diameter poppet/spool, and this leads to increased actuation power. The nominal pressure drop is set at 0.5 MPa, and the average actuation power is limited to 1 W. Table 5.2 summarizes the small-scale digital switching valve design requirements.

Table 5.2 Requirements of digital switching valve

Requirement	Value	Unit
Switching time	< 1	ms
Continuous switching frequency	100	Hz
Nominal flow rate	40	cc/s
Nominal pressure drop	0.5 (73)	MPa (psi)
Max. pressure drop	21 (3000)	MPa (psi)
Ave. actuation power	< 1	W
Minimal size and weight		

5.2.3 Valve geometry

Three valve control geometries are compared for use in the final design; poppet, spool with annular flow, and spool with rectangular slot flow (Fig 5.9). The poppet geometry has the benefit of requiring a single seal, while the spool geometry requires two seals. The spool geometries have balanced pressure forces, while the poppet has to act against a pressure gradient when closing. The slot style spool valve allows larger flow rates for smaller diameter spools and displacements compared to an annular orifice at the expense of a more complex geometry to manufacture.

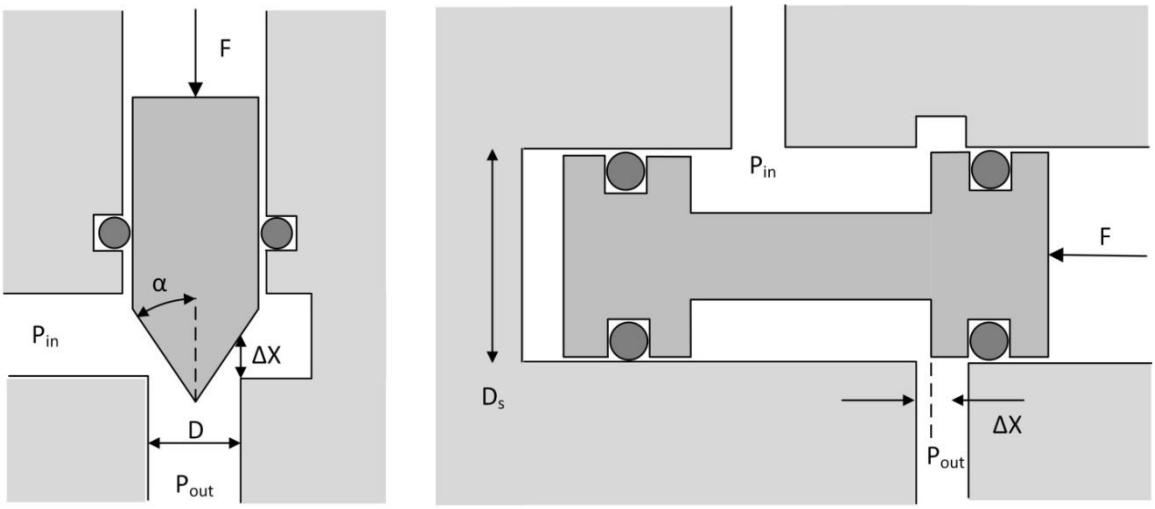

Figure 5.9 Cross-section of poppet and spool valve geometry

The total opening and closing forces generated by seal friction, the pressure gradient, and the change in fluid momentum are calculated with equations 2.7, 5.5, and 5.6 are shown in fig. 5.10. The sign convention is a positive force opposes the direction of poppet/spool deflection, while a negative force assists movement. All the forces considered in this analysis are dynamic, except seal friction force which is assumed constant across deflection. The inertial forces are significant in this application due to high accelerations. However, inertial forces are neglected from this analysis due to the fact they should have similar magnitudes between all compared designs. The fluid pressure and momentum forces in the poppet geometry are assisting the opening of the valve while acting against the closing of the valve. This is reversed for the spool geometries with

the fluid momentum forces acting to close the valve. The flow forces are assumed equal and opposite in closing and opening, so the energy required to actuate the valve is mainly a function of seal forces with them constantly acting against the poppet/spool.

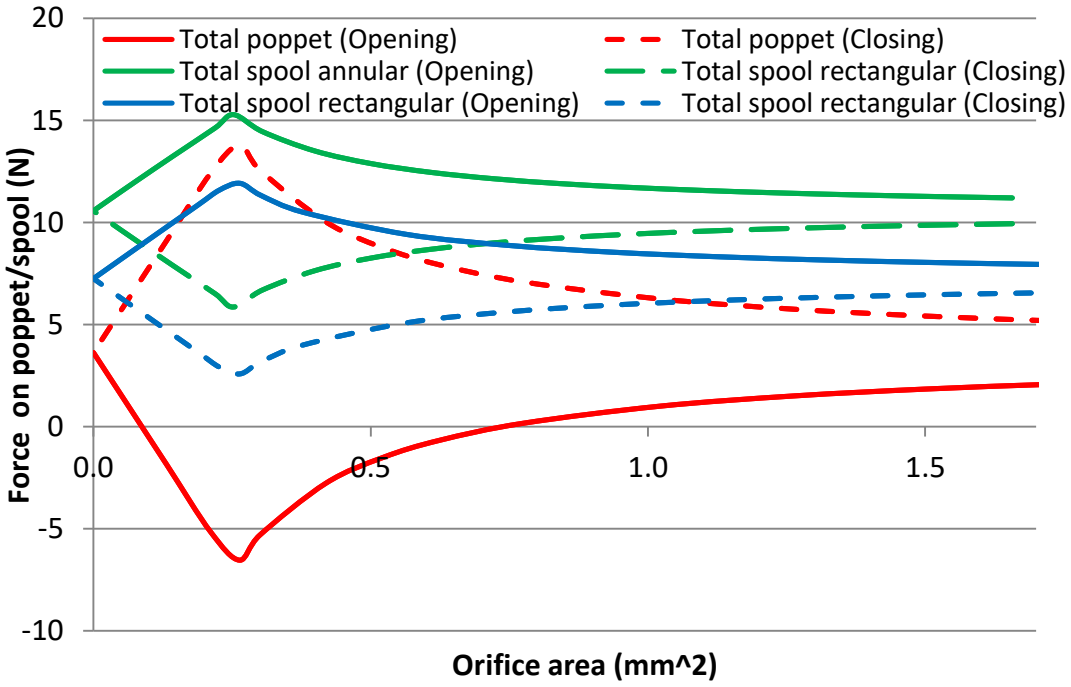

Figure 5.10 Open and closing forces with poppet and spool valve geometries

Table 5.3 Valve geometry performance comparison

Valve geometry	Poppet	Spool with annular orifice	Spool with rectangular orifice
Poppet/spool diameter (mm)	2.4	3.5	2.4
Required Actuation Distance (um)	350	800	250
Opening Work per cycle (mJ)	0.01	9.83	2.20
Closing Work per cycle (mJ)	2.62	7.08	1.42
Total Work per Cycle (mJ)	2.64	16.9	3.62
Ave. Power at 100 Hz. (W)	0.26	1.69	0.36

Table 5.3 summarizes the performance properties of the different valve geometries. The standard orifice equation (2.32) can be solved using the nominal pressure drop and flow rate to

determine the required orifice area is 1.65 mm ^{2}. The general analysis on the valve geometry factor illustrates that poppet/spool actuation distances should be minimized to decrease valve work. In addition, to allow the valve to have the ability to be piezoelectrically actuated, the poppet/spool actuation distances are limited to 0.8 mm. This is an approximate maximum deflection of commercially available, mechanical amplified, piezoelectric stack actuators.
A single annular orifice on a spool valve requires a large amount of spool deflection for large orifice areas compared to the other geometries. This results in the design incorporating a larger spool diameter, which ensued in higher seal forces to actuate against. A slotted spool with a rectangular orifice, can obtain the required orifice area with much smaller spool actuation distances and a smaller spool diameter. The minimum spool diameter is limited to 2.4 mm due to commercial sealing availability and recommendations.

Ultimately the poppet style geometry was selected for the final design. First, the poppet geometry has a lower average switching power consumption due to the use of a single seal. Second, the stable un-energized state of the valve is open, keeping the hydraulic system at rest. If the un-energized state of the valve is closed, the hydraulics will be powered in event of electrical valve failures. Third, the fabrication of a slotted 2.4 mm spool requires high precision and special machining capabilities, while an angled 2.4 mm poppet requires less precise operations.

5.2.4 Valve actuation

Two methods of actuation were considered for moving the valve member, electromagnetic (solenoid) and piezoelectric based on the requirements of the application. The valve control member only requires a small displacement, but a fairly large amount of force must be generated to actuate against the summed seal, pressure, and fluid momentum forces. In order to increase the response time of the system, all methods of indirect actuation like pilot stages were not considered for the final design. The two methods of actuation were compared by examining the properties of a custom designed solenoid coil and plunger against commercial, mechanical amplified, piezoelectric stack actuators.

A solenoid coil can only generate force in one direction, so a small spring is attached to the plunger to assist bidirectional actuation. The spring ensures that the poppet can be actuated to

the fully open position under all operating conditions. The spring preload force is set equal to the seal friction force with a small safety factor, while the stiffness is estimated by assuming a 0.5 N increase in force across the poppet displacement. The total spring force as a function of actuation distance is calculated with eq. 5.10 and the spring parameters in table 5.4.

$$F_S = k\Delta x + F_P \quad (5.10)$$

The solenoid is designed based on a comparison of the valve force requirements and the force generated by a coil (5.11) [111] consuming 1 W of electrical power (5.12 & 5.13). The electromagnetic force is inversely proportional to deflection distance squared. Since there are several design variables, the coil diameter and the number of turns are set at the values listed in table 5.4. The ratio between voltage and current is varied by using different wire gauges having different resistances per length. Current can be increased by using smaller gauge wires and decreasing the resistance; however, smaller gauge wires lead to heavier coils.

$$F_E = \frac{u_0 \pi D_S^2 N^2 I^2}{8\Delta x^2} \quad (5.11)\ [111] \qquad P = VI = I^2 R \quad (5.12) \qquad R = \pi D_S \gamma \quad (5.13)$$

Table 5.4 Valve solenoid parameters

Sym.	Description	Value	Unit	Sym.	Description	Value	Unit
D_S	Solenoid diameter	5	mm	N	Number of turns	144	-
F_E	Solenoid force	-	N	P	Power	1	W
F_S	Spring force	-	N	R	Wire resistance	-	Ω
F_P	Spring preload force	4.0	N	U_0	Magnetic Permeability (Free space)	$4\pi x10^{-7}$	N/A^2
I	Current	-	A	V	Voltage	-	V
k	Spring stiffness	1.5	kN/m	ΔX	Plunger actuation distance	-	M
l_S	Coil length	-	m	γ	Resistance per length wire	-	Ω/m
L	Coil inductance	-	H				

Figure 5.11 compares the valve closing force requirements to that of the proposed solenoid design using different gauge wires. The colored lines represent the maximum force capabilities of the coil at that deflection distance and operated at 1 W. The coil must be AWG 24 wire to generate sufficient force to actuate the valve.

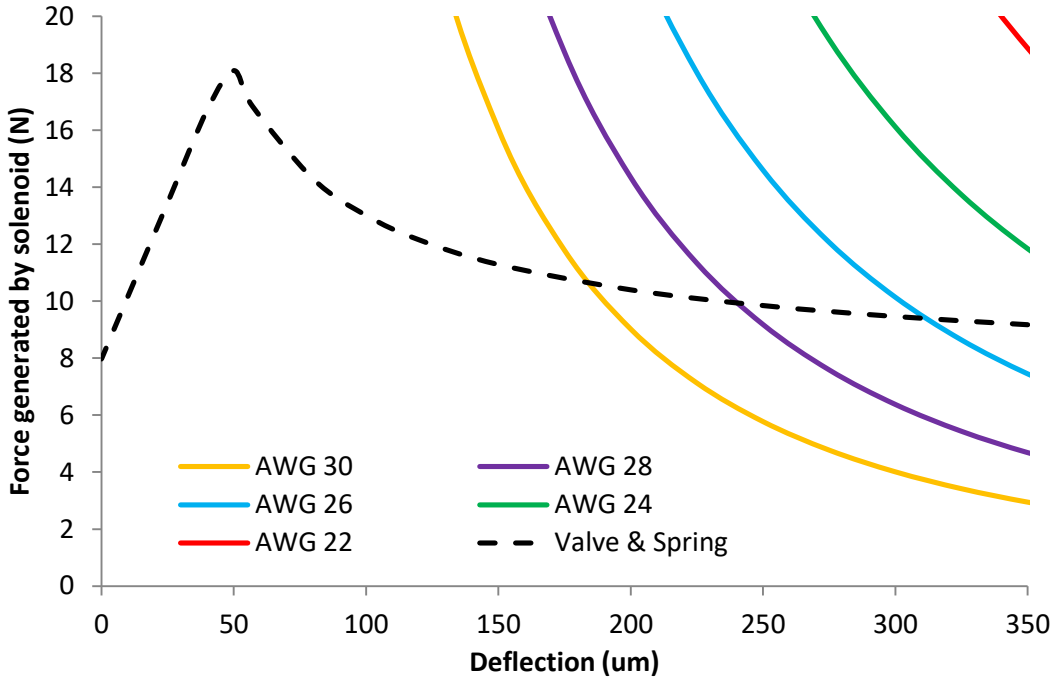

Figure 5.11 Solenoid force as a function of plunger distance & wire gauge

Figure 5.12 is a depiction of the required coil current for a specified deflection and force. All of the predicted operating conditions are within 1 W, but valve energy consumption could be further reduced by controlling the coil current to trace the valve operation. The required coil currents range ideally from 0 A to hold at 0 um deflection to 1.6 A at a deflection of 350 um. The force required to keep the valve closed is equal to the spring force at the poppet closed position with a margin of safety. The valve closed position represents a horizontal asymptote of solenoid force, so the required holding current is estimated assuming a deflection distance of 10 um. The holding force and current are 5 N and 41 mA.

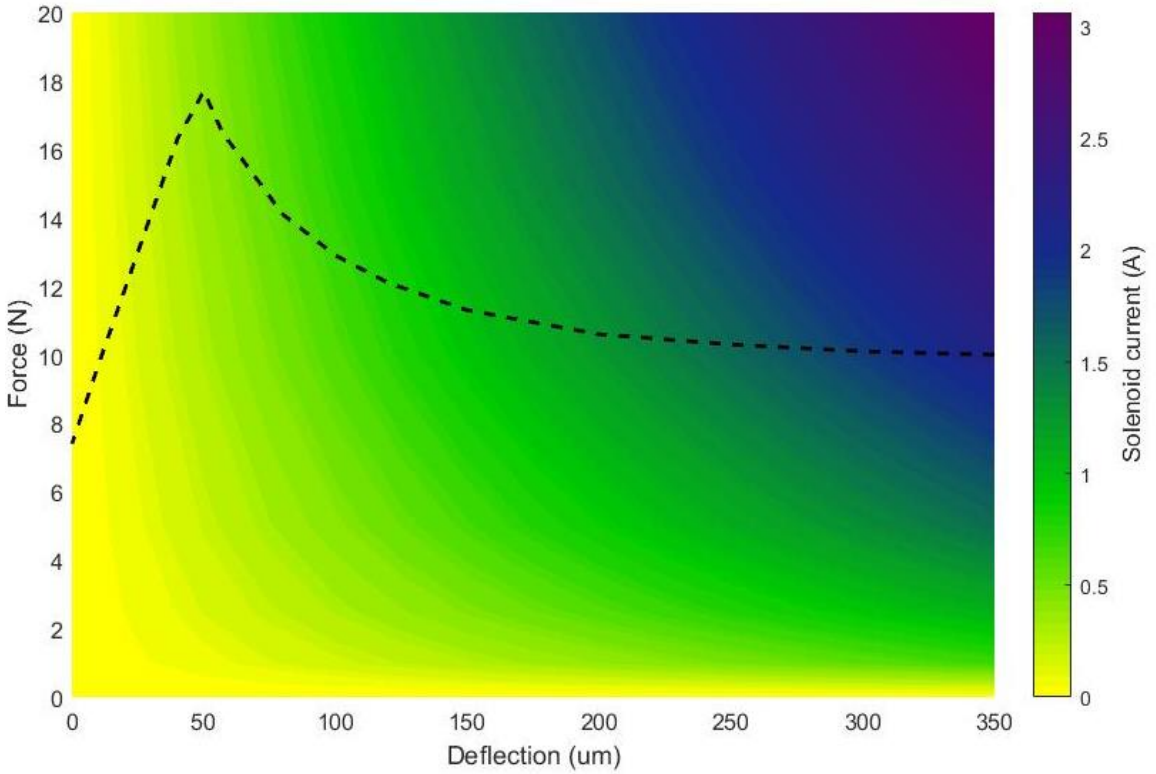

Figure 5.12 Solenoid force as a function of deflection and current

The solenoid coil can be modeled as a first order system with resistance and inductance in series. The Laplace transfer function for the system is eq. 5.14 with a time constant eq. 5.15. The electrical inductance of the coil can be calculated with eq. 5.16. The estimated time constant and bandwidth are listed in summary table 5.5. It is important to note that this is an upper limit of frequency response that does not take into consideration inertial acceleration of the plunger.

$$\frac{I(s)}{V(s)} = \frac{1/R}{L/R\,s+1} \quad (5.14) \qquad \tau = \frac{L}{R} \quad (5.15) \qquad L = \frac{\pi \mu_0 N^2 D_S^2}{4 l_S} \quad (5.16)$$

The size and weight of the coil composed of enameled copper wire, the iron inner core and plunger, along with spring are estimated assuming a coil wrapping geometry of 12 X 12 for a total of 144 turns.

Piezoelectric actuation is considered for three reasons for actuating a digital high frequency valve. The first reason is piezo electric actuators behave like electrical capacitors where the unused electrical energy can be returned to a power source, resulting in high efficiency piezoelectric actuators. Lead zirconate titanate is a typical piezoelectric material that has dielectric losses within 1-3% [112]. As a result, piezoelectric actuators require little to no energy to maintain a constant position. The second reason is the mechanical energy can be harvested from piezo electric actuators with a so called switch-shunt, DC-DC buck converter where the efficiencies range between 80 -95% [112]. Piezoelectric actuators are typically capable of reaching higher bandwidth capabilities than electromagnetic solenoids. Finally piezoelectric actuation is limited in actuation distance; however, this application only requires displacements up to 0.5 mm which is within the range of mechanically amplified piezoelectric stack actuators.

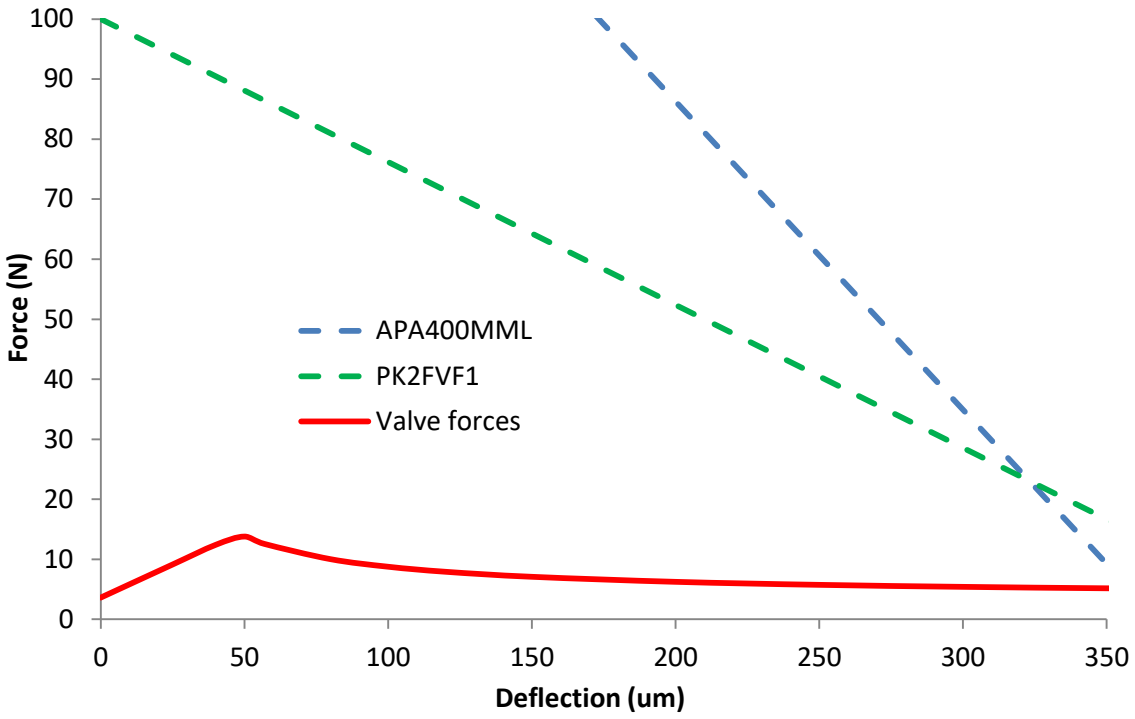

Figure 5.13 Comparison of valve force requirements and commercial piezoelectric actuators

Figure 5.13 compares the closing force requirements of a digital value with the force capabilities of two commercial piezoelectric stack actuators (PN: APA400MML, CEDRAT Technologies, Meylan Cedex, France) and (PN: Pk2FVF1, Thorlabs, Newton, New Jersey, USA). The force

capabilities of a piezo electric stack actuation are defined with a maximum blocking force at zero deflection and linear decreasing stiffness to the maximum deflection. Since piezoelectric actuators are composed of ceramics, it is typically suggested to limit the tensile force in the actuator to 10% of the blocking force. With the flow forces assisting valve opening, the required tensile forces are small and stay within this requirement.

Table 5.5 Comparison of digital valve actuation methods

Actuation Method	**Electromagnetic actuation (Solenoid)**	**Commercial mechanically amplified piezoelectric stack actuator**	
Part Number	Custom design	PK2FVF1	APA400MML
Actuation closing energy (mJ)	4.1	46	113
Average power to hold closed (mW)	3.5	< 1	< 1
Time constant (ms)	0.44	1	0.79
Bandwidth (kHz)	2.3	1	0.63
Weight (g)	15.2	42.2	47.5
Volume (cc)	3.59	13.5	18.7

Table 5.5 compares estimated parameters of the custom solenoid with that of two commercial piezoelectric actuators. This analysis has demonstrated that either actuation method should meet the design specifications. The current mechanical amplified piezoelectric stack actuators are larger, heavier, and more expensive. Piezoelectric material requires more energy to actuate than the solenoid; however, the majority of it is recoverable. The current applications of piezoelectric technology are focused on micrometer positioning systems with low bandwidth. This digital switching valve calls for a robust actuator design with high bandwidth capabilities. It is because of these reasons that solenoid actuation is better suited for use in a digital high frequency switching valve. A drawback of using solenoids is the continuous use of energy to hold a position. However, the addition of a small spring ensures one stable position requiring no input energy, and a second position that consumes a small amount of energy as the solenoid deflection distance is small. A bistable configuration introduced in section 5.1.2 could be used. This requires no energy to hold the control member open or closed at the cost of a higher actuation energy due to the resistive magnetic force of the permanent magnetic.

5.2.3 Digital high frequency switching solenoid valve design

A CAD model of the proposed digital switching valve is illustrated in fig. 5.14. The total estimated weight of the valve design is 34 g with an approximate size of 2.5 cm in diameter by 5.9 cm in length. The valve is designed to be secured to another manifold with two screws on the bottom of the valve block. An external face O-ring provides a seal between the manifolds at the outlet port, while a hose adapter is threaded in at the inlet port. The solenoid case and poppet must be composed of magnetic materials like steel to allow the wrapped enamelled copper wire to generate sufficient electromagnetic force. The valve block in composed of high strength aluminum to reduce weight, and is secured to the solenoid case using two screws that pass through the valve block.

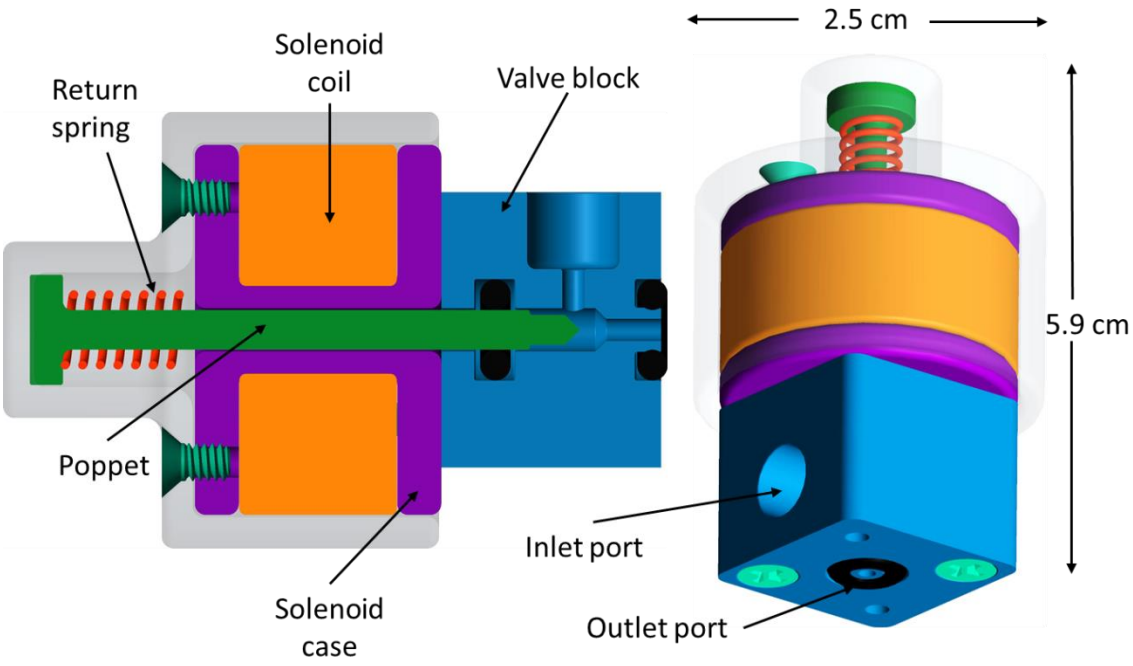

Figure 5.14 CAD model of digital high frequency switching valve with solenoid actuation

The clearance gap around the poppet is sealed with an internal O-ring. Other specialized high pressure rod seal types should be explored if the valve operation pressure is above 10.3 MPa (1500 psi). A return spring provides a passive force to fully open the valve orifice as the solenoid coil is de-energized. This is important for safe operation, as the flow will be diverted to the tank

if the electrical power is interrupted. An ABS cover is installed over the return spring and solenoid to prevent damage from contamination.

5.2.4 Simulated performance comparison of proportional and digital actuation

The objective of this analysis is to compare the performance of a high frequency, digital switching valve actuation system with that of a traditional proportional, servo valve controlled actuation system (Fig 5.15). In addition, the switching frequency is varied to determine how it affects performance and to determine what is the minimum switching frequency required to allow proper control.

The two hydraulic systems compared in this analysis use the same electric motor, hydraulic pump, actuation cylinder and undergo identical loading conditions, actuating against a 1000N force for a displaced of 8 cm. The proportional hydraulic system uses a two stage servo valve with the main orifice area sized to have 3.5 MPa pressure drop at the 40 cc/s. In addition, the proportional circuit incorporates a pressure relief valve allowing additional flow to bypass the servo valve. The cracking pressure of the relief valve is determined by calculating the maximum pressure drop across the servo valve (3.5 MPa) and adding that to the load pressure (5 MPa). This pressure summation is multiplied by 10% to provide a buffer that accounts for the inefficiencies across the conduit, actuator, and inertia acceleration.

The digital hydraulic circuit uses the parameters of the high frequency switching valve (1) design in the previous section. In addition, a small 1 cc spring accumulator and a check valve are used to smooth out the digital flow rate provided by the digital valve. The accumulator parameters of preload force (F_p = 450 N) and spring stiffness (k_s =20 kN/m) are based on the load pressure. In order to allow bidirectional actuation, second two way control valve (2) is need to change the direction of the flow supplied to the actuator.

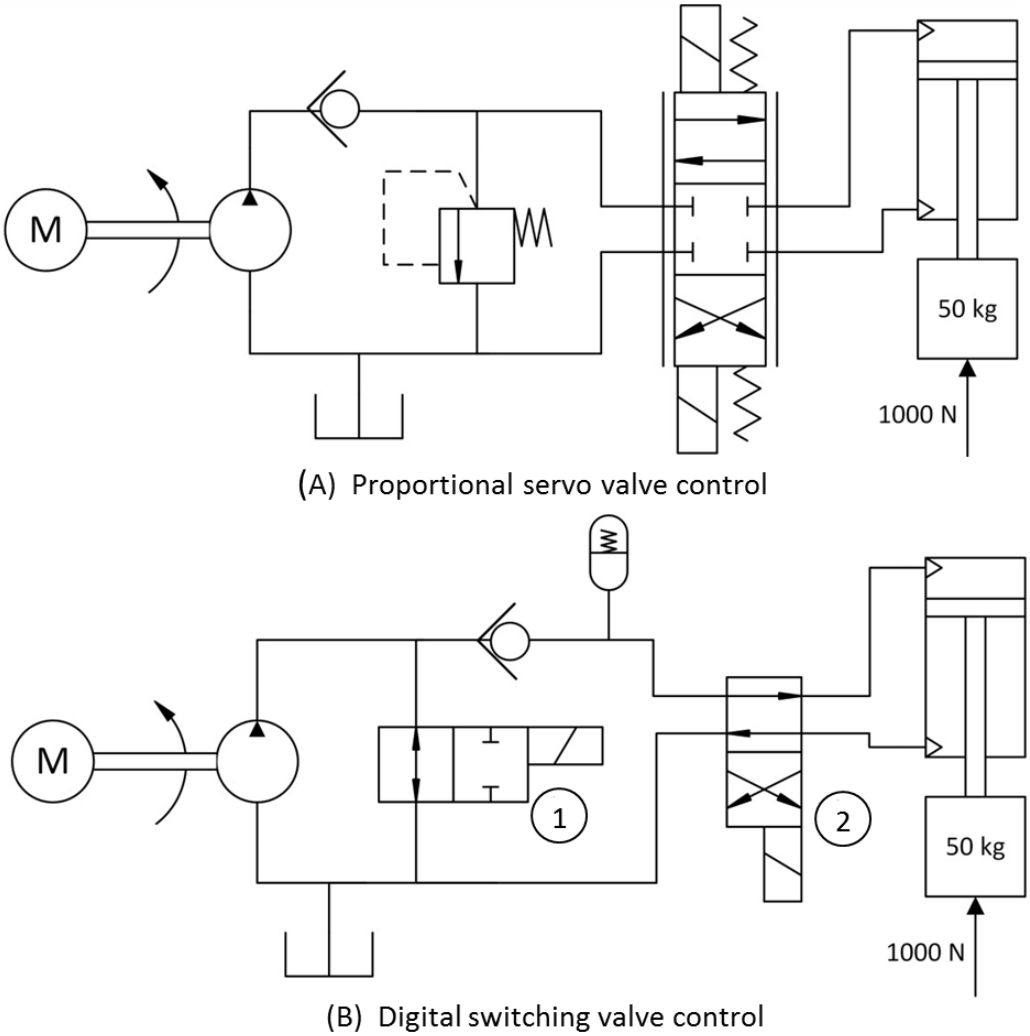

Figure 5.15 Hydraulic circuit for proportional servo valve control (A) and high frequency, digital, switching valve control (B)

The control variables of the simulations are the current to the servo valve torque motor and the duty cycle of the digital valve PWM input signal. The duty cycle of the PWM input signal is inversely proportional to the flow rate provided to the system. The input variables are controlled using proportional, integral, derivative (PID) control methods and a negative feedback control loop that monitors the flow rate provided to the system. The controller sampling rate is set at 10 kHz with the input to the control loop being the desired flow rate.

5.3 Results

5.3.1 Performance comparison of proportional and digital actuation using simulation

Figure 5.16 illustrates the inversely proportional relation between PWM duty cycle and valve flow rate. The theoretical line illustrates ideal valve operation as a function of duty cycle. Under ideal valve operation the flow rate at 0% duty cycle is equal to the pump flow, and there will be no flow at 100% duty cycle. However, the open loop simulation data takes into consideration valve opening/closing time, compression losses, leakages, and other inefficiencies that are not accounted for in the theoretical line. These losses are commonly referred to as switching losses, and are represented in fig. 5.16 by the vertical distance between the theoretical line and the simulation line at the same duty cycle. The switching losses increase with control frequency at the same valve duty cycle, as there are more opening/closing valve cycles within the same time.

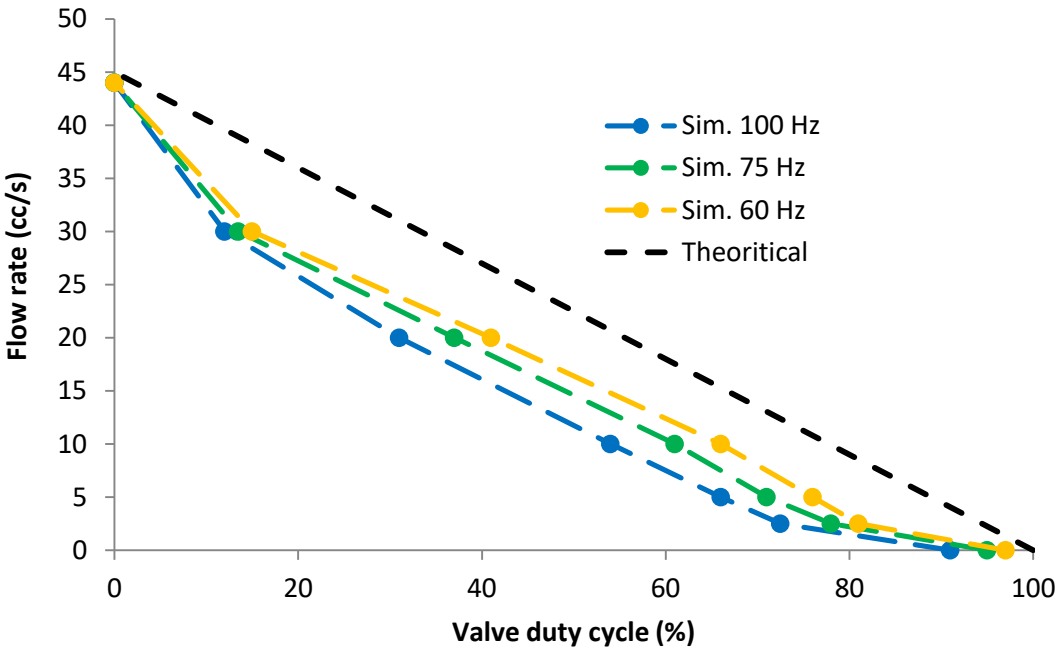

Figure 5.16 Case study: Flow rate as a function of duty cycle and switching frequency

The performance of the closed loop digital and proportional hydraulic actuation systems are compared in fig. 5.17. The desired flow rate is 20 cc/s with a PWM frequency of 75 Hz. The area of piston within the actuation cylinders is 2 cm^2, so the desired piston velocity is 10 cm/s. The

digital hydraulic actuation system illustrates a significantly higher overshoot and setting time in tracking piston velocity compared to the proportional hydraulic system. This performance could likely be improved using a more specialized digital PWM control algorithm for hydraulic applications similar to control algorithms used in electrical PWM switching amplifiers and converters [113, 114].

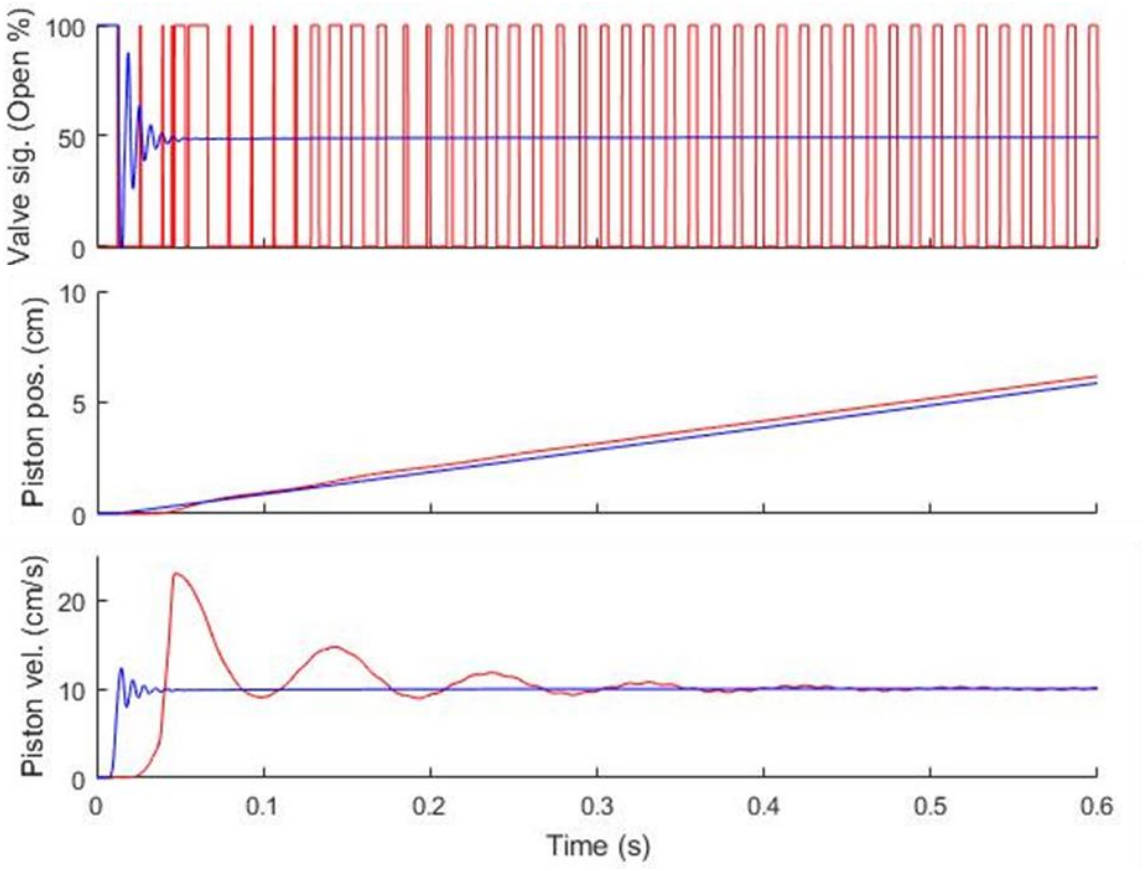

Figure 5.17 Case Study: Closed loop velocity tracking of digital (red) and proportional (blue) hydraulic systems

In simulation the digital switching valve tracked slow velocities poorly. At low duty cycles there exists a minimum switching leakage flow across the valve due to the fact the valve is opening and immediately closing. This switching leakage flow could be reduced with an algorithm that adapts the switching frequencies based on the desired velocity. At low velocities it is desirable to have a lower switching frequency to reduce switching leakage as the cost of more flow rate

fluctuations. The switching leakage flow can further be reduced by decreasing the valve actuation time.

Figure 5.18 illustrates the flow rates and pressure within the digital actuation system. The accumulator flow rate is defined as positive for charging and negative for discharging. The control flow to the cylinder is composed of alternating supply and accumulator flow. When the digital valve is opened allowing fluid to flow directly to tank, the supply pressure decreases from load pressure to the pressure across the digital valve (0.5 MPa). This digital relief flow dissipates less energy compared to a traditional relief valve due to the decrease relief pressure. In addition, since the flow rate is not controlled with a metering orifice, there is a much smaller pressure drop across a valve using PWM to control flow rate. The load pressure experiences a large spike when accelerating the system. The pressure fluctuation was decreased with the additional of a second control variable monitoring load pressure along with flow rate.

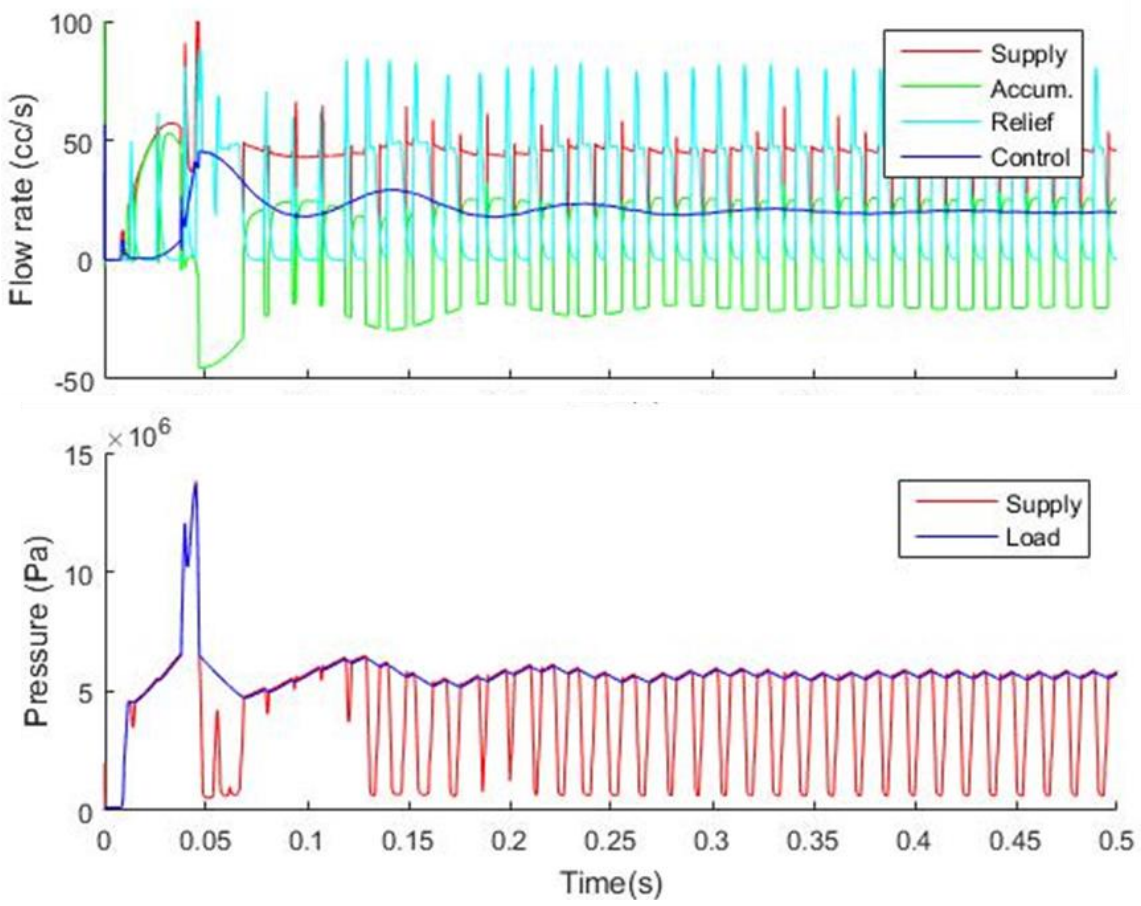

Figure 5.18 Case study: Performance of high frequency digital switching valve actuation system

Figure 5.19 compares the average system efficiency of the proportional actuation system using a relief valve with that of the digital system using three different PWM frequencies. The digital actuation system illustrates higher system level efficiency across all flow rates with a maximum system efficiency of 64%. The efficiency of a digital hydraulic actuation system increases as the PWM frequency is decreased. As switching frequency is decreased, the amplitude of the flow rate fluctuations increases. The ability to control the flow rate using switching frequencies less than 60 Hz was limited due the presence of large flow rate errors and system instability. Flow rate is the observation variable in the feedback loop controlling duty cycle, so fluctuations in flow rate will lead to large fluctuations in the control signal and system instability.

The load cycle took 1.44 seconds to complete extension and retraction. At the 60, 75, and 100 Hz switching frequencies there were 87, 108, and 145 valve cycles per load cycle. As a result the

design of high frequency switching valves will have to take special consideration of material fatigue and wear.

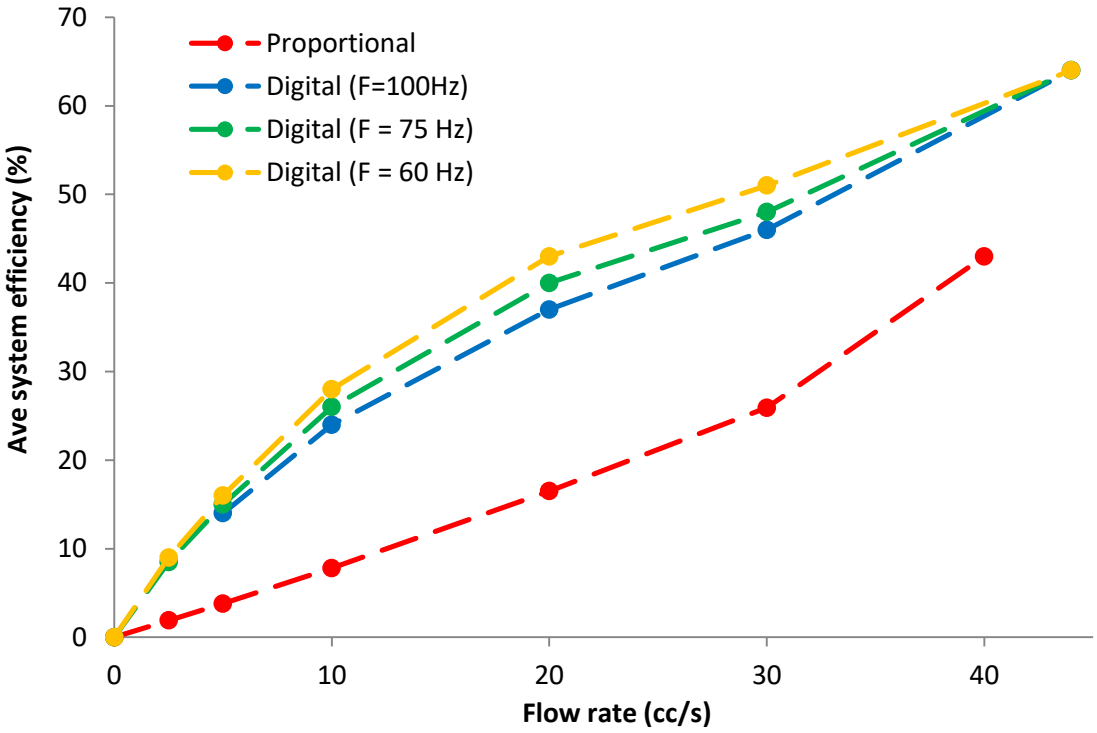

Figure 5.19 Case Study: Comparison of proportional and digital system efficiencies

5.4 Discussion

5.4.1 Conclusions

One of the main drawbacks of hydraulic technology is the poor efficiency due to metering valve losses [6, 80]. The innovative small-scale digital switching valve described in this test has the ability to improve valve efficiency, filling the void in current technology. The research has also shown that as digital switching technology is scaled to smaller flow rates, the proportion of switching energy to nominal valve power decreases. This trend results in digital switching technology being more efficient for small-scale applications compared to large-scale applications where switching energy becomes a large percentage of the losses.

The simulated performance of a high frequency digital switching valve illustrates an increase in system efficiency across a range of small-scale flow rates compared to throttling valve. There exists a trade-off between controllability and valve efficiency that is controlled by varying the switching frequency. Lower switching frequencies will have high efficiencies, but also decreased controllability with increased system instability. This design space should be explored during digital valve design to determine the optimal switching frequency for an application.

The efficiency of the valve is strongly correlated to the time it takes the valve member to actuate. The valve actuation time should be minimized to increase efficiency. The smoothing of the digital fluid flow requires precise tuning of the capacitance and inertia before and after the valve. This was accomplished through the addition of a small accumulator and/or longer conduit.

A second benefit of using a digital valve is a reduction in the susceptibility of contamination failure with a reduced manufacturing cost. Small-scale servo valves require tiny orifices in the pilot stage to control the main spool. These pilot orifices can often be damaged by particles from 1- 10 um. Systems employing the use of the small-scale servo valves required a high level of filtration, resulting in additional weight and pressure losses. In comparison, digital hydraulic valves use large orifices that can handle particles up to 250 um. In addition, the fabrication costs of the digital switching valves using solenoid actuation will be less than small-scale servo valves requiring high precision and tight tolerances in the construction of their pilot stages and torque motors.

In 3.7 hours a digital switching valve operating at 75 Hz does a million cycles. This significantly increases the probably of fatigue failure compared to a traditional servo valve. This can be reduced by using an array of digital switching valves. The valves can then be operated at slower frequencies by alternating valves. An addition method of reducing valve wear is to have the control algorithm prevent the valve from opening and closing when the actuator is at rest.

5.4.2 Limitations of research

This chapter presents research on the feasibility and possible benefits of scaling down digital hydraulic technology for use in small-scale applications. The proposed design and simulated performance of a small-scale digital switching valve is presented; however, the performance of

the valve has not been validated with physical hardware. The next step in the process of this research is the fabrication and performance testing of a small-scale digital switching valve.

The design of the solenoid coil is roughly approximated with empirical formulas. The design of the solenoid coil should be optimized using electromagnetic modeling software to improve efficiency and to ensure that the solenoid will generate adequate forces to actuate the valve. In addition, the use of bistable solenoid geometry can be explored to decrease valve actuation energy.

Chapter 6 Design, Simulation, Prototyping and Performance Testing of a Hydraulic Powered Ankle-Foot Orthosis

6.1 Introduction

This chapter was published in ASME Journal of Medical Devices volume 10, issue 4, 2016. Additional material has been supplemented into the chapter for further detail and explanation.

6.1.1 Objective

An objective of this research is to construct a dynamic model and prototype of the hydraulic powered ankle-foot orthosis (HAFO). This prototype will illustrate benefits of the modeling techniques developed in earlier chapters by assisting in the development of small-scale, hydraulic powered, human assistive machine. An accurate simulation of the orthosis performance give engineers the capabilities to adjust different design parameters and observe how the expected performance changes. This allows engineers to explore their design space quicker with accurate quantitative comparisons, allowing the development of more efficient and light-weight systems. In addition, this research will provide additional validation for the modeling techniques developed in this dissertation by comparing the simulated performance of the hydraulic powered orthosis with the measured performance of the prototype.

The second objective of this study is to explore the potential of small-scale hydraulics for untethered exoskeletons, using the AFO as an example. Despite the advantages of hydraulics described in chapter 1, designing a small-scale, hydraulic system has significant challenges that include the lack of off-the-shelf small-scale, hydraulic components, sealing of components to eliminate fluid leaks and configuring an integrated system to minimize size and weight. The HAFO described in this chapter is one example of how these challenges can be met and shows promise for applications such as muscle strengthening or assisted walking. Proving the feasibility for a specific clinical application is not the purpose of this study, as that will require additional work in system optimization and control. This chapter describes the design requirements, performance modeling, and engineering bench test results, leaving the presentation of clinical data with human participants for future work.

6.1.2 Applications

An ankle foot orthosis (AFO) is an assistive device used to correct temporary or chronic motor impairments of the ankle [115]. The two most common conditions that an AFO is prescribed for are foot drop [116] and muscle spasticity [117]. Foot drop is the inability to lift the front of the foot with respect to the ankle (dorsiflexion), while spasticity is typically characterized by poor muscle control and stiff muscles that actuate the ankle through dorsiflexion and plantar flexion.

Foot drop and ankle spasticity are caused by nerve injuries, brain and spinal disorders, and muscle disorders and are common symptoms of cerebral palsy and multiple sclerosis. Cerebral palsy is the leading cause of disability in children occurring in 0.2-0.5% of normal births and 12-15% of premature births [118]. Disorders that may also lead to foot drop include muscular dystrophy, Lou Gehrig's disease, and polio [116]. Another use of AFOs is when a person needs positional support. An AFO can also be used to completely immobilize the foot and ankle for the treatment of Charcot Feet, fractures, arthritis, and wound management [115].

6.1.3 Gait Cycle Dynamics

Gait is defined as a cyclical motion pattern incorporating the ankle, knee, and hips joints. The gait cycle is often referred to in percentages that are initiated and ended as the heel of the same foot strikes the ground. Gait can be separated into six different events; heel strike, foot flat, midstance, heel off, toe off, and mid-swing (Fig 6.1) [119, 120].

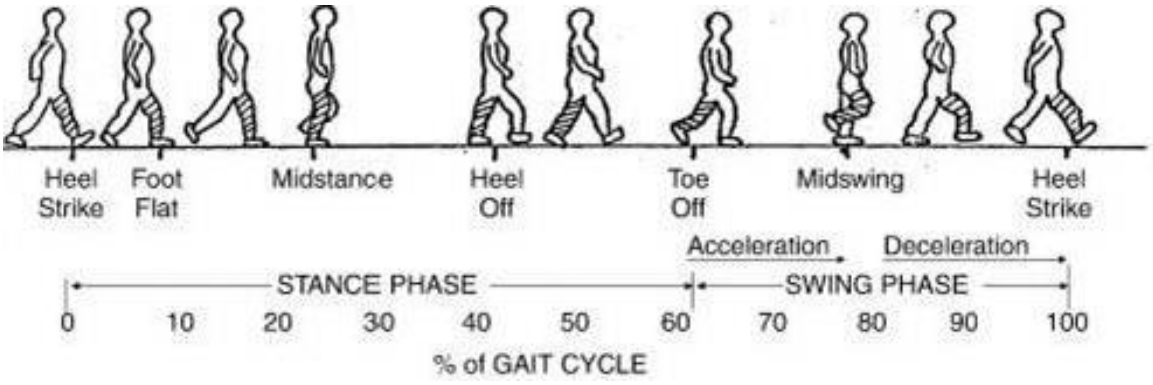

Figure 6.1 Gait cycle events and phases [119]

The normal average gait dynamics of an 80 kg male are illustrated in fig. 6.2 [120]. The negative angular position refers to plantar flexion and positive refers to dorsiflexion. The data illustrates an ankle dorsiflexion of 7° and a plantar flexion of 21°. The approx. maximum ankle angular velocity of -250 deg/s occurs slightly before toe off. The ankle generates only minor amounts of torque in dorsiflexion compared to -90 Nm of torque generated as the ankle plantar flexes between heel and toe off. The weight normalized values for the maximum torque have found to be ≈-1.25 Nm/kg [121]. The ankle power during the gait cycle is highly intermittent with spike of around 250W occurring around 50% of the gait cycle.

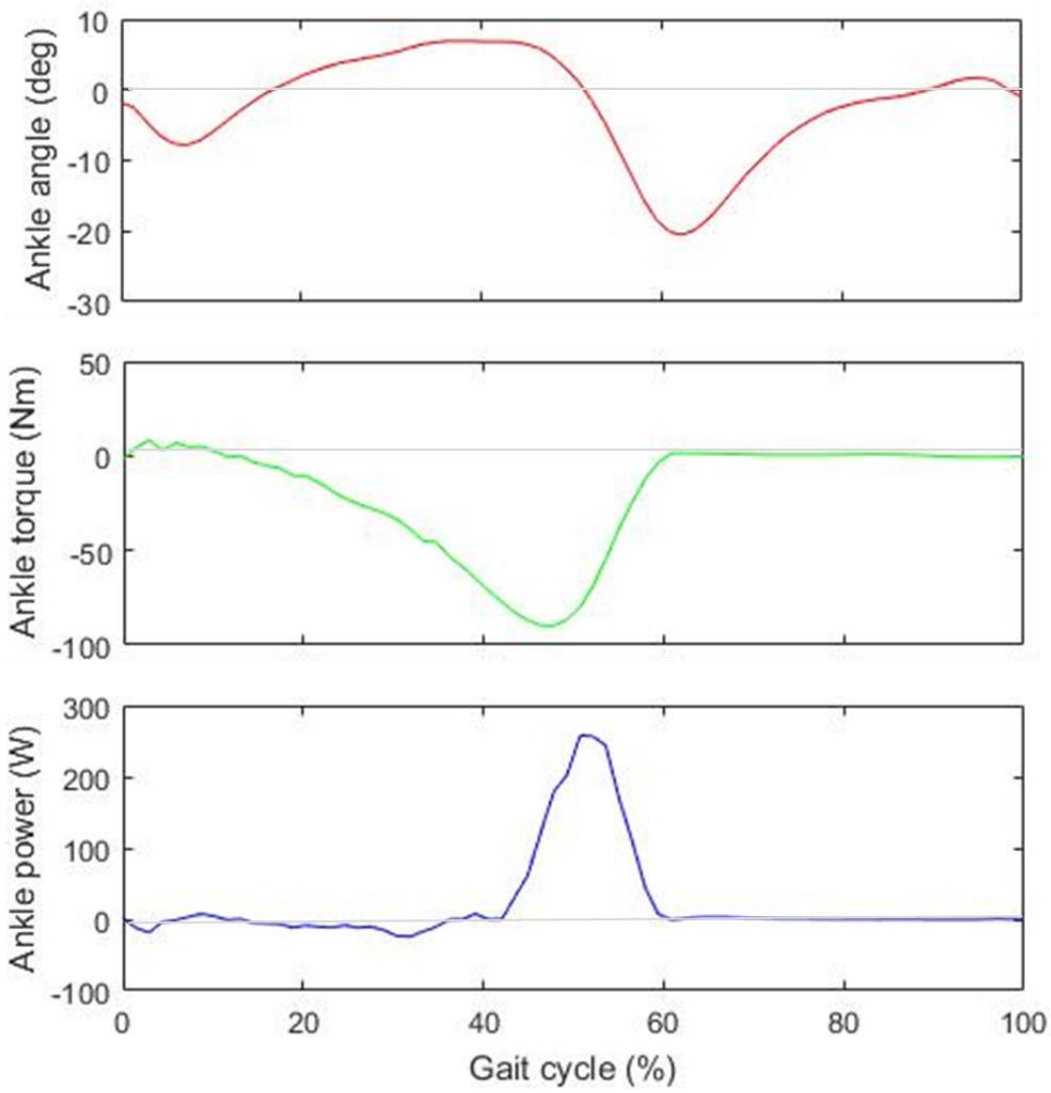

Figure 6.2 Ankle angular position, torque, and power with the gait cycle

6.1.4 Passive Ankle-Foot Orthosis

There are three categories of passive AFOs: articulated joint, posterior leaf spring joint (PLS), and solid joint. The articulated or hinged joint AFO provides stiffness to the ankle by using torsional springs and angle stops positioned on the medial and lateral sides of the ankle to guide the ankle through dorsiflexion and plantar flexion. Articulated AFOs are used in treating dorsiflexion, plantar flexion, inversion, and eversion paralysis; the prevention and correction of deformities; reduction of weight bearing; and reducing the cost of ambulation [115].

A posterior leaf spring (PLS) AFO is composed of a calf support connected to foot support with a thin flexible segment centered behind the Achilles tendon. The PLS orthosis is designed to provide dorsiflexion torque assistance during swing phase, while the patient overpowers the brace during plantar flexion push-off phase [115]. The stiffness of the AFO is adjusted by varying the dimension and/or the material of the section connecting the calf and foot supports.

The solid joint AFO is designed to provide mediolateral ankle stability for treating knee and ankle weakness, limiting arthritis pain, and severe muscle spasticity. The solid joint AFO immobilizes the tibiotalar and subtalar joints of the ankle, which is often necessary in treating wounds and fractures [115]. Solid ankle joint and PLS AFOs are light and inexpensive, because they are typically custom-molded of a single piece of the thermal plastic to the patient's ankle.

Gait energetic studies have shown that a large portion of the energy required for gait comes from the ankle [122, 123]. In addition, muscles and tendons at the ankle exhibit an efficiency of two to six times greater during gait compared to isolated muscle efficiency [122]. This is thought to be the result of the Achilles tendon storing elastic energy that can be used for ankle plantar flexion. This research has driven the design of a passive AFO that uses a mechanical clutch and elastic springs to off-load the muscle tension, thereby reducing metabolic energy [123, 124]. At heal strike, the clutch engages and the spring is stretched until midstance. The energy stored in the spring assists the ankle during plantar flexion, and the clutch disengages at toe off to allow free motion. The orthosis has demonstrated an energy savings of 7.2% during normal gait of a healthy subject [124].

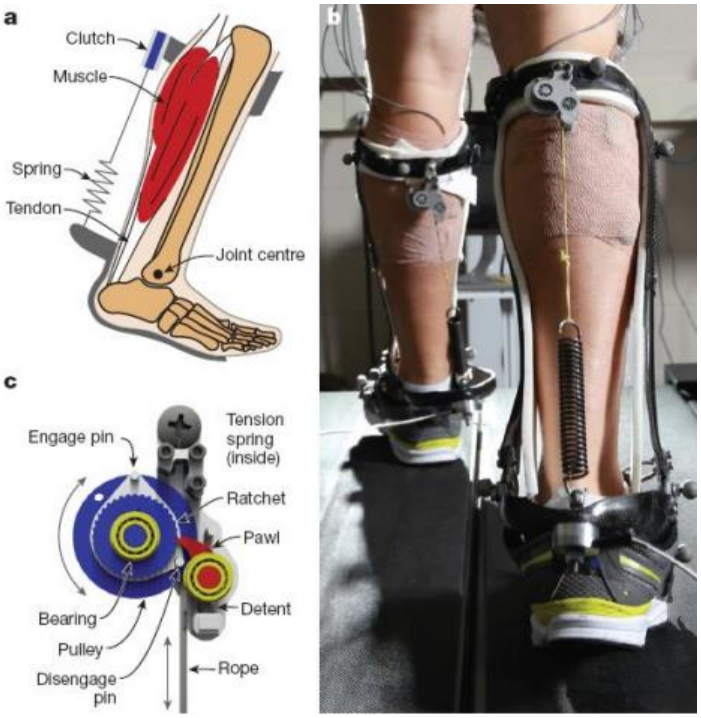

Figure 6.3 Quasi-active clutch spring AFO [124]

6.1.5 Powered Ankle-Foot Orthosis

Passive AFOs are limited to providing the mechanics of a passive, fixed spring. For patients with severe ankle impairments, torque assistance provided by a passive spring is not sufficient to restore normal gait dynamics. In contrast, a powered AFO uses an energy source and a power transmission to augment torque at the ankle. Further, the dynamic properties of a powered AFO are easily changed through computer control. In the past decade a variety of passive and powered ankle-foot orthoses have been developed in laboratories, and this exploration of previous art focuses on four of the more developed and evaluated designs. A more detailed review of single joint robotic orthoses is in Hussain et al [125]and of passive, semi-active, and powered ankle-foot orthoses in Shorter et al [126] and another by Dollar et al [127].

In 2005 a powered AFO uses McKibben type pneumatic actuators that shorten when compressed air is applied [128, 129] (Fig. 6.4). The device generated 70 Nm in plantar flexion and 38 Nm in dorsiflexion operating at 480 kPa (70 psi). While the device was light (1.6 kg), it

was tethered to a fixed air supply and was not sufficiently small to fit under a pair of pants. The orthosis user's intent was deciphered using two methods: electromyography (EMG) and a kinematic foot switch controller [130]. The performances of both controllers were compared with unilateral plantarflexion on healthy subjects, and the results illustrate that the EMG-controller showed larger reduction in muscle activation and better gait kinematics. The use of McKibben actuators to replicated human muscle dynamics has also been demonstrated with the use of hydraulic fluid in [9].

Figure 6.4 McKibben pneumatic AFO [129]

The electromechanical active AFO developed at Massachusetts Institute of Technology (MIT) and robotic tendon AFO developed at Arizona State University (ASU) that use series elastic actuators (SEA) to produce both dorsi- and plantar flexor assistance [126, 127, 131, 121, 125]

(Fig. 6.5). A SEA uses an elastic element in series with the motor to store mechanical energy. The use of SEA reduces the peak power requirement of the motor, reducing the overall weight of the system. In addition, an SEA better mimics the elastic dynamics of tendons [122, 131, 132]. The MIT active AFO and the ASU robotic tendon AFO weigh 2.6 Kg and 1.0 kg and are tethered to electric power supplies. The MIT active AFO has illustrated a reduction in the frequency of foot slaps and foot drop during swing phase [126]. The ASU robotic tendon AFO can produce up to 250W, the full power required for gait [131, 121].

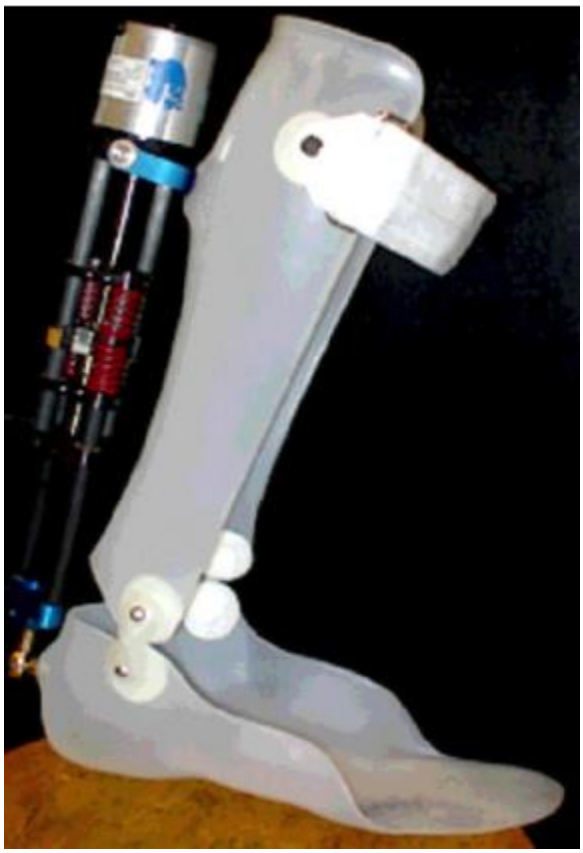

Figure 6.5 Electromechanical series elastic AFO [126]

The first untethered CO_2 powered AFO uses a bidirectional, rotary, pneumatic motor attached to the ankle and a CO_2 bottle with a regulator attached at the waist [133, 134, 135] (Fig. 6.6). The total system weight was 3.1 kg with 1.9 kg at the ankle actuator. The power supply being separated from the actuator minimizes the weight at the ankle. While portable, the device could

generate only 9 Nm of torque when operating at 0.62 MPa (90 psi), which is sufficient only for applications where modest torque assist is needed. The portable powered AFO consumes 33 J per gait cycle. The second generation of the orthosis implemented energy regeneration, improving efficiency 25% using exhaust gases from high power plantar flexion to power the low power dorsiflexion. In a second generation, the rotary actuator has been replaced with a pair of linear pneumatic cylinders [135]. A rack and pinion mechanism converts the linear force to rotary torque, suppling up to 40 Nm of torque assistance to the ankle.

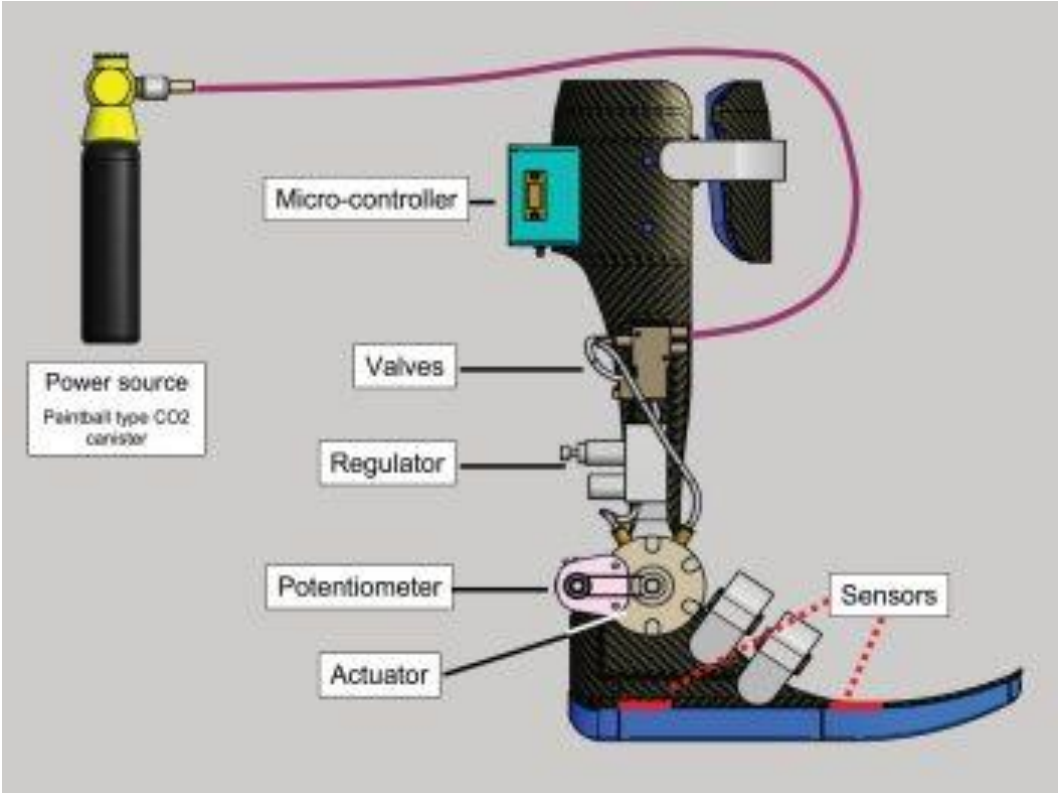

Figure 6.6 Portable pneumatic CO_2 powered AFO [133]

In Yu et al [136, 137] a hydraulic powered below knee prosthesis is presented that uses an EHA to actuate the ankle. A unique feature of the design is that the pump and electric motor are packaged with the cylinder at the ankle, while a battery and control electronics are carried in a backpack (Fig 6.7). A piece of compliant power steering hose is directly attached to the actuator to act as an accumulator for dampening and regeneration. The design incorporates a passive mode to absorb vibrations and support body weight. The device also uses a powered assistance

mode to provide torque assistance during certain times of the walking cycle like toe push-off. It also provides torque assistance for ascending and descending inclines, ramps, and steps.

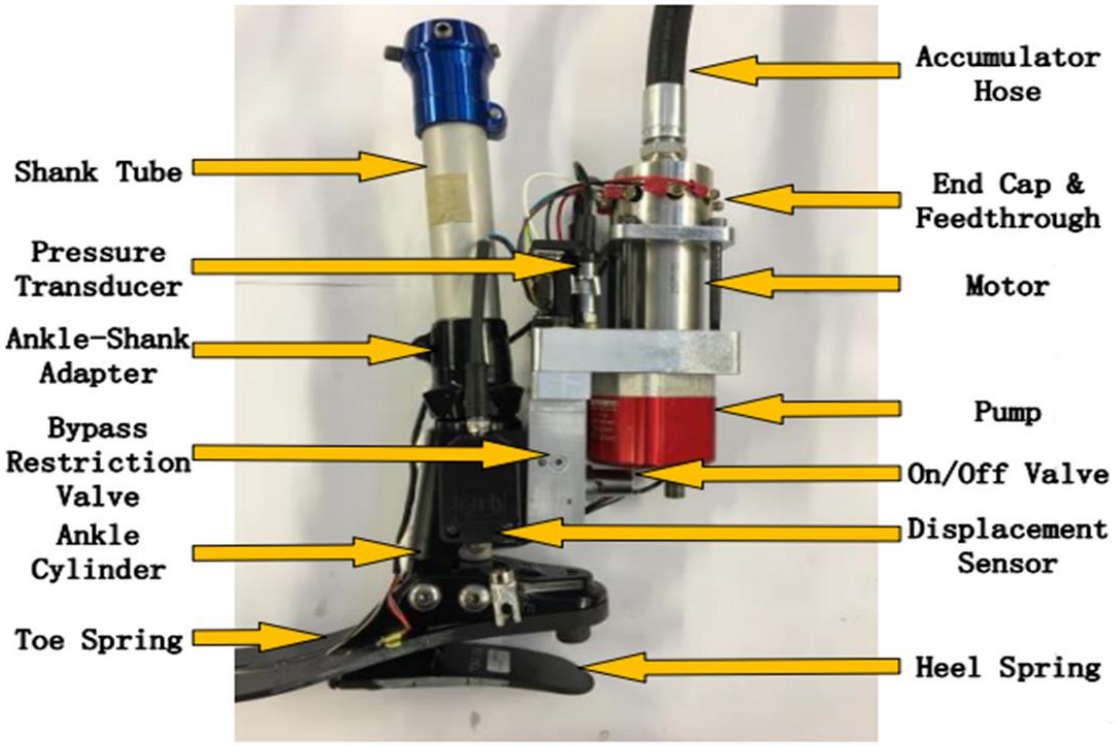

Figure 6.7 Hydraulic powered below knee prosthesis [137]

6.1.6 Why Hydraulic Powered Orthotics

Hydraulic technology has illustrated great potential for use in AFO applications, because of its exceptionally high power and force density of the actuators compared to electromechanical systems limited only by the pressure of the working fluid [138, 139, 140, 7]. For example, a recent study showed that 10 to 1000 W hydraulic actuation systems have a lighter overall system weight compared to an equivalent electromechanical system when operated above 500 psi [69]. In addition, hydraulic actuators are capable of generating high forces at low velocities compared to electric motors that operate most efficiently at high angular velocities and low torque. Thus, hydraulic actuators are a good match for powered prostheses and orthoses that also require high forces at low velocities.

The use of hydraulics allows the power supply generating the pressurized fluid to be separated from the actuator through hoses. An electromechanical system would require heavy gears and motor to be positioned at the ankle or a cumbersome pulley and cable transmission transmitting power to the ankle. While pneumatic systems also have the ability to transport power through hoses, the compressibility of the gas adds compliance to the system that essentially eliminates the possibility of a stiff control system particularly when long transmission lines are involved. In contrast, hydraulic systems have a high stiffness where the compliance can easily be adjusted with the addition of a small elastic accumulator. The high stiffness allows fast loaded system responses compared to electrical and pneumatic actuation, which can also result in less positional errors [138, 15].

The use of hydraulic technology for powered orthoses and prostheses does introduce a few challenges including the use of stiff hoses. Hoses can hamper mobility, add overall weigh to the system, and be difficult to conceal. In addition, small external hydraulic leaks could be a nuisance as the working fluid soaks into the user's clothing or shoes. Finally, hydraulic systems can be noisy, and the use of the device could be distracting in quite environments.

6.2 Methods

6.2.1 Design Requirements

We developed the design requirements (Table 6.1) for the HAFO by considering the force and velocity profiles of the ankle for the average 80 kg male [120]. The AFO must provide 90 Nm of plantar flexion torque assistance and have a maximum angular velocity of 250 deg/s to replicate the gait cycle [120].

Table 6.1 Design requirements for HAFO

Maximum Torque Generation	Plantar flexion	90 Nm
	Dorsiflexion	10 Nm
Range of Motion	Plantar flexion	50°
	Dorsiflexion	20º
Maximum Angular Velocity	250 deg/sec	
Gait Cycles Before Recharge	6000	
Weight Positioned on Ankle	< 1.0 kg	
Total System Weight	< 3.5 kg	

The weight and weight distribution of the AFO is critical. Studies on the oxygen consumption during normal and loaded gait have shown that placing 20 kg on the trunk causes little to no increase in O2 consumption. However, if as little as 2 kg is attached to the foot, the rate of oxygen consumption increases 30% [141] even though gait kinematics are unaffected [142]. Because of this, the weight of the HAFO components at the ankle must be less than 1.0 kg and the weight of the components at the waist must be less than 2.5 kg. This led to the design choice of placing the power supply at the waist and the actuator at the ankle. We wanted the HAFO to be small, and set an additional requirement that the component at the ankle must fit under a pair of loose-fitting pants and inside a pair of shoes.

The H AFO was designed to be un-tethered with a wearable power supply. Our target for the number of gait cycles before recharging the power source was 6,000 cycles, based on the approximate average of 6,500 steps per day for U.S. adults [143, 144, 145].
Finally, recognizing that the AFO is worn, has a high power requirement, runs at high pressures and is capable of generating a large torque, safety is critical. Therefore, the pressurized chambers must have a high safety factor. In addition, guards and mechanical limit stops must be incorporated into the structure. These requirements in combination with the system-level design script in chapter 3 and the modeling technique in chapters 2 and 4 were used to assist in component selection and design of the HAFO.

6.2.2 Design Description

The HAFO has two sections: a hydraulic power supply at the waist and hydraulic actuators at the ankle with the two sections connected by a pair of thin hydraulic hoses. The power supply consists of a battery, an electric motor, a hydraulic pump and a set of valves. The actuator component has two pairs of unidirectional pull-pull hydraulic cylinders, one medial and one lateral. They provide power to rotate the ankle with the actuators integrated into an AFO structure that transfers forces to the foot and lower limb. The fluid power circuit is configured as an electrohydraulic actuator (EHA) controlled by varying the current or voltage supplied to the electric motor, which eliminates losses due to pressure drops across throttling valves. The following sections provide a detailed description of each section of the HAFO.

Electrohydraulic Power supply

The energy storage for the power supply is a 29.6V, 3300 mAh, lithium-ion polymer battery (TP3300-8SPP25, Thunder Power) that supplies the motor driver and control electronics. Lithium polymer was selected, because it is lighter (150 Wh/kg) and more compact (300 Wh/L) than other battery chemistries (section 3.2.5) [146]. The four-quadrant PWM motor driver (414533, Maxon Motors) provides 3 A of continuous and 9 A of intermittent current at 36V. A brushless DC motor (397172, Maxon Motor) drives a 3.7 to 1 gearbox connected to a hydraulic axial piston pump with a flexible coupling. The motor has a maximum angular velocity of 10,000 rpm that is limited to 7800 rpm by the voltage that can be supplied from the battery through the motor driver. The stall torque of the motor is 1.46 Nm that is limited to 0.33 Nm by the motor driver current limit. Because the demand on the power supply is cyclic with transient peaks, the motor was sized based on a heat dissipation method that used the estimated RMS of motor torque.

The Maxon motor driver was commanded in either current or velocity control mode via an analog input signal. The analog input signal is generated with an external DAC that communicates with a microcontroller using serial peripheral interface (SPI). A second serial port on the microcontroller is connected to a Bluetooth module. This allows the user of the orthosis to adjust the control and functionality of the system using a Bluetooth device like a cell phone or tablet.

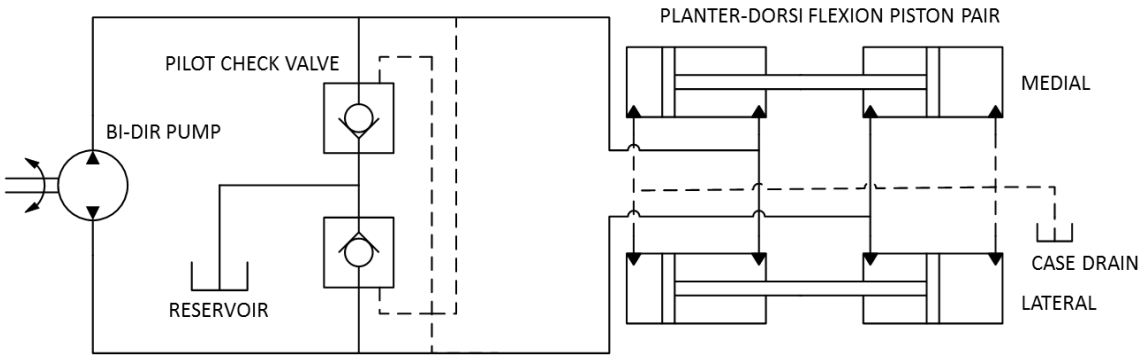

Figure 6.8 Fluid power circuit for HAFO

The miniature, fixed-displacement, axial, piston pump (TFH-040, Takako) has a fluid displacement of 0.414 cc/rev, maximum operating pressure of 138 bar (2000 psi), and maximum angular velocity of 2000 rpm. The fluid power circuit (Fig. 6.8) has two pilot operated check valves (CPRA2506005A, The Lee Company) and a reservoir. The check valves supply additional fluid from the reservoir to replace fluid lost due to leaks. The hydraulic circuit is housed in a manifold fabricated from 7075-T6 aluminum that is fixed to the axial piston pump. Ports on the manifold connect to two 3.5 mm hoses (600-03, Goodrich Fluid Transfer) that supply the hydraulic cylinders at the ankle. Mineral oil was used as the working fluid.

The components of the power supply (Fig. 6.9) are attached to a plastic housing and a cushioned belt distributes the weight of the power supply to the lower back and hips. The power supply has a plastic cover to protect the user from pinch points and provide shielding in the event of high pressure leaks.

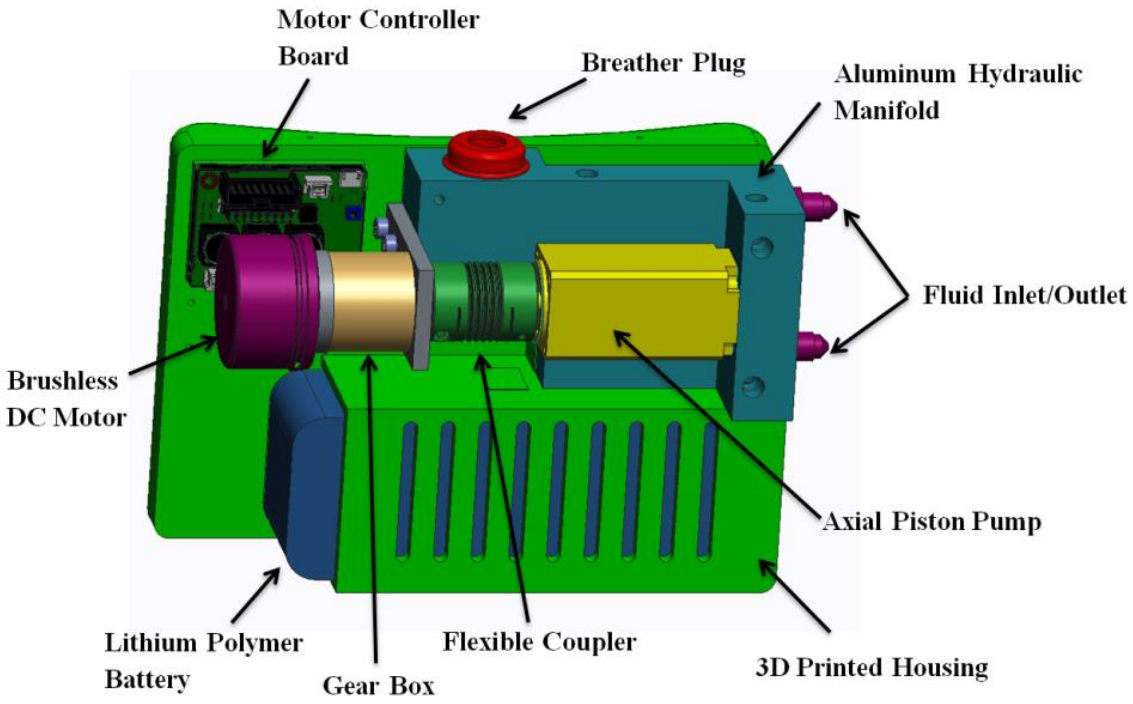

Figure 6.9 HAFO hydraulic power supply

Ankle Actuator

The ankle component of the HAFO moves the ankle through sagittal plane dorsi- and plantar flexion and contains a shin support, medial and lateral actuators, and a foot plate (Fig. 6.10). The shin support attaches to the calf and shin using Velcro straps and is fastened to aluminum bars connected with the tops of the medial and lateral actuators. The foot plate distributes the torque generated by the actuators on the shoe and the foot. The foot secured to the plate using a conventional shoe that is two sizes larger than the user's shoe size.

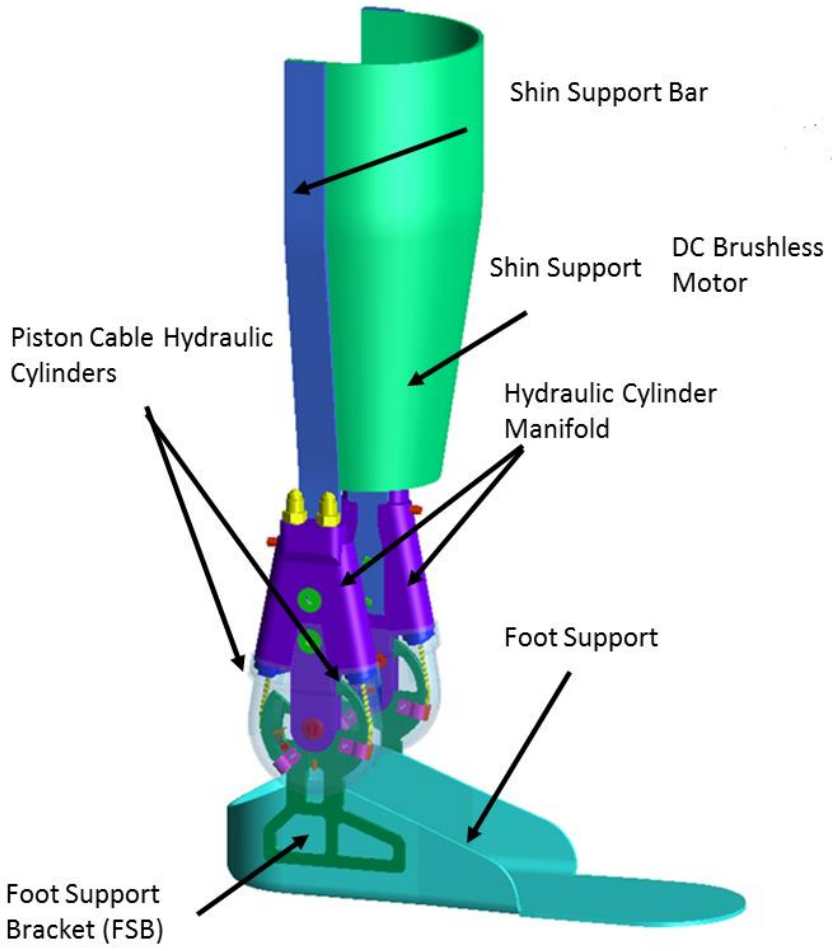

Figure 6.10 HAFO ankle actuator assembly

The medial and lateral actuators each have a pair of hydraulic cylinders that were configured to provide unidirectional force when retracting. An analysis of the actuator configuration is in appendix A.6.1. In addition, a structural analysis of the ankle actuator assembly and material selection are described in further detail in appendix A.6.2. Rather than a conventional rigid rod, each cylinder uses a 1/8 in. nylon coated stainless steel cable to transmit the force from the piston (Fig. 6.11). During the development of the orthosis initial testing on sealing high pressure fluid around the cable was performed on a separate test stand described in appendix A.6.3. This test stand was also used to measure seal friction force for use in the simulations.

The coated cable is wrapped around a pulley positioned to rotate about the ankle joint, which provides linear to rotary transmission. The cable was attached by crimping a stop sleeve to the

end and encasing it within a two piece press-fit piston to secure the cable. Nitrile rubber O-rings placed in standard-sized grooves were used to seal the piston and cable. A low viscosity epoxy was wicked into the cable using a vacuum, to form a seal that prevents oil from escaping the cylinder by traveling through the interior of the cable. To protect the cable coating from wear, an ultra-high molecular weight polyethylene bearing was included as part of the cylinder cap assembly.

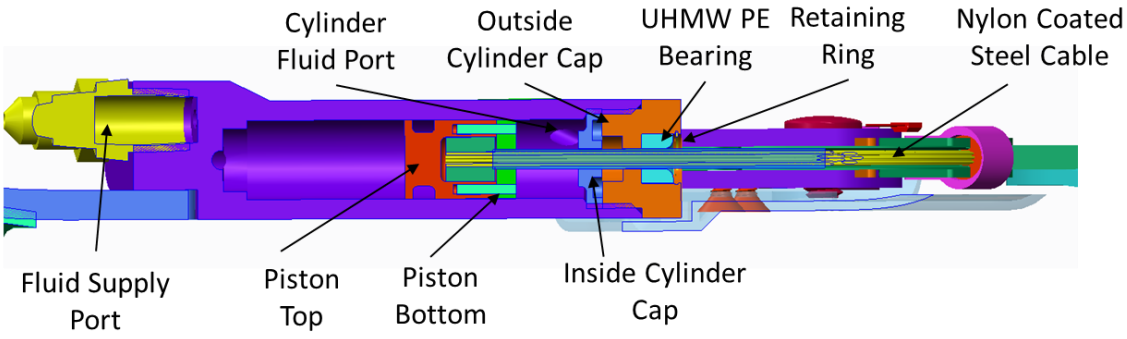

Figure 6.11 Cross-section of piston cable hydraulic cylinder

The angular position was measured with a Hall-Effect sensor (A1326LUA-T, Allergo Micro Systems) and two neodymium magnets (Fig. 6.12). The sensor signal was shifted, amplified to a 0-5V range and filtered with an analog, second order, low pass Butterworth filter with a cut-off frequency of approx. 100 Hz (Appendix A.6.4). The sensor signal is nonlinear and monotonic, so the measurement system is easily calibrated as voltage is compared with angular position.

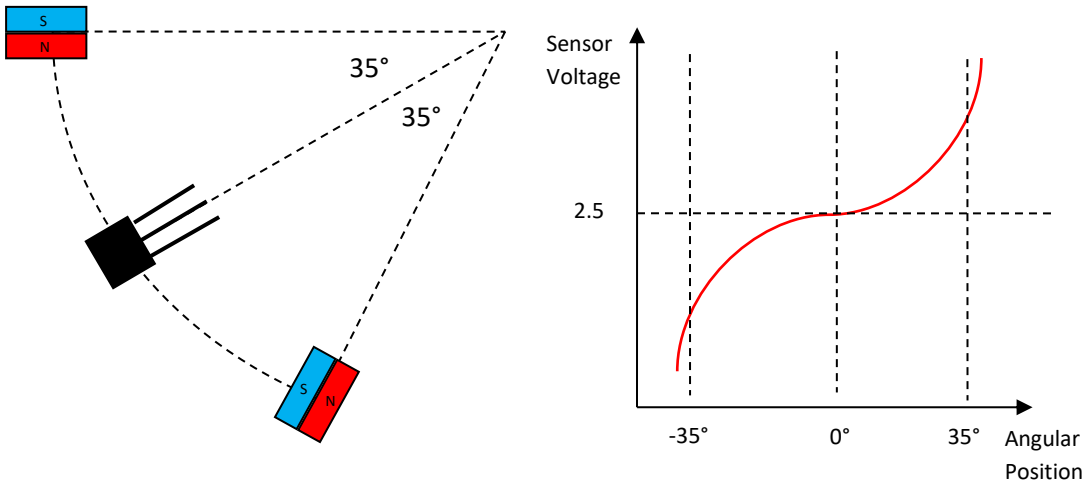

Figure 6.12 Hall-effect sensor setup (left) & example sensor output (right)

6.2.3 Evaluation Methods

Test apparatus

Two test stands were constructed to collect performance data for the HAFO, one for isometric torque and one for dynamic loading. For the dynamic loading fixture, the foot plate was replaced with a pulley installed between the actuators (Fig. 6.13). The pulley cable connected to a hanging weight, simulating a constant load torque. In the isometric torque test stand the pulley was replaced with 50 cm arm. The arm had a handle attached to it with a load cell (MLP-50, Transducer Techniques) in series. The load torque was generated by pulling and pushing on the handle. The motor input and output, angle sensor, and load cell signals were sampled at 1 KHz with a data acquisition unit (DAQ-6002, National Instruments).

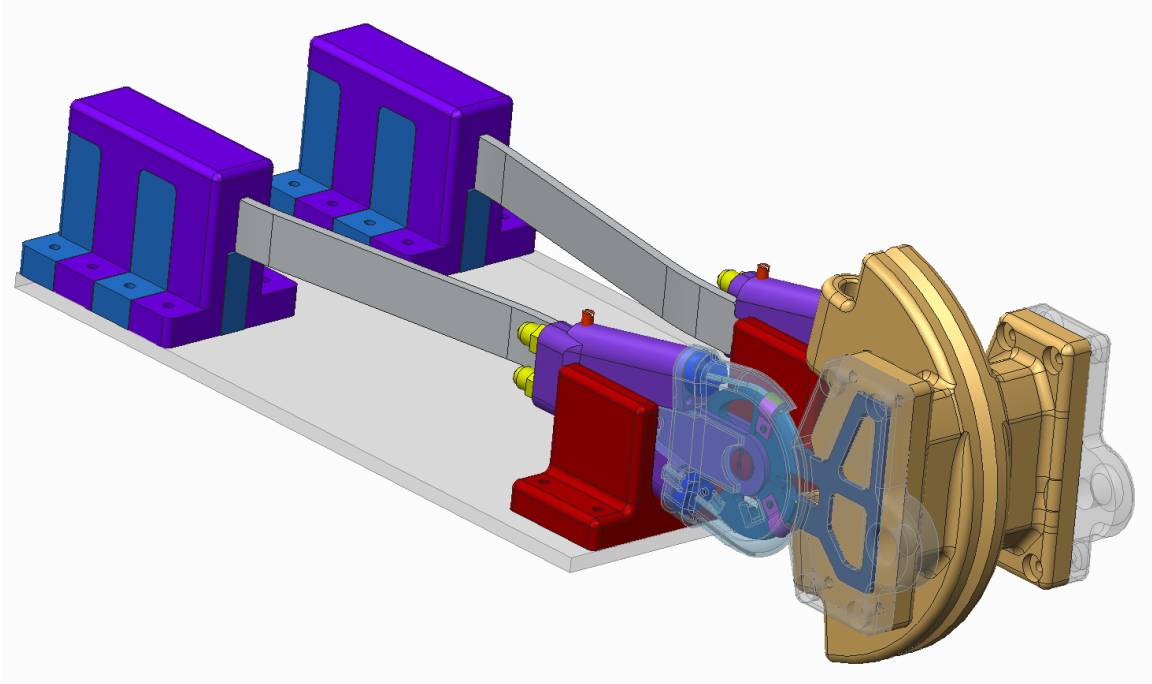

Figure 6.13 CAD model of dynamic load HAFO Test Stand

Torque & velocity measurements

This test determined the steady-state torque-velocity characteristic of the HAFO, which is needed to determine whether the HAFO can track the human gait cycle. The angular velocity of the motor was set to a maximum using the motor driver closed-loop velocity controller. The load range was varied from 0 to 65 Nm, with the upper limit dictated by the load limit of the supporting fixture. This was not a serious limitation, because the efficiency of a hydraulic system levels off at higher loadings, which means performance at loads above 65 Nm could be reasonably extrapolated from the measured data. Another testing constraint was the thermal overload limit of the motor controller that allowed performance data to be collected with high accuracy only up to 7 MPa. Above 7 MPa, the motor driver could only supply the desired current for less than 15 seconds, which decreased the accuracy and repeatability of the flow rate measurements. Still another constraint was the short travel distance of the actuator, which meant that under high velocity conditions, data could only be collected for a brief period.

Dynamic Response

This test determined the system dynamic response by performing open-loop, isometric torque step and frequency response, and open-loop, unloaded velocity frequency response. These tests can be used to determine the speed of the system, and how well the system could respond to dynamic events when under closed loop control.

The torque step response was collected using the motor driver in current control mode with input current steps of 1.31, 1.96, 2.62, and 3.27 A, which would correspond to 20, 30 40, and 50 Nm of ankle torque if it is assumed the pump, hoses and cylinders have a mechanical efficiency of 100%. The torque frequency response used a sine wave command input that resulted in a motor current amplitude of 1.96 A (corresponding to a motor torque of 72.3 mNm and an ankle torque of 30 Nm) with frequency between 0.3 and 10 Hz. The velocity frequency response was conducted with the motor driver in velocity mode. The input was sinusoidal with amplitude 3000 RPM and frequency between 0.3 and 10 Hz. During data collection, the data was collected for 10 s, and the response, which was sometimes nonlinear, was fit to a sine wave to calculate its magnitude and phase.

Efficiencies measurements

Efficiency tests of subsections and the overall system are useful for estimating how large a battery is needed for the desired run time, as well as for identifying where design optimization efforts should be directed for the next-generation device. The flow rate, pressure, and efficiency of the hydraulic power supply were tested with the supply circulating fluid from a reservoir and using an adjustable needle valve (EN10S, Deltrol Fluid Products) for loading the fluid power output. A 25 micron particle filter (9052V-10, Arrow Pneumatics) was included in the hydraulic circuit to prevent particles from contaminating the supply and causing pressure fluctuations as particles pass through the needle valve orifice. The load pressure was measured with a transducer (PX309-2K65V, Omega) that had a measurement range of 13.9 MPa (2000 psi). The average flow rate was measured by collecting fluid in a graduated cylinder over a specific time period with an accuracy of 0.41 cc/s. The input current and motor angular velocity were estimated using signals provided by the motor driver. The mechanical and volumetric efficiencies of the hydraulic power supply were calculated using eqns. (6.1) and (6.2) whose parameters are defined in Table 6.2.

Table 6.2 Variable definitions for efficiency HAFO metrics

Symbol	Description	Value	Unit	Symbol	Description	Value	Unit
A_p	Area of actuator pistons	2.375	cm^2	R_{act}	Radius of actuator pulley	3.00	cm
D_p	Pump displacement	0.414	cc/rev	R_g	Gear ratio	3.7	-
I_{motor}	Averaged motor current	Measured	A	T_{ankle}	Averaged ankle torque	Measured	Nm
K_T	Motor torque constant	36.9	mNm/ A	Δt	Time of data collection	Measured	sec
K_V	Motor velocity constant	259	RPM/ V	ΔV	Volume of fluid	Measured	cc
K	Motor velocity/torque gradient	14.3	RPM/ mNm	ω_{ankle}	Averaged ankle angular velocity	Measured	RPM
P	Pressure	Measured	Pa	ω_{motor}	Averaged motor angular velocity	Measured	RPM

$$\eta_m = \frac{D_p \cdot P}{2\pi \times 10^3 \cdot R_g \cdot K_T \cdot I_{motor}} \quad (6.1) \qquad \eta_v = \frac{60 \cdot R_g \cdot \left(\Delta V / \Delta t\right)}{D_p \cdot \omega_{motor}} \quad (6.2)$$

The system mechanical and volumetric efficiencies were calculated using eqns. (6.3) and (6.4) with the motor shaft torque and velocity as inputs and the ankle torque and velocity as outputs. The motor shaft torque was estimated from the motor current using the motor torque constant. The motor efficiency was estimated using eqn. (6.5) with parameters taken from the motor data sheet. Including motor efficiency is necessary; because while an electric motor operating at its peak efficiency point is highly efficient, efficiently drops rapidly when operating near its no-load speed or stall torque points. This will likely occur as power is supplied to the ankle between heel and toe off in the gait cycle.

$$\eta_{mech} = \left(\frac{10^3 D_p}{2\pi \cdot R_g \cdot A_p \cdot R_{act} \cdot K_T}\right)\frac{T_{ankle}}{I_{motor}} \quad (6.3) \qquad \eta_{vol} = \left(\frac{\pi \cdot R_g \cdot A_p \cdot R_{act}}{3 \cdot D_p}\right)\frac{\omega_{ankle}}{\omega_{motor}} \quad (6.4)$$

$$\eta_{motor} = \frac{K_T \cdot K_V \cdot \omega_{motor}}{\omega_{motor} + K \cdot K_T \cdot I_{motor}} \quad (6.5)$$

Closed loop position response

Closed loop proportional (P) and proportional integral (PI) position controllers were implemented using the angle sensor signal and a microcontroller with the motor driver in velocity and current modes. Controller sampling rate was 1250 Hz and control gains were set by Ziegler-Nichols tuning or by manual iteration to reach a critically damped response. Closed loop response was measured for input steps of 10, 20, 30 and 40 deg. This test was useful for determining response speed under close-loop control.

6.2.4 Dynamic performance simulations

The dynamic performance of the HAFO is simulated using the techniques discussed in chapters 2-4. The purpose of the simulations was to gather an understanding of the system performance during the design of the system. In the following sections the simulations are compared to the measured metrics as supplementary validation of the modeling techniques employed throughout this research.

6.3 Results

6.3.1 Size and Weight of the Prototype

The prototype actuator assembly and electrohydraulic power supply are shown in figs. 6.14 and 6.15. The ankle actuator weighed 0.97 kg and the power supply weighed 2.16 kg with the majority of power supply weight being the lithium polymer battery and the hydraulic manifold.

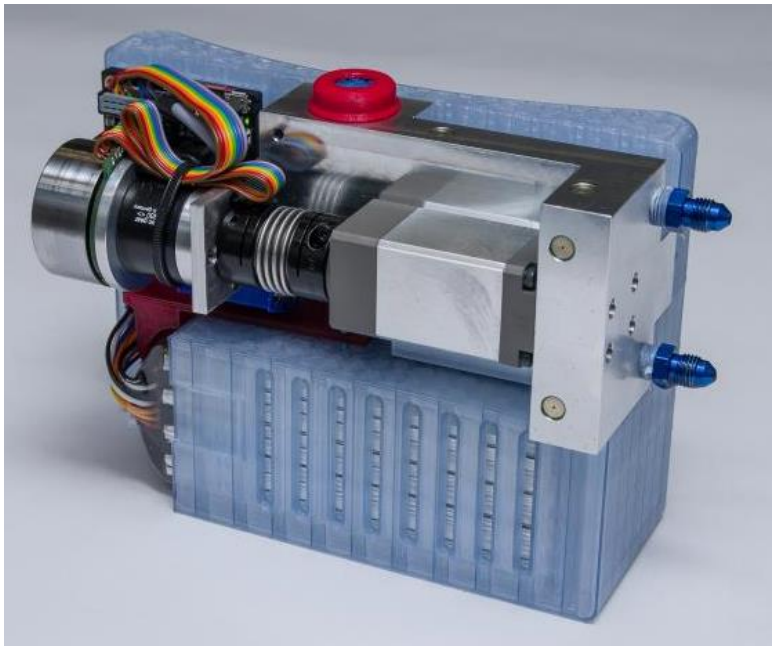

Figure 6.14 Hydraulic power supply prototype

Figure 6.15 Prototype ankle foot actuator (left) and power supply positioning on a user (right)

The total weight of the HAFO including hoses, fluid, and cushioned belt was 3.30 kg. Figure 6.16 shows the weight by component, which is useful for future design optimization.

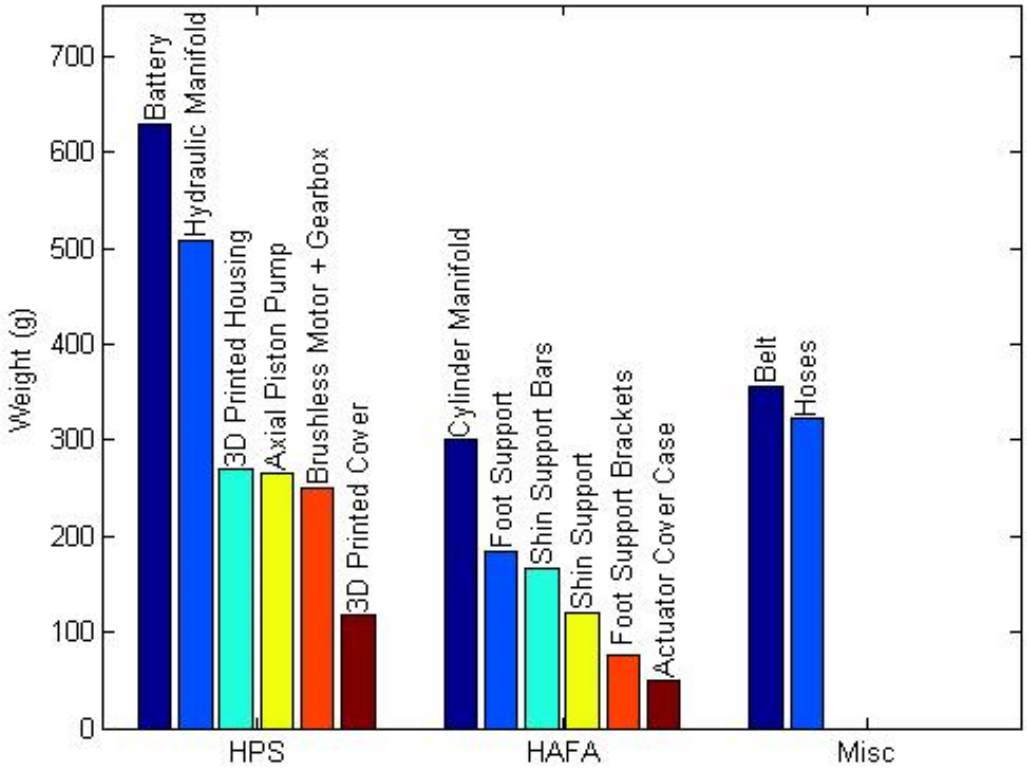

Figure 6.16 Weight distribution for system components

6.3.2 Torque-Velocity

The steady-state torque-velocity (T-V) performance for the full HAFO system and for ideal operation of the HAFO based on the motor T-V curve are in fig. 6.17 and define the key capabilities of the system. The motor T-V data was transformed to ankle torque and velocity coordinates assuming 100% mechanical and volumetric efficiencies for the pump, valves, hose and motor to enable direct examination of hydraulic system efficiencies. The dashed line is the projected performance of the HAFO past the maximum measured data point, assuming the mechanical efficiency and volumetric of the system are constant at high loads. The HAFA no-load ankle angular velocity was 105 deg/s and the maximum measured HAFA ankle torque was 65.2 Nm, which occurred at an angular velocity of 56.2 deg/s.

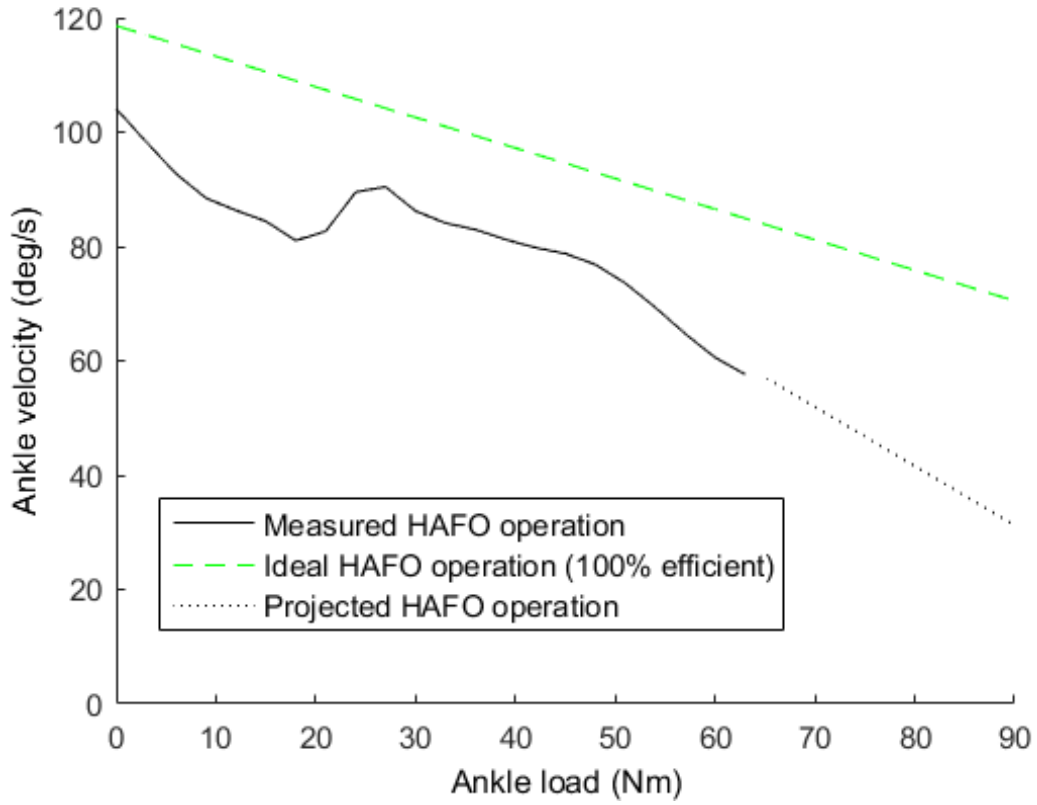

Figure 6.17 Ideal and measured torque-velocity performance

As can be seen by the overlapping T-V curves, the system torque-velocity performance is dominated by the T-V properties of the DC motor, modified by the efficiency of the hydraulic pump, which is low at low pressures [7]. In fig. 6.17 this is seen at the top left where the system T-V curve falls to the left of the motor T-V curve because of the low efficiency of the pump. For the region between 20 and 30 Nm of ankle torque, the pump is operating at higher pressures where efficiency rapidly improves, resulting in the jump in the HAFO T-V curve.

6.3.3 Open-Loop Frequency Response

Figure 6.18 illustrates the measured magnitude and phase of the motor along with the overall HAFO system for an open-loop velocity frequency response. In addition, the results include computer simulated open-loop frequency response. This test was conducted using the motor driver in open-loop velocity mode, which provides a constant voltage to the motor. The -3 dB cut-off for the measured motor and overall HAFO were both about 3.4 Hz, but the full system

had a high frequency roll-off of -97 dB/dec while the motor alone was -19 dB/dec. The faster roll-off of the complete system is due to the additional hydraulic dynamics like compressibility of the fluid. The compression and expansion of the fluid introduces a phase lag, delaying angular movement of the ankle.

In comparing the frequency responses of the simulated and measured HAFO, the computer simulation accurately predicts lower frequency dynamics with larger amounts of error as frequency is increased. This increasing error is likely the result of differences between the modeled and prototype system compliance. Small differences in the elastic expansion of hose and the percentage of air entrapped in the working fluid can have large effects on performance if the displaced fluid is small. The percentage of air trapped within the hydraulic fluid alters the bulk modulus drastically as shown in section 2.2, changing the compressibility of the fluid. At high frequencies the hydraulic system only has time to displace small amounts of fluid, exponentially increasing the influences of these system parameters. In addition, the HAFO uses long, small diameter hoses, which magnify the influence of these compliance parameters. In general, if high frequency dynamics need to be modeled for small-scale hydraulic systems, the total system compliance should be directly measured.

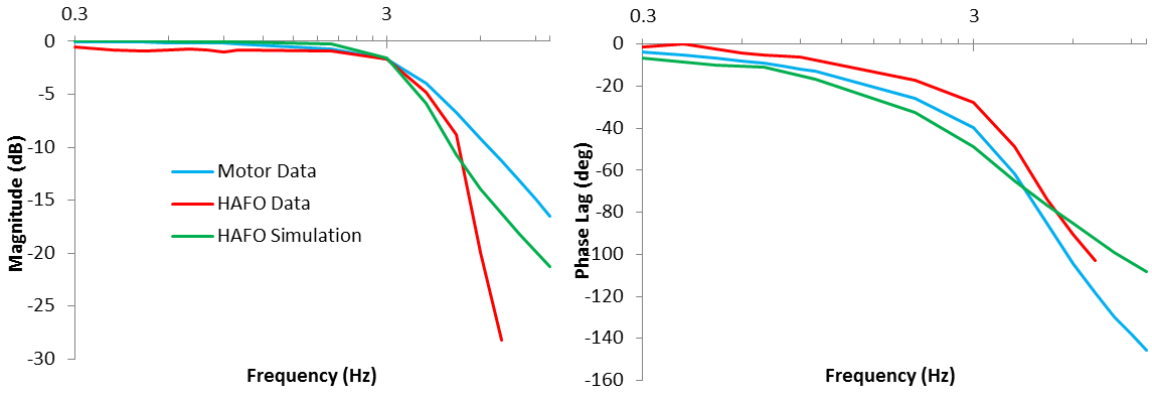

Figure 6.18 Open-loop unloaded velocity frequency response

Figure 6.19 shows the isometric torque frequency response with the motor driver in current mode. The -3 dB cut-off frequencies for the HAFO and motor were 2.2 Hz and 3.4 Hz. The high frequency roll-off for the HAFO was -109 dB/dec while the motor was -19 dB/dec. A significant

source of the additional high frequency dynamics in the overall system is the piston and valve structure of the pump, as under isometric conditions the pump turns only a small amount to compress the fluid, which magnifies the discrete nature of the pump pistons. The torque frequency response in fig. 6.19 rises above 0 dB at low frequencies. This is a resonance phenomenon caused by the inertia and compressibility of the fluid in the long transmission lines.

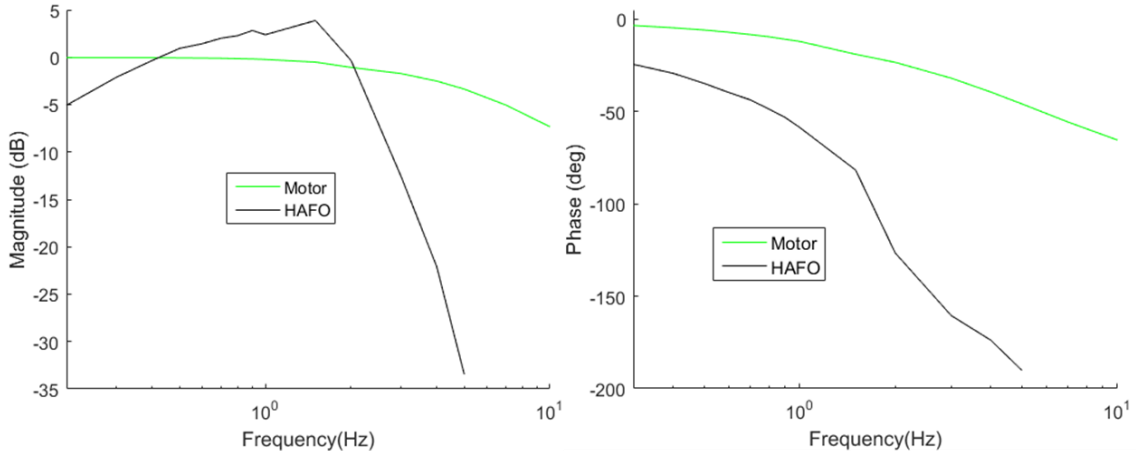

Figure 6.19 Open-loop isometric torque frequency response

6.3.4 Open-Loop Step Response

Figure 6.20 shows the isometric toque step response for the HAFO, along with the step response for just the motor. The motor torque is transformed to ankle torque coordinates assuming 100% mechanical efficiency for the hydraulic components to facilitate analysis of hydraulic losses. The pump is more efficient at high pressure, which can be seen by the gap between the motor and pump responses decreasing as the target torque and consequently the pressure increases.

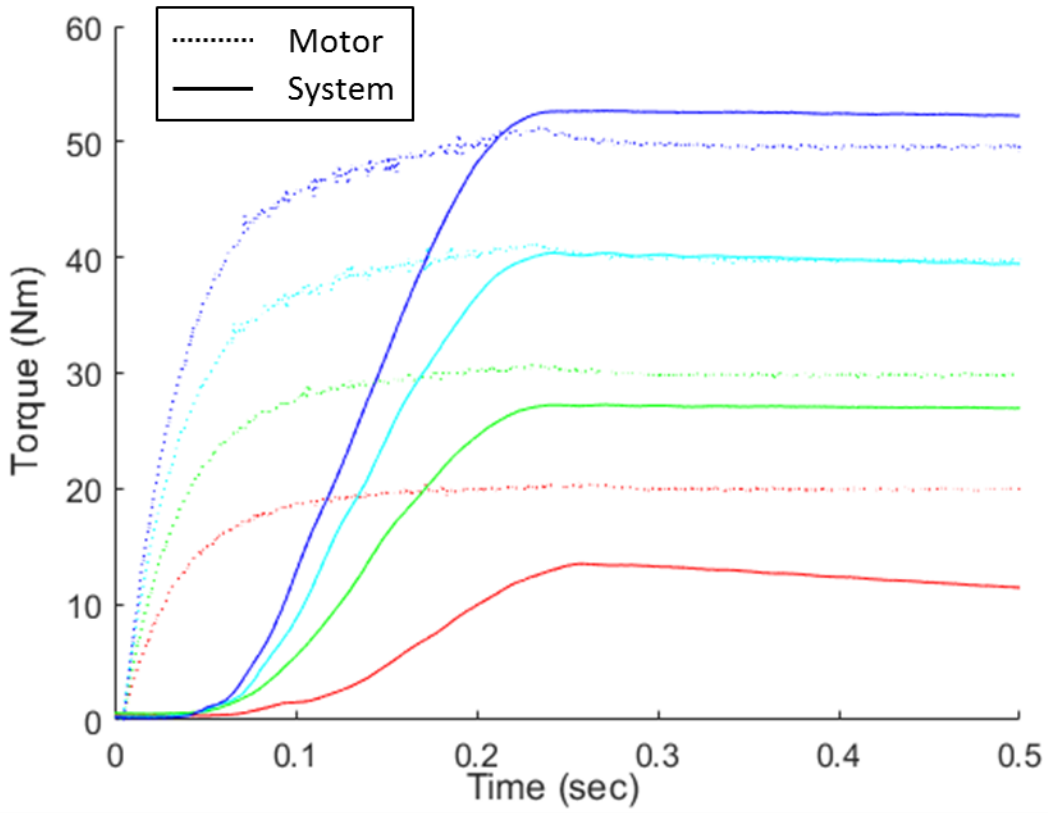

Figure 6.20 Open loop isometric torque step response for steps of 20, 30, 40, 50 Nm

The 10-90% rise time for the motor was 128 ms and for the entire HAFO was 152 ms, with rise times independent of the size of the step. The response of the HAFO lagged behind that of the motor because of the delay in building up pressurized fluid.

6.3.5 Closed-Loop Step Response

The unloaded closed-loop step response using P and PI controllers with motor driver in current control mode resulted in large steady state errors and long settling times. This is due to large amounts of static friction and nonlinear dynamics within the system. With the motor driver in velocity control mode, adequate control was achieved with a P control (Fig. 6.21). The proportional gain was selected by determining a value that made the system critically dampened. The measured response had less than 0.5 deg steady state error with no overshoot. The ankle response was slew-rate limited to 105 deg/s based on the maximum BLDC motor speed. The results illustrated a 0.5 s settling time for a 40 deg step, which can be attributed to the time required to build pressure and accelerate the inertia of the system.

The computer simulations accurately predicted the performance of the orthosis with a maximum error of 3°. The simulation demonstrated slightly longer settling times. This is likely due to an unaccounted for source of dampening within the system or a slightly lower amount of proportional gain was used in simulation.

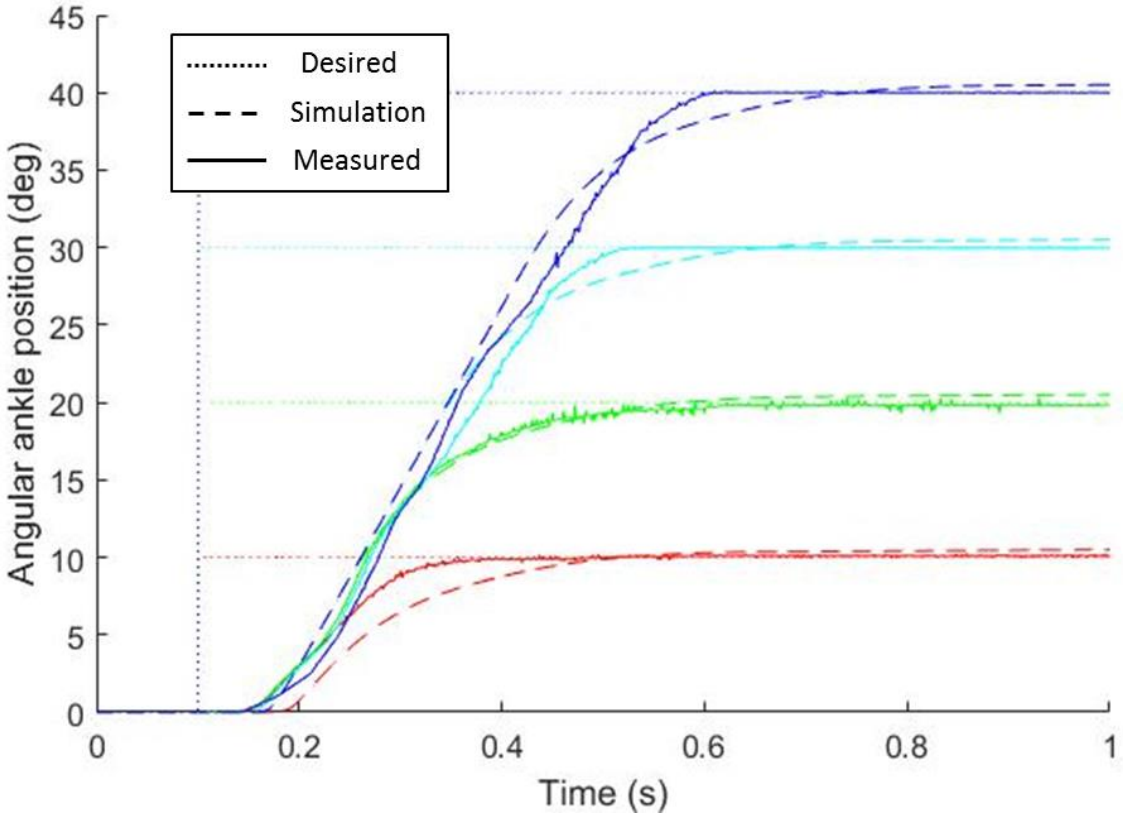

Figure 6.21 Closed-loop P control unloaded position step response

This proportional positional controller was then used to track the ankle angular position of two gait cycles in fig. 6.22. In addition, fig. 6.22 includes the computer-simulated orthosis performance using an identical controller to track the desired angular position and assuming 2.5% entrapped air in the working fluid. The simulation and measured performances illustrate similar behaviors with comparable errors and phase shifts at the same times within the gait cycle.

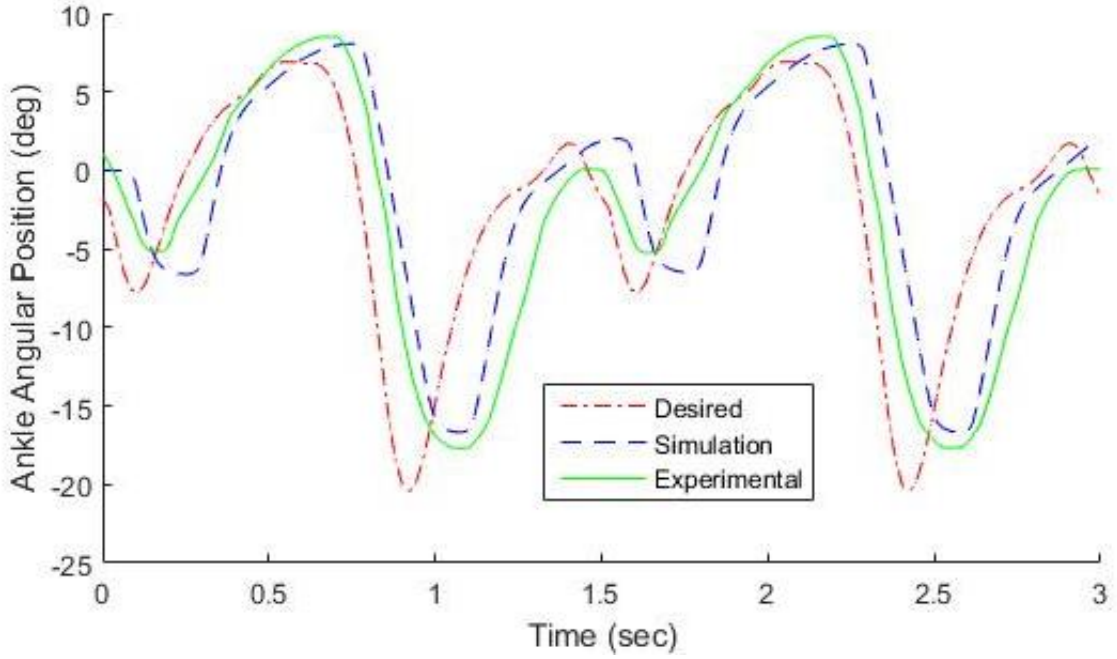

Figure 6.22 Measured and simulated HAFO tracking angular position of a gait cycle

6.3.6 Power Supply Efficiency

The mechanical efficiency of the power supply excluding the electric motor is shown in fig. 6.23 and is dominated by the efficiency of the hydraulic axial piston pump, which varies with pressure [7]. The pump is specified by the manufacturer to have an efficiency in the range of 82-85% at high pressure with efficiency rapidly decreasing as pressure decreases. The manufacturer specifies the mechanical efficiency of the gearbox to be constant at 80%. The power supply volumetric efficiency was 94-99% for the measured operating conditions, which means leakage does not play a significant role in overall efficiency at low operating pressures.

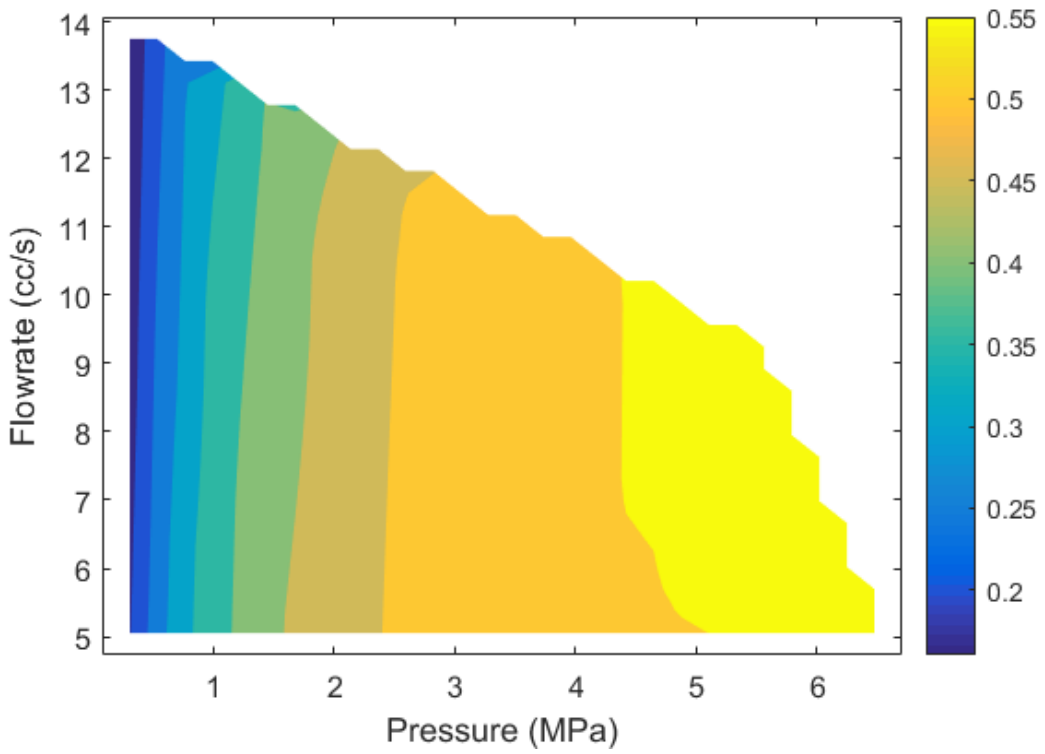

Figure 6.23 Measured mechanical efficiency of hydraulic power supply excluding electric motor

6.3.7 System Efficiency

The mechanical, volumetric, and total efficiencies of the entire HAFO system are shown in figs. 6.24 and 6.25 where fig. 6.25 excludes the electric motor efficiency. Three key features are illustrated. First, the mechanical efficiency of the axial piston pump decreases rapidly at pressures lower than 5 MPa, which explains the low mechanical system efficiency seen in the region below 10 Nm of load for all velocities. Second, the volumetric efficiency of the axial piston pump is somewhat lower at high pressures and low flow rates. The high pressure causes leakage to increase though sealing surfaces within the pump. Third, the efficiency of the brushless electric motor is low when operating close to its stall torque, which is why the total efficiency (Fig. 6.26) has a low efficiency band around the perimeter of the plot.

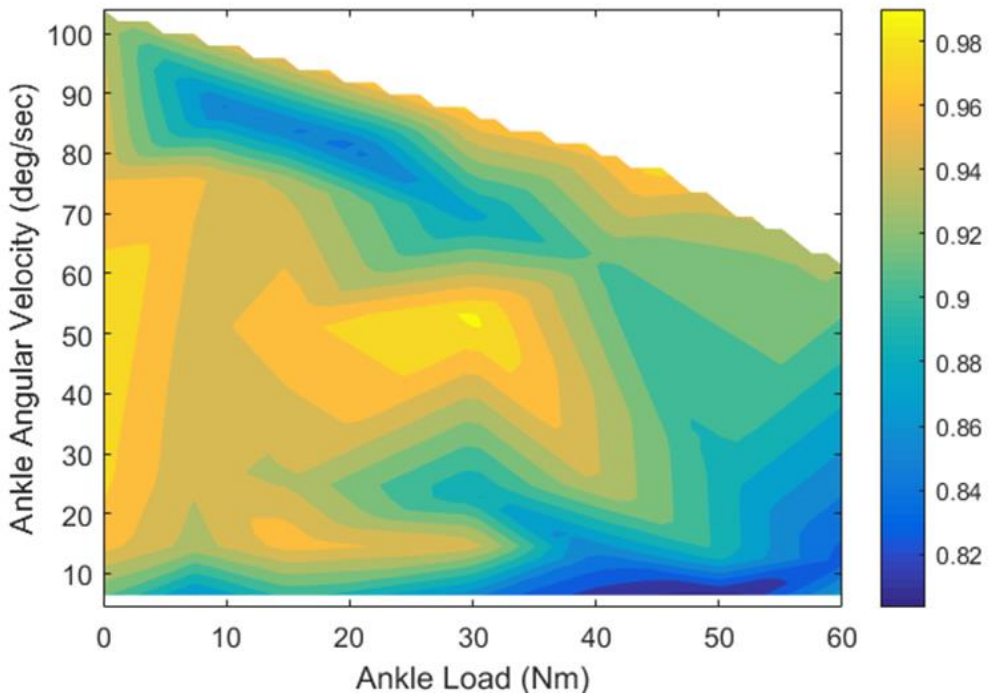

Figure 6.24 Measured system volumetric efficiency

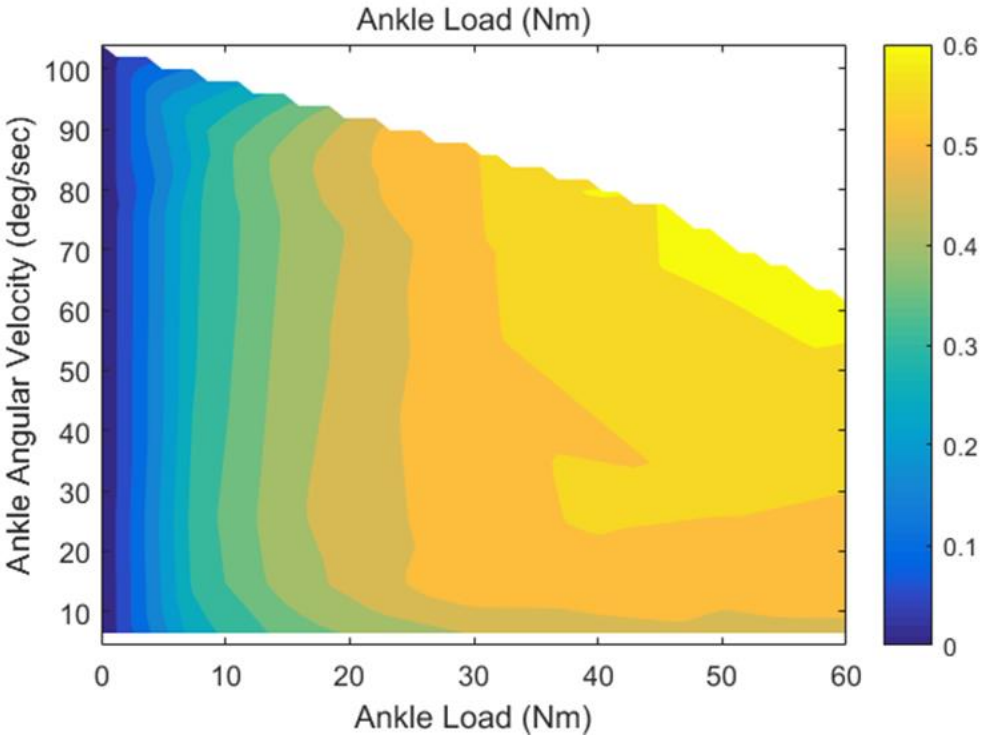

Figure 6.25 Measured system mechanical efficiency excluding electric motor

One gait cycle requires 63 J of mechanical energy at the ankle [120]. Using the system efficiency maps, we estimated that the battery specified in our design would last for about 5,600 gait cycles before needing to be recharged, just under the design target of 6,000 cycles. Additional run time can be achieved by increasing the battery capacity or by improving the system efficiency.

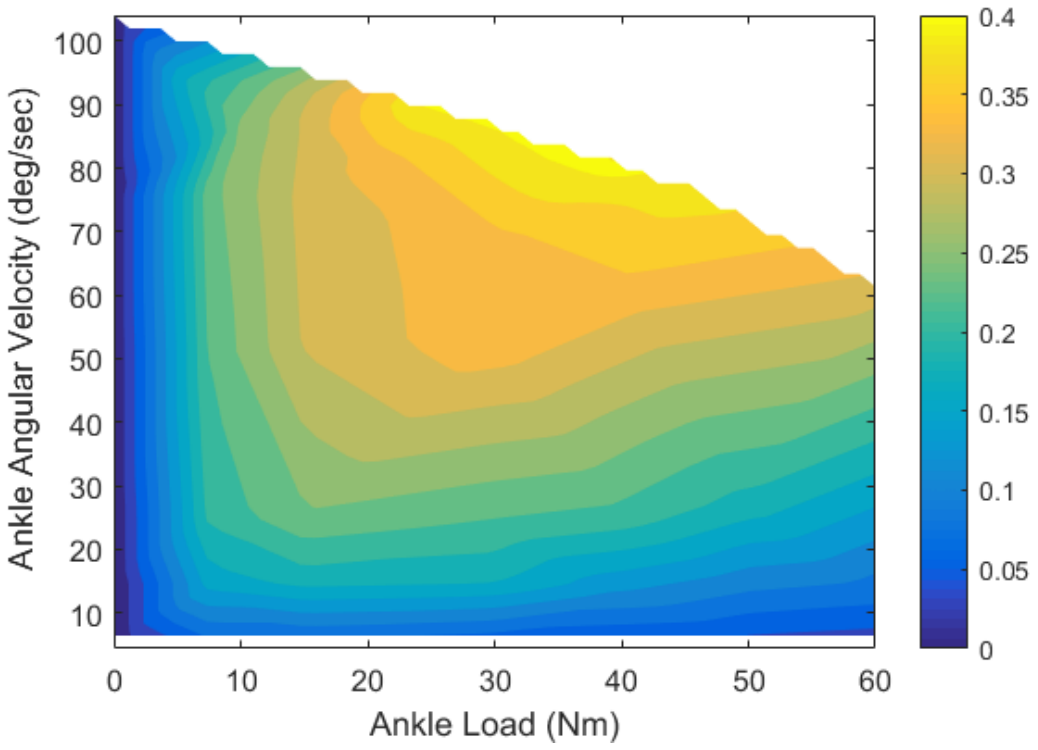

Figure 6.26 System total measured efficiency

6.4 Discussion

The weight of the ankle actuator and power supply components met the design requirements of 1.0 kg at the ankle and 3.5 kg at the waist, which affirms the benefit of hydraulic actuators. While the total system weight is the same or more than an electromechanical system, light hydraulic actuators results in the weight at the ankle being significantly lower than the electromechanical equivalent. Additional weight reductions could be achieved using additive manufacturing methods to construct, for example, the hydraulic manifold [147, 148].

The size of the ankle section of the prototype met the design requirement of fitting under loose pants, and we believe this is the first powered exoskeleton that is sufficiently small to achieve this goal. The power supply is approximately 18 x 13 x 9 cm in size. Figure 6.15 shows it positioned on the back at the waist. While this position works for walking, when sitting, the user is 9 cm away from the chair back. Other positions, including in a slim backpack are possible for the power supply.

The T-V data of the HAFO is useful for interpreting its overall performance capability. One design objective was to replicate the T-V properties of the ankle during normal walking, which would include the ability to track the ankle torque profile during a gait cycle.

Figure 6.27 is a T-V phase plot that compares the performance of the HAFO to the T-V curve for one step of an 80 kg male [120]. The figure shows that the operating range of the HAFO prototype does not reach all of the requirements for gait. During gait, up to 90 Nm of plantar flexion torque is required. The HAFO is designed and should be able to reach this torque, but our performance tests only went to 65 Nm as shown in the figure.

The speed of the HAFO with the current electric motor and controller is well under the 250 deg/s required for gait, which means the prototype would not be able to keep up with the toe-off speed spike during walking. The axial piston pump manufacture's maximum shaft angular velocity limitation has recently been increased from 2000 rpm to 5000 rpm allowing the portable hydraulic power supply to produce up to 33 cc/s. Operating the axial piston pump at these conditions requires a larger DC motor and driver, but will allow the HAFO to get up to 210 °/s. While Fig. 6.27 provides a summary of the HAFO capabilities, an experiment to measure the torque curve during a gait cycle would require an evaluation test using human participants, which was outside the scope of the present study.

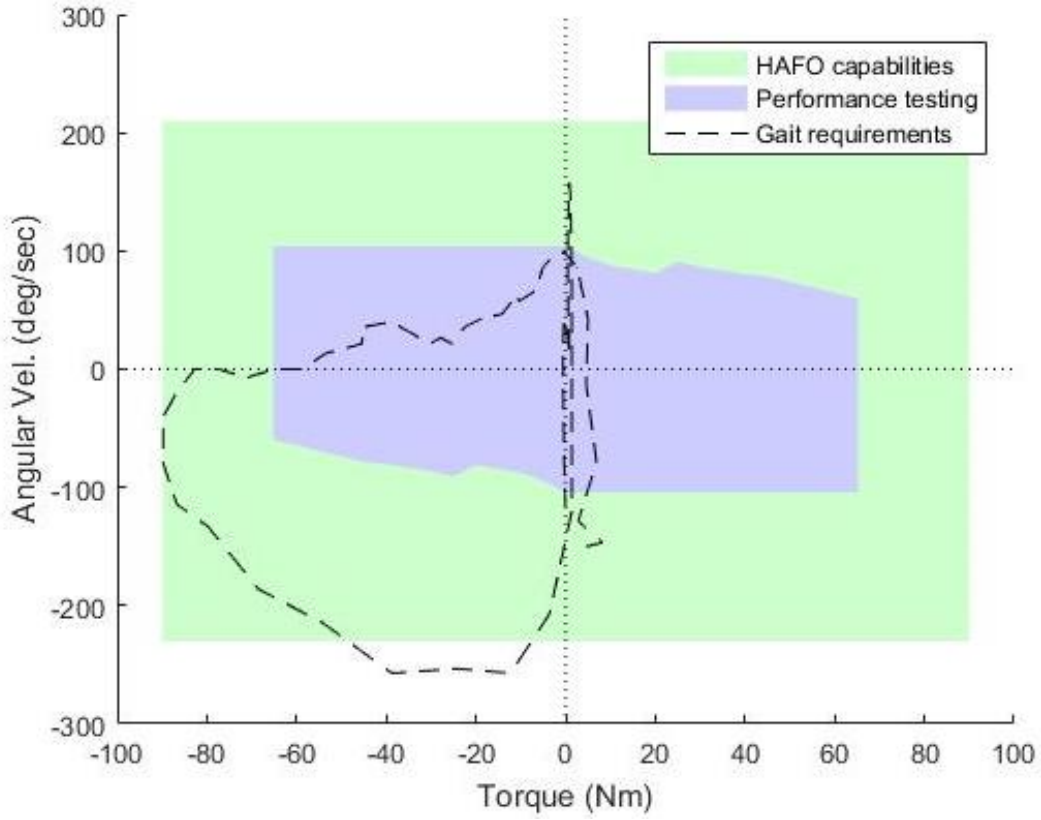

Figure 6.27 Torque-velocity of HAFO compared to torque-velocity of the gait cycle

The prototype was designed with safety in mind, recognizing that all powered exoskeletons present a risk when strong actuators are secured to or near limbs. The power supply and ankle actuator had shielding to protect the user in the event of a pin-hole hydraulic leak. Future versions of the power supply and actuator that use additive manufacturing for component integration will be even safer, as leaks in hydraulic systems tend to occur at the interfaces between components. The hoses used in the prototype are rated for a working pressure of 290 bar and a burst pressure of 870 bar, well above the 138 bar maximum pressure for the HAFO. Further, the hoses are abrasion and vibration resistant and can handle the modest bending that occurs with knee flexion. At the same time, the hoses are not so stiff that they interfere with knee flexion. Another safety consideration is if the device leaks mineral oil on the heel, which would be a slip hazard. The prototype has shown no leaks to date, but a practical device may require seal replacement after a certain number of operating cycles as a part of routine maintenance. Still another safety consideration is the lithium ion battery, which can be

hazardous if exposed to fire or if improperly recharged. When proper use is followed, however, modern batteries are a safe form of energy storage as evidenced by their pervasive use in hand-held power tools. A useful safety feature would be a battery temperature sensor, so the computer control could shut down the system if battery overheating was detected.

6.4.1 Limitations

The performance of the HAFO is limited by the choice of the axial piston pump, electric motor and motor driver. The maximum operating conditions of the current pump are 2000 RPM and 138 bar which corresponds to 111.0 deg/s and 98.2 Nm at the ankle neglecting actuator friction losses. Pump speed is limited by cavitation, and pump pressure is limited by the structural strength of pump components. To meet the full requirements of walking, the HAFO pump would need to generate 222 W of fluid power, but the current pump only generates 187 W. The next larger commercially available pump is 0.8 cc/rev and can generate 840 W of fluid power but is too heavy for our application. The solution that we are undertaking is to custom design a pump with optimal specifications for our applications. A further advantage of a custom design is that the current gearbox that is needed to match the current motor to the current pump can be eliminated, saving significant weight and increasing the power supply efficiency.

Another limitation is the motor driver that could only supply up to 9 A for short periods, corresponding to an ankle torque of 132 Nm if the HAFO had 100% mechanical efficiency. Accounting for mechanical losses caps the ankle torque at this motor current at 65.2 Nm. Using a motor driver with higher current capacity would enable the pump to output its full pressure of 138 bar, leading to an estimated ankle torque of 98.2 Nm after losses are accounted for.

Another consideration is response speed. The closed-loop P control performance (fig. 6.21) has low steady state error but is slow. This is due to the same speed limitation shown in the T-V results of Fig. 6.27, and means the current prototype cannot track a normal 1 s gait cycle. Faster response will result from the optimized pump, motor and motor driver described above. Still faster response is possible if the HAFO were controlled using a small, high-performance servo valve [7], an approach we are currently exploring, but one that comes at the expense of lower efficiency. For example, the E024 servo valve from Moog is small, weighs only 92 gm and has a 250 Hz bandwidth.

Right after heel strike, the ankle dissipates energy, which in Fig. 6.27 is shown in the top left quadrant. During this time, the HAFO is being back-driven and special care in the control must be taken to avoid low pressures and cavitation in the driving cylinder as the pump transitions to a motor. Also, the cables must be properly tensioned so that they do not collapse during this portion of the cycle.

The computer performance models were able to accurately predict low frequency behavior; however, a better measure of system compliance is needed to properly model high frequency dynamics. Fig. 6.27 illustrates a computer simulation of the HAFO undergoing an unloaded maximum velocity step response, while varying the percentage of air entrapped in the working fluid. The purpose of this simulation is to illustrate how a compliance parameter that has higher levels of uncertainty can have a significant effect on the system performance. An increase of entrapped air within the working fluid from 0.1 to 10% results in a large 50 ms delayed response.

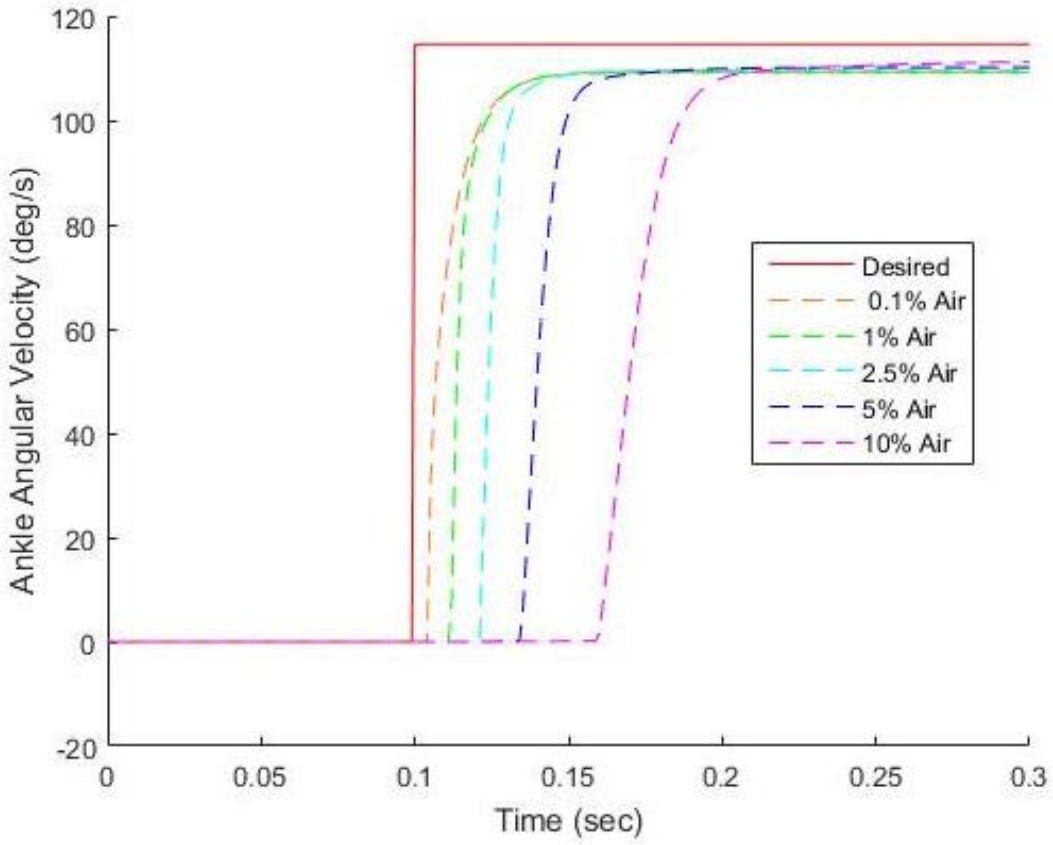

Figure 6.28 Simulated closed-loop velocity step response

6.4.2 Design Alternatives

Several design alternatives are possible for the HAFO. While stiff actuators are common in walking system for users with spinal cord injuries [149], some have explored series elastic actuators that place a spring in series with an electric motor for use in a powered ankle orthosis [131, 150], and others have used a smart passive elastic actuator [123, 124]. These devices are intended to more closely imitate the configuration of an isometric muscle plus elastic tendon [132, 151], and can be more energy efficient by storing and releasing energy during the gait cycle as well as providing an elastic response to perturbations. The current HAFO has stiff, non-back-drivable actuation, and while bandwidth-limited compliance could be achieved through control, another approach would be to add a physical compliance. Hydraulics can provide compliance through the addition of an accumulator, which may have a packaging advantage over a traditional spring. One option would be the light, compact hydraulic strain-energy

accumulator currently under development [152], with a pneumatic version having been evaluated in a pneumatic powered AFO [134].

Another design alternative to consider, which may solve the torque-speed limitations of the current HAFO prototype, would be to add a continuously variable transmission (CVT) to the system that would emulate the variable transmission of pennate biological muscle [153]. For example, others have used a modified McKibben type pneumatic actuator as a CVT for a tethered powered ankle exoskeleton [154]. The equivalent CVT for hydraulics is variable displacement pump whose transmission ratio can be changed by varying the angle of the swashplate [7]. This type of pump is heavier and more complex than the fixed displacement pump used in the prototype.

6.4.3 Potential Applications

While the purpose of this study was to create and understand a technology platform that takes advantage of the force and power density of hydraulics, it is useful to speculate on how well that technology might match particular applications. One application is assisted walking for those with mobility impairments. While the prototype was too slow to keep up with walking at normal speeds, it would be appropriate for the slower speeds that are typical when those with spinal cord injury walk using assistive exoskeletons [149, 155] .

The HAFO could also be used as a wearable robot to restore muscle strength, including motor rehabilitation following stroke, because for many robotic treatment protocols, high speed is not needed. Compared to other ankle robots for stroke rehabilitation [156, 157, 158], the HAFO ankle component is exceptionally small and light.

Still another application explored further in chapter 7 is to use the HAFO as a passive AFO emulator where the compliance of the AFO being emulated is under computer control. Here, the application is for children ages 8 to 11 with cerebral palsy. Unlike other pediatric powered AFOs [159], in this application the device must be worn while walking, which is possible with the minimal-weight hydraulic actuation approach.

6.5 Conclusions

Small-scale hydraulics is an appropriate match for light-weight, powerful, wearable, assistive exoskeletons, including the HAFO described here. The ability to separate the power supply from the actuator results in an exceptionally light-weight powered joint. The EHA configuration for the fluid power circuit is reasonably efficient, but slow. While our HAFO does not reach the peak power of the human ankle during walking, that can be solved with a custom hydraulic pump and an appropriately matched motor driver. Further, additive manufacturing can be used to reduce the size and weight of the power supply and actuator without sacrificing performance.

The modeling techniques introduced in this research have provided an accurate representation of the performance of the HAFO. The simulations provided an accurate estimation of rise time, settling time, and bandwidth of the device. The only noticeable deviations were during frequency response measurements above 20 Hz, and this is likely due to a pocket of air shifting around within the conduit causing variable compliance. The modeling techniques have proven to be essential tools in the design of small-scale hydraulic human assistive machines.

Chapter 7 Simulation Based Design of a Pediatric Ankle-Foot Orthosis

7.1 Introduction

The objective of this research in this chapter is to use the modeling techniques developed in chapters 2,3 and 4 to conduct a simulation based design of a pediatric-sized hydraulic powered ankle- foot orthosis (AFO) with computer controlled stiffness. This orthosis will be used as a prescription tool that emulates the dynamics of a passive AFO. In a clinical setting, the orthosis allows a clinician to vary ankle stiffness, while gait performance metrics are collected to determine the optimal value. This will decrease the time and required resources in the AFO prescription process while improving the healthcare of the patient.

The design and evaluation of the prototype orthosis supports that the attributes of small-scale hydraulic power align well with wearable assistive robotics. Hydraulic technology has high force and power densities compared to electromechanical systems which are essential properties in making a powered orthosis light-weight [2, 3, 80]. Electromechanical systems require the addition of heavy and bulky gear transmission to convert high velocity, low torque mechanical power generated by an electric motor, to high torque, low velocity actuation required for human joint assistance or augmentation. In contrast, hydraulic transmission only requires increasing or decreasing the surface area of the reciprocating pistons to create high torque and low velocity actuation. Hydraulic power is also easily transmitted over large distances and around irregular geometries with flexible hoses. This allows the separation of the power generation and actuators which allows the weight distribution to be optimized. The power supply can be positioned on a part of the body where there is less metabolic cost, while the light-weight hydraulic actuators can be positioned on the limbs.

Another objective of this research is to illustrate the benefits of using additive manufacturing processes in the production of orthotics and hydraulic technology. One of the design requirements is to minimize the weight of the powered AFO prototype so that it best matches current existing passive AFOs. This is accomplished by using structural finite element analysis (FEA) in combination with additive manufacturing processes (AM) to eliminate all unnecessary

material from the actuators while increasing hydraulic efficiency and improving the ability to quickly create interfaces that are optimized for the user's comfort.

7.1.1 Application

Cerebral palsy (CP) is the most prevalent severe motor disability in children [160, 161] occurring in approx. 3 out of 1000 births within the United States [161, 162, 163]. CP is a permanent neurological disorder where lesions develop on an immature brain as a result of a stroke, genetic disorder, or injury. In nearly 50% of children with cerebral palsy, the condition causes severe gait impairments requiring the prescription of a passive AFO [164]. The computer-controlled variable stiffness AFO is being designed to assist clinicians at Gillette Children's Specialty Healthcare (St. Paul) in prescribing AFOs to children with CP.

A major motivation for the development of pediatric-sized ankle-foot orthosis (AFO) with computer controlled stiffness is to reduce time and resources in the prescription process. The Center for Disease and Control (CDC) estimated the lifetime care cost of an individual with CP is a million dollars [161]. The medical costs for children with CP are 10 times higher compared to without CP or an intellectual disability [161]. The current AFO prescription process requires users to don and doff a variety of AFOs as user performance metrics like speed, step length, metabolic energetics, gait deviation index (GDI), and ankle gait variable score (GVS) are collected and compared. This process often takes multiple days and visits to the clinic. In the current prescription process, it is common for several versions of an AFO to be fabricated to test a range of stiffnesses. A computer-controlled powered orthosis has the capability to mimic the dynamics of all passive AFOs. The stiffness of the orthosis is controlled electronically, and the user never has to put on more than one orthosis. This will reduce the time and effort in the prescriptions process as, as well as decrease the labor and resources required to construct the multiple AFOs.

There are currently no standardized methods used in the AFO prescription process, leaving a clinician to use their intuition and qualitative judgements to decipher what type and properties the orthosis should have to maximize the benefits to the user. As a result, there exists variability in whether the AFO users experiences beneficial or detrimental results [165, 166]. Studies have illustrated that children with CP respond differently to identical orthoses [167, 168], and there is a need for a high degree of customization in the design and fabrication of AFOs for children with

CP. A computer-controller variable stiffness AFO will allow a more detailed study into what properties a passive AFO should have to maximize the benefits for different disabilities. This research will drive the development of more logical and quantitative AFO prescription processes. In addition, another potential application of this powered orthosis is the research of control strategies for powered ankle-foot orthotics and prosthetics.

7.1.2 Bi-articular Reciprocating Universal Compliance Estimator (BRUCE)

A state-of-the-art method for quantifying the mechanical stiffness and neutral angle of an ankle-foot orthosis is the BRUCE measurement system [169]. The BRUCE measurement device will be used to validate that the measured stiffness and neutral angle of the powered orthosis matches the desired values. The neutral angle of the AFO is defined as the ankle angular position where there is no external moment.

The BRUCE measurement system uses a manually driven linkage to replicate the motion of the human leg (fig 7.1). The positions of the joint centers are adjustable and designed to accommodate a range of AFO sizes. In order to change the foot length, the model foot must be switched out to one of six different sizes. After adjusting and securing the AFO, the manually driven linkage loads the AFO anatomically similarly to dorsiflexion and plantar flexion of the foot and shank. BRUCE is capable of measuring the ankle and metatarsal-phalangeal (MTP) joint angular positions and torques. Performance testing of the device has shown accuracy and repeatability in the ankle and MTP joint measurements [169]. A limitation of BRUCE is that it is only capable of measuring AFO stiffness during dorsiflexion and small degrees of plantar flexion. The reciprocating support arm for the shank impedes plantar flexing the shank linkage. This is less of a limitation for AFOs prescribed for CP, as most CP AFO users experience some degree of limited ankle plantar flexion.

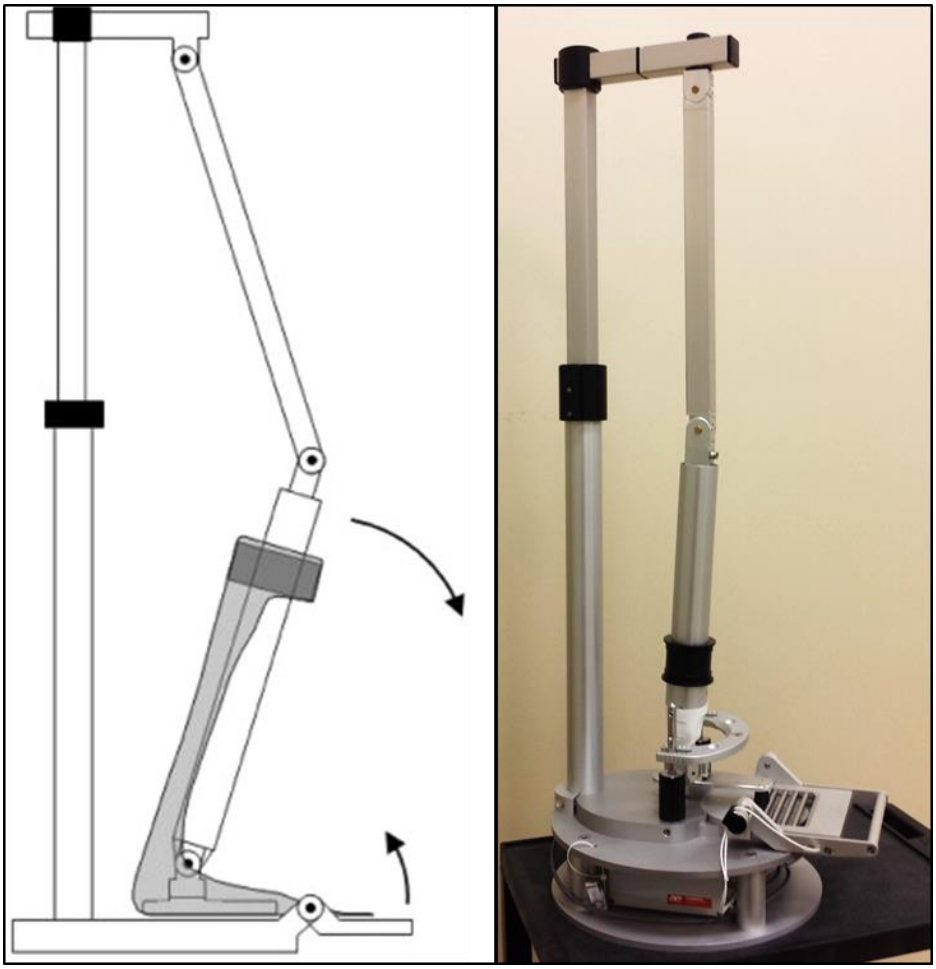

Figure 7.1 BRUCE stiffness measurement system

7.1.3 Additive manufacturing in hydraulic technology and orthosis fabrication

Additive manufacturing (AM) uses the process of dispersed-accumulated forming, taking the construction of a 3-dimensional solid and dividing the manufacturing process into a series of simpler manufacturing steps that build upon each other. All AM processes begin with a computer aided design modeling of the 3-dimensional solid. The part model is discretized in a single direction to form layers. This direction is commonly referred to as the build direction, and is typically vertical. Machine commands are generated layer by layer and passed along to the AM construction platform. These devices use a variety of technologies to assemble the 3-D solid by stacking layers of material on top of one another.

A review of state-of-the-art additive manufacturing processes

The following is a review of additive manufacturing (AM) technologies being explored for use in orthotics and hydraulic technology, because they have the ability to decrease manufacturing resources while improving performance. A more detailed review of the AM processes is given in Gibson et al [170] and Yongnian et al [171].

In liquid polymer stereolithography (SLA) droplets of a liquid are deposited on the build surface or mold and are cured using UV laser radiation or another method of solidification. There are three methods of photo-polymerization. The most common method is the use of a scanning laser in a point approach. The second method uses a Digital Micromirror Device (DMD) and a source of UV radiation to cure a surface. The third method is where curing takes place at the intersection of two scanning laser beams. The two-photon polymerization has resolution capabilities down to 100 nm for microfabrication by using precise control of the time and space of the laser energy [172]. These high accuracy AM processes are good for the fabrication of parts requiring high precision like micro fluidic pumps and valves. However, the cost of the UV curable material limits their use to low volume parts. In addition, UV curable photo polymers are low strength materials, while UV curable resins are high strength and brittle. It is optimal to have materials with high strength and ductility in high pressure hydraulic applications.

There are four methods of using discrete particles to build solid objects. In selective laser sintering (SLS), selective layer melting (SLM), and electron beam melting (EBM) a thin layer of the material particles are applied uniformly to the build surface and a laser or an electron beam in a high vacuum passes over the desired geometry providing thermal energy to sinter or melt the discrete particles together. Common materials used in SLS and SLM are metal powder, polystyrene (PS), acrylonitrile butadiene styrene (ABS), polycarbonate (PC), nylon (PA), and coated ceramic powder. The accuracy of SLS and SLM are limited due to the discrete particle size and the shifting of material in the sintering and melting processes. The fourth method known as 3-D printing (3DP) begins with a thin layer of the material particles applied to the build surface. The desired geometry is constructed by placing drops of liquid binder on top of the particle bed. 3DP can be used with any material where there exists a binding fluid. This is a common method of constructing ceramic molds where the melting temperature of material is high [170].

EBM is a AM technology that demonstrates several benefits over laser sintering and melting technologies [173]. EBM has a higher system efficiency as the electrons are emitted from high temperature filament and accelerated through an electric field to half the speed of light. In addition, the deflection and focusing of the beam is accomplished with magnetic fields, so there is a limited number of moving parts resulting in faster build speeds and lower maintenance. Finally, the melting takes place in a vacuum resulting in a material that has identical properties to the solid material eliminating impurities like oxides and nitrides. The drawbacks of this technology are the limited accuracy of ± 0.3 mm and additional equipment required to create a vacuum. EBM has been demonstrated with tool steels, low alloy steels, and titanium alloys.

In molten extrusion AM processes, the solid material is melted and placed upon the build surface in the desired geometry as the material solidifies. Fused deposition modeling (FDM) is the most common method where the melted solid is forced through precise controlled extrusion heads. In order to support structures that are free standing on the build surface, a second material is used that can be mechanically removed, chemically dissolved or thermally melted upon completion of the print.

Additive manufacturing in orthoses

There are several benefits of using additive manufacturing methods for the production of orthoses and prostheses compared to convention manufacturing methods. The fabrication of orthoses and prostheses need to be customizable to account for the user's abilities and anatomy. AM technologies have allowed a higher degree of customization and faster product development as computer aided design (CAD) software is directly integrated with computer controlled AM processes [170, 171]. Recent technological advances allow a digital model of the user's anatomy to be created with a 3D laser scanner [174, 175, 176]. An orthosis or prosthesis can be designed using the 3D digital scan as a custom template within CAD software. Finally the digital orthosis or prosthetic design can be uploaded and fabricated with an AM platform. This outline design and fabrication process has eliminating the need to construct positive and negative molds of the user's anatomy. The process has condensed the manufacturing of an orthosis and prosthetic into a single automated process as opposed to other multistep and iterative manufacturing processes that require lots of time, tooling, skilled technicians, and other resources.

The advent of AM orthosis fabrication and CAD has allowed finite element modeling FEM to further improve the mechanical performance of passive orthoses and decrease weight [175, 176, 177]. In 2008 Faustini et al [177] fabricated passive ankle-foot orthoses with glass-fiber filled nylon using SLS (fig 7.2). The mechanical performance test results illustrated that the AFO fabricated with SLS had a stiffness matching their FEM models and exhibited decreased dampening compared to a traditionally manufactured carbon fiber AFO. An analysis conducted by Schrank and Stanhope [178] determined an AFO manufactured with SLS had improved dimensional accuracy and decreased fabrication expenses compared to a traditionally manufactured AFO (fig. 7.2). An AFO orthosis in Telfer et al [179] uses gas springs to supplement torque assistance to an additively manufactured articulating AFO (fig 7.2). In 2013 Schrank et al [180] a virtual prototyping process is described in detail where CAD and FEM are utilized to predict and tune the functional characteristics of an AFO, and then the orthosis is manufactured with FDM. The prescription tool that this research aims to design and build is the key in collecting the desired functional characteristics required for such a fabrication process.

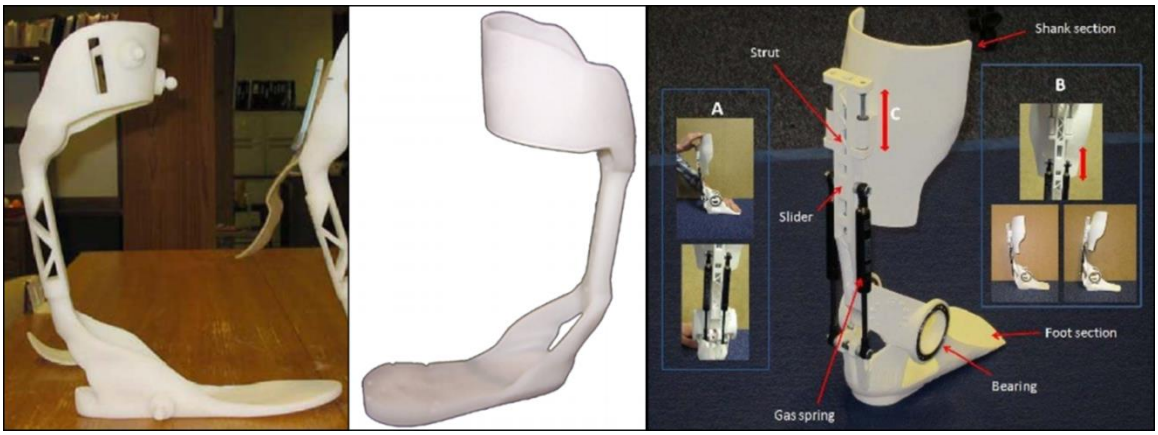

Figure 7.2 Additively manufactured orthoses [177, 178, 179]

Additive manufacturing in hydraulics

The fabrication of high pressure hydraulic components requires materials with high yield stresses and elastic moduli that can withstand the large hydrostatic and hydrodynamic forces within the conduit. This requires the use of metallic materials, which have only been demonstrated in SLS, SLM, and EBM technologies [170, 171, 181, 182].

The use of AM to fabricate hydraulic components can improve hydraulic performance by reducing pressures losses within the conduit and reduce the weight of the overall system [181]. The traditional subtractive production methods of hydraulic manifolds are limited to boring and drilling. These often result in large angles, expansions, and contractions within the conduits resulting in unnecessary pressure drops. In addition, boring and drilling limit internal conduit geometries to the intersection of two straight channels. AM processes combined with CAD allow the production of complicated geometries that can eliminate sharp angles, contraction, and expansions. In Cooper et al [181], structural, hydraulic performance, porosity, surface roughness, and hardness testing were performed on a titanium alloy hydraulic conduit manufactured with SLS. The thin wall (0.5 mm) conduit fabricated with SLS experienced no mechanical failures or leakages when operated at 25 MPa and illustrated a 250% improvement in hydraulic efficiency compared to a conduit manufactured with traditional methods.

In addition, AM allows the manufacture of internal conduits that contour around irregular shaped objects, so that the outside profile of a hydraulic manifold is more compact. Fig 7.3 illustrates a titanium hydraulic powered hand developed at Oak Ridge National Laboratories (ORNL) where the conduits and actuators are all integrated into a single structure manufactured with EBM [182, 183]. ORNL also used EBM to produce a modular hydraulic robotic arm (fig 7.3) having all the internal conduits integrated into the structure [182, 183]. The robotic arm is 60" long with 7 DOFs capable of actuating 180 degrees at each joint. The actuators are controlled with custom miniature valves that are actuated via liquid-cooled shape memory alloy (SMA).

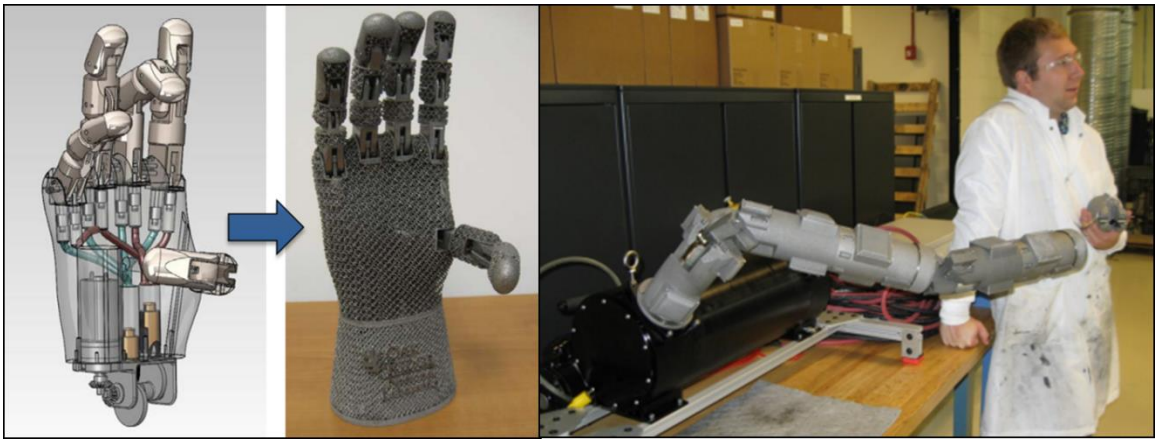

Figure 7.3 AM hydraulic titanium prosthetic hand (left), Hydraulic robotics arm (right) [182, 183]

Figure 7.4 depicts the leg of the Boston's Dynamics robot ATLAS, and a sketched design that illustrates proposed future improvements using AM [184]. The future vision using AM illustrates characteristics of human anatomy using arterial structure for cooling and internal lattices in structure members like bone tissue.

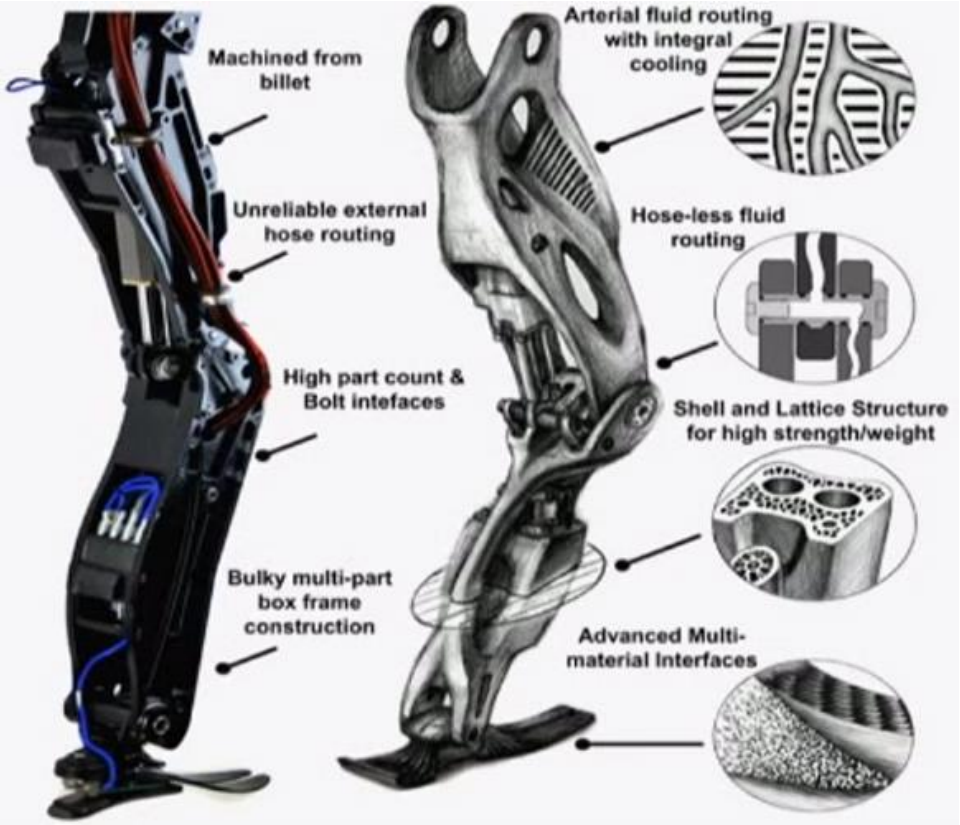

Figure 7.4 ATLAS robot current and proposed future leg design [184]

The limitations of SLS, SLM, and EBM are the laborious removal of support material, the quality of the surface finishes, and the print resolution. Finish parts are buried in a bed of metal powder. It is a tedious process to remove this powder from all internal cavities. Special precautions must be made to ensure that the part design has no sealed cavities as the support material will not be able to be removed. A high surface roughness on the internal wall of hydraulic conduits can cause a decrease in efficiency, so there is a need for further research in post surface treatments like anodizing, electro-polishing, or circulating an abrasive fluid to polish inner conduits. With surface finish and resolution being limited, hydraulic mating parts need to be post machined to create hydraulic seals around moving parts.

7.2 Methods

7.2.1 Design Requirements

The ankle-foot orthosis with computer- controlled stiffness is designed as prescription tool for children ages 8-11 with CP. For this population the active torque provided by the ankle during gait has been measured to be 1.5 Nm/kg [185, 186]. The AFO must be able to provide up to 82.5 Nm of torque assistance based on the mean body weight at age 11 with two standard deviations 40 ± 15 kg [187]. An initial study done at Gillette Children's Specialty Healthcare (GCSH) in St. Paul, MN with BRUCE determined that the majority of AFO ankle stiffnesses are within 0.5-4 Nm/deg. The maximum ankle angular velocity for children (ages 3.7 to 14.8 years) with and without CP are 120 and 200 deg/sec during gait [188]. According to the American Medical Association and the Academy of Orthopedic Surgeons, the range of motion of the ankle is 20° dorsiflexion and 45° in plantar flexion [189].

The weight placed on the ankle must be minimized to not significantly increase the metabolic energy for gait or negatively impact gait dynamics [141, 190]. The weight of a typical thermoformed plastic AFO weighs between 0.2-0.4 Kg. The weight of actuator at the ankle will be minimized to get as close to the weight range of passive AFOs as technologically possible. The anatomical dimensions of the AFO are based on initial measurements collected at GCSH of 667 subjects ages 8-11. The heel-fifth-metatarsal-head length is 13.5 ± 1.28 cm (mean ± std. dev.), foot width is 7.7 ± .8 cm, and the floor to ankle height is 5.7 ± .8 cm. The average heal to toe length is 21 ± 1.3 cm [191].

7.2.2 Design of the Pediatric Hydraulic Ankle-Foot Orthosis

The pediatric hydraulic ankle-foot orthosis (PHAFO) is composed of two piston cable actuators secured to the medial and lateral sides of the ankle along with a separate electrohydraulic power supply (EHPS). In the first generation prototype the EHPS and the control electronics are secured to a cart that can be pushed along with the AFO users. The mobile power station is supplied with electrical power from a standard wall outlet.

In the first generation of the PHAFO the piston cable actuators were fabricated using traditional machining methods. This allowed the design of the first generation to focus efforts on seal design and using finite element analysis to minimize unnecessary material. However, the

conduits are still composed of various fittings and hoses due to the limitations of current milling and turning operations. A second generation of the orthosis uses metal additive manufacturing methods, allowing the fluid conduits to be integrated into the structure of the actuator. This will allow a significantly lighter and smaller system to produce equivalent ankle torque assistance.

In addition, the second generation of the EHPS will be battery powered and fabricated using light-weight components. The controlling electronics will be integrated into a wearable package with Bluetooth communication to the clinician's laptop computer.

Design description for first generation PHAFO

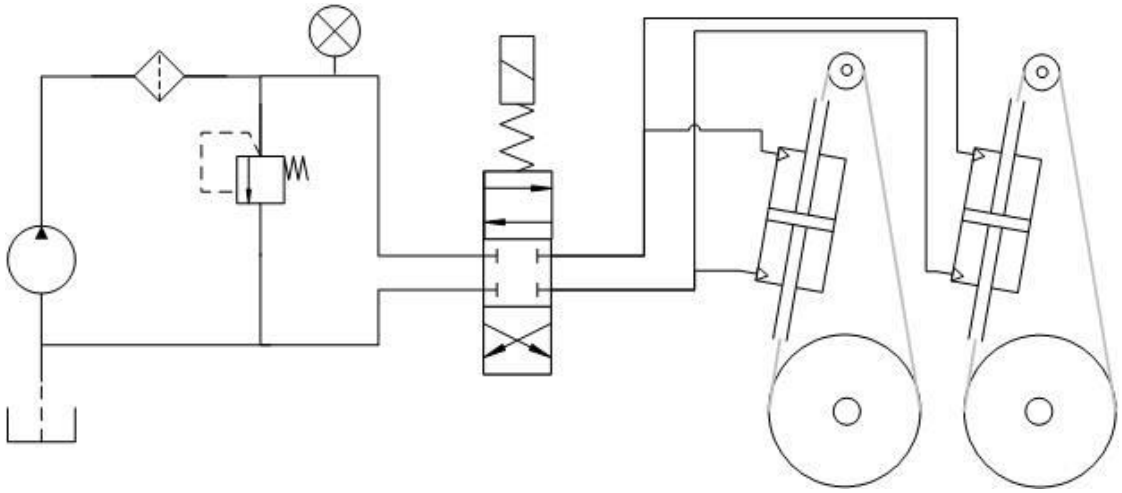

Figure 7.5 PHAFO hydraulic schematic

The PHAFO uses a servo valve hydraulic circuit with a pressure relief valve to maintain a constant pressure at the servo valve supply port (Fig. 7.5). The first generation EHPS in fig. 7.6 uses a brushed DC electro motor (PN: A40-300, AmpFlow) to drive a fixed displacement 0.8 cc/rev axial piston pump (PN: TFH-080-U-SV, Takako Industries) with a maximum operating flowrate and pressure of 40 cc/s and 21 MPa. The EHPS uses the same motor voltage controller and optical encoder discussed in section 4.2.2 to control and monitor the angular velocity of the motor.

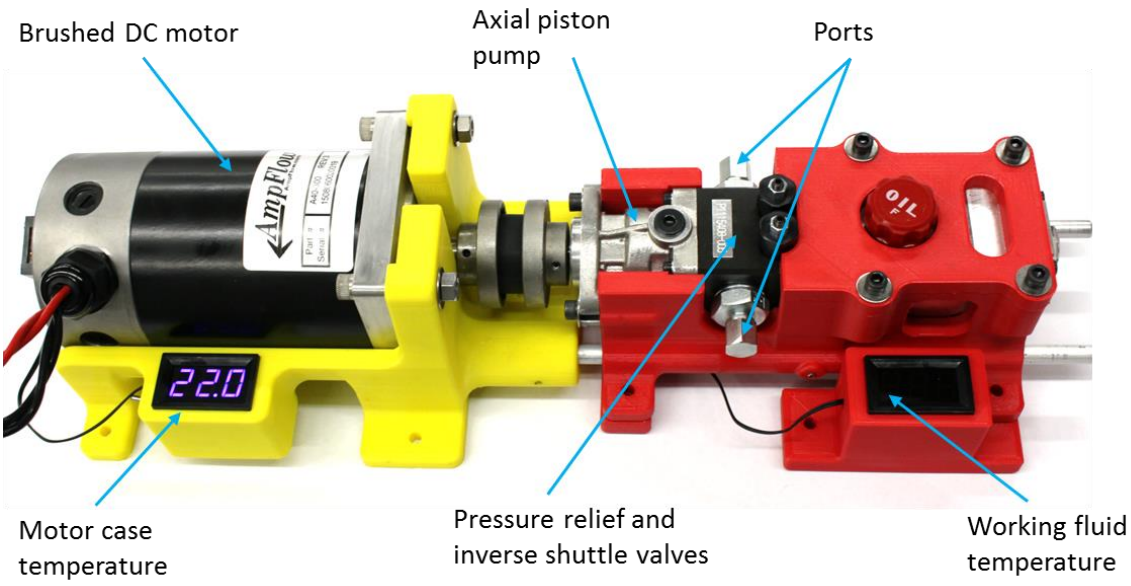

Figure 7.6 Electrohydraulic power supply (EHPS)

The EHPS is designed for intermittent operation and does not have adequate heat transfer for continuous operation; therefore, temperature monitors have been installed on the motor case and in the reservoir to ensure that the motor winding and working fluid are operated at safe temperatures. There is a significant amount of heat generated as high pressure fluid is dumped across the pressure relief valve when the actuator is at rest. In order for continuous operation, a heat exchanger is used to draw heat from the working fluid. A second option explored in testing is the use of proportional pressure control to minimize the energy dissipated across the relief valve allowing continuous operation of the EHPS.

The hydraulic actuators at the ankle are controlled with a flow control servo valve (E024-Q38H21YGA15VAR2Y, Moog) with a maximum rated flow of 63.3 cc/s and a response time less than 1.8 ms. The A relief valve was installed with a cracking pressure of 14 MPa to protect the pump and servo valve from large pressure fluctuations.

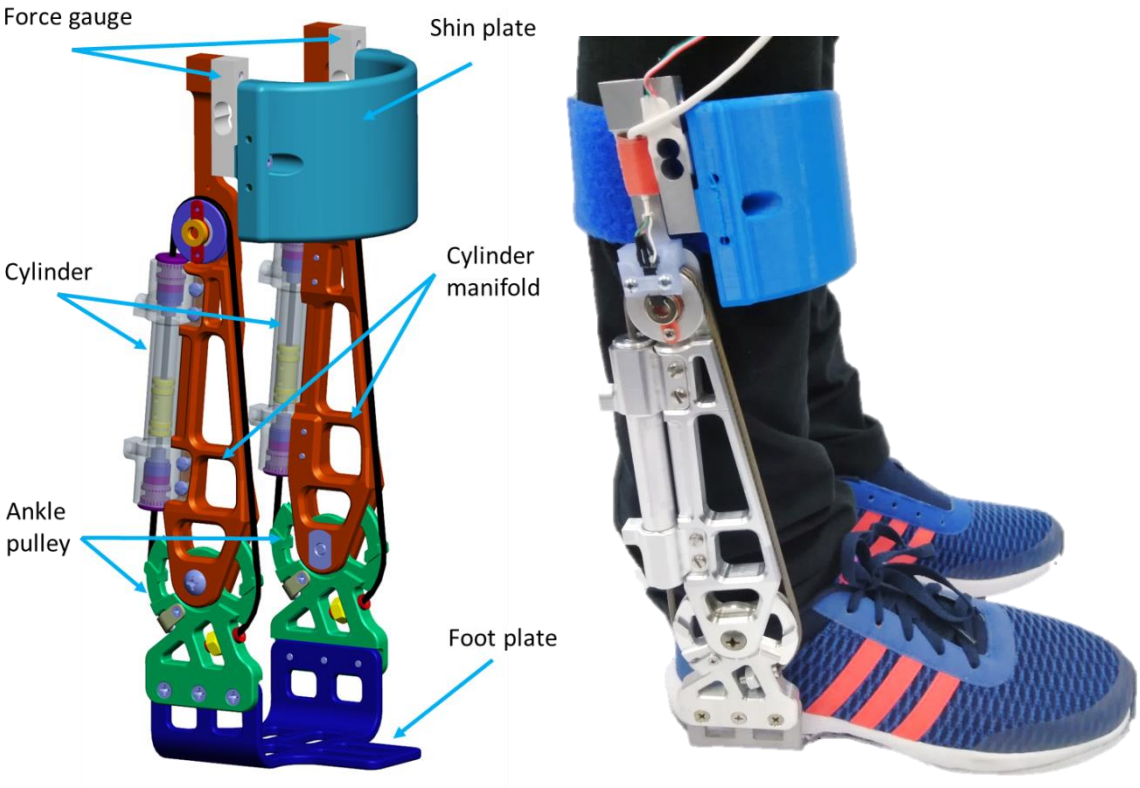

Figure 7.7 PHAFO CAD model (Left) and PHAFO prototype right

The ankle actuator is composed of a shin plate that is secured to the user's ankle with Velcro straps, two piston cable actuators on the medial and lateral sides of the ankle, and a foot plate that is secured into the sole of a user's shoe (Fig. 7.7). The piston cable actuators are composed of three main assemblies: the cylinder manifold, the piston-cable cylinder, and the ankle pulley. Each piece has undergone FEA to eliminate unnecessary material and are machined of high strength 7075 aluminum. The cable is routed in an elliptical path and is secured on both sides of the ankle pulley (Fig. 7.8). One side of the cable is attached to a threaded stop sleeve, allowing the cable to be pretensioned. The cylinders are designed to be removable from the manifold to allow for leak testing and performance testing on separate testing apparatuses.

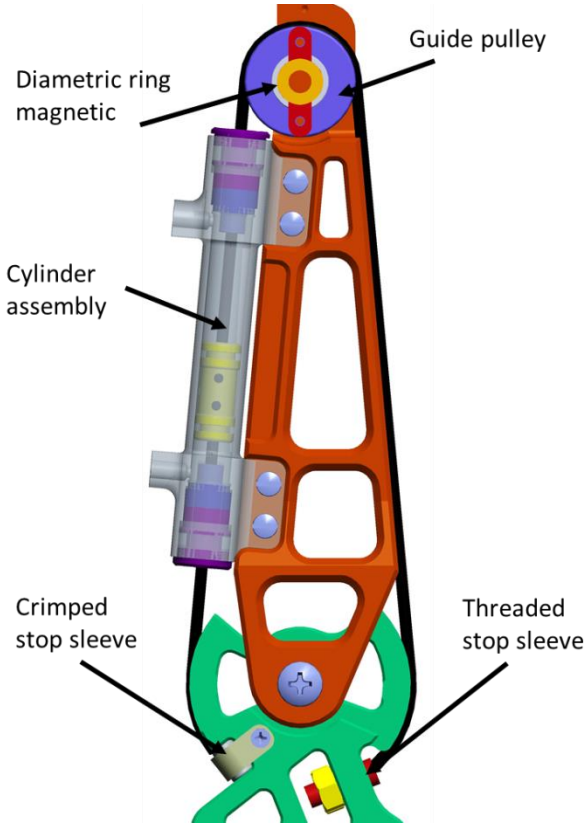

Figure 7.8 Elliptical cable routing on ankle actuator

The ankle torque transmitted to the AFO is measured by bilateral loads cells that connect the shin plate to the actuator manifold. The ankle angular position is measured by a magnetic angle sensor module (KMA210, NXP Semiconductors) in conjunction with a diametric ring magnetic placed on the cable pulley. In initial testing, the torque was estimated using a force balance across the piston by measuring the fluid pressure on both sides. The pressure difference was a good estimator of torque under dynamic conditions where the seal friction and viscous losses can be calculated. However, the controller cannot determine the magnitude and direction of the static seal friction when the piston is static. This causes a blackout region within the control that is proportional in size to the amount of static friction. In high pressure hydraulic systems the static friction is typically high, and therefore pressure cannot be used as an estimate of how much tension is on the cable attached to the piston. The electrical design of the sensors and control electronics are illustrated in appendix A.7.1. All control and sensor signals have first order low pass filters with a cut-off frequency of 159 Hz to reduce noise.

Figure 7.9 PHAFO foot plate

The PHAFO interfaces to the front of the user's shin as Velcro straps wrap around the back of the calf. The shin plate is composed of ABS and fabricated using FDM. This allows the shin plate to be easily customized to the user's needs and fabricated quickly out of inexpensive materials. In addition, the internal lattice structure allows designers to decrease the weight while maintaining the necessary strength. The PHAFO interfaces with the foot by directly connecting to an aluminum foot plate built into the sole of a shoe (Fig. 7.9). After experiments with different foot plates, users found wearing their own shoes was significantly more comfortable than inserting the AFO directly into the shoes as with traditional AFOs. Since a shoe needs to be able to flex at the metatarsal-phalangeal joint, the aluminum foot plate only extends across the dorsal half of the sole. The aluminum foot plate is covered with thermoformed co-polymer polypropylene that extends throughout the entire sole to better transmit some of the AFO torque to the forefoot and ground during ankle plantar flexion.

Figure 7.10 Prototype miniature piston cable hydraulic cylinders

The miniature piston cable hydraulic cylinders machined out of high strength 7075 aluminum are illustrated in fig. 7.10. The cylinders have a bore size of 11.1 mm (0.437 in) and a stroke length of 36.8 mm (1.45 in).

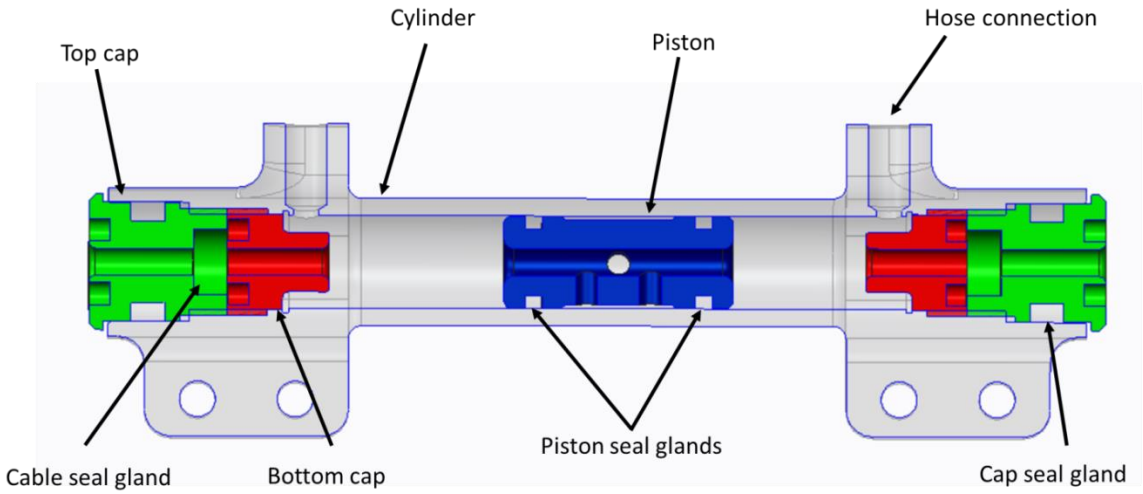

Figure 7.11 Cross-section of miniature piston cable hydraulic cylinder

Quad seals (4104366Y, 4110366Y, 4011366Y, MN Rubber) are used for the cable, cap, and piston seals, and are rated to approximately 14 MPa with the current clearances between mating surfaces (Fig. 7.11). PTFE backup rings are also used on the cap and cable seals to prevent seal extrusion at higher pressures. The cable seal is housed in a two-piece cap design similar to HAFO design in chapter 6. The piston is secured to the cable with the use of three set screws that are orientated 90° to each other. The set screws must contact the woven stainless steel strands to achieve adequate strength, so the nylon coating must be removed within the piston. This method of securing the piston to the cable was bench tested with loads up to 1800 N. When operated at 14 MPa, the two actuators are capable of producing 74.6 Nm of ankle torque assistance or resistance.

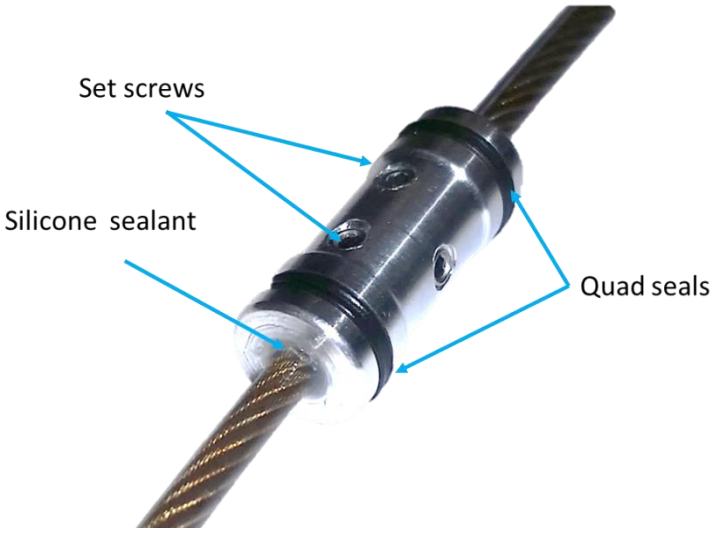

Figure 7.12 Piston cable interface

The removal of the cable coating allows pressurized fluid to travel within the nylon coating of the cable and out of the cylinder. In order to prevent this unwanted leakage, a small ring of silicone sealant (1363118, Loctite) is added where the cable enters the piston. The silicone sealant should have similar mechanical properties to nylon and bond readily with nylon and aluminum. A small groove must be machined into the surface of the piston to allow the sealant to create a flush surface (Fig. 7.12). Without this groove, the repeated bottoming of the piston will destroy the seal as the sealant impacts the caps.

Control methods

The spring stiffness control structure uses admittance control. Admittance control requires a force input with a proportional position output, while impedance control uses a position input with a force output. Since admittance control measures force, this control strategy is limited in the ability to measure low force and stiffness systems like free space but is good at measuring high force resistance systems like springs [192]. Hydraulic systems are mechanically stiff systems and are not easily back-driven [193]. It would be difficult for a user to generate enough force to move the piston within the cylinders any measureable distance. Admittance control is implemented by dividing the torque measured using the load cells attached to the shin plate by the digital spring constant to determine the desired angular position. Proportional, integral,

derivative (PID) positional control is used to control the servo valve to match the AFO measured angular position with the desired angular position.

In an effort to reduce energy consumption, efficiency results were compared using constant and variable motor voltage. This is identical to the simulated proportional pressure control in section 4.3.4. The principle of varying the motor voltage is to reduce the flow dissipated over the relief valve while still maintaining a high supply pressure at the servo valve. The hydraulic power supply generates hydraulic power proportional to the actuator power requirements.

In simulation, this was accomplished by setting a desired system pressure and comparing it against the measured system pressure to get an error signal. In the simulations, the hydraulic power provided by the pump is uniform in pressure and flow rate for a given input torque and angular velocity. In reality, the discrete events of the pistons within the pump create fluctuations in pressure and flow rate causing a significant amount of variability in the measurements. This is more prevalent at slow angular velocities and low flow rates. When this was implemented on the test bench, the level of proportional gain required to get the system pressure to track the desired system pressure caused system instability. The source of the system instability is the presence of measured pressure fluctuations caused from discrete pump events.

A different observer of the required hydraulic energy needed to be used, since measurements of system pressure contained too many fluctuations without the addition of hydraulic dampening. If it is assumed the system pressure is maintained relatively constant, then the flow rate through the valve is proportional to the valve signal plus a constant to account for pilot flow. The flow rate error signal is calculated by comparing this against the flow provided by the pump while accounting for volumetric efficiency. An additional constant is added for a buffer between the estimates of generated and required flow. Proportional flow rate control of the EHPS is defined by eq. 7.1.

Table 7.1 Variable definitions for EHPS control

Symbol	Description	Units	Symbol	Description	Units
D_p	Pump displacement	cc/rev	Q_{pilot}	Pilot flow rate constant	cc/s
e(s)	Flow rate error signal	cc/s	$x_v(s)$	Valve signal	mA
K_V	Valve flow rate constant	cc/s/mA	η_v	Pump volumetric efficiency	-
Q_{buff}	Pilot flow rate constant	cc/s	ω(s)	Measured motor angular velocity	rev/min

$$e(s) = \left(K_v x_v(s) + Q_{pilot}\right) - \frac{D_p \eta_v}{60}\omega(s) + Q_{buff} \quad (7.1)$$

Preliminary design for second generation, additively manufactured PHAFO

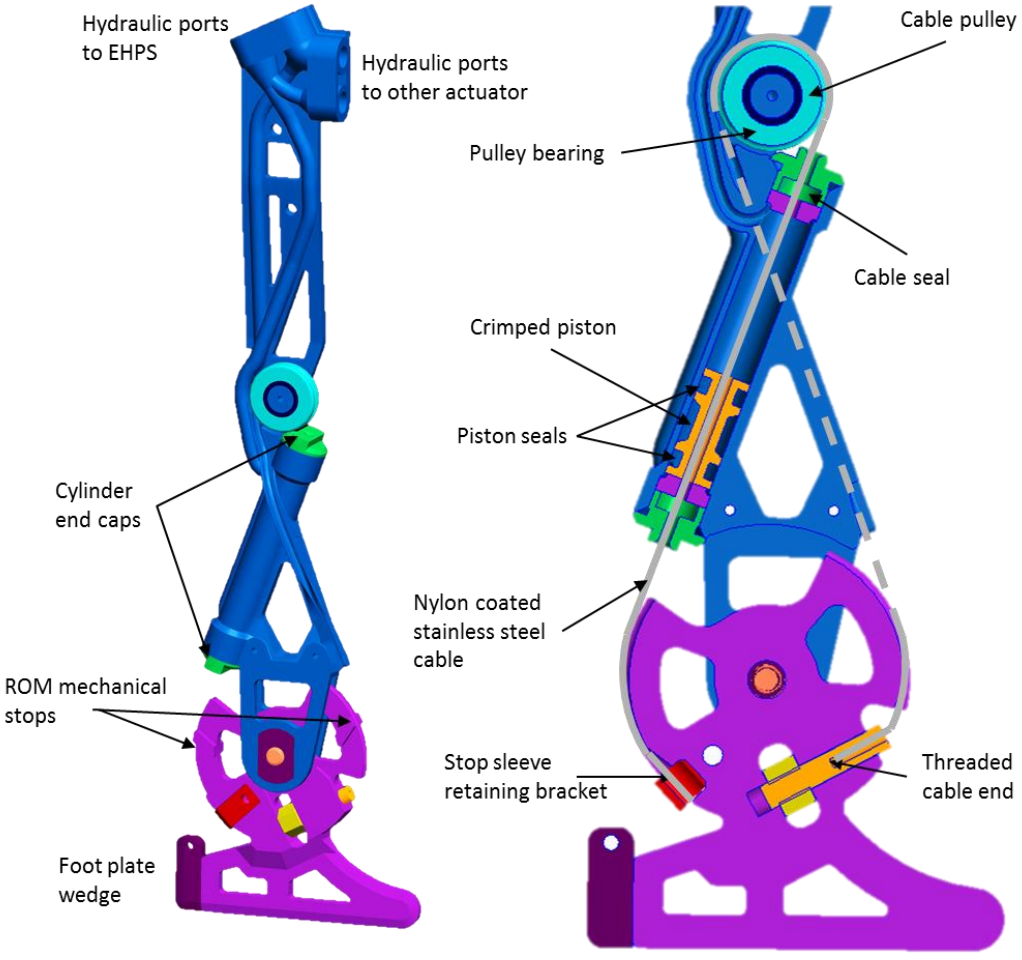

Figure 7.13 Second generation additively manufactured PHAFO actuators

There are four major variations between the first and second generations of the actuator design. First, the cylinder is not designed to be removable. This allowed easier seal and cylinder testing in the first generation at the cost of additional weight. Second, in order to decrease the size of the actuator, the cable is routed in a figure 8 geometry. This geometry allows easier access to the cylinder cap near the pulley. Third, the use of AM allows the hydraulic conduits to be routed through the connecting structure reducing hose length and weight. Finally, the actuator is designed to operate up to 21 MPa instead of 14 MPa to allow reduced cylinder size.

Each actuator assembly (fig. 7.13) uses a bidirectional, 10.3 mm diameter hydraulic cylinder capable of generating 1640 N at 3000 psi and assuming no pressure losses. The hydraulic cylinder piston is secured to 1.98 mm diameter nylon coated cable by crimping the material in the middle of the piston to a portion of the cable where the coating has been removed. The other ends of the cable are secured to the ankle bracket with a crimped on stop sleeve and threaded end. The thread end can be used to remove slack and pretension the cable. The piston uses two balanced O-ring seals, while the cable uses a PolyPak (461512500093, Parker Hannifin Corporation) capable of sealing a reciprocating surface up to 5000 psi. The ankle bracket incorporates a 3 cm moment arm transferring the linear cable force into a total of 99.6 Nm of torque.

The cylinder manifold and ankle bracket will be fabricated with a state-of-the-art Arcam EMB machine and composed of a titanium alloy (Ti6Al4V) to maximize the strength to weight ratio of the structure. This also allows the fluid conduits to be built into the structural support of the orthosis to further decrease the weight. The ankle angular position will be monitored with a reflective encoder on the hydraulic manifold, while the reflective disc is secured to the ankle bracket.

7.2.3 PHAFO performance simulations

The same techniques that were employed in chapter 2, 3, and 4 for simulating small-scale hydraulic systems were used to simulate the performance of the proposed PHAFO design. The input to the system is a variable torque input at the ankle, while the output is the PHAFO repositioning to the appropriate angular position. The simulation frequency is 10 kHz, while the controller frequency is 2 kHz. A proportional position controller was used to track the desired

position. The proportional gain was selected by determining the value that critically dampened the system for a 50° step input.

7.2.4 PHAFO test stand

Figure 7.14 shows the test stand that was used to collect performance data on the PHAFO system as well as tune the stiffness control algorithms. The test stand secures the two PHAFO cylinders in parallel. The cables on one side of cylinders are attached to a load pulley that includes a variety of transmission ratios with the largest being a 4 to 1. In order to prevent the cables from kinking inside the cylinders on the unloaded side, these cables are secure to a small weight to keep them in tension.

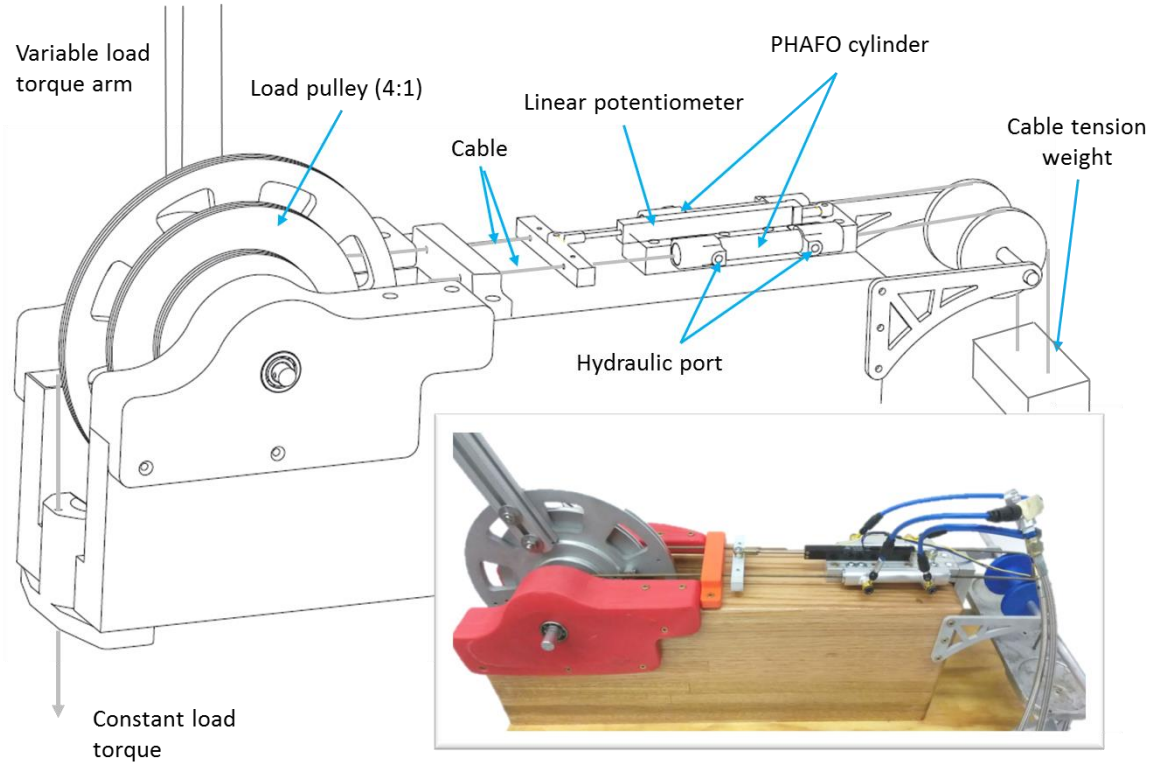

Figure 7.14 PHAFO test stand

The pulley is loaded with a constant torque by hanging a weight off the pulley. The pulley also has a 50 cm arm secured to it. A handle with a force gauge built into it is attached to the end of the arm and can measure variable human induced loading. The linear position and velocity of the piston are measured with a linear potentiometer. Finally, the system pressure and both

cylinder chamber pressures are measured with the use of analog pressure transducers connected to the supply lines.

7.3 Results

7.3.1 Simulated PHAFO performance

In order to ensure that the current orthosis design would have the capabilities to emulate passive AFOs worn by children with CP, the performance of the PHAFO was simulated and compared against data collected at GCSH of CP AFO users. AFO stiffness measurements were collected with BRUCE measurement apparatus discussed in section 7.1.2. In addition, measurements of the user's ankle angular position while walking with the AFO were acquired with a 3D motion capture environment. All the passive AFOs tested were fabricated from vacuum thermoforming co-polymer polypropylene sheets. This material yields at 23.4 MPa and has a tensile modulus of elasticity of 1.05 GPa. Additional data sets of ankle stiffness and ankle angular position are illustrated in appendix A.7.2. A low, medium, and high stiffness were selected to compare against simulated PHAFO performance.

The desired AFO angular position is the measured ankle angular position using the motion capture system while the patient is wearing the passive AFO. The desired AFO angular position in the first data set illustrates an AFO user that is only capable of passive ankle dorsiflexion (fig. 7.15). This means that they are not actively using their muscles to actuate the ankle through dorsiflexion or plantar flexion, but the weight of their body and orientation of the shank dorsiflexes the ankle a small amount. The BRUCE stiffness data illustrated a significant amount of non-linear behavior and hysteresis. The non-linear behavior is likely the result of plastic deformation of the AFO material, as the side flanges of the AFO buckle at large deflections from the neutral angle. This results in linear behavior with small deflections around the neutral angle, gradually switching to nonlinear behavior with less torque needed for deflection. The hysteresis illustrates that the AFO does not behave completely like a spring in that the torque is not only dependent on a difference in angular position from the neutral angle but also the current angular position.

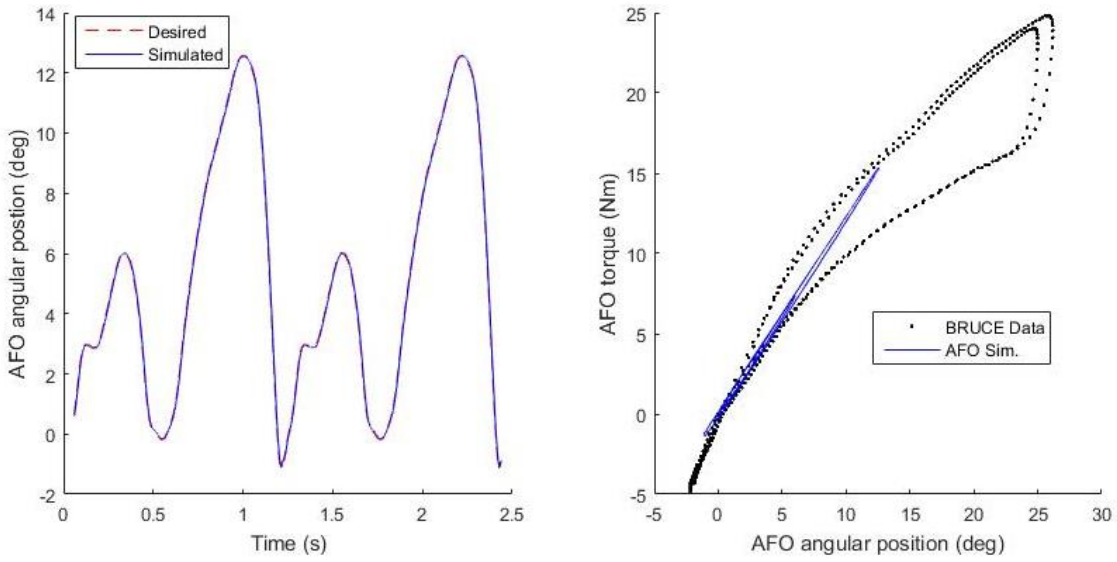

Figure 7.15 Comparison of measured and simulated data for a low stiffness AFO

The BRUCE data acquisition software calculated a linear AFO stiffness of 0.83 Nm/° for the entire 28°manual input stroke. The motion capture angular position data shows the AFO user dorsiflexing the ankle 12° and plantar flexing 1° from the neutral angle. A new line with a stiffness of 1.22 Nm/° is fit to the BRUCE data that accounts for the range of motion of the AFO user. The simulated AFO angular position of the PHAFO matches the desired within 1% error while maintaining spring dynamics with K = 1.22 Nm/°.

The computer simulations provide an estimate of ideal system performance, as there is no noise built into the system measurements of torque and angular position. It is difficult to estimate the noise in measurement signals without taking into account electromagnetic interfaces within the surroundings and within the electrical systems. With no noise in the simulated measurement signals, the control gains can be made artificially high allowing for better control tracking in simulation than reality.

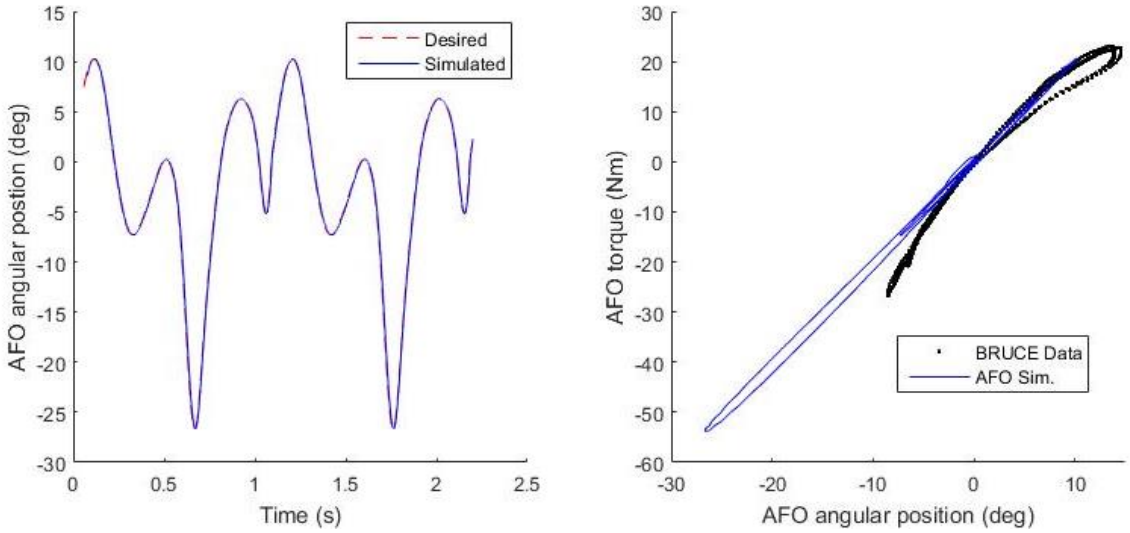

Figure 7.16 Comparison of measured and simulated data for medium stiffness AFO

Figure 7.16 illustrates a medium stiffness AFO user capable of actively plantar flexing and dorsiflexing the AFO. As a result of BRUCE's limited plantar flexion AFO stiffness measurements, the mechanical behavior of the AFO was assumed to be the same in plantar flexion as it was in dorsiflexion. The measured AFO stiffness was 2.02 Nm/°. In general, the AFO illustrated more linear behavior and less hysteresis the higher the stiffness. This is most likely attributed to less material reaching the yielding point and absorbing energy during testing. The simulated PHAFO angular position traces the desired within 2% error. The simulated performance demonstrated a small amount of hysteresis.

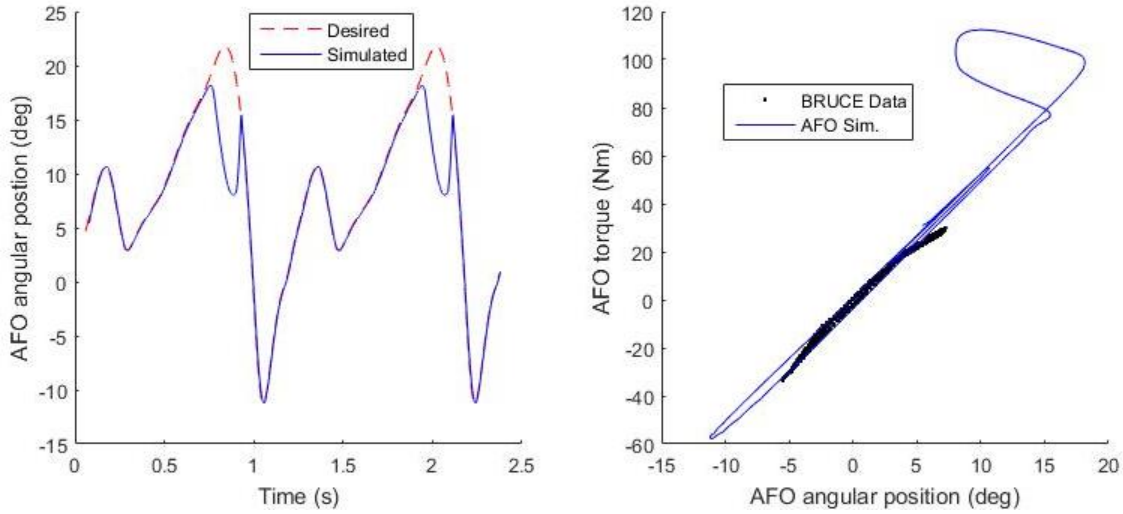

Figure 7.17 High stiffness PHAFO

Figure 7.17 illustrates a high stiffness AFO user that is capable of generating a large amount of ankle torque in plantar and dorsiflexion. The high stiffness AFO demonstrates linear and low hysteresis behavior with a linear fitted stiffness of 5.16 Nm/°. In the simulation the PHAFO is forced to depart from linear behavior around 76 Nm as the user torque exerted on the AFO surpasses the torque generated by the hydraulic actuators.

Figure 7.18 illustrates the maximum angular defection of the PHAFO as a function of the simulated spring constant. The governing relation is a torque balance between hydraulic actuator and the virtual rotary spring. The shaded region of fig. 7.18 represents the operational range of the PHAFO, while dots represent specific operating conditions of the three passive AFO's described. The user of the high stiffness AFO (3) exerts 112 Nm on the AFO, while the PHAFO hydraulic actuators are capable of generating a maximum of 74.6 Nm assuming no conduit, valve, or actuator losses.

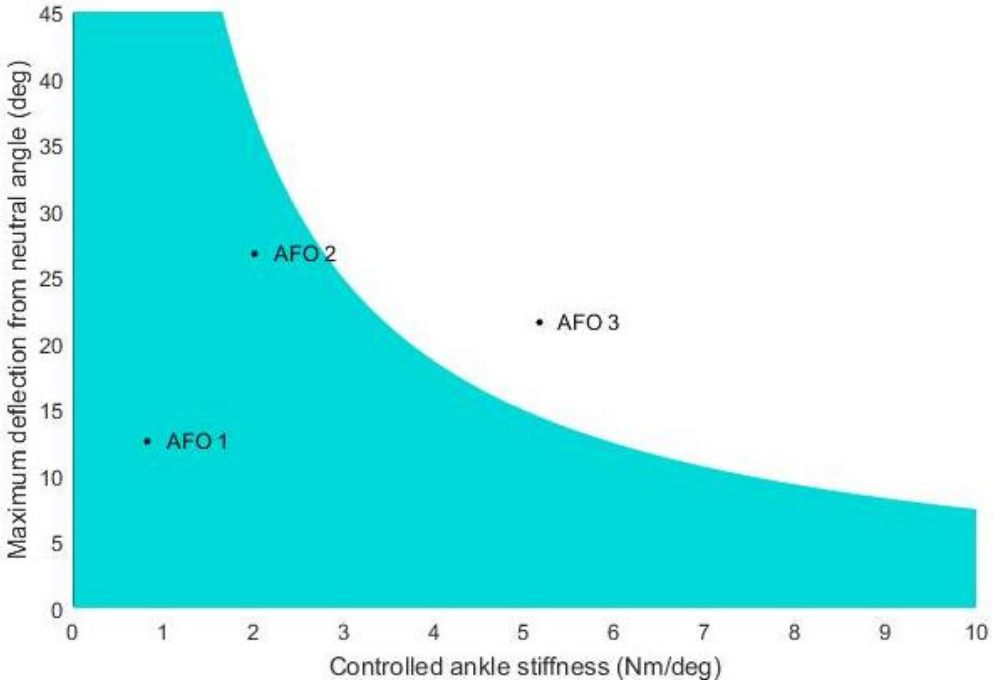

Figure 7.18 Deflection limitations as a function of controlled stiffness

Active assistance mode

The PHAFO was developed to emulate the dynamics of traditional passive AFOs. However, the system can be switched to an active assistance mode to provide powered gait assistance. Figure A.32 is a simulation of using the PHAFO in the active assistance mode.

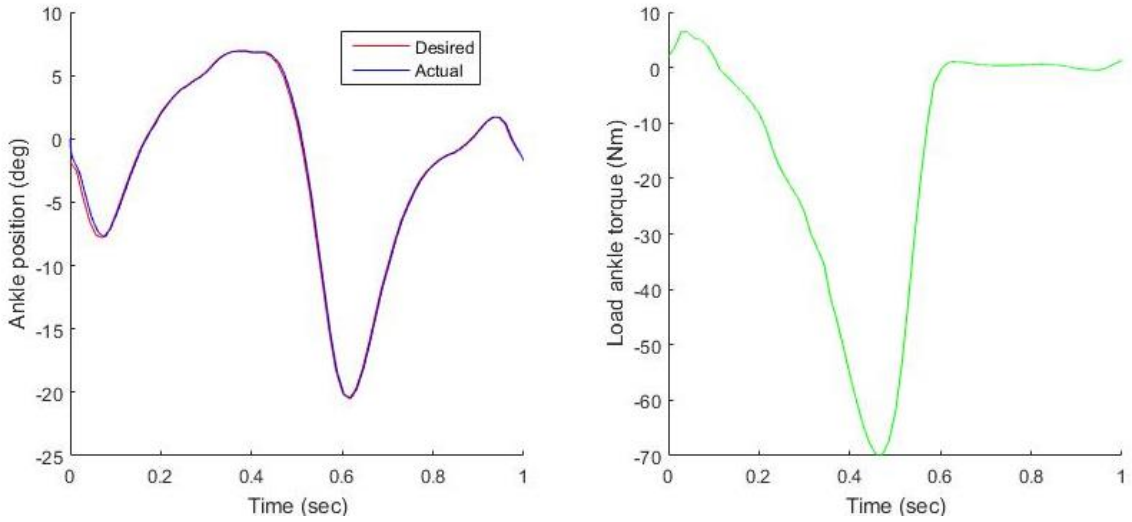

Figure 7.19 Simulation of PHAFO providing active gait assistance during gait

The active mode simulations illustrate the PHAFO design will be able to track the gait cycle providing the full torque assistance required for gait. In previous hardware experiments, a high level of noise has been detected in several sensor signals due to electromagnetic interfenerce of the DC motor controller. This has been reduced with real time analog and digital filtering. In the simulations, signal noise is incorporated by adding a small disturtance to the measurement signal being feedback into the controller. High gains are required to track the desired angular position, and therefore a good signal to noise ratio must be upheld to maintain system stability.

7.3.2 Efficiency testing of PHAFO

The steady state efficiency of the PHAFO was measured across 24 different operating conditions (Fig. 7.18). The contour plot in fig. 7.18 uses a linear interpolation between the 24 data points. The input power is defined as the current and voltage being supplied to the motor controller, while output power is the actuator angular velocity multiplied by a constant load torque.

The maximum tested ankle torque was set at a 40 Nm which corresponds to 1330 N (300 lb). This limit represents the maximum ankle torque measured in the initial gait study of patient's with CP; however, patients without CP will generate more ankle torque than tested. The maximum tested ankle angular velocity of 200°/sec corresponds to the fastest gait speed of a patient without CP. The EHPS was operated at approximately 1800 RPM to generate a flow rate of 23.4 cc/s at a pressure of 14 MPa. The flow rate of 23.4 cc/s corresponds to an ankle angular velocity of 250 °/sec without accounting for pilot flow losses, while the pressure of 14 MPa corresponds to 74.6 Nm without accounting for losses over the conduit, valve, and piston friction.

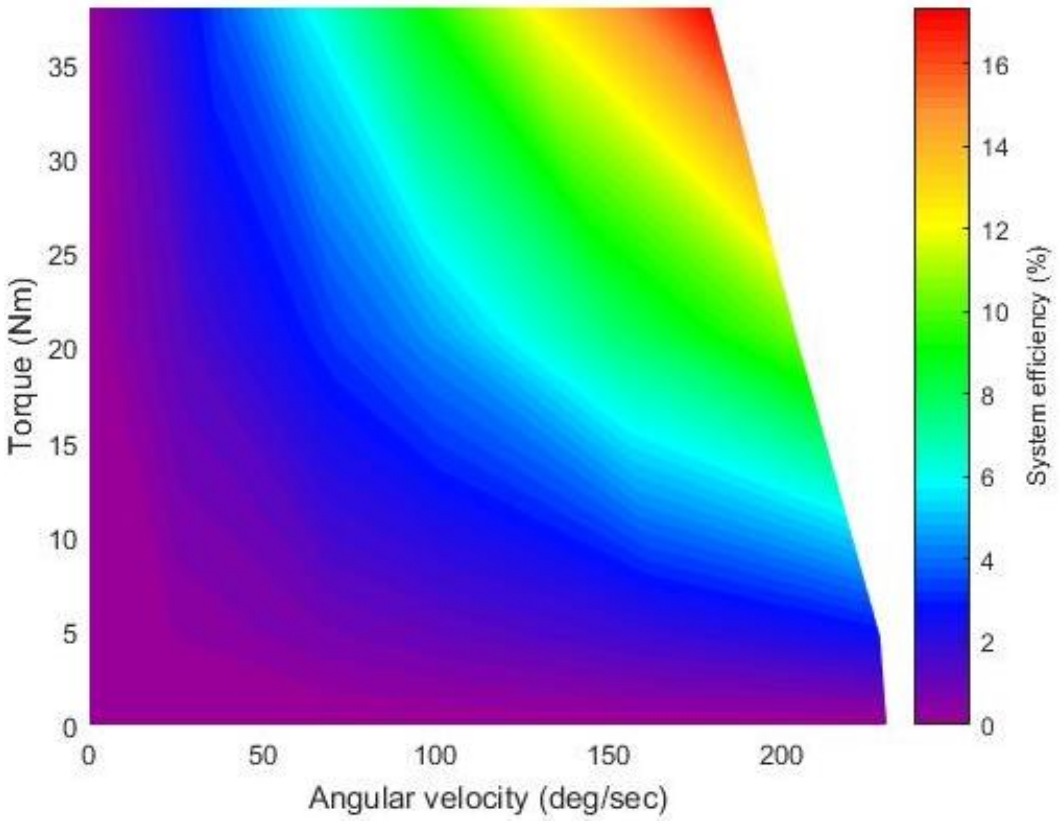

Figure 7.20 Measured efficiency of PHAFO

Figure 7.19 illustrates the PHAFO has a relatively low efficiency under traditional valve control. At low angular velocities the system is dumping the majority of the flow across a relief valve, and at low forces the majority of the pressure drop is across the valve instead of the actuator. The efficiency of the motor driver, brushed DC motor, and pump are relatively constant, because operating conditions of the EHPS are held constant.

During the steady state performance validation of the simulations, the system was simulated under the same loading conditions as the performance testing. The efficiency of the motor controller at the operating conditions was assumed to be constant at 95% according to the manufacturer's specifications. The percentage error between the measured and simulated efficiency is illustrated in fig. 7.20.

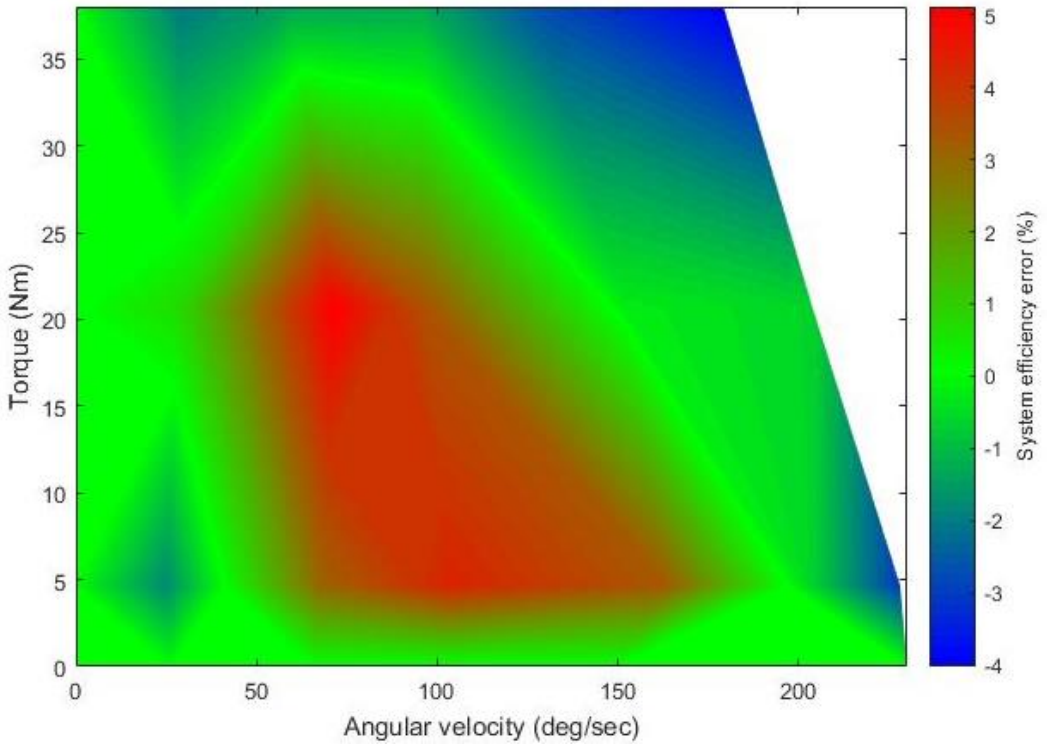

Figure 7.21 Error between measured and simulated efficiency

The maximum percentage error between the measured and simulated systems was less than 5%. This suggests that the simulations are an accurate depiction of the steady-state efficiency. It is likely the majority of the remaining error is caused by variations within the short measurement window. The stroke length of the cylinder in only 36.8 mm, and the time to complete a load cycle can be as low as 350 ms. It takes the system 100 - 150 ms to reach steady-state conditions, so the data can be average over a window as small as 200 ms.

Fig. 7.20 illustrates the measured additional efficiency savings while using proportional flow rate control to vary the motor voltage in the EHPS. At the high angular velocities, the efficiency increase is fairly small as the maximum and required pump flow rates are approximately the same. However, at low angular velocities the required flow rate is much lower than the maximum flow rate. Proportional flow rate control will slow the motor down, resulting in up to a 300% increase in efficiency as less energy is dissipated across the relief valve. There is never a point where the EHPS will stop, as the valve requires a pilot flow, and the control algorithm has a flow rate constant buffer between estimated and supplied.

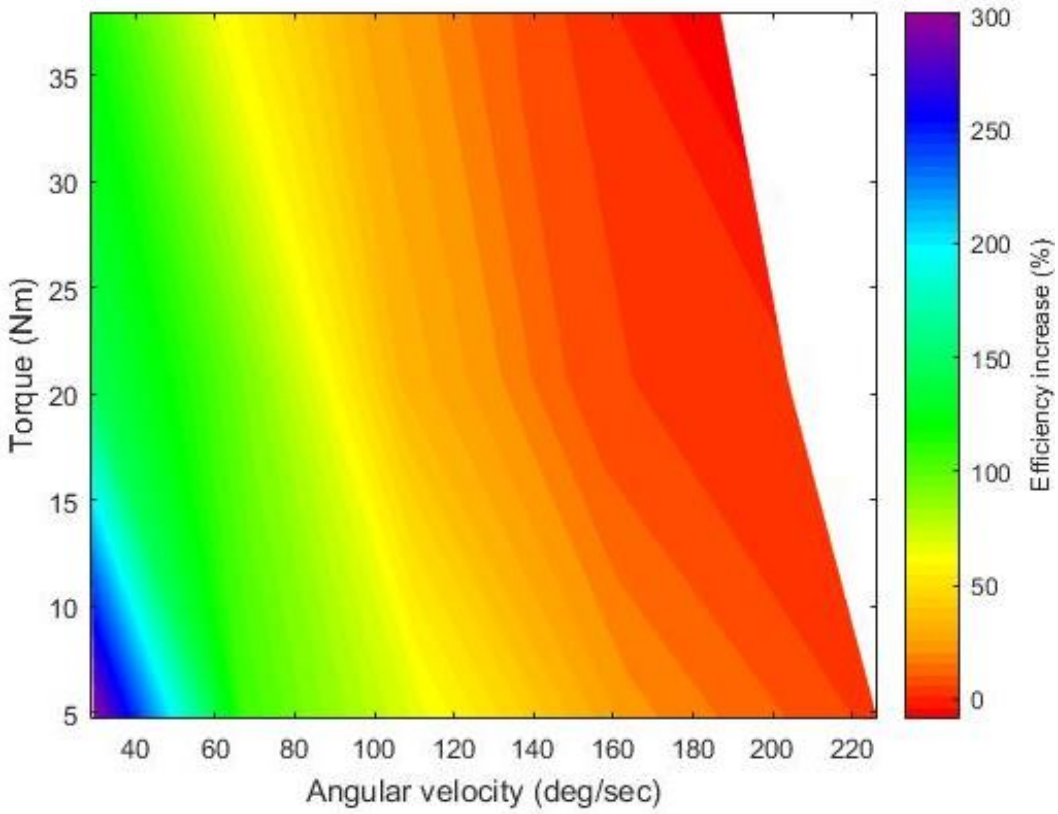

Figure 7.22 Measured percentage efficiency increase using EHPS proportional flow rate control

7.3.3 PHAFO control performance

Figure 7.21 is the measured 50° step response of the PHAFO under two different load conditions and two different EHPS operating conditions. The pressure relief valve setting was maintained at 14 MPa, while the voltage supplied to the motor was held constant, so that the angular velocity of the motor/pump shaft was approximately 2000 and 3000 RPM when the valve was closed.

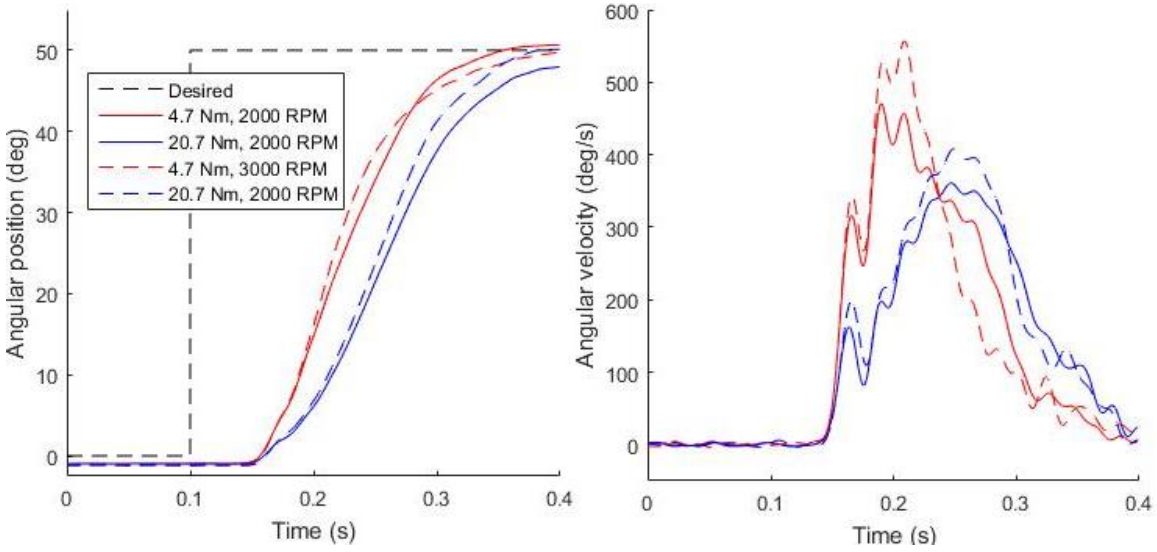

Figure 7.23 Measured PHAFO position step response

The positional tracking illustrated no overshoot and small amounts of steady-state error that can likely be eliminated with a higher proportion of integral feedback. It took approximately 340 ms to actuate the ankle 50°. The angular velocity was irregular. This can be attributed to the high amount of friction within the actuators in combination with discrete pump events. The acceleration and deceleration appeared to be smoother for higher loadings. This is likely caused by a lower ratio of seal friction to cable force. In addition the system contained additional inertia to be accelerated or decelerated.

The step response showed there is nearly a 50 ms delay between the valve opening and when the actuator started moving. This time delay represents the time it takes the valve to respond to the command signal, and the actuator conduits to pressurize to the point where seal static friction is overcome. These delays were higher than expected when the valve has bandwidth capabilities around 200 Hz. Computer models were used to determine that the source of the delay is the percentage of entrapped air in combination with long conduits.

The higher loading did result in a significantly slower response. Under the test conditions, the valve is initially opened nearly all the way allowing the pump and cylinder load to be directly connected. Since the pump pressure and cylinder load are correlated, the electric motor experiences more torque under heavy loads. This slows down the motor when the supply

voltage is being held constant. When the voltage supplied to the motor was controlled to maintain a constant angular velocity, the effect of the ankle load on system rise and settling response times diminishes.

The additional flow rate capabilities appeared to provide little decrease in the time it took to accelerate and decelerate the system. The higher flow rate did allow the system to achieve a higher maximum angular velocity. The majority of response time was spent accelerating and decelerating the system due to a short actuating length, so little time was spent with the system at the steady-state maximum flow rate. As a result, additional flow rate supplied by the EHPS only resulted in a marginally faster response.

The primary design objective was to ensure that the PHAFO can mimic the dynamics of a passive PHAFO. Fig. 7.23 illustrates the PHAFO's ability to track a linear stiffness within the range of 0.5 and 4 Nm/deg. Higher stiffnesses can be achieved, but the window of angular position decreases proportionally in accordance with fig. 7.18. The high levels of input torque needed to test the system were generated with a long arm and handle attached to the load pulley on the test stand. By pulling the arm back and forth, the system is loaded with a variety of torques at a variety of different angular velocities that range from 0 to 200 °/s to create the trajectories in fig. 7.23. The measured angular velocity range matches the expected ankle angular velocity of children with and without CP.

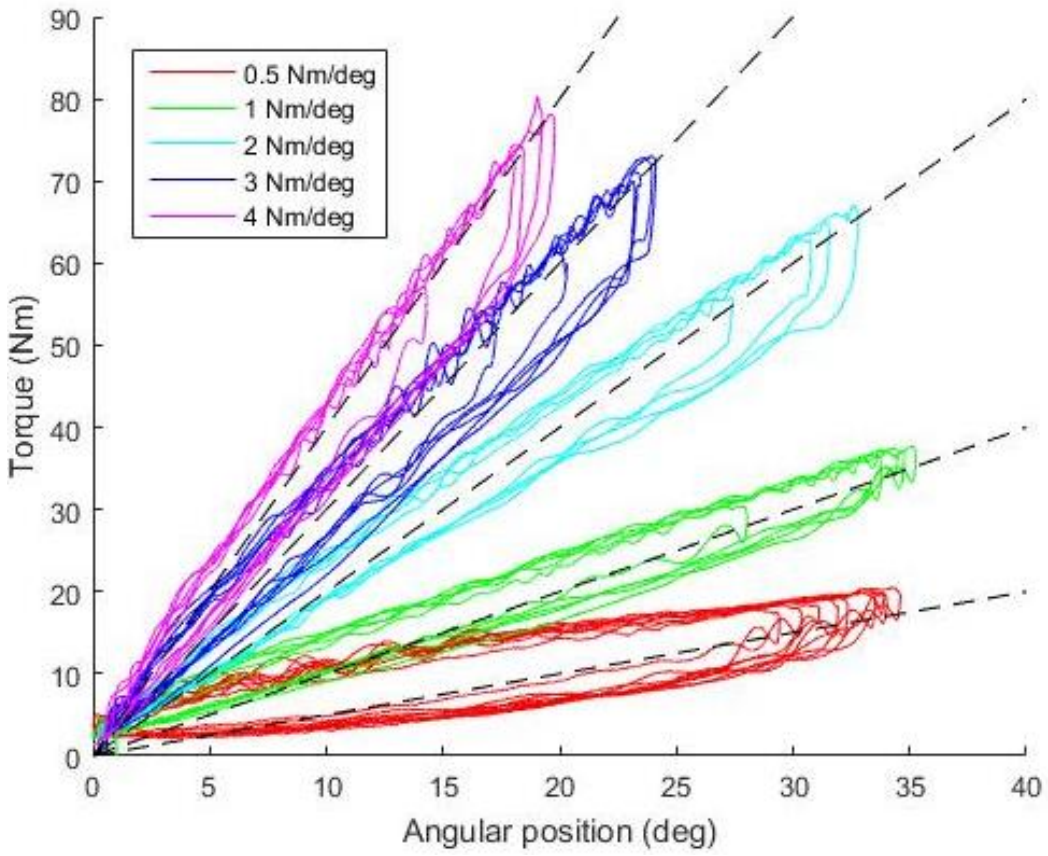

Figure 7.24 Stiffness tracking of PHAFO

The emulated stiffnesses each exhibit hysteresis; however, the average linear stiffness were all within ± 0.2 Nm/deg. A small amount of hysteresis is of little concern, because the passive AFO's measured with BRUCE all demonstrate varying degrees of hysteresis as well. In order for the system to emulate low stiffness systems, the control gains need to be lower to maintain stability. In performance testing the PHAFO prototype was able to generate up to 76 Nm/deg at 250 °/sec under the specified EHPS operating conditions. The steady-state angular velocity of the actuator can be increased up to 410 °/s when the EHPS flow rate is maximized. Operating the EHPS at these conditions is unnecessary as the maximum expected ankle angular velocity of a child with and without CP are 100 and 200 °/sec. The torque performance is saturated, as operating the EHPS at higher system pressure is likely to cause the piston-cable seals to leak.

7.4 Discussion

A computer model of small-scale hydraulic system was validated and used to simulate the performance of a pediatric hydraulic ankle-foot orthosis (PHAFO). The computer models were further validated by comparing the measured performance of the HAFO with simulation results. The computer simulations were useful tools in selecting hardware by predicting performance and also diagnosing performance problems during the prototyping of this device.

When modeling the system lumped capacitance assumptions are made. These assumptions include a uniform fluid and no discrete pump events. A significant portion of the error seen between the measurements and simulations are likely due to an uneven distribution of air within the fluid. If a pocket of air passes through an orifice, the system can experience brief periods of acceleration due to the dramatic decrease in fluid viscosity and pressure drop across the orifice. In addition, trapped air significantly reduces the bulk modulus of the fluid, increasing the compressibility and response time of the system. The pump ripple should be considered in future simulations, because it causes additional pressure fluctuations that can become significant at low pump flow rates. Finally if the simulations are to be used to judge the performance of the controller, measurement noise has to be estimated and considered.

The first generation prototype with an ankle actuator weight of 1.1 kg has demonstrated it can provide torque assistance and resistance up to approximately 78 Nm at an angular velocity of 200°/sec. This is within the design specifications of a patient with CP, but the system provides less torque assistance than is necessary for normal gait. There is a small fraction of high stiffness AFOs that the PHAFO will not be able to simulate through large ranges of motion. This is represented in AFO 3 as the user exerts 112 Nm on the passive AFO. The proposed design of the second generation PHAFO is nearly identical in weight and can produce up to 98 Nm of torque.

The PHAFO accurately tracked linear stiffness within ± 0.2 Nm/° for stiffness within the range of 0.5 - 4 Nm/°. The traditional AFOs demonstrated more hysteresis for low stiffness AFOs, while the performance of high stiffness AFOs were linear. The PHAFO exhibited similar behavior due to the lowering of the control gains at lower stiffnesses. The best method found to decrease hysteresis was to decrease the noise within the measurement signal by improving the analog

low pass filters and digital filters. Less noise allowed the control gains to be further increased resulting in improved positional tracking with the load disturbances.

The delay of the actuator between valve signal and initial movement of the actuator should be decreased in the second design. Further simulations have illustrated that the three best methods for decreasing the delay are increasing the bulk modulus of the fluid, reducing conduct length between valve and actuator, and operating at high pressures. In the gen. 2 design, the control valve will be moved from the power supply to the actuator, adding more weight at the ankle but reducing time delay by 55%. In addition, the higher operating pressure of 21 MPa further reduces the delay. In the current design the pressure is limited due to variation in the outside diameter of the nylon coated cable, lead to variability of the piston cable seal clearance. A high seal clearance tolerance must be held to seal high pressure fluid. Therefore, the tolerance of the outside diameter of the cable must be improved in the original manufacturing process or a secondary die extrusion process. Entrapped air within the conducts is ultimately the source of performance limitation and additional methods of removing would be explored.

Additional performance testing includes calibrating the exact stiffness of the PHAFO prototype with the BRUCE measurement system. This will also help ensure that the PHAFO performs mechanically similar to the passive orthosis at the ankle and metatarsal-phalangeal joints. After ankle stiffness has been verified for range of stiffness 0.5 to 4 Nm/°, the first generation PHAFO will begin clinical testing at GCSH.

Future work on this project includes the construction and performance testing of the second generation PHAFO. The medial and lateral actuator assemblies fabricated with EBM will have to undergo several post processing operations including cleaning and polishing the internal hydraulic conduits and machining the piston bore, as well as other small operations to improve surface finish in localized areas. As a result of using this new AM process in a high stress application, the actuator assemblies will undergo rigorous loaded fatigue and pressure testing to ensure mechanical integrity and leak free construction.

Chapter 8 Conclusions and Future Research

Traditionally hydraulic power has been used in large-scale applications such as earth moving equipment or large manufacturing equipment. This equipment is often bulky and heavy as it is used in applications where overall system weight is of little concern. Hydraulic power also has a reputation as being inefficient and difficult to control due to the presence of nonlinear dynamics. Finally, the majority of hydraulic systems have undergone little change in the previous decades as many consider fluid power a obsolete technology. This research addresses these limitations and lays the foundation for scaling hydraulic technology down for use in portable human assistive machines.

The first accomplishment of this research is the development of a computer algorithm that uses actuation requirements to design an ideal pump or valve controlled hydraulic system under steady-state conditions. This design algorithm appropriately sizes the components, while predicting the system energy density, fluid operating temperatures, weight, and other performance parameters. This tool assists engineers in improving the performance while minimizing the weight of future small-scale hydraulic systems. By quantifying inefficiencies within the system, future research and development efforts can be better targeted to improve performance.

The research is unique in that it takes an integrated system-level approach in analyzing small-scale hydraulic systems as opposed to individual components. An individual component analysis can result in improved performance of a specific component, while diminishing the performance of the overall system. An optimal system can only be discovered when considering the interrelated dynamics between components. In addition, several dynamics like heat transfer are poorly defined at a component-level approach, while a system-level analysis provides a complete picture.

A second accomplishment of this research is the development of design guidelines for the use of small-scale hydraulic systems in human assistive machines. In general, system operating pressure should be held above 4 MPa to achieve high power and energy densities, as system efficiency quickly drops for lower system pressures. As the operating pressure is further increased, the system efficiency generally reaches a maximum value, as surpassing this pressure

will result in increased volumetric losses within the pump. The proper selection of the conduit inner diameter, fluid viscosity, and clearances within the axial piston pump can significantly improve hydraulic efficiency, resulting in higher system energy densities. Finally, pump controlled systems illustrate significantly higher power and energy densities compared to valve controlled. As a result, valve controlled systems will likely require the addition of a heat exchanger if the application requires intermittent operation. This will only further increase weight and decrease energy density of valve controlled systems. Taking into consideration these guidelines will result in the development of lighter and more efficient hydraulics systems that will be better suited for use in human assistive machines.

A large portion of the losses within valve and pump controlled systems reside in the hydraulic power supply. Future research should be focused on optimizing the efficiency of the pump coupled with the BLDC motor. This research would include an exploration of pump and winding design variables like swash plate angle, piston bore, number of pistons, number of windings, and diameter of wire. In addition, there is likely a potential weight and volume savings by integrating the packaging of the pump and windings together to allow removal of redundant bearings. The working fluid could potentially be used to increase heat transfer of the windings, thus allowing the use of smaller motors operated at higher power levels. Finally, the design algorithm assumed steady-state full-scale operation when sizing the different components; however, it should be adapted for intermittent operation including the integration of accumulators.

A third objective accomplished by this research is the development of a dynamic computer model that accurately predicts the rise time, average efficiency over a duty cycle, and other dynamic performance metrics of a small-scale hydraulic system. The computer models have been shown to be valid by comparing simulated system metrics with identical metrics measured on physical hardware.

The computer simulations and validations assisted in quantifying sources of compliance in hydraulic systems to study how they affect rise time. If the objective of the actuation system is to replicate the dynamics of human muscle tissue, then some compliance is necessary [16], but too much will decrease rise times and control bandwidth. The three most significant methods found to decrease system compliance include: reduction of flexible conduits with walls that

elastically stretch, elimination of air in the fluid, and reduction of long conduits. The effect of entrapped air within the working fluid is more significant for small-scale hydraulic systems where small amounts of air can devastatingly increase the effective bulk modulus of the fluid. Several experiments demonstrated responses that were delayed 50-100 ms due to the presence of entrapped air. Entrapped air can be difficult to remove from hydraulic lines especially in auxiliary actuation lines that do not continuously circulate through the tank. This is another reason to maintain higher working pressures as the reduction of the effective bulk modulus due to entrapped air lessens with increasing working fluid pressure. A future area of research that could significantly improve hydraulic system performance is the development of a working fluid that dissolves air, so the effective bulk modulus remains constant.

The rise time of pump controlled system is typically an order of magnitude longer compared to valve controlled systems due to more sources of compliance and additional mechanical and fluid inertia that need to be accelerated. The variable displacement and fixed displacement pump illustrated similar rise times with a hydraulically actuated swash plate, but faster rise times could be achieved with the use of a different actuator or a larger charge pump. Typically forces on a swash plate are large enough to require hydraulic actuation, but in small-scale applications electrical actuation is possible and should be a future avenue of research.

If a hydraulic system is operated below 70% duty cycle, the use of an accumulator will significantly improve energy savings and storage with only a small amount of compliance added to the system. The addition of an accumulator can also be used to effectively boost flow rate capabilities for intermittent operation, allowing the use of a smaller hydraulic power supply. The case study results illustrated that a variable displacement pump with swash plate actuation should be used at high duty cycles to achieve the highest efficiency, while a constant displacement pump with on/off operation is more efficient at lower duty cycles. The use of a proportional pressure or flow rate feedback control loop on the motor voltage demonstrated the ability to triple system efficiency with a negligible increase in rise time. In comparing the results of steady-state design algorithm and dynamic simulations, pump control should be used for all single DOF applications to achieve higher efficiencies, higher energy densities, and a lower system weight unless a rise time of less than 40 ms or a bandwidth of greater than 25 Hz is

required. In addition, this can only be achieved if the control valve is placed near the actuator to eliminate compliance.

A significant limitation of hydraulic technology is the poor system level efficiencies. In an effort to improve efficiency by reducing valve throttling losses, the design and simulated use of a digital high frequency switching valve was explored for use in small-scale human assistive machines. The results showed that the proportion of valve switching energy to nominal valve power decreases as the valve is scaled smaller. This makes digital switching technology ideal for small-scale applications. The proposed high frequency digital switching valve demonstrated significant increases in system efficiency across a range of flow rates and switching frequencies.

A future avenue of research is the prototyping of the proposed digital valve design. The prototype can be used to validate the simulation results. Future research should also include exploring different methods of smoothing out the digital fluid flow with the additional source of fluid capacitance and inertia. This could also be accomplished by exploring different control strategies besides PWM. In the simulations small accumulators were used, but it might be possible to get the same amount of capacitance from the elastic stretch of a hose, eliminating the additional expense and weight of an accumulator. Since the ratio of switching energy to nominal valve power decreases with orifice size, multiple orifice valves should be explored to create higher flow rate capacities.

The final objective of this research was to use this body of knowledge and translate that in the construction of two prototypes illustrating hydraulic powered human assistive machines. The application selected was a powered ankle-foot orthosis (AFO) due to the particularly challenging high torque requirements from an actuator that needs to be lightweight and compact so as not negatively impact gait dynamics. The design of the adult hydraulic AFO focused on achieving the highest energy density possible to make the entire system fully portable, being carried on the body. The pediatric AFO design focused on a lightweight actuator capable of achieving the fastest rise time and a large control bandwidth. New metal additive manufacturing technologies are explored in a second generation design to further reduce the weight of actuator, valve, and pump manifolds, while increasing the heat dissipated from the working fluid. The scientific

significance of this research is illustrated in how the tools and principles discovered in chapter 2-5 helped guide the designs of the human assistive machines in chapter 6 and 7.

This research addresses several of the challenges that come with scaling the size of the technology down and making it lightweight for portable systems. This research illustrates how the properties of hydraulic systems allow these systems to replicate human muscle dynamics, making them ideal for assistive machines. The validated models and simulations will allow engineers to better understand and optimize the dynamics to improve efficiency and other metrics. In addition, the innovative concepts of digital hydraulics have the ability to revolutionize control valves and pumps. This body of knowledge in combination with state-of-art technologies like digital hydraulic valves and additive manufacturing are the innovative spark hydraulic technology needs to expand beyond large-scale applications to small-scale human assistive machines.

Bibliography

[1] "Work-Related Musculoskeletal Disorders (WMSD) Prevention," Centers for Disease Control and Prevention, 2013.

[2] J. Watton, Fundamentals of Fluid Power Control, New York: Cambridge University Press, 2009.

[3] J. W. Hollerbach, I. W. Hunter and J. Ballantyne, "A comparative analysis of actuator technologies for robotics," *The Robotics Review,* no. 2, pp. 299-342, 1992.

[4] C. Jean-Mistral, S. Basrour, J. Chaillout and A. Bonvilain, "A Complete Study of Electroactive Polymers for Energy Scavenging: Modeling and Experiements," in *Symposium on Design, Test, Integration and Packaging of MEMS/MOEMS*, Stresa, 2007.

[5] I. W. Hunter and S. Lafontaine, "A comparison of musce with articial actuators," in *Solid-State Sensor and Actuator Workshop, 1992 5th Technical Digest IEEE*, 1992.

[6] A. Akers, M. Gassman and R. Smith, Hydraulic Power System Analysis, Boca Raton: CRC Press, 2006.

[7] H. E. Merritt, Hydraulic Control Systems, John Wiley & Sons, 1976.

[8] R. P. Lambeck, Hydraulic Pumps and Motors, New York: Marcel Dekker Inc., 1983.

[9] R. Tiwari, M. A. Meller, K. B. Wajcs, C. Moses, I. Reveles and E. Garcia, "Hydraulic articifical muscles," *Journal of Intelligent Material, System and Structures,* vol. 23, no. 3, pp. 301-312, 2012.

[10] P. G. McCormick, "On the practical efficiency of shape memory engines," *Scripta Metallurgica,* vol. 21, pp. 99-101, 1987.

[11] W. Tong, Mechanical Design of Electric Motors, Boca Raton: CRC Press, 2014.

[12] K. Merrill, M. Holland, M. Batdorff and J. Lumkes, "Comparative study of digital hydraulics and digital electronics," *International Journal of Fluid Power,* vol. 11, no. 3, pp. 45-51, 2010.

[13] J. L. Pons, Emerging Actuator Technologies: A Micromechatronic Approach, Hoboken, NJ: John Wiley & Sons Inc., 2005.

[14] I. W. Hunter, S. Lafontaine, J. M. Hollerbach and P. J. Hunter, "Fast reversible NiTi fibers for use in microrobotics," in *Proceedings IEEE Micro Electro Mechanical System*, 1991.

[15] N. D. Manring, Hydraulic Control Systems, Hoboken, New Jersey: John Wiley& Sons, 2005.

[16] G. K. Klute, J. M. Czerniecki and B. Hannaford, "Artificial Muscles:Actuators for Biorobotic Systems," *The International Journal of Robotics Research,* vol. 21, no. 4, pp. 295-309, 2002.

[17] Y. C. Fung, Biomechanics: Mechanical Properties of Living Tissues, New York: Springer Science+Business Media, 1993.

[18] T. Virvalo and M. Vilenius, "The Influence of Pump and Valves on Efficiency of a Hydraulic Boom," *Developments in fluid Power Control Machinery,* pp. 183-208, 2000.

[19] J. Xia and W. K. Durfee, "Modeling of tiny hydraulic cylinders," in *52nd Annual National Conference of Fluid Power*, 2011.

[20] J. Peirs, D. Reynaerts and H. Van Brussel, "Design of miniature parallel manipulars for integration in a self-propelling endoscope," *Sensors and Actuators A: Physcial,* vol. 85, no. 1-3, pp. 409-417, 2000.

[21] J. Peirs, D. Reynaerts and H. Van Brussel, "A miniature hydraulic parallel manipulator for integration in a self-propelling endoscope," in *Proceedings of the 13th European Conference on Solid State Transducers (Eurosensors XIII)*, Hague, 1999.

[22] Y. Chen, K.-W. Kwok and Z. T. Ho Tse, "A MR-conditional High-torque Pneumatic Stepper Motor for MRI-Guided and Robot-Assisted Intervention," *Annals Biomedial Engineering,* vol. 42, no. 9, pp. 1823-1833, 2014.

[23] W. Shang, H. Su, G. Li and G. S. Fischer, "Teleoperation System with Hybrid Pneumatic Piezoelectric Actuation for MRI-Guided Needle Insertion with Haptic Feedback," in *Prooceedings of the IEEE/RSJ International Conference on Intelligent Robots and Systems*, Tokyo, 2013.

[24] E. Franco, "Design and control of needle positioner for MRI-guided laser ablation of the liver," in *IEEE/ASME 10th Internation Conference of Mechatronic and Embedded Systems and Applications*, Senigallia, 2014.

[25] D. B. Comber, E. J. Barth and R. J. Webster III, "Design and Control of a Magnetic Resonance Compatible Precision Pneumatic Active Cannula Robot," *Journal of Medical Devices,* vol. 8, pp. 011003-1/7, 2014.

[26] D. Kim, E. Kobayashi, T. Dohi and I. Sakuma, "A new, compact MR-compatible surgical manipulator for minimally invasive liver surgery," in *International Conference on Medical Image Computing and Computer-Assisted Intervention*, Tokyo, 2002.

[27] L. Love, R. Lind and J. Jansen, "Mesofluidic actuation for articulated finger and hand prosthetics," *IEEE Internation Conference on Intelligent Robots and Systems,* pp. 2586-2591, 2009.

[28] S. Schulz, C. Pylatiuk, M. Reischl, J. Martin, R. Mikut and G. Bretthauer, "A hydraulic driven multifunctional prosthetic hand," *Robotica,* vol. 23, no. 3, pp. 293-299, 2005.

[29] A. Zoss, H. Kazerooni and A. Chu, "On the Mechanical Design of the Berkely Lower Extremity Exoskeleton (BLEEX)," in *IEEE/RSJ International Conference of Intelligent Robots and Systems*, Alberta, 2005.

[30] H. Kazerooni, "Exoskeletons for Human Power Augmentation," in *IEEE/RSJ Internal Conference of Intelligent Robots and Systems*, Alberta, 2005.

[31] J. W. Raade, K. R. Amundson and H. Kazerooni, "Development of Hydraulic-Electric Power Units for Mobile Robots," in *ASME International Mechanical Engineering Congress and Exposition*, Orlando, 2005.

[32] "Research Projects> Exoskeletons," Berkeley Robotics & Human Engineering Laboratory, [Online]. Available: http://bleex.me.berkeley.edu/research/exoskeleton/. [Accessed 1 4 2016].

[33] A. M. Dollar and H. Herr, "Lower Extremity Exoskeletons and Active Orthoses: Challenges and State-of-the-Art," *IEEE Transactions on Robotics,* vol. 24, pp. 144-158, 2008.

[34] R. Bogue, "Exoskeletons and robotic prosthetics: a review of recent developments," *Industrial Robot: An International Journal,* vol. 36, no. 5, pp. 421-427, 2009.

[35] S. Karlin, "Raytheon Sacros's Exoskeleton Nears Production," IEEE Spectrum, 2011.

[36] E. Ackerman and E. Guizzo, "The Next Generation of Boston Dynamics' ATLAS Robot Is Quiest, Robust, and Tether Free," IEEE Spectrum, 2016.

[37] E. Guizzo and E. Ackerman, "Boston Dynamics' Marc Raibert on Next-Gen ATLAS: "A Huge Amount of Work"," IEEE Spectrum, 2016.

[38] D. Wooden, M. Malchano, K. Blankespoor, A. Howardy, A. A. Rizzi and M. Raibert,

"Autonomous navigation for BigDog," in *IEEE International Conference on Robotic and Automation*, Anchorage, 2010.

[39] E. Ackerman, "BigDog Throw Cinder Blocks with Huge Robotic Face-Arm," IEEE Spectrum, 2013.

[40] E. Guizzo, "Marc Raibert: What's New Since BigDog? (IROS 2013 Keynote)," IEEE Spectrum, 2013.

[41] Z. Y. Li, Z. Y. Yu and S. D. Yang, "The Development and Perspective of Water Hydraulics," in *Proceedings of the JFPS International Symposium on Fluid Power*, Japan, 1999.

[42] S. M. Soini, K. T. Koskinen, M. J. Vilenius and J. A. Puhakka, "Effects of fluid-flow velocity and water quality on planktonic and sessile microbial growth in water hydraulic system," *Water Research,* vol. 36, no. 15, pp. 3812-3820, 2002.

[43] S. L. Nie, G. H. Huang and Y. P. Li, "Tribological study on hydrostatic slipper bearing with annular orifice damper for water hydraulic axial piston motor," *Tribology Internation,* vol. 39, no. 11, pp. 1342-1354, 2006.

[44] T. Takahashi, C. Yamashina and S. Miyakawa, "Development of Water Hydraulic Proportional Control Valve," in *Proceedings o the JFPS International Symposium on Fluid Power*, Japan, 1999.

[45] E. Urata, S. Miyakawa, C. Yamashina, Y. Nakao, Y. Usami and M. Shinoda, "Development of a Water Hydraulic Servo Valve," *JSME Internation Journal Series B Fluids and Thermal Engineering,* vol. 41, pp. 286-294, 1998.

[46] G. W. Stachowiak and A. W. Batchelor, "Oil Viscosity," in *Engineering Tribology*, Amsterdam, Elsevier, 1993, pp. 12-50.

[47] J. Wang, G. Gong and H. Yang, "Control of Bulk Modulus of Oil in Hydraulic Systems," in *Proceedings of the 2008 IEEE/ASME International Conference on Advanced Intelligent Mechatronics*, Xian, China, 2008.

[48] N. K. Agarwal and C. P. Lawson, "A practical method to account for seal friction in aircraft hydraulic actuator preliminary design," *Proceedings of the Institution of Mechanical Engineers, Part G: Jounral of Aerospace Engineering,* vol. 0, no. 0, pp. 1-10, 2016.

[49] J. Xia and W. K. Durfee, "Experimentally Validated Models of O-rings seals for Tiny Hydraulic Cylinder," in *Proceedings of ASME/Bath 2014 Symposium on Fluid Power &*

Motion Control, Bath, United Kingdom, 2014.

[50] B. Brushan, Priniciples and Applications of Tribology, Second Edition, John Wiley & Sons, 2013.

[51] R. W. Fox, P. J. Pritchard and A. T. McDonald, Introduction to Fluid Mechanics, Hoboken: John Wiley & Sons, 2009.

[52] P. Swamee and A. Jain, "Explicit equations for pipe-flow problems," *Journal of the Hydraulic Division (ASCE),* vol. 102, no. 5, pp. 657-664, 1973.

[53] S. Haaland, "Simple and Explicit Formulas for the Friction Factor in Turbulent Flow," *Transactions of ASME Journal of Fluids Engineering,* vol. 103, pp. 89-90, 1983.

[54] Eaton, Industrial Hydraulics Manual, Maumee, OH: Eaton Corporation, 2010.

[55] J. M. Gere and B. J. Goodno, "Applications of Plane Stress (Pressure Vessels, Beams, and Combined Loadings)," in *Mechanics of Materials*, Toronto, Cengage Learning, 2009, pp. 619-630.

[56] K. Myers, in *Mechanical engineers' handbook*, John Wiley & Sons Inc., 1998, pp. 229-242.

[57] R. C. Juvinall and K. M. Marshek, Fundamentals of Machine Component Design, Danvers: John Wiley & Sons, 2005.

[58] M. J. Moran and H. N. Shapiro, Fundamentals of Engineering, Danvers: John Wiley & Sons Inc., 2008.

[59] F. D. Norville, Electrohydraulic Control Systems, Upper Saddle River: Prentice Hall Inc., 2000.

[60] J. Johnson, "Proportional valves vs. servo valves," *Hydraulics & Pneumatics,* 10 08 2011.

[61] "Servovalve, Hydraulic - Description," 2013. [Online]. Available: http://www.daerospace.com/HydraulicSystems/ServovalveDesc.php. [Accessed 12 08 2015].

[62] B. Scrosati and J. Garche, "Lithium batteries: Status, prospects and future," *Jounral of Power Sources,* vol. 195, no. 9, pp. 2419-2430, 2010.

[63] G. Zeiger and A. Akers, "Torque on the Swash Plate of an Axial-Piston Pump," *ASME*

Journal of Dynamic system, Measurement and Control, vol. 107, pp. 220-226, 1985.

[64] G. Zeiger and A. Akers, "Dynamic Analysis of an Axial-Pump Swash Plate Control," in *Proceedings of the Institution of Mechanical Engineers*, London, England, 1986.

[65] N. D. Manring and R. Johnson, "Modeling and Designing Variable Displacement Open-Loop Pump," *ASME Journal of Dynamic Systems, MEasurement, and Control,* vol. 118, pp. 267-271, 1996.

[66] X. Zhang, J. Cho, S. S. Nair and N. D. Manring, "New Swash Plate Dampening Model for Hydraulic Axial-Piston Pump," *Journal of Dynamic Systems, Measurement, and Control,* vol. 123, pp. 463-470, 2001.

[67] J. M. Bergada, S. Kumar, D. L. Davies and J. Watton, "A complete analysis of axial piston pump leakage and output flow ripples," *Applied Mathematical Modeling,* vol. 36, pp. 1731-1751, 2012.

[68] J. M. Bergada, J. Watton and S. Kumar, "Pressure, Flow, Force, and Torque Between the Barrel and Port Plate in an Axial Piston Pump," *Journal of Dynamics Systems, Measurement, and Control,* vol. 130, 2008.

[69] J. Xia and W. Durfee, "Analysis of Small Scale Hydraulic Actuation Systems," *Journal of Mechanical Design,* vol. 135, no. 9, 2013.

[70] J. M. Gere and B. J. Goodno, Mechanics of Materials, Toronto: Cengage Learning, 2009.

[71] M. K, "Mechanical Engineers Handbook," John Wiley & Sons, 1998, pp. 229-242.

[72] N. D. Manring, "The Discharge Glow Ripple of an Axial-Piston Swash-Plate Type Hydrostatic Pump," *Journal of Dynamic Systems, Measurement and Control,* vol. 122, no. 2, pp. 263-268, 1998.

[73] J. D. Ede, Z. Q. Zhu and D. Howe, "Optimal split ratio for high-speed permanent magnet brushless DC motors," in *Fifth Internation Conference on Electrical Machines and Systems*, Piscataway, New Jersey, 2001.

[74] G.-A. Nazri and G. Pistoia, Lithium Batteries, New York: Springer Science, 2009.

[75] N. Omar, M. Daowd, P. v. d. Bossche, O. Hegazy, J. Smekens, T. Coosemans and J. v. Mierlo, "Rechargeable Energy Storage for Plu-in Hydrid Electric Vehicles-Assessment of Electrical Characteristics," *Energies,* vol. 5, pp. 2952-2988, 2012.

[76] K. Merrill, M. Holland, M. Batdorff and J. lumkes, "Comparative Study of Digital Hydraulic and Digital Electronics," *International Journal of Fluid Power,* vol. 11, no. 3, pp. 45-51, 2014.

[77] F. P. Incropera and D. P. DeWitt, Fundamentals of Heat and Mass Transfer, Jon Wiley & Sons Inc., 2002.

[78] R. W. Selles, J. B. Bussmann, A. V. Soest and H. J. Stam, "The effect of prosthetic mass properties on the gait of transtibial amputees- a mathematical model," *Journal of Disability and Rehabilitation,* vol. 26, no. 12, pp. 694-704, 2004.

[79] T. Lenzi and J. Sensinger, "Optimization of lower-limb motorized prosthese design based on patient body weight," in *American Academy of Orthotists & Prosthetists 40th Academy Annual Meeting & Scientific Symposium*, Chicago, 2014.

[80] H. E. Merrit, Hydraulic Control Systems, Wiley, 1991.

[81] T. Lennon, "Model-based design for mechatronics systems," Machine Design, 2017.

[82] A. O'Dwyer, Handbook of PI and PID Controller Tuning Rules, London: Imperial College Press, 2009.

[83] H. Ortwig, "Experimental and analytical vibration analysis in fluid power systems," *International Journal of Solid and Structures,* vol. 42, no. 21, pp. 5821-5830, 2005.

[84] N. D. Manring and R. E. Johnson, "Modeling and Design a Variable-Displacement Open-Loop Pump," *Journal of Dynamic Systems, Measurement, and Control,* vol. 118, pp. 267-271, 1996.

[85] H. Du and N. D. Manring, "A Single-Actuator control Design for Hydraulic Variable Displacment Pumps," in *Proceedings of the america Control Conference*, Arlington, VA, 2001.

[86] M. Linjama, M. Huova, P. Bostrom, A. Laamanen and L. Siivonen, "Design and Implmentation of Energy Saving Digital Hydraulic Control System," in *The Tenth Scandinavian International Conference on Fluid Power*, Tampere, 2007.

[87] M. Linjama and M. Vilenius, "Energy-Efficient Motion Control of a Digital Hydraulic Joint Actuator," in *Proceedings of the 6th JFPS International Symposium on Fluid Power*, Tsukuba, Finland, 2005.

[88] L. Siivonen, M. Linjama and M. Vilenius, "Analysis of fault tolerance of digital hydraulic system," in *Power Transmission and Motion Control*, Bath, 2005.

[89] "Fault Detection and Diagnosis of Digital Hydraulic Valve System," in *The Tenth Scandinavian International Conference on Fluid Power*, Tampere, 2007.

[90] M. Linjama, "Digital Fluid Power- State of the Art," in *The Twelfth Scandinavian International Conference in Fluid Power*, Tampere, Finland, 2011.

[91] M. Linjama and M. Vilenius, "Digital Hydraulics- Towards Perfect Valve Technology," in *The Tenth Scandinavian International Conference on Fluid Power*, Tampere, 2007.

[92] M. Linjama, R. Scheidl and S. Schmidt, "Discussion: Is the future of fluid power digital?," *Journal of Systems and Control Engineering,* vol. 226, no. 6, pp. 724-727, 2012.

[93] D. H. Graham and A. Ball, "Particle erosion of candidate materials for hydraulic valves," *Wear,* vol. 133, no. 1, pp. 125-132, 1989.

[94] M. Ehsan, W. Rampen and S. Salter, "Modeling of Digital-Displacment Pump-Motors and Their Application as Hydraulic Drives for Nonuniform Loads," *ASME Journal of Dynamic Systems, Measurement, and Control,* vol. 122, pp. 210-215, 2000.

[95] M. B. Rannow, H. C. Tu, P. Y. Li and T. R. Chase, "Software Enable Variable Displacment Pumps-Experimental Studies," in *ASME International Mechanical Engineering Congress & Exposition*, Chicago, Illinois, USA, 2006.

[96] N. Manring, "Digital Hydraulic: A Theoretical Study Comparing Hydraulic Power Units," in *Proceedings of the BATH/ASME Symposium on Fluid Power and Motion Control*, Bath, UK, 2016.

[97] B. Winkler, "Development of a Fast Seat Type Switching Valve for Big Flow Rates," in *The Tenth Scandinavian International Conference on Fluid Power*, Tampere, Finland, 2007.

[98] A. Plockinger, R. Scheidl and B. Winkler, "Performance, Durability and Application of a Fast Switching Valve," in *Proceedings of the Second Workshop on Digital Fluid Power*, Linz, 2009.

[99] D. T. Branson, F. C. Wang, D. N. Johnston, C. R. Bowen and P. S. Keogh, "Piezoelectrically actuated hydraulic vlave design for high bandwidth and flow performance," *Journal of System and Control Engineering,* vol. 255, no. 3, pp. 345-369, 2011.

[100] B.-Y. Bang, C.-S. Joo, K.-I. Lee, J.-W. Hur and W.-K. Lim, "Development of a Two-Stage High Spped Electrohydraulic Servovalve System Using Stack-Type Piezoelectric Elements," in *Prooceedings of the IEEE/ASME International Advanced Intelligent Mechatronics*, Port Island, Kobe, Japan, 2003.

[101] M. Reichert, "Development of piezo-driven pilot stage highly dynamic hydraulic valves," in *International Fluid Power Conference*, Aachen, Germany, 2006.

[102] X. Ouyang, D. Tilley, P. Keogh, H. Yang, N. Johnson, C. Bowen and P. Hopkins, "Piezoelectric Actuators for Screw-in Cartridge Valves," in *International Conference on Intelligent Mechatronics*, Xian, China, 2008.

[103] M. Reichert and H. Murrenhoff, "New Concepts and Design of High Response Hyraulic Valves Using Piezo-Technology," in *Power Transmission and Motion Control*, Bath, 2006.

[104] H. Yamada, S. Tsuchiya, T. Muto and Y. Suematsu, "Development of a Low Cost High-Speed On/Off Digital Valve Using a Bimorpth PZT Actuator," in *Proceeding of the JFPS International Symposium on Fluid Power*, Japan, 1999.

[105] J.-P. Uusitalo, L. Soderlund, L. Kettunen, M. Linjama and M. Vilenius, "Dynamic analysis of a bistable actuator for digital hydraulics," *IET Science Measurement Technology,* vol. 3, no. 3, pp. 235-243, 2009.

[106] J.-P. Uusitalo, V. Ahola, L. Soederlund and L. Kettunen, "Novel Bistable Hammer Valve for Digital Hydraulics," *International Journal for Fluid Power,* vol. 11, no. 3, pp. 35-44, 2010.

[107] J.-P. Uusitalo, T. Lauttamus, M. Linjama and L. Soderlund, "Miniaturized Bistable Seat Valve," in *The Tenth Scandinavian International Conference on Fluid Power*, Tampere, 2007.

[108] H. C. Tu, M. B. Rannow, M. Wang, P. Y. Li and T. R. Chase, "Modeling and Validation of a High Speed Rotary PWM On/Off Valve," in *ASME Dyanmics Systems and Control Conference*, Hollywood, California, USA, 2009.

[109] H. Tu, M. Rannow, M. Wang, P. Li and T. Chase, "The Advantages and Feasibility of Externally Actuating a High-speed Rotary On/Off Valve," in *Proceedings of the 52nd National Conference on Fluid Power*, Las Vegas, Nevada, USA, 2011.

[110] N. Fikru and T. R. Chase, "A review of MEMS Based Pneumatic Valves," in *Proceedings of the 52nd National Conference on Fluid Power*, Las Vegas, 2011.

[111] I. E. Alber, "Linear-solenoid fundamentals," in *Aerospace Engineering on the Back of an Envelope*, Norfolk, UK, Springer, 2012, pp. 51-65.

[112] K. Uchino, Ferroelectric Devices, Boca Raton, FL: CRC Press, 2010, pp. 224-227.

[113] A. V. Peterchev, "Digital Pulse-Width modulation Control in Power Electronics Theory and Applications," University of California at Berkeley, Berkeley, USA, 2005.

[114] H. Sira-Ramirez, R. Tarantinio-Alvarado and O. Llanes-Santiago, "Adapative feedback stabilization in PWM-controlled DC to DC power supplies," *International Jounral of Control,* vol. 57, no. 3, pp. 599-625, 1993.

[115] U. Heikki and E. Baerga, "Prosthetics and Orthotics," in *Physical Medicine and Rehabilitation Board Review*, New York, Demos Medical Publishing, 2004, pp. 466-474.

[116] "NINDS Foot Drop Information Page," National Institutes of Health, 29 January 2009. [Online]. Available: http://www.ninds.nih.gov/disorders/foot_drop/foot_drop.htm. [Accessed 6 September 2013].

[117] "NINDS Spasticity Information Page," National Institutes of Health, 4 October 2011. [Online]. Available: http://www.ninds.nih.gov/disorders/spasticity/spasticity.htm. [Accessed 6 September 2012].

[118] B. M. Lawler, J. Wening and M. Oros, "A functional comparison of solid and articulated AFOs during walking and running in children with spastic hemiplegic cerebral palsy," American Academy of Orthotists & Prosthetists, Oak Park, 2007.

[119] K. D. Koster, "Gait," Physiopedia, 2015.

[120] D. A. Winter, Biomechanics and Motor Control of Human Movement, Hoboken: John Wiley & Sons, 2009.

[121] J. Hitt, A. M. Oymagil, T. Sugar, K. Hollander, A. Boehler and J. Fleeger, "Dynamically controlled ankle-foot orthosis (DCO) with regenerative kinetics: incrementally attaining user portability," in *Robotics and Automation*, Roma, 2007.

[122] G. S. Sawicki, C. L. Lewis and D. P. Ferris, "It pays to have a spring in your step," *Exercise Sport Science Reviews,* vol. 37, no. 3, p. 130, 2009.

[123] M. B. Wiggin, G. S. Sawicki and S. H. Collins, "An exoskeleton using controlled energy storage and release to aid ankle propulsion," in *Rehabilitation Robotics (ICORR) IEEE*

Internal Conference, 2011.

[124] S. H. Collins, M. B. Wiggin and G. S. Sawicki, "Reducing the energy cost of human walking using an unpowered exoskeleton," *Nature,* vol. 522, pp. 212-215, 2015.

[125] S. Hussain, P. Jamwal and M. Ghayesh, "Single Joint Robotic Orthoses for Gait Rehabilitation: An Educational Technical Review," *Journal of Rehabilitation Medicine,* vol. 48, 2016.

[126] A. K. Shorter, J. Xia, E. T. Hsiao-Wecksler, W. K. Durfee and G. F. Kogler, "Technologies for Powered Ankle-Foot Orthotic Systems: Possibilities and Challenges," *IEEE/ASME Transactions on Mechatronics,* vol. 18, no. 1, pp. 337-347, 2011.

[127] A. M. Dollar and H. Herr, "Active Orthoses for Lower-Limbs: Challenges and State of the Art," in *Rehabilitation Robotics IEEE International Conference* , Noordwijk, 2007.

[128] D. P. Ferris and J. M. Czerniecki, "An Ankle-Foot Orthosis Powered by Artificial Pneumatic Muscles," *Journal of Applied Biomechanics,* vol. 21, no. 2, pp. 189-197, 2005.

[129] K. E. Gordon, G. S. Sawicki and D. P. Ferris, "Mechanical performance of artificial pneumatic muscles to power an ankle-foot orthosis," *Journal of Biomechanics,* vol. 39, no. 10, pp. 1832-1841, 2006.

[130] S. M. Cain, K. E. Gordon and P. D. Ferris, "Locomotor adaption to a powered ankle-foot orthosis depends on control method," *Journal neuroengineering Rehabilitation,* vol. 4, no. 48, 2007.

[131] K. W. Hollander, R. Ilg, T. G. Sugar and D. Herring, "An efficient robotic tendon for gait assistance," *Journal of Biomedical Engineering,* vol. 128, no. 5, pp. 788-791, 2006.

[132] R. M. Alexander, Elastic mechanisms in animal movement, New York: Cambridge University Press, 1988.

[133] A. K. Shorter, G. F. Kogler, E. Loth, W. K. Durfee and E. T. Hsiao-Wecksler, "A Portable Powered Ankle-Foot Orthosis for Rehabilitation," *Journal of Rehabilitation Research & Development,* vol. 48, no. 4, pp. 459-472, 2011.

[134] M. K. Boes, M. Islam, Y. D. Li and E. T. Hsiao-Wecksler, "Fuel efficiency of a portable powered ankle-foot orthosis," in *Rehabilitation Robotics (ICORR) IEEE International Conference*, Seattle, 2013.

[135] Z. Wang and E. T. Hsiao-Wecksler, "Design of a Compact High-Torque Actuation System for portable Powered Ankle-Foot Orthosis," *Journal of Medical Devices,* vol. 10, no. 3, p. 030963, 2016.

[136] T. Yu, A. Plummer, P. Iravani and J. Bhatti, "The Design of a Powered Ankle Prosthesis With Electrohydrostatic Actuation," in *Proceedings of the BATH/ASME Symposium on Fluid Power and Motion Control*, Chicago, Illinois, 2015.

[137] T. Yu, A. Plummer, P. Iravani, J. Bhatti, S. Zahedia and D. Moser, "The Design, Analysis and Testing of a Compact Electrohydrostatic Powered Ankle Prothesis," in *Proceedings of the BATH/ASME 2016 Symposium on Fluid Power and Motion Control* , Bath, UK, 2016.

[138] A. Akers, M. Gassman and R. Smith, Hydraulic Power Systems Analysis, Boca Raton, FL: CRC Press, 2006.

[139] W. Durfee and Z. Sun, Fluid Power System Dynamics, Center for Compact and Efficient Fluid Power, 2009.

[140] T. M. Hunt and N. Vaughan, The Hydraulic Handbook, Elsevier, 1996.

[141] R. L. Waters and S. Mulroy, "The energy expenditure of normal pathologic gait," *Gait and Posture,* vol. 9, no. 3, pp. 207-231, 1999.

[142] H. Skinner and R. Barrack, "Ankle weighting effect on gait in able-bodied adults," *Archives of physical medicine and rehabilitation,* vol. 71, no. 2, pp. 112-115, 1990.

[143] C. E. Tudor-Locke and A. M. Myers, "Methodological considerations for researchers and practioners using pedometer to measure physical (ambulatory) activity"," *Research Quarterly Exercise and Sport,* vol. 72, no. 1, pp. 1-12, 2001.

[144] C. Tudor-Locke, W. D. Johnson and P. T. Katzmarzyk, "Accelerometer-determined steps per day is US adults," *Medicine Science Sports Exercise,* vol. 41, no. 7, pp. 1384-1391, 2009.

[145] C. Tudor-Locke, C. L. Craig, J. W. Brown, S. A. Clemes, K. De Cocker, B. Giles-Corti, Y. Hatano, S. Inoue, S. M. Matsudo, N. Mutrie, J. M. Oppert, D. A. Rowe, M. D. Schmidt, G. M. Schofield, J. C. Spence, P. J. Teixeria, M. A. Tully and S. N. Blair, "How many steps/day are enough? For Adults," *International Journal Behavioral Nutrition Physical Activity,* vol. 8, p. 79, 2011.

[146] J. M. Tarascon and M. Armand, "Issues and challenges facing rechargeable lithium batteries"," *Nature,* vol. 414, no. 6861, pp. 359-367, 2001.

[147] L. J. Love, B. Richardson, R. Lind, R. Dehoff, B. Peter, L. Lowe and C. Blue, "Freeform fluidics," *Mechanical Engineering,* vol. 135, no. 6, p. S17, 2013.

[148] L. Williams, "ORNL-group show how it's done, one layer at time," *Additive Manufacturing,* 2013.

[149] V. Lajeunesse, C. Vincent, F. Routhier, E. Careau and F. Michaud, "Exoskeletons' design and usefulness evidence according to a systematic review of lower limb exoskeletons used for functional mobility by people with spinal cord injury," *Disability and Rehabiliation: Assistive Technology,* pp. 1-13, 2015.

[150] L. M. Mooney, E. J. Rouse and H. M. Herr, "Autonomous exoskeleton reduces metabolic cost of human walking," *Journal of Neuroengineering and Rehabilitation,* vol. 11, no. 1, p. 151, 2014.

[151] T. Fukunaga, K. Kubo, Y. Kawakami, S. Fukashiro, H. Kanehisa and C. N. Maganaris, "In vivo behavior of human muscle tendon during walking," *Proceedings of the Royal Society of London B: Biological Sciences,* vol. 268, no. 1464, pp. 229-233, 2001.

[152] A. Pedchenko and E. J. Barth, "Design and validation of high energy density accumulator using polyurethane," in *ASMR Dynamic System and Control Conference*, Hollywood, 2009.

[153] E. Azizi, E. L. Brainerd and T. J. Roberts, "Variable gearing in pennate muscles," *Proceedings of the National Academy of Sciences,* vol. 105, no. 5, pp. 1745-1750, 2008.

[154] E. Azizi and T. J. Roberts, "Variable gearing in a biological inspired pneumatic actuator array," *Bioinspiration & Biomimetics,* vol. 8, no. 2, 2013.

[155] D. R. Louie, J. J. Eng and T. Lam, "Gait speed using powered robotic exoskeletons after spinal cord injury: a systematic review and correlational study," *Journal of Neurengineering and Rehabilitation,* vol. 12, no. 1, p. 1, 2015.

[156] L. W. Forrester, A. Roy, R. N. Goodman, J. Rietschel, J. E. Barton, H. I. Krebs and R. F. Macko, "Clinical application of modular ankle robot for stroke rehabilitation," *NeuroRehabilitation,* vol. 33, no. 1, pp. 85-97, 2012.

[157] A. Mireiman, B. L. Patritti, P. Bonato and J. E. Deutsch, "Effect of cirtual training on gait biomechanics of individuals post-stroke," *Gait & Posture,* vol. 31, no. 4, pp. 433-437, 2010.

[158] M. Zhang, T. C. Davies and S. Xie, "Effectiveness of robot-assisted therapy on ankle rehabilitation-a systematic review," *Journal of Neuroengineering Rehabilitation,* vol. 10,

no. 1, p. 30, 2013.

[159] H. Krebs, S. Rossi, S. J. Kim, P. K. Artemiadis, D. Williams, E. Castelli, P. Cappa and et al, "Pediatric anklebot," in *Rehabilitation Robots (ICORR) IEEE International Conference*, Zurich, 2011.

[160] C. L. Arneson, M. S. Durken, R. E. Benedict, R. S. Kirby, M. Yeargin-Allsopp, K. Van Naarden Braun and N. S. Doernberg, "Prevalence of cerebral palsy: Autism and development disabilities monitoring network," *Disability and Health Journal,* vol. 2, no. 1, pp. 45-48, 2009.

[161] "Data & statistics for cerebral palsy," Centeres for Disease Control and Prevention (CDC), 31 7 2015. [Online]. Available: http://www.cdc.gov/ncbddd/cp/data.html. [Accessed 2 3 2016].

[162] N. Paneth, T. Hong and S. Korzeniewski, "The descriptive epidemiology of cerebral palsy," *Clinics in perinatology,* vol. 33, no. 2, pp. 251-267, 2006.

[163] R. D. Tugui and D. Antonescu, "Cerebral Palsy, Clinical Importance," *Maedica a Journal of Clinical Medicine,* vol. 8, no. 4, pp. 388-393, 2013.

[164] C. Morris, "Orthotic management of children with cerebral palsy," *Journal of Prosthetics and Orthotics,* vol. 14, no. 4, pp. 150-158, 2002.

[165] M. A. Brehm, J. Harlaar and M. Schwartz, "Effect of ankle-foot orthoses on walking efficiency and gait in children with cerebral palsy," *Journal of Rehabilitation Medicine,* vol. 40, no. 7, pp. 529-534, 2008.

[166] A. J. Ries, A. J. Rozumalski, M. H. Schwartz and T. N. Novacheck, "Do ankle-foot orthoses improve gait for indviduals with cerebral palsy," in *Abstracts of the American Academy for Cerebral Plasy and Development Medicine 66th Annual Meeting*, Toronto, 2012.

[167] E. M. Figueiredo, G. B. Ferreira, R. C. M. Moreira, R. N. Kirkwood and L. Fetters, "Efficacy of ankle-foot orthoses on gait of children with cerebral palsy: systematic review of the literature," *Pediatric Physical Therapy,* vol. 20, no. 3, pp. 207-223, 2008.

[168] C. Morris, "A review of the efficacy of lower-limb orthoses used fro cerebral palsy," *Developmental Medicine & Child Neurology,* vol. 44, no. 3, pp. 205-211, 2002.

[169] D. J. Bregman, A. Rozumalski, D. Koops, V. Groot, M. Schwarts and J. Harlaar, "A new method for evaluating ankle foot orthosis characteristics: Bruce," *Gait & Posture,* vol. 30,

no. 2, pp. 144-149, 2009.

[170] I. Gibson, D. Rosen and B. Stucker, Additive Manufacturing Technologies, New York: Springer, 2005.

[171] Y. Youngian, L. Shengije, Z. Renji, L. Feng, W. Rendong, L. Qingping, X. Zhuo and W. Xiaohong, "Rapid Prototyping and Manufacturing Technology: Principle, Representative Technics, Application, and Development Trends," *Tsinghua Science and Technology,* vol. 14, no. 1, pp. 1-12, 2009.

[172] A. Ostendorf and B. N. Chichkov, "Two-Photon Polymerization: A New Approach to Mircomachining," *Photonics Spectra,* 2006.

[173] M. Larsson, U. Lindhe and O. Harrysson, "Rapid Manufacturing with Electron Beam Melting (EBM)-A manufacturing revolution," Arcam, 2003.

[174] Y.-a. Jin, J. Plott, R. Chen, J. Wensman and A. Shih, "Additive Manufacturing of Custom Orthoses and Prostheses- A Review," *Procedia CIRP,* vol. 36, pp. 199-204, 2015.

[175] J. Pallari, K. W. Dalgarno, J. Munguia, L. Muraru, L. Peeraer, S. Telfer and J. Woodburn, "Design and additive fabriction of foot and ankle-foot orthosis," in *Proceedings of the 21st Annual Internation Solit Freeform Fabrication Symposium-An Additive Manufacturing Conference*, Austin, 2012.

[176] J. Pallari, K. Dalgarno and J. Woodburn, "Mass customization of foot orthoses for rheumatoid arthritis using selective laser sintering," *IEEE Transactions on Biomedical Engineering,* vol. 57, no. 7, pp. 1750-1756, 2010.

[177] M. C. Faustini, R. R. Neptune, R. H. Crawford and S. J. Stanhope, "Manufacture of passive dynamic ankle-foot orthosis using selective laser sintering," *IEEE Transactions on Biomedical Engineering,* vol. 55, no. 2, pp. 784-790, 2008.

[178] E. S. Schrank and S. J. Stanhope, "Dimensional accuracy of ankle-foot orthoses constructed by rapid customization and manufacturing framework," *Journal of Rehabilitation Research & Development,* vol. 48, no. 1, pp. 31-42, 2011.

[179] S. Telfer, J. Pallari, J. Munguia, K. Dalgarno, M. McGeough and J. Woodburn, "Embracing additive manufacture: implication for foot and ankle orthosis design," *BMC Musculoskeletal Disorders,* vol. 13, no. 84, pp. 13-84, 2012.

[180] E. S. Schrank, L. Hitch, K. Wallace, R. Moore and S. J. Stanhope, "Assessment of a virtual

functional prototyping process for rapid manufacture of passive-dynamic ankle-foot orthoses," *Journal of Biomechanical Engineering,* vol. 135, no. 10, pp. 101011-7, 2013.

[181] D. E. Cooper, M. Stanford, K. A. Kibble and G. J. Gibbons, "Additive manufacturing for product improvement at Red Bull Technology," *Materials & Design,* vol. 41, pp. 226-230, 2012.

[182] T. J. Horn and O. L. Harrysson, "Overview of current additive manufacturing technologies and selected applications," *Science Progress,* vol. 95, no. 3, pp. 255-282, 2012.

[183] L. Love, "Fluid Power Applications for Emerging Trends in Additive Manufacturing," U.S. Department of Energy, Oak Ridge, 2013.

[184] E. Ackerman, "What Boston Dynamics Is Working on Next," IEEE Spectrum, 2015.

[185] S. Hwang, J. Kim, J. Yi, K. Tae, K. Ryu and Y. Kim, "Development of an active ankle foot orthosis for the prevention of foot drop and toe drag," in *International Conference on Biomedical and Pharmaceutical Engineering*, Singapore, 2006.

[186] M. A. Alexander and D. J. Matthews, Pediatric Rehabilitation-Principles and Practice, New York: Demos Medical Publishing, 2015.

[187] "National Center for Health Statictics-CDC growth charts," U.S. Department of Health & Human Services, Alanta, 2010.

[188] K. P. Granata, M. F. Abel and D. L. Damiano, "Joint angular velocity in spastic gait and the influence of muscle-tendon lengthening," *The Journal of Bone & Joint Surgery,* vol. 82, no. 2, pp. 174-186, 2000.

[189] L. C. Boucher, M. W. Chaudhari, Y. S. Kang and J. Bolte IV, "Range of motion and stiffness of pediatric ankle and implications for current ATDs," in *International Research Council on the Biomechanics of Injury*, Gothenburg, 2013.

[190] H. B. Skinner and R. L. Barrack, "Ankle weighting effect on gait in able-bodied adults," *Archives of Physical Medicine & Rehabilitation,* vol. 71, no. 2, pp. 112-115, 1990.

[191] D. A. Winter, H. G. Sidwall and D. A. Hobson, "Measurement and reduction of noise in kinematics of locomotion," *Journal of BioMechanics,* vol. 7, no. 2, pp. 157-159, 1974.

[192] K. Wen, D. Necsulescu and J. Sasiadek, "Haptic force control based on impediance/admittance control aided by visual feedback," *Multimedia Tools and*

Applications, vol. 37, no. 1, pp. 39-52, 2008.

[193] M. V. Sivaselvan, A. M. Reinhorn, X. Shao and S. Weinreber, "Dynamic force control with hydraulic actuators using added compliance and displacment compensation," *Earthquake Engineering and Structural Dynamics,* vol. 37, no. 15, pp. 1785-1800, 2008.

[194] "Raytheon XOS exoskeleton, second-generation robotics suit," 2015. [Online]. Available: http://www.army-technology.com/projects/raytheon-xos-2-exoskeleton-us.

[195] L. Love, R. Lind and J. F. Jansen, "Mesofluidic actuation for articulated finger and hand prosthetics," in *IEEE Conference on Intelligent Robot and Systems*, 2009.

Appendix

A.3.1 Hydraulic cylinder design

This section describes how hydraulic cylinder wall and piston thicknesses were calculated to estimate cylinder weight in section 3.2.1.

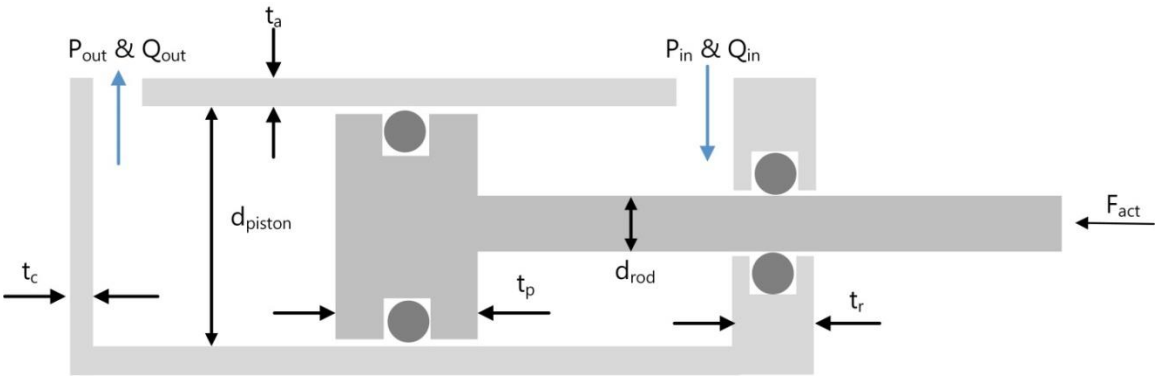

Figure A.1 Cylinder cross-section and dimension

The thicknesses of the cylinder piston and rod end walls t_c and t_r and the piston thickness t_p are calculated using thin plate formulas from [4] where N_{hyd} is the hydraulic safety factor, P_{max} maximum actuator pressure, ν is poisson's ratio, and the yield strength σ_y of cylinder material.

$$t_c = \sqrt{\frac{3 \cdot d_{bore}^2 N_{hyd} \cdot P_{\max} \cdot (\nu + 1)}{32 \cdot \sigma_y}} \quad \text{(A1)} \qquad t_r = \sqrt{\frac{3 \cdot N_{hyd} \cdot P_{\max} \cdot X}{4 \cdot \nu \cdot \sigma_y}} \quad \text{(A2)}$$

$$t_p = \sqrt{\frac{3 \cdot N_{hyd} \cdot P_{\max} \cdot \nu \cdot Y}{4 \cdot \sigma_y}} \quad \text{(A3)}$$

$$X = \frac{d_{rod}^4 \cdot (1-\nu) - 4 \cdot d_{rod}^4 (1+\nu) \log \frac{d_{bore}}{d_{rod}} + d_{bore}^2 \cdot d_{rod}^2 (1+\nu)}{4D_{bore}^2 (1-\nu) + 4D_{rod}^2 (1+\nu)} + \frac{d_{bore}^2}{4} - \frac{d_{rod}^2}{2} \quad \text{(A4)}$$

$$Y = \frac{4d_{rod}^4 (1+\nu) \log \frac{d_{bore}}{d_{rod}} + 4\nu d_{bore}^2 \cdot d_{rod}^2 (1-\nu) - d_{bore}^4 (1+3\nu)}{4\nu \left(d_{bore}^2 - d_{rod}^2\right)} \quad \text{(A5)}$$

A.3.2 Axial piston pump scaling validation

In order to validate the axial piston pump model, the simulation results were compared to commercial pumps to ensure the pump was scaling appropriately with flow rate requirements. The following figures A.3.2 and A.3.3 illustrate a weight comparison between the modeled and measured components within the axial piston pumps.

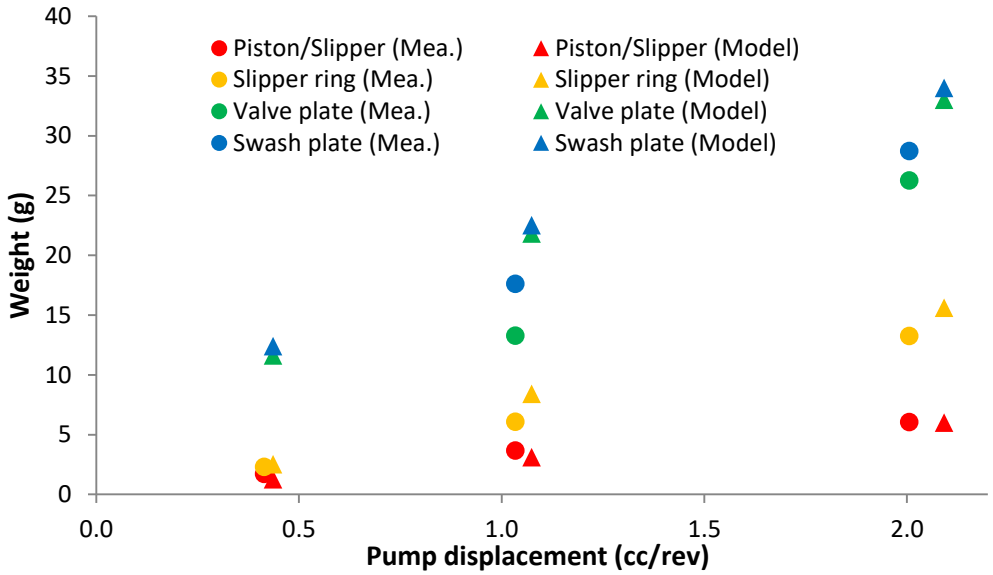

Figure A.2 Axial piston pump component weights

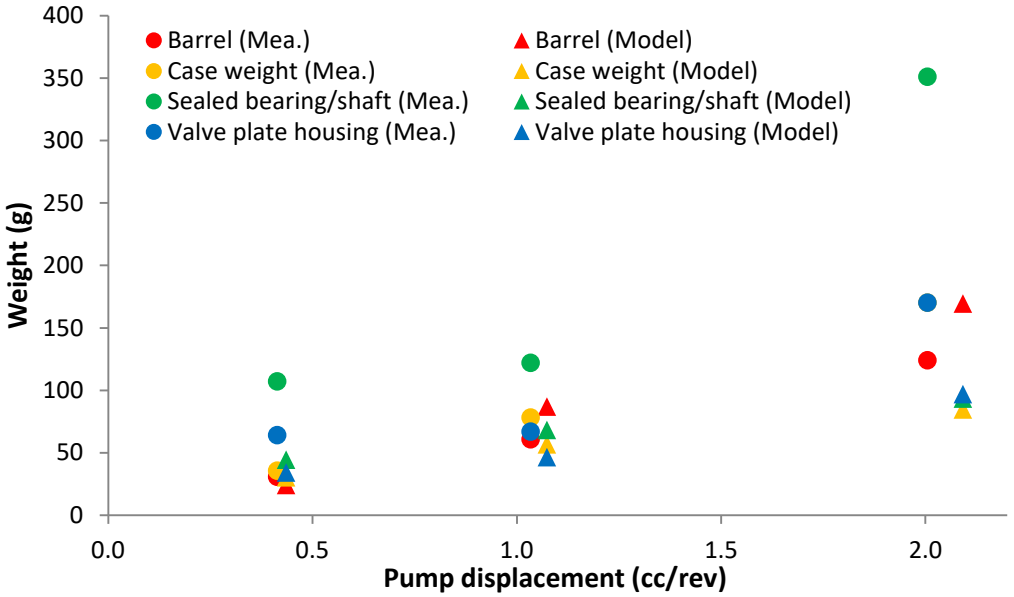

Figure A.3 Axial piston pump component weights

A.3.3 Commerical motor data

Figures A.3.4 and A.3.5 illustrate DC brushless pump catalog data from the manufactures of Maxon Motors, MicroMo, and Applied Motion Products. The linearly fit relating nominal motor power with mass was found to have a high correlation coefficient of 0.95.

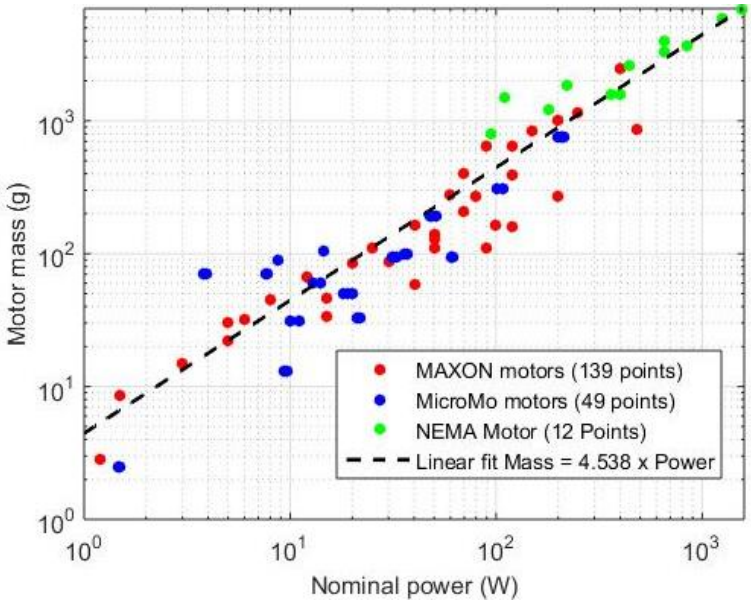

Figure A.4 Comparison of commercial brushless DC motor nominal power and mass

The correlation between nominal power and maximum efficiency was found to be exponential with a fit of 0.87.

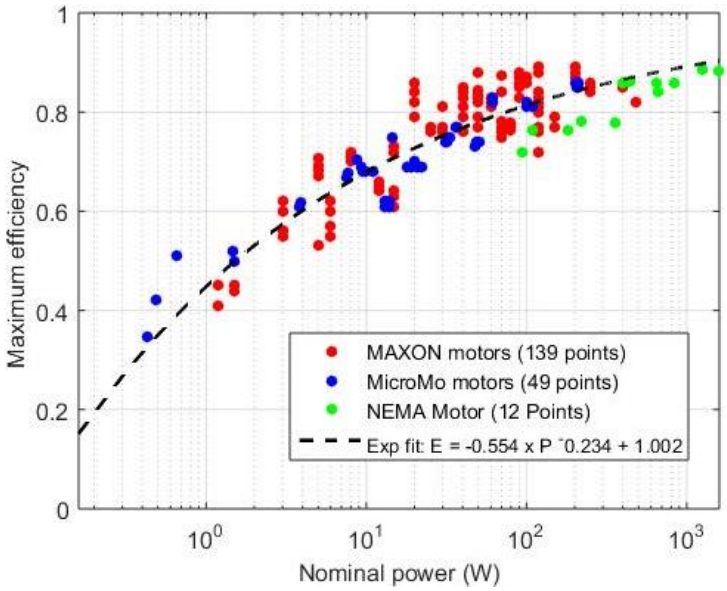

Figure A.5 Comparison of commercial brushless DC motor nominal power and maximum efficiency

A.3.4 Commercial battery data

Figures A.3.6 and A.3.7 compare different battery technologies using listed commercial capacities, weight, and volume data. The volumetric and weight energy densities of the battery technology recorded in table 3.3 were determined by fitting a best fit line to the data in figures A.3.6 and A.3.7.

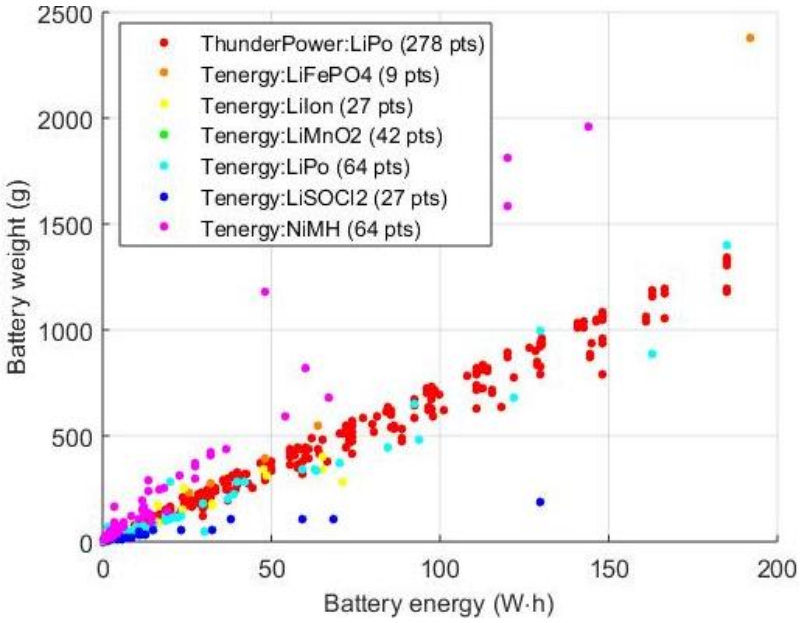

Figure A.6 Battery energy capacity vs weight

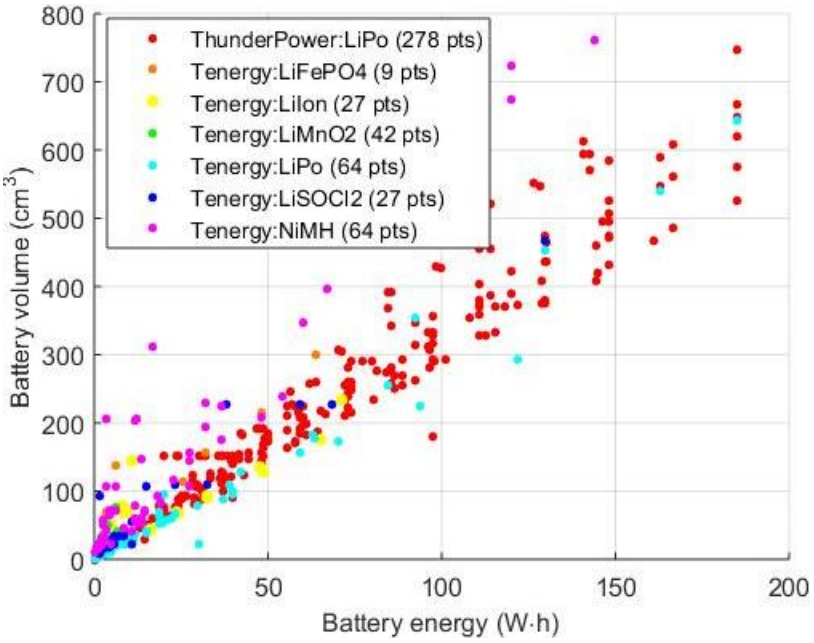

Figure A.7 Battery energy capacity vs volume

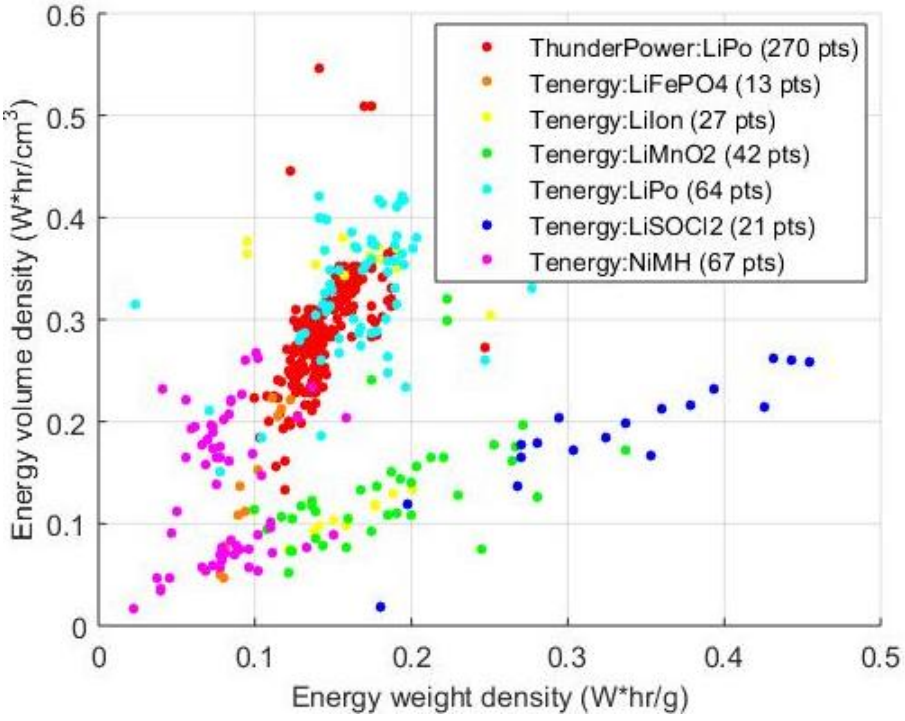

Figure A.8 Volumetric energy density vs. weight energy density for different battery technologies

A.4.1 Electrical design for hydraulic circuit validation test stand

The following section illustrates the electrical design of the validation test stand. This includes the design of a ±10 mA current control system for the torque motor in the servo valve (Fig. A.4.1). The motor controller and servo valve are controlled with digital to analog converters (DAC) connected to an Arduino microcontroller using SPI communication. The motor controller and valve input signals were filtered with a first order RC filter to reduce noise within the system.

Table A.1 Arduino and DAQ inputs & output pins for validation test stand

Arduino analog		**Arduino digital**		**DAQ USB-6002**	
1	Pressure (top)	2	LED Indicator	0	Potentiometer
2	System pressure	3	SS DAC 2	4	System pressure
3	Pressure (bottom)	6	SS Counter	1/5	Servo valve current
4	Potentiometer	9	SS DAC 1	2	Motor velocity
5	Force gauge	10	SS DAC 3	6	Pressure (bottom)
		11	MOSI	3	Pressure (top)
		12	MISO	7	Force gauge or Motor current
		13	SCK		

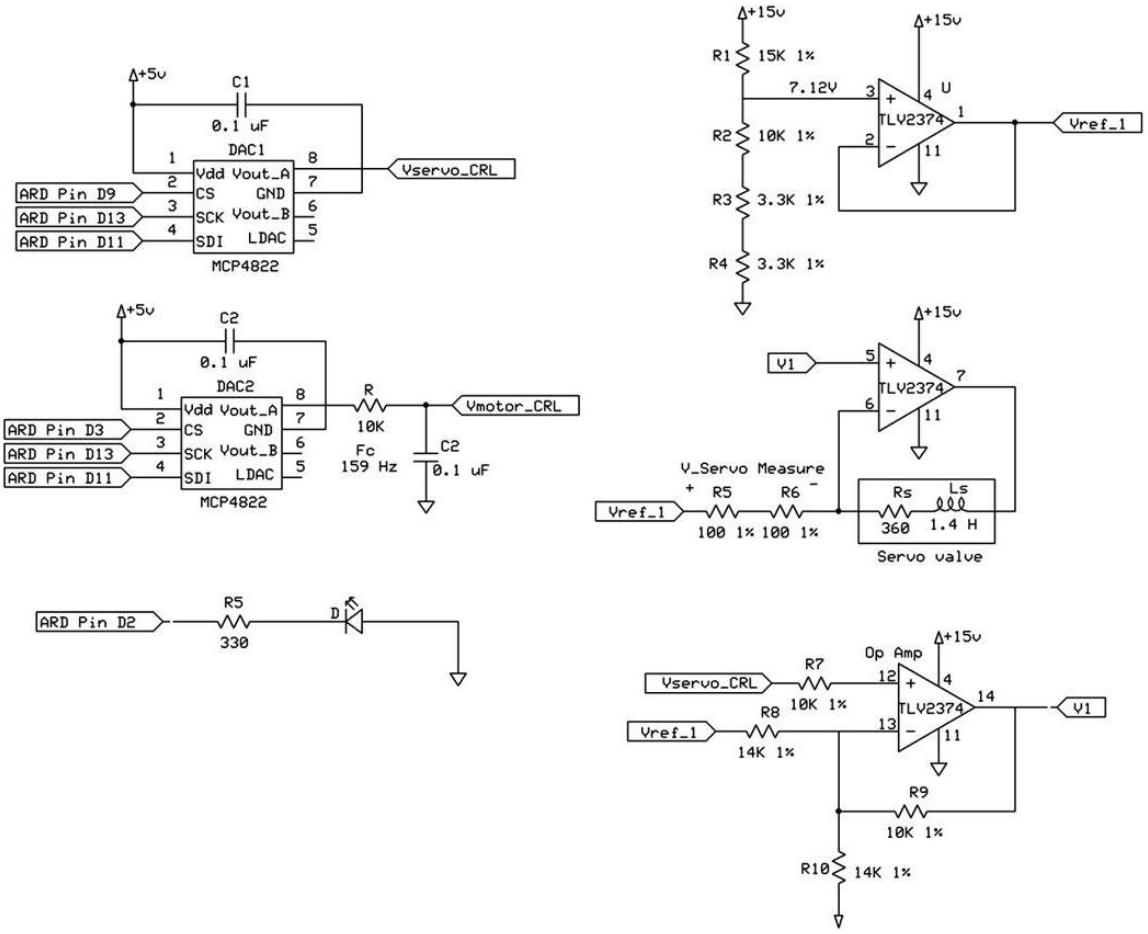

Figure A.9 Electrical schematic: Digital control of servo valve and motor

An optical encoder is used to measure the position of the pump shaft with an accuracy of 1000 clicks per revolution (CPR). The quadrature signal is decoded and counted, and the information is sent digitally to the Arduino microcontroller using SPI communication (Fig. A.4.2).

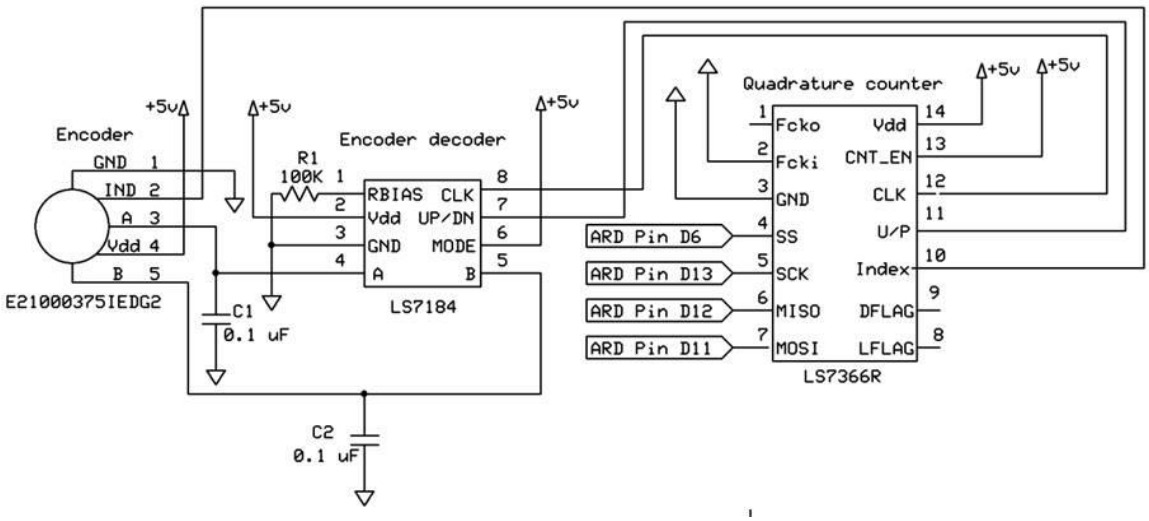

Figure A.10 Electrical schematic: Pump shaft angular position measurement with optical encoder

The motor controller current was measured by placing a power resistor in series with the motor controller. The negative voltage drop measured across the resistor is magnified by a factor of -4 by an inverting operational amplifier. The amplified signal voltage was filtered using a first order RC filter with a 106 Hz cut-off-frequency.

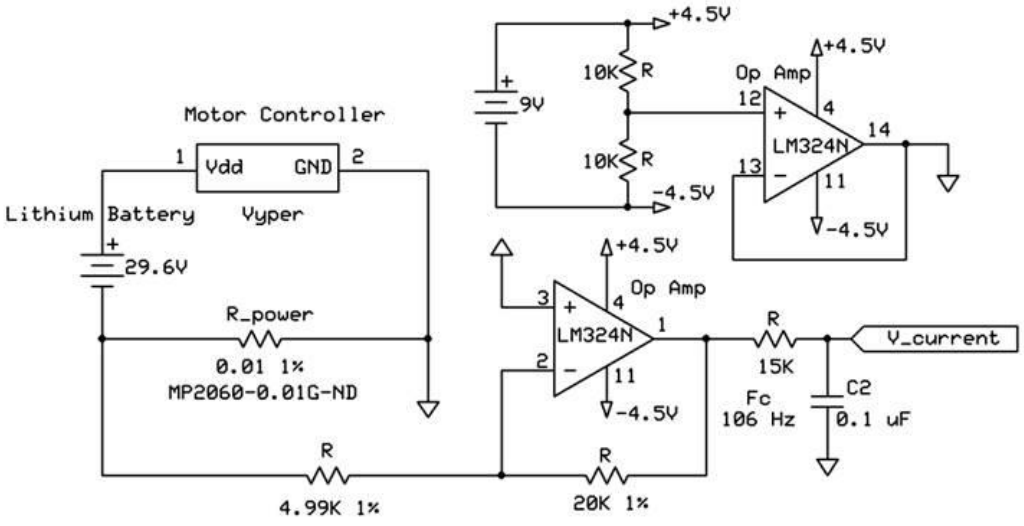

Figure A.11 Electrical schematic: Motor controller current amplification and measurement

The force generated by the hydraulic cylinder was measure by a force gauge with a 1000 lb capacity. The millivolt signal generated by the force gauge was magnified by a factor of 85 with an instrumentation amplifier (Fig A.4.4).

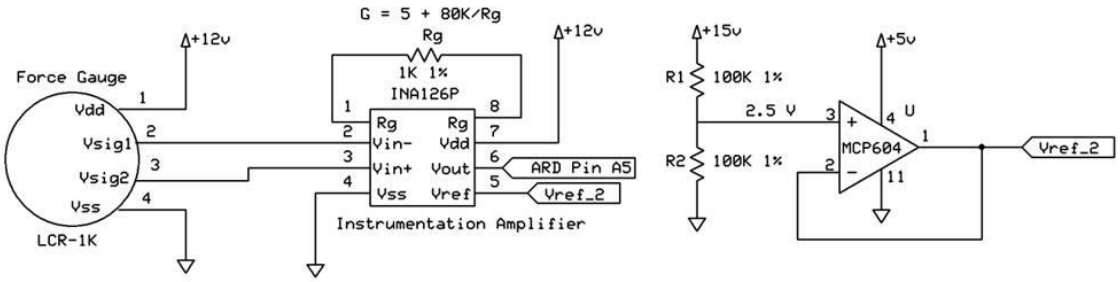

Figure A.12 Electrical schematic: Force gauge signal amplification and measurement

The system, cap, and rod side pressure were measured using three analog pressure transducers, while the piston position was measured with a linear potentiometer.

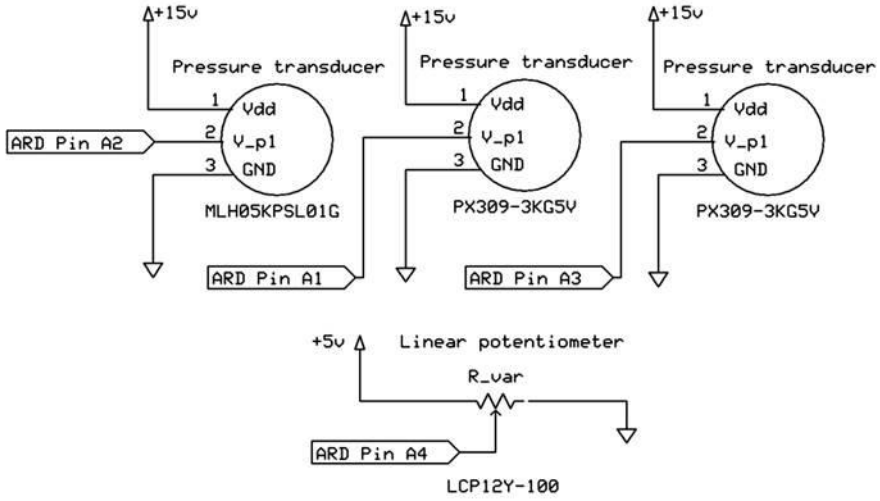

Figure A.13 Electrical schematic: Piston position and pressure sensors

A.4.2 Custom dynamic component models for the simulation of small-scale hydraulic systems

Electric motor

In the simulations the electric motor is modeled as a voltage controlled DC motor with a resistance R, inductance L, and a counter electromotive force (EMF) all in series (A6) (Fig. A.4.6). The counter EMF is modeled with equation (A7), where the counter EMF voltage (V_m) is proportional to the motor shaft velocity ω. The torque generated by the motor T_m is assumed to be proportional to current (i) (A7). Finally, a torque balance is applied to the motor shaft taking into consideration bearing friction T_F, shaft inertia J, load torque from the gearbox and pump T_L,

and the torque supplied by the motor (A8). If motor was controlled by varying the current, the motor dynamics are simplified due to the current being equal is series elements. All the parameters of the electric motors were measured or listed on the manufacturer specification sheets.

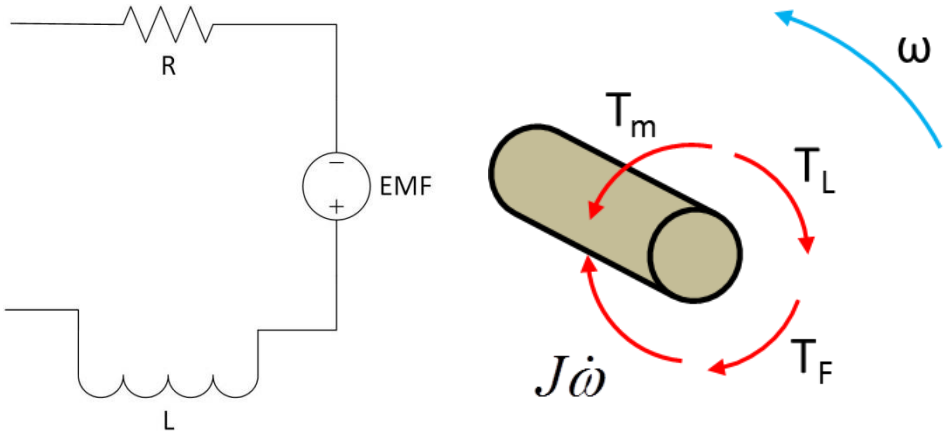

Figure A.14 Electric motor dynamics

$$V_s = Ri + L\frac{di}{dt} + K\omega \quad \text{(A6)} \qquad V_m = K_m\omega \quad \text{(A7)} \qquad T_m = K_m i \quad \text{(A8)}$$

$$T_m = J\dot{\omega} + T_F + T_L \quad \text{(A9)}$$

Inverse shuttle valve

An inverse shuttle valve is a three way valve with two controlling ports and a passive port. A standard shuttle valve functions to connect the high pressure control port with the passive port, whereas an inverse shuttle valve connects the low pressure control port to the passive port. In the model of an inverse shuttle valve the controlling pressure P_c is the difference of the two inlet port pressures P_1 and P_2 (A10). A comparison of the control pressure and the valve's specified cracking and opening pressures P_{crack} and P_{open} adjusts the control member and the two orifice areas A_1 and A_2 at the control ports (A11-A13). The flow rates through the inlet ports are calculated using the standard orifice model along with knowing the orifices maximum area A_{max}, discharge coefficient C_d, and leakage area A_{leak}.

$$P_c = P_1 - P_2 \quad \text{(A10)} \qquad A_1 = \begin{cases} A_{leak} & p_c \geq p_{crack} \\ A_{leak} + k \cdot (p_c - p_{crack}) & p_{crack} < p_c > (p_{crack} + p_{open}) \\ A_{\max} & p_c \leq (p_{crack} + p_{open}) \end{cases}$$

(A11)

$$A_2 = \begin{cases} A_{leak} & p_c \le (p_{crack} + p_{open}) \\ A_{leak} + k \cdot (p_c - p_{crack}) & p_{crack} > p_c < (p_{crack} + p_{open}) \\ A_{\max} & p_c \ge p_{crack} \end{cases} \quad \text{(A12)}$$

$$k = \frac{A_{\max} - A_{leak}}{p_{open}} \quad \text{(A13)}$$

Spring loaded accumulator

The reservoir and piston within a spring loaded accumulator are modeled as a traditional single acting hydraulic cylinder. The preloaded spring within the accumulator is modeled as the summation of a constant force and a spring. The steady state force balance between port pressure P and spring force in the accumulator is a function of fluid displacement V_d, piston area A_P, spring constant K, and the spring preload force F_p (A14). The spring preload force sets the minimum pressure that will charge the accumulator. The spring stiffness constant and piston area determine the gain between fluid displacement and port pressure. The energy stored in the accumulator E is equivalent to the spring force integrated over displacement (A15).

$$\frac{P}{A_p} = \frac{K}{A_p} V_d + F_p \quad \text{(A14)} \qquad E = \int F_s dx = \frac{1}{2} K \Delta x^2 + F_p \Delta x \quad \text{(A15)}$$

A.4.3 Supplemental materials for dynamic model validation

Figure A.15 and A.16 are comparisons between the measured and simulated responses of a needle valve loaded bidirectional pump discussed in section 4.3.1. In figures A.15 and A.16 the brushed DC motor is being supplied 12.6 V and 14.6V. The needle valve setting was held constant, so that higher flow rate generated a larger pressure drop with a constant orifice area. Simulation 1 neglects hose compliance and fluid inertia while simulation 2 takes these dynamics into consideration.

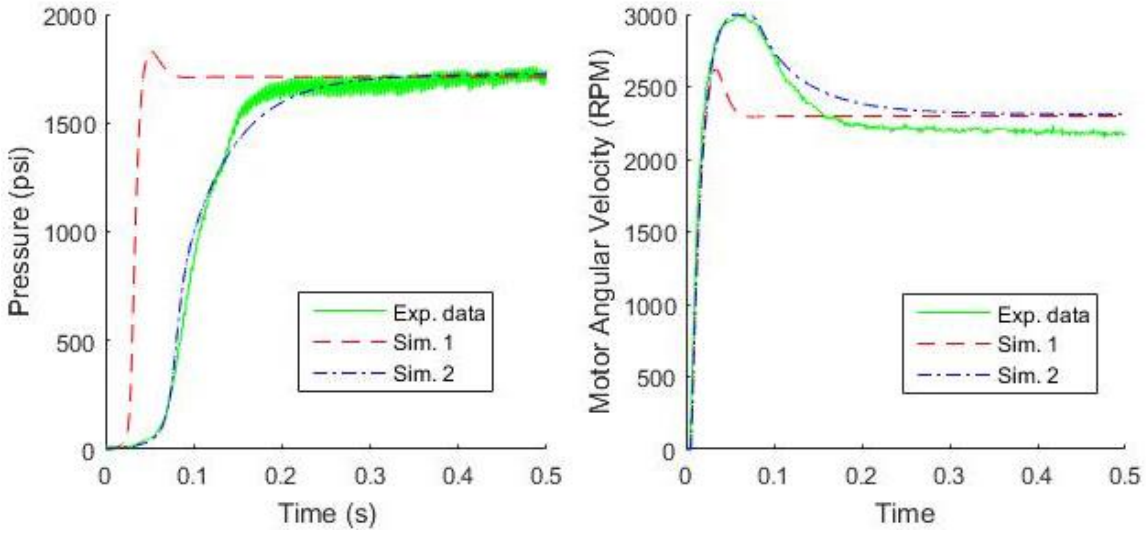

Figure A.15 Comparison of measured and simulated response of a needle valve loaded bidirectional pump (Motor voltage 12.6V)

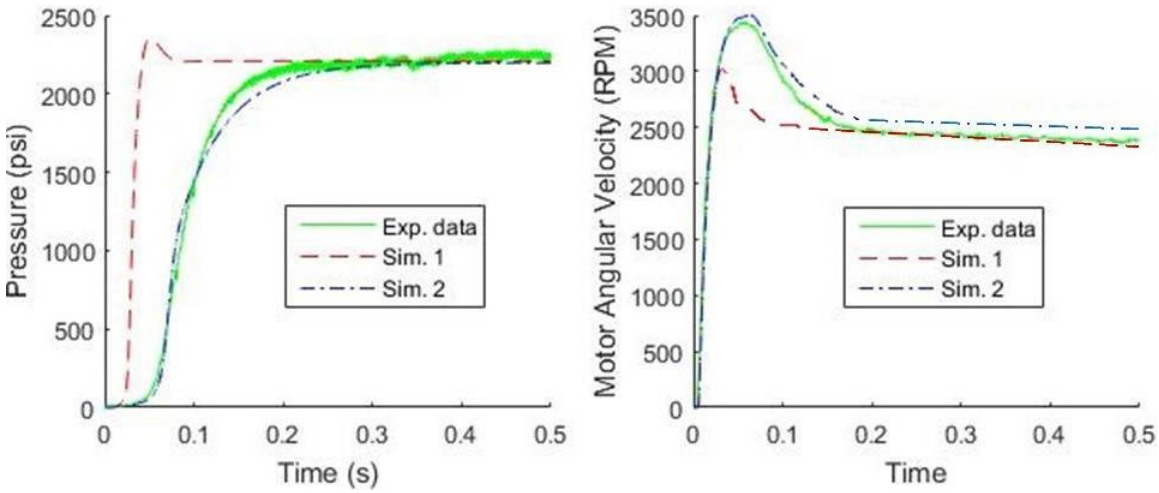

Figure A.16 Comparison of measured and simulated response of a needle valve loaded bidirectional pump (Motor voltage 14.6V)

Both data sets illustrate that the simulation 2 is an accurate representation of the dynamic performance of the needle valve loaded bidirectional pump. The data sets also illustrate the significant influence hose compliance and fluid inertia have in delaying the response of small-scale hydraulic systems.

A.6.1 Analysis of HAFO actuator configuration

The hydraulic cylinder manifolds on the medial and lateral sides of the HAFO house two identical bore and length cylinders that were angled in a 22° V-shape that mirrored across the frontal plane. There are two main reasons why linear cylinders were used as opposed to rotary actuators. The size of the ankle actuators is smaller than commercially available actuators; therefore, the actuator housings will have to be custom designed and machined. Rotary hydraulic actuators or motors typically involve sealed bearings, custom seal interfaces, and high tolerance machining making these components heavy and expensive to manufacturer. In contrast, there is a good selection of commercially available seals for linear cylinders. A linear cylinder can be constructed with a simple milling operation, using a high tolerance reamer. The second reason for using linear as opposed to rotary actuators is the ability to place the actuator as close to the body as possible. Linear cylinders can be position along the sides of the shin or calf making a compact width profile, while rotary actuators must be connected directly to the sides of the ankle at the center of rotation (COR), creating a wide and bulky profile.

The main objective of the ankle actuator assembly is to biomimic the torque generation and range of motion (ROM) of healthy muscle tissue, tendons, and ligaments at the ankle; so the actuators need to replicate physical traits and capabilities of this system. In the cylinder assemblies, the piston is connected to the ankle pulley using a flexible nylon coated steel cable replacing the rigid rod. The nylon coated steel cable is capable of better replicating the capabilities and dynamics of flexible tendons. The cylinders assemblies can only be used to generate a tension force in the cable, because the stainless steel cable is not cable of holding axial compression loads. The cable cylinder assemblies better replicate the dynamics of muscle tissue by only providing a tensional force in contraction. The nylon coated cable is wrapped around a thin pulley at the COR to convert the linear force of the cylinders to torque at the ankle, eliminating the need for a heavy linkage.

There were three cylinder assembly configurations considered. The linear cylinder could be positioned on the medial or lateral sides of the ankle or both sides. A third configuration analyzed was centering the cylinder behind the calf. The reason for not placing the actuator on the front of the foot is to avoid interfering with the tongue of shoes. The HAFO should be able to be worn without modifying the shoes and needs to fit under traditional clothing.

In order to decide whether to position the hydraulic cylinders on the lateral and/or medial sides of the ankle or centered behind the calf, the geometries were modeled and compared to determine the basic dimensions. In figures A.14 and A.15 the anthropometric dimensions and design variables are shown for the cylinder assemblies placed on the sides of the ankle and the other centered on the calf. The three anthropometric dimensions are based on a sampling of measurements. The perpendicular height from the bottom surface of the sole to the COR of the ankle is H = 10 cm. The length from the back of the heel to the COR parallel to the base of the

foot is L_A = 7 cm. The moment arm R of the ankle joint is limited in size if the packaging of the actuator assemblies is to fit within a normal unaltered shoe. The moment arm is constrained to be 3 cm.

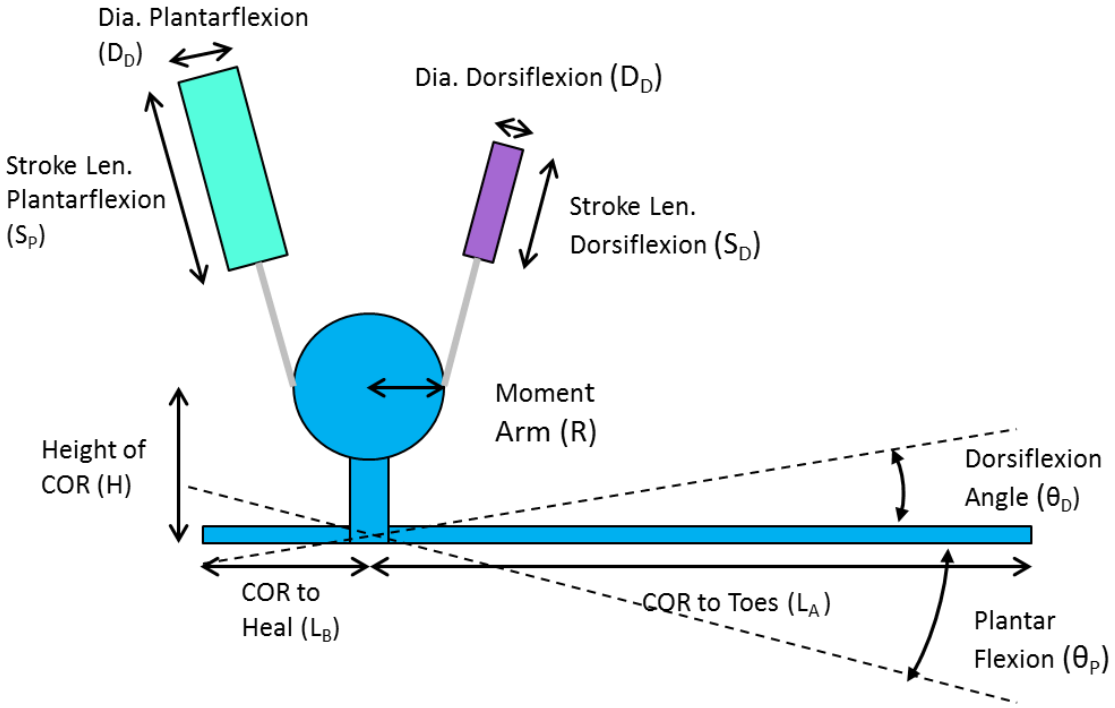

Figure A.17 Geometric model of cylinders positioned on lateral side of the ankle

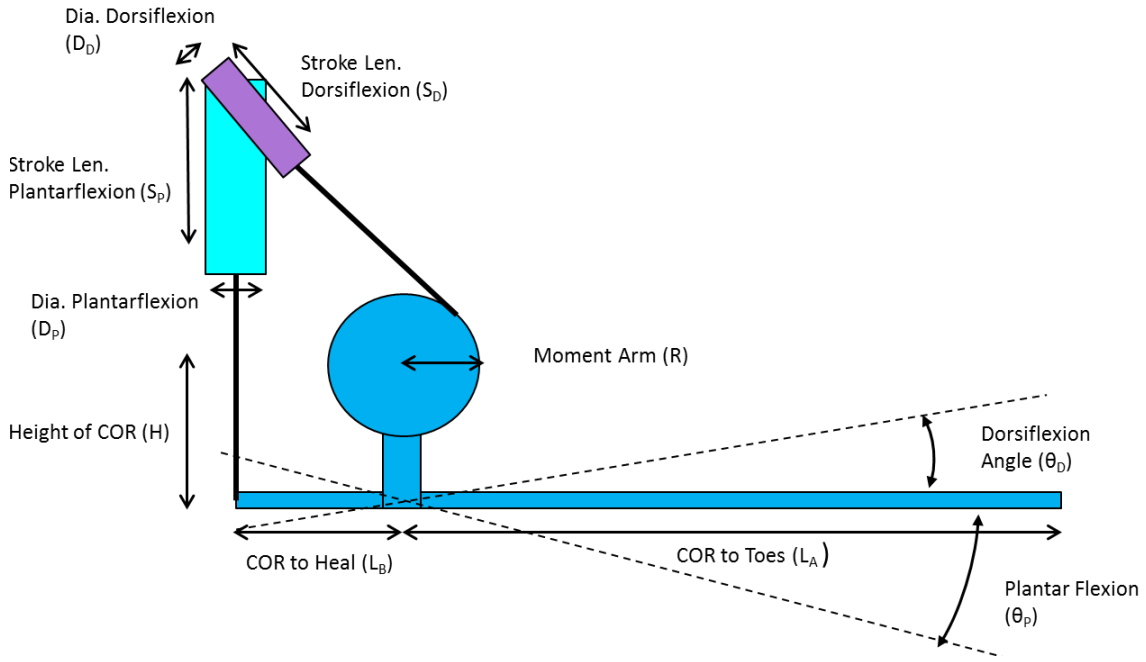

Figure A.18 Geometric model of cylinders positioned at central calf

Using geometric relations and element laws, the required tension force ($F_{D,P}$) in the cable during dorsiflexion and plantar flexion for the lateral configuration was calculated using (A16) where $T_{D,P}$ is the required torque generation based on the design requirements in table 6.1. The tension force in the cable during dorsiflexion for the central calf configuration is the same as the lateral configuration. The maximum tension force for plantar flexion for the central calf configuration can be approximated with (A17). The central calf configuration has a variable moment arm, and the tension is at a maximum at the end of plantar flexion (θ_P = 50°).

The diameter of the cylinder ($D_{D,P}$) required to generate the torque for dorsiflexion and plantar flexion at a pressure of P= 2000 psi can be calculated using eq. (A18) where D_c is the diameter of the cable. The diameter of the cable (D_c) was determine based on comparing the breaking strength of commercially available nylon coated steel cables and the tension required in the cable with a minimum safety factor of 2. The stroke length ($S_{D,P}$) for the lateral/medial configuration dorsiflexion and plantar flexion along with the dorsiflexion of the central heel configuration can be calculated using (A19) where θ_P = 50° and θ_D = 20°. Finally the stroke length for plantar flexion of the central ankle configuration can be approximated with (A20).

$$F_{D,P} = \frac{T_{D,P}}{R} \quad \text{(A16)} \qquad F_P \approx \frac{T_P}{\sqrt{L_A^2 + H^2}\cos\left(\frac{\pi}{2} - \theta_P - \tan^{-1}\left(L_A/H\right)\right)} \quad \text{(A17)}$$

$$D_{D,P} = \sqrt{\frac{4F_{D,P}}{\pi P} + D_C^2} \quad \text{(A18)} \qquad S_{D,P} = R\theta_{D,P} \quad \text{(A19)} \qquad S_P \approx \tan(\theta_P) L_A \quad \text{(A20)}$$

A third configuration explored was positioning cylinders on the medial and lateral sides of the ankle. All the same equations used to calculate the lateral configuration can be used to calculate the dimensions of the medial/lateral configuration starting with half the required torque. The results are summarized in the table A.2 below.

Table A.2 Comparison of cylinder configurations in HAFA

Cylinder Position	Action	Cable Tensions N (lb)	Diameter of Cylinder cm (in)	Stroke Length of Cylinder cm (in)
Lateral Ankle Position	Plantar Flexion	3000 (674)	1.66 (0.655)	2.62 (1.03)
	Dorsiflexion	333 (75)	0.55 (0.218)	1.05 (0.412)
Central Calf Position	Plantar Flexion	740 (166)	0.83 (0.325)	8.34 (3.28)
	Dorsiflexion	333 (75)	0.55 (0.218)	1.05 (0.412)
Lateral and Medial Ankle Position	Plantar Flexion	1500 (337)	1.18 (0.463)	2.62 (1.03)
	Dorsiflexion	167 (38)	0.32 (0.154)	1.05 (0.412)

The configuration with the cylinders positioned on the lateral side of the ankle has two main drawbacks. This configuration requires a cable tension of 3000 N (675 lb) during ankle plantar flexion. With a minimum safety factor of 2, the breaking strength of the nylon coated cable has to be greater than 6000 N (1350 lb). The smallest commercially available cable that meets this requirement is a 3/16 in. diameter nylon coated steel cable with breaking strength of 2000 lbs .

A cable bend radius/sheave diameter of 3.75 in. only harnesses 90% of the strength of this cable. Running a 3/16 in. cable around a pulley with a 2.4 in. (6 cm) diameter will significantly decrease the strength of the cable. The trade-off between the strength of the cable and the allowable bend radius does not make the lateral ankle position configuration feasible. Also the diameter of the cylinder is 0.66 in. If the HAFA sticks out from the lateral side of the ankle, the device will be bulky and not easily concealed under clothing.

The central calf position configuration has two discernible drawbacks. The first drawback is the central calf configuration has a variable length moment arm generating the torque at the ankle. This will make the modeling of the torque generation and the design of the HAFO controller more complex. The second drawback is that plantar flexion stroke length is considerably large, so the cylinder manifold will be long and heavy.

The lateral and medial ankle position configuration only requires half the cable tension force, and this leads to a cable breaking strength of greater than 3000 N (675 lb). The commercially available cable that has the highest breaking strength and smallest diameter that meets this requirement is a 1/8 in. diameter nylon coated steel cable with breaking strength of 1000 lbs. A cable bend radius/sheave diameter of 2.5 in. harnesses 90% of the strength of this cable. The breaking strength of the cable is not significantly reduced when the cable is wrapped around the 2.4 in. (6 cm). The dimension of the cylinders are also reasonable and do not require a bulky manifold.

In order to simplify the overall design, it was decided early in the design process to make the cylinders for dorsiflexion and plantar flexion the same bore size and length. If the stroke lengths are not equal, a clutch is required to compensate for the difference between dorsiflexion and plantar flexion stroke lengths. In addition, the HAFO controller will be easier to design, because a given fluid flowrate will correspond to the same piston velocity in both dorsiflexion and plantar flexion.

A.6.2 Material selection and structural analysis of HAFO

The materials of parts in the electrohydraulic power supply (EHPS) and the ankle actuator of the HAFO are selected by first defining a material property index for each assembly. In addition, the stresses and deflections of each part under the load requirements were calculated using body deformation mechanics and ANSYS simulations. A material was selected based on the material indices and a comparison of the observed simulated stresses and the yield stress of the material. In addition, these calculations and simulations were used to adjust dimensions and eliminate unnecessary material within the part.

An essential design requirement is that all components of the actuator can not yield against the loads that are generated with applying a 90 Nm torque. A second design requirement is that the

weight of the power supply and actuator assemblies should be minimized. Based on these two requirements, the material index selected is the ratio of material yield stress to density. Cost is not considered in the material index, because the volume of material need to machine the components for the actuator assemblies is fairly small compared to the machining labor cost.

After analyzing reference plots of this material index calculated for a variety of different material groups, the best materials groups for this application are aluminum alloys, composite materials, steel alloys and titanium alloys [15]. Ten commercially available alloys/materials from these categories were selected and the material density and yield stress are plotted in figure A.17 [16]. The best materials for EHPS and actuator assemblies have the highest material index and are located in the upper left hand corner of the plot. The composite carbon fiber is particularly brittle and not considered to have a yield stress, so the ultimate tensile strength parallel to the fiber was used. It is important to remember that strength of carbon fiber is significantly reduced when the load is not parallel to the fiber.

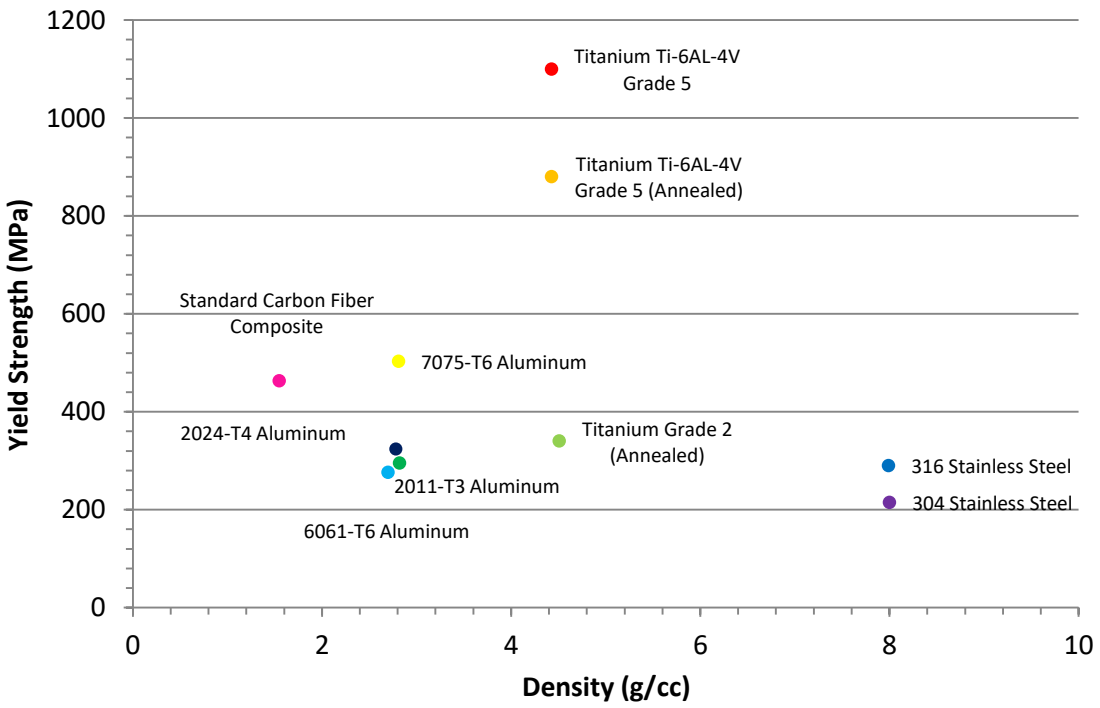

Figure A.19 Comparison of material indices (strength / density)

The cylinders experience a cyclic pressure of 14 MPa (2000 psi). The stresses around the cylinders were calculated and computer simulated to ensure safe operation. The axial σ_a, circumferential σ_c, and radial stresses σ_r in the cylinder walls are approximated with (A18-A21) where P_i is the fluid pressure inside, P_o is the outside fluid pressure, r_o is the outside radius, r_i is the inside radius, and r is the observation radius [17]. The stresses are maximum on the inside

wall, ($r = r_i$). The outside radius of the cylinder r_o is constrained to be 8.9 mm to allow a threaded cap to be installed on the front of the hydraulic cylinder. The inside radius is equal to the piston bore of 6.4mm (0.25 in). The Von Mises stress in the material are then calculated using eq. #9. The results of the calculations are show in table 4.

$$\sigma_a = \frac{P_i r_i^2 - P_o r_o^2}{r_o^2 - r_i^2} \quad \text{(A18)} \qquad \sigma_a = \frac{P_i r_i^2 - P_o r_o^2}{r_o^2 - r_i^2} - \frac{r_i^2 r_o^2 \left(P_o - P_i\right)}{r^2 \left(r_o^2 - r_i^2\right)} \quad \text{(A19)}$$

$$\sigma_a = \frac{P_i r_i^2 - P_o r_o^2}{r_o^2 - r_i^2} + \frac{r_i^2 r_o^2 \left(P_o - P_i\right)}{r^2 \left(r_o^2 - r_i^2\right)} \quad \text{(A20)}$$

$$\sigma_M = \sqrt{\frac{\left(\sigma_a - \sigma_r\right)^2 + \left(\sigma_r - \sigma_c\right)^2 + \left(\sigma_c - \sigma_a\right)^2}{2}} \quad \text{(A21)}$$

Table A.3 Stress in cylinder walls

Stress	Value (MPa/ksi)
Axial	14.4/2.08
Circumferential	42.5/6.17
Radial	-13.8/-2.00
Von Mises	48.8/7.08

Using a safety factor of 3, these calculations show that the cylinder material must have a yield stress above 146 MPa. The aluminum alloy 7075-T6 was selected due to the high material index, and the yield stress is above the calculated maximum Von Mises stress. Titanium alloys would also be a good candidate material; however, higher strength material is not required and the density is higher compared to aluminum 7075-T6. In addition, the machining costs are higher using titanium alloys as specific tooling is required for such high strength materials. The cylinder manifold has lots of intricate machining operations causing it to be significantly more expensive if it is machined out of titanium alloys.

In the simulation a rigidly joined actuator assembly is constructed with the cylinder manifold, shin support bar, cylinder caps, and the plugs. The top of the shin support bar is constrained to allow no movement, simulating it rigidly secured to the shin. The inside surfaces of the cylinder casing and bottoms of the cylinder caps are loaded with a 14 MPa (2000 psi) pressure. Only one cylinder is loaded with the pressure at a time to simulate normal operation. The cylinder manifold stresses are simulated using the material properties of aluminum 7075-T6.

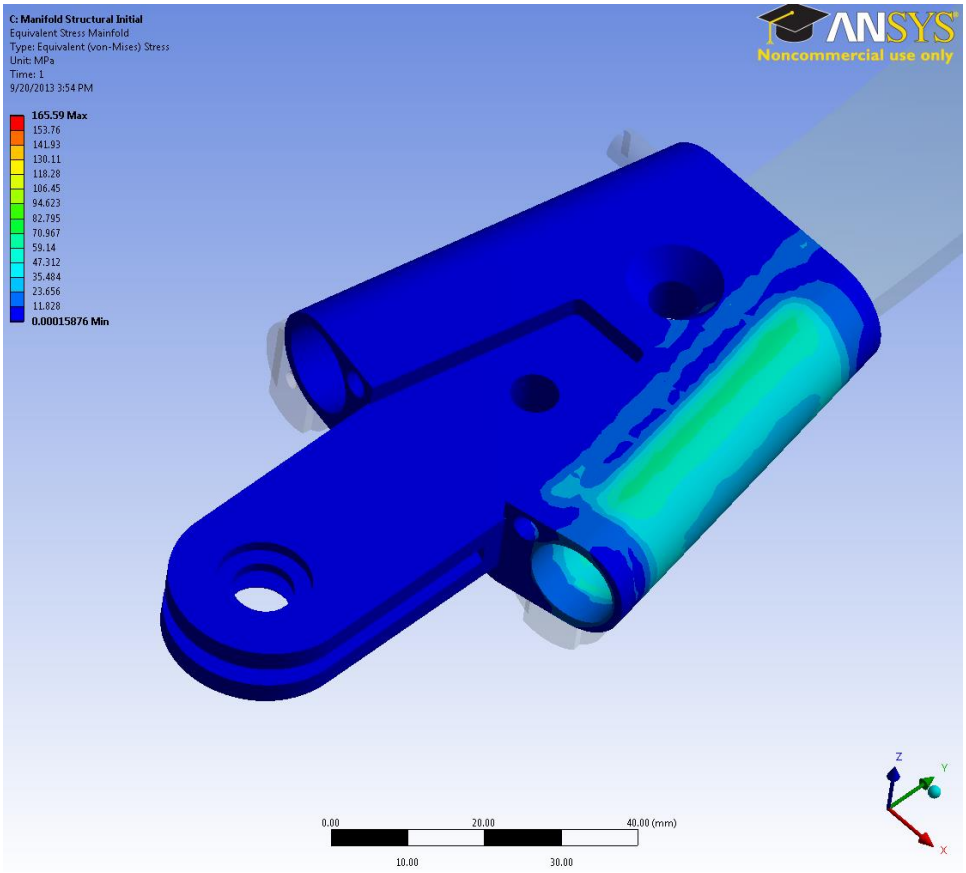

Figure A.20 Simulated Von Mises stress in cylinder manifold (Exterior view)

The simulation results in figures A.18 and A.19 show the maximum Von Mises stress in the cylinder walls is ≈ 70 MPa. The maximum Von Mises stresses in the simulation occur between the interface of the cylinder manifold and shin support bar. This is not a true representation of the stress in this region. There are artificial stress concentrations caused by the limited size and shape of the discretized elements. The stress in this region should be approximated with an average of ≈120 MPa. The simulated Von Mises stresses under maximum loading conditions of the cylinder manifold have a safety factor greater than 3 when compared to the yield stress of aluminum 7075-T6.

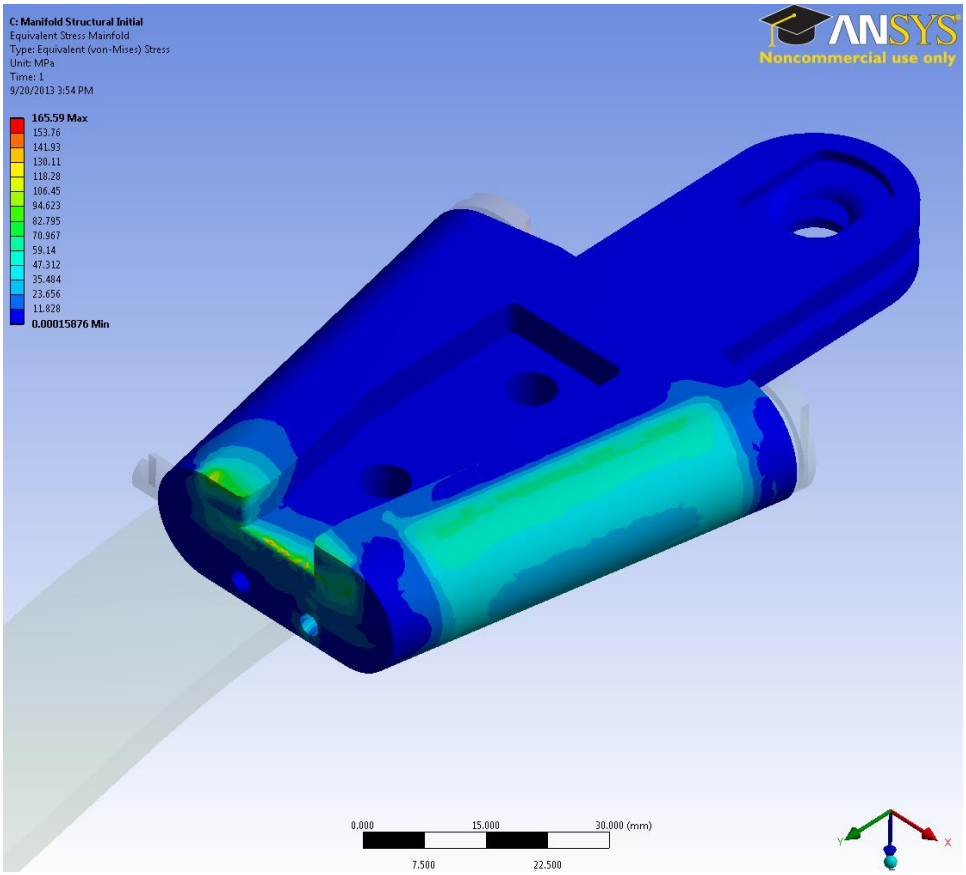

Figure A.21 Simulated Von Mises stresses in cylinder manifold (Interior view)

The shin support bar securing the cylinder manifold to the shin support experiences a cable tension force F during dorsiflexion and plantar flexion. The force and moment are modeled according to A.20. The normal stress σ_N in the shin support bar due to the cable tension can be calculated using (A22), where A is the cross-sectional area of the bar. The bending stress σ_B of the support bar can be calculated with (A23) where I is the moment of inertia, W is the width, and L is moment arm between the cable attachment and the middle of the shin support. The shear stress is negligible, because the angle of cable tension θ force is small. The maximum total stress σ in the shin support bar is located at the neck region connecting to the cylinder manifold (A24).

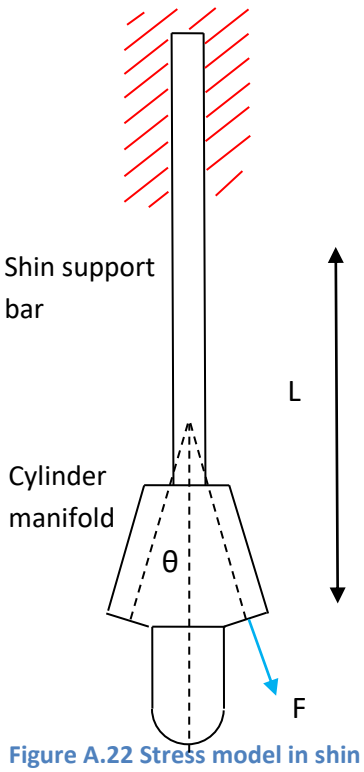

Figure A.22 Stress model in shin support bar

$$\sigma_N = \frac{F\cos(\theta)}{A} \quad \text{(A22)} \qquad \sigma_B = \frac{F\sin(\theta)L\left(W/2\right)}{I} \quad \text{(A23)}$$

$$\sigma = \sigma_B + \sigma_N \quad \text{(A24)}$$

Table A.4 Maximum stresses on the SSB

Cable Tension (F)	**Cable Angle (θ)**	**Cross-Sectional Area (A)**	**Length of Moment Arm (L)**
1500/337 (N/lbf)	11°	4.18 x 10^{-2} in^2	9.2 in
Width of SSB(W)	**Moment of Inertia (I)**	**Max Normal Stress (σ_N)**	**Max Bending Stress (σ_M)**
0.22 in	8.09 x 10^{-3} in^4	7.92/54.6 (ksi/MPa)	16.1/111 (ksi/MPa)

The total stress in the shin support bar is approx. ≈165.5 MPa. With a safety factor of 3, the support bar material requires a yield stress of above 496.5 MPa. The support bar is bent and machined out of aluminum 7075-T6, because it is the lightest material that meets the manufacturing and strength requirements.

The Von Mises stresses in the support bar were simulated during the maximum loading conditions (plantar flexion), and with the material properties of aluminum 7075-T6 (Fig. A21). The stresses in the necking region of the support bar match the calculated maximum stress. There are some artificial stress concentrations due to the element shape and size where the cylinder manifold and the support bar interface with one another. If these artificial stress concentrations are ignored, the maximum stress in the support bar during plantar flexion loading is approx. 180-200 MPa. Based on the above calculations and simulations, the Von Mises stresses within the support bar under normal loading conditions have a safety factor greater than 2.5 when compared to the yield stress of aluminum 7075-T6.

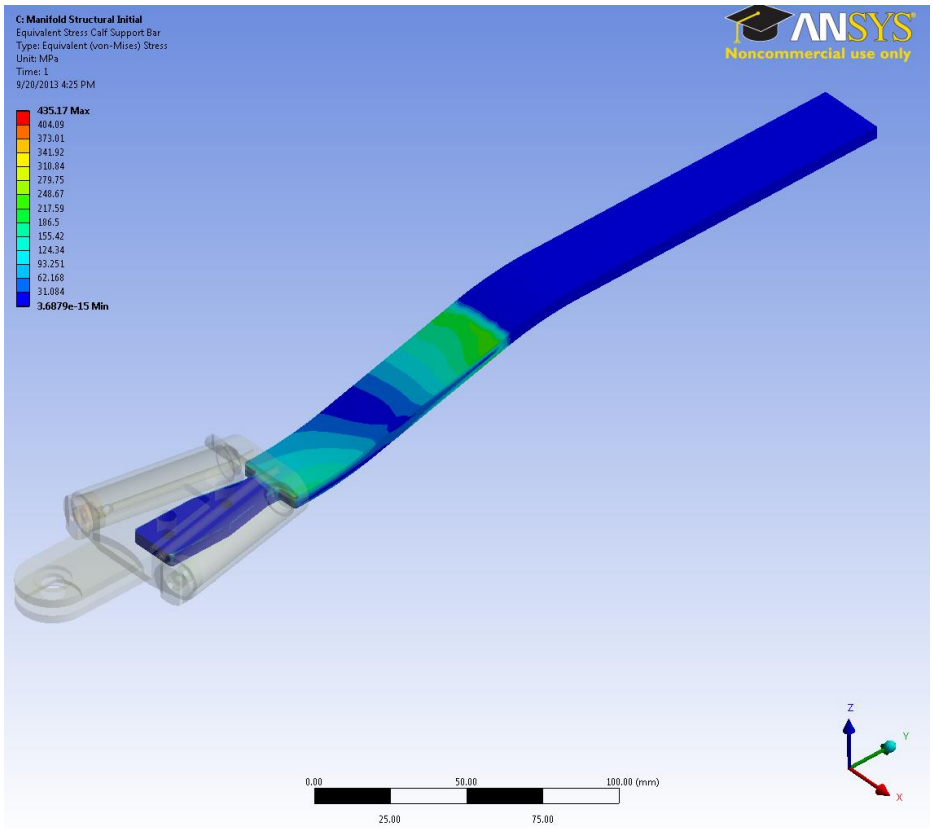

Figure A.23 Simulated Von Mises stresses in the shin support bar

The foot support bracket is the component of the actuator assembly that converts the tension in the nylon coated steel cables to a torque actuating on the foot support plate. There are two regions of the bracket that experience high levels of stress. The first region houses the stop sleeve secured to the nylon coated steel cable. The second region is the necking portion of the bracket between the circular pulley and the attachment to the foot support. The stresses in the necking region of the foot support bracket are estimated using (A22-A24). The results of this calculation are shown in table A5.

Table A.5 Maximum stresses in the FSB neck region

Cable Tension (F)	**Cable Angle (θ)**	**Cross-Sectional Area (A)**	**Length of Moment Arm (L)**
1500/337 (N/lbf)	90°	0.128 in^2	1.2 in
Width of SSB(W)	**Moment of Inertia (I)**	**Max Normal Stress (σ_N)**	**Max Bending Stress (σ_M)**
0.625 in	2.36 x 10^{-2} in^4	2.64/18.2 (ksi/MPa)	10.7/73.9 (ksi/MPa)

The total stress σ_T in the necking region is 92.1 MPa and with additional safety factor of 3 is 276 MPa. The foot support bracket will also be machined out of 7075-T6 aluminum, because this material has the lowest density and satisfies the strength requirement.

The stresses in the two regions were modeled using an ANSYS simulation. The base of the foot bracket is constrained not to move, to simulate being rigidly attached to the foot support plate. A cyclic pressure load is applied on the notch surfaces where the stop sleeve is secured (Fig. A.22).

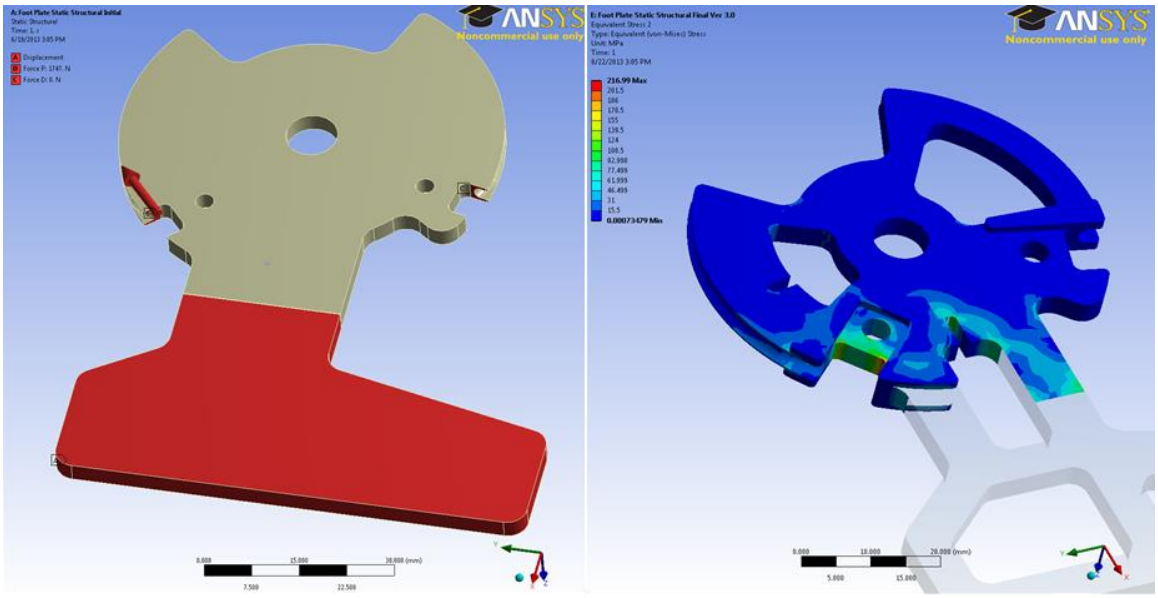

Figure A.24 Simulated Von Mises loading (left) and stresses (right) on the foot support bracket

The results of the initial ANSYS simulation show that the stresses in the region where the stop sleeve is housed in the foot support bracket are too high for the required safety and the

strengths of any of the selected materials. Using the results of the simulation, the dimensions and features are altered to decrease the material stress around the stop sleeve housing. In addition, material experiencing low stress is removed to decrease weight. The process of adjusting the feature dimensions and re-running the simulation is repeated until the maximum stress is below 220 MPa (Fig A.22). Based on the above calculations and simulations under maximum loading conditions, the Von Mises stresses within the foot support bracket have a safety factor of 2.5.

A.6.3 Hydraulic cable seal test stand

The hydraulic cable seal test stand (HCSTS) was designed and built to prove the concept that hydraulic fluid up to 14 MPa can be sealed efficiently around nylon coated steel cable using an O-ring. (Fig. A.17) The actuator cable seal needs to prevent all fluid leakage, while not significantly increasing the friction forces on the surface of the cable. The HCSTS quantifies the seal friction force, the seal fluid pressure, and the tension in the steel cable measured with a load cell.

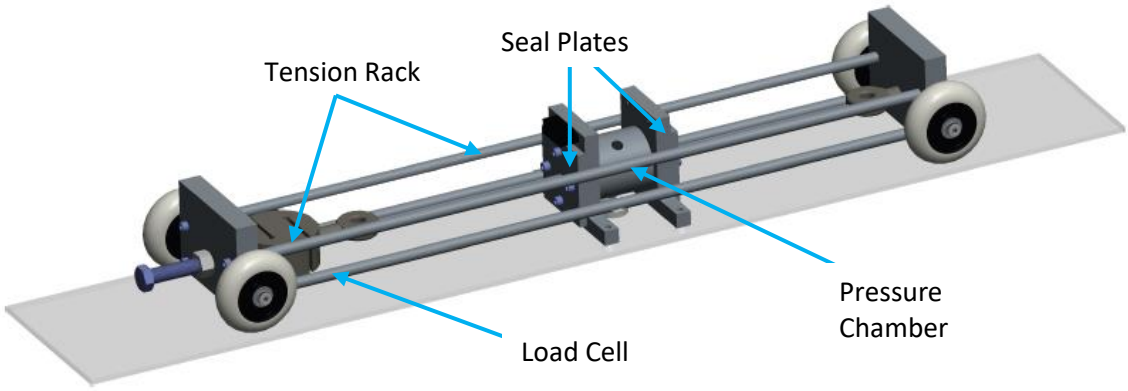

Figure A.25 CAD model of hydraulic cable seal test stand (HCSTS)

The HCSTS is composed of a cylindrical pressure chamber that is secured to an acrylic base board. The pressure chamber is connected to a hydraulic circuit composed of a pressure gauge, a manually hand actuated hand pump, a needle valve, check valve, and a reservoir. When the needle valve is closed, pressure P_a is allowed to build in the pressure chamber (Fig A.18). The measurements of the pressure sensor are collected with a National Instruments Data Acquisition (NI DAQ) managed with LabVIEW software.

On both sides of the pressure chamber there are interchangeable seal plates that house the seals being tested. The cable being tested is threaded through the seal plates and pressure chamber, attached in series with a load cell, and secured to one end of the tension rack. Tension in the cable is controlled by a threaded drive that attaches the load cell to the tension rack. The

load cell signal passes through an amplifier and a low pass filter before being collected by the NI DAQ managed with LabVIEW software.

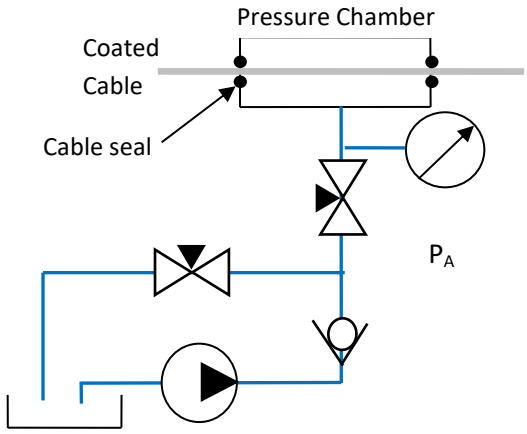

Figure A.26 Hydraulic circuit of HCSTS

Seal plates on both sides of the pressure chamber used standard O-rings. Nylon coated cables with outer diameters 2.39, 3.18, and 4.75 mm (0.094, 0.125, and 0.187 in.) were loaded up to 2000 N in the tension rack. The motivation behind loading the cables is there is a significant reduction in outer diameter under tension, and the test verifies that the seal prevents leakages over a range of loadings. In order to test the seal in a dynamic environment, the tension rack rides on four low friction wheels. The low friction tension rack was cycled back and forth to represent piston actuation. The tension rack is pulled across the base with a handheld load cell to measure an average seal friction force.

The fluid was pumped into the pressure chamber until the testing pressure was reached, and the needle valves were shut to eliminate backflow. The pressure inside the chamber was monitored as a metric of seal performance in addition to visional inspection. The O-ring seals on all the nylon coated cables were leak free during static testing up to 2000 psi. There was a small negligible amount of leakage occurred during dynamic testing as the cable coating had a thin layer of oil on it. This could be eliminated with the addition of a special wiper seal.

The HCSTS was also used to validate the breaking strength of the piston-cable harness assemblies for the HAFO and PHAFO. Material crimping and set screws were used to secure the stop sleeves and the pistons to the cable harnesses. There was limited literature on the holding strength of both connection types, especially with custom aluminum stop sleeve. The cable assemblies were loaded up to 130 percent of the operation tension on the HCSTS to ensure the connection had sufficient holding strength. The final set screw design uses three 8-32 screws orientated 90° to one another.

A.6.4 Electrical design of HAFO control and measurement systems

An Arduino Uno microcontroller is used to generate the Maxon brushless DC motor control signal and read the ankle angular measurements. The micro controller uses SPI communication with a DAC chip to generate the 0-5V control signal for the motor controller (Fig. A.27). In addition, the microcontroller is connected with a Bluetooth module that allows the user of the orthosis to adjust the control and functionality from a Bluetooth device like a cell phone.

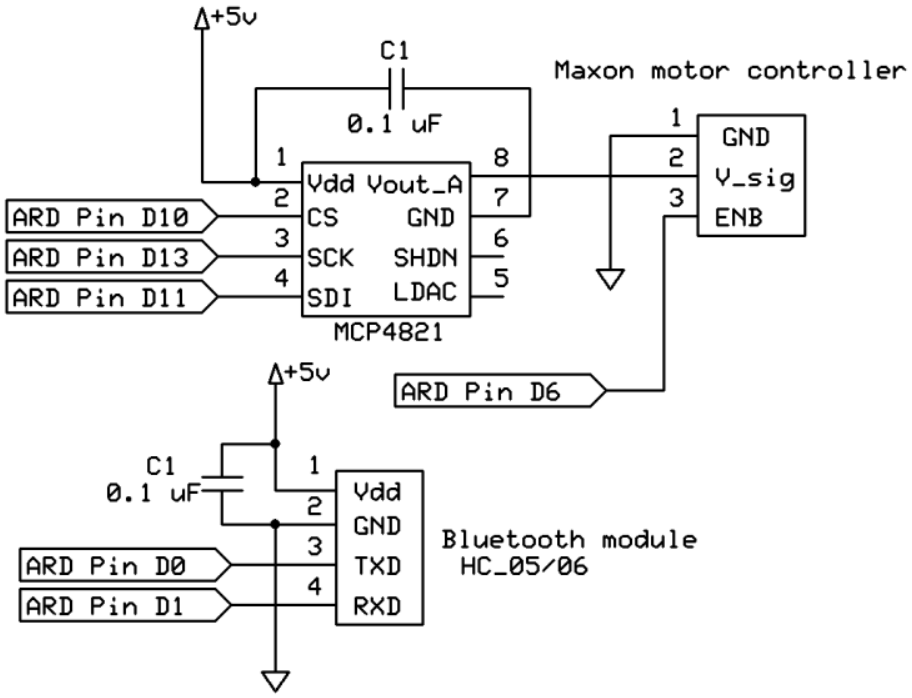

Figure A.27 Electrical schematic of HAFO control system

The angular position of the ankle was measured using two (A1326LUA-T, Allergo Micro Systems) Hall Effect sensors. The signal from the sensors was shifted and magnified using operational amplifiers. Finally a second order 100 Hz Butterworth filter with a cut-off frequency of 100 Hz was used to filter the signal measured by the analog ADC on the Arduino microcontroller and the data acquisition unit.

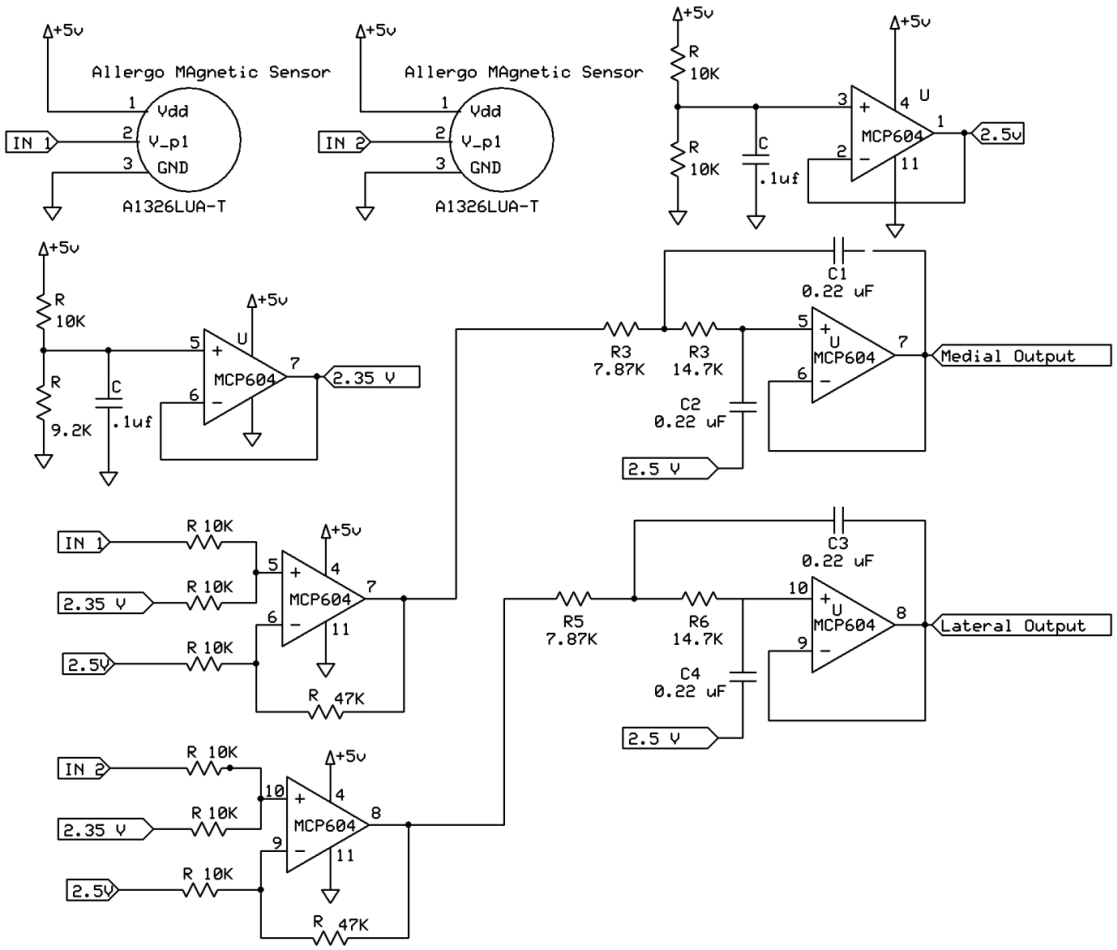

Figure A.28 Electrical schematic of HAFO angular measurement system

A.7.1 Electrical design for pediatric hydraulic ankle-foot-orthosis

The following section illustrates the sensors and measurement system used in the pediatric HAFO. The control inputs for the motor and servo valve along with the pump shaft angular measurement system are illustrated in section A.4.1.

Table A.6 Arduino and DAQ inputs & output pins for pediatric HAFO

Arduino analog		Arduino digital		DAQ USB-6002	
0	Angle sensor 1	2	LED Indicator	0	Angle sensor (left)
1	Load cell 1	3	SS DAC 2	4	System pressure
2	Supply pressure	6	SS Counter	1/5	Servo valve current
3	Actuator rod pressure	9	SS DAC 1	2	Motor velocity
4	Angle sensor 2	11	MOSI	6	Pressure (bottom)
5	Load cell 2	12	MISO	3	Pressure (top)
		13	SCK	7	Angle sensor (right)

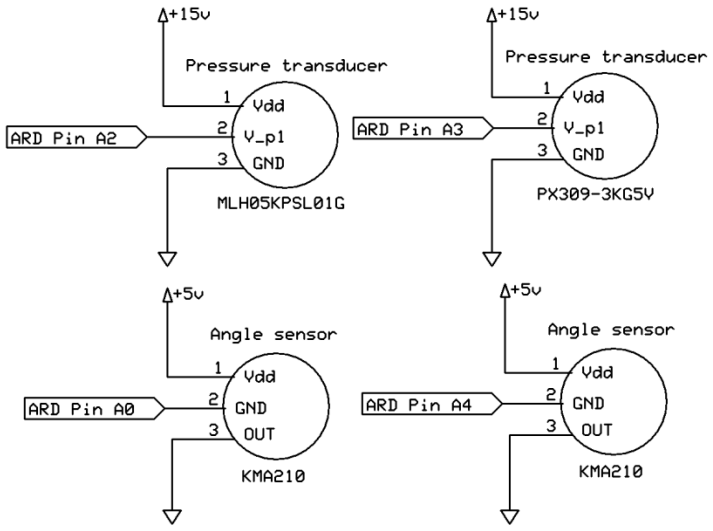

Figure A.29 Electrical schematic: Angular position and pressure measurements

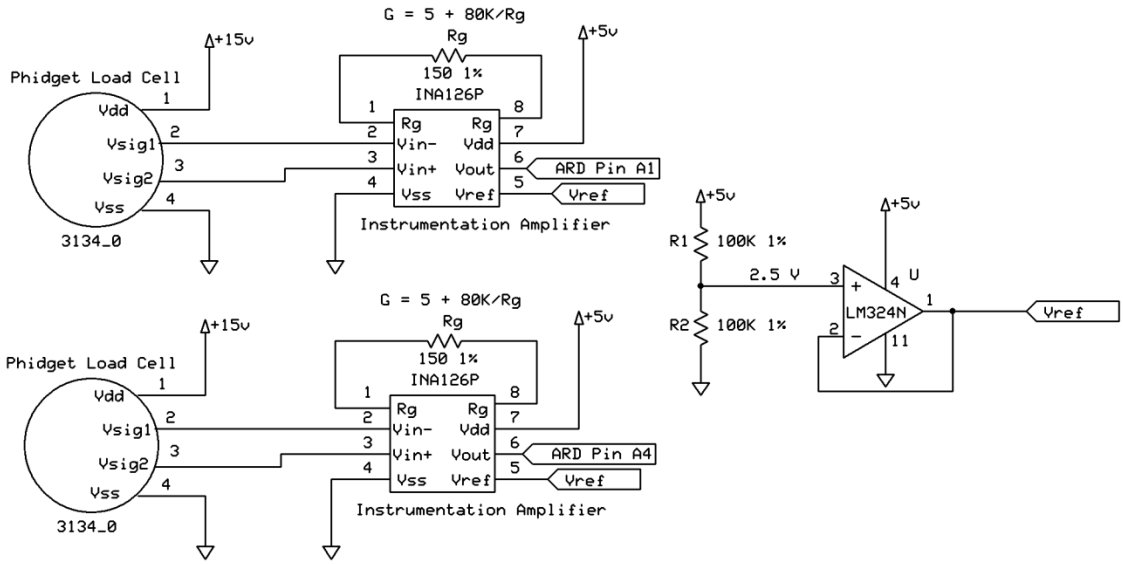

Figure A.30 Ankle torque measurement system

The load cell signals required significant amplification, so instrumentation amplifiers (INA126P, MicroPower) were used to create a gain of 538.3.

A.7.2 Passive AFO stiffness and angular position data collected with BRUCE and 3D motion capture

The following figures are individual data sets of AFO stiffnesses collected with BRUCE and fittted to a linear stiffness. In addition ankle angular position was measured with a 3D motion capture as the user is wearing the orthosis during gait. Ankle neutral position is 0° in the data. This data is collected with assistance of Gillette Children's Speciality Healthcare.

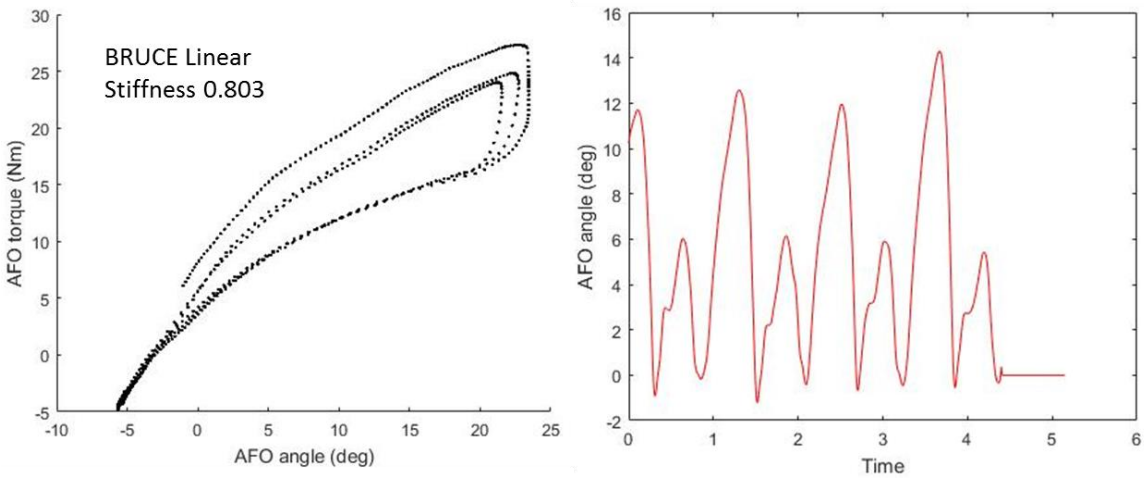

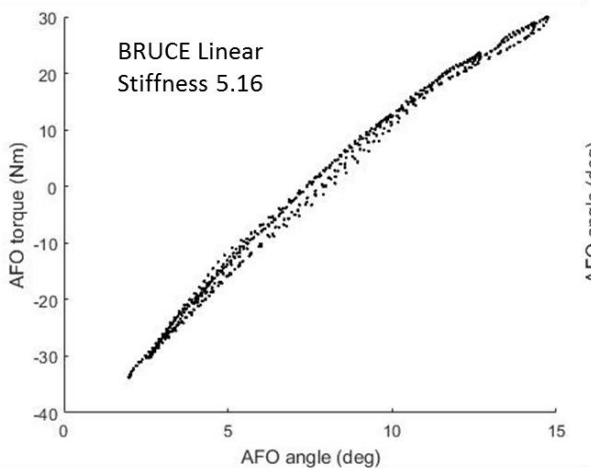
BRUCE Linear
Stiffness 5.16
AFO torque (Nm)
AFO angle (deg)

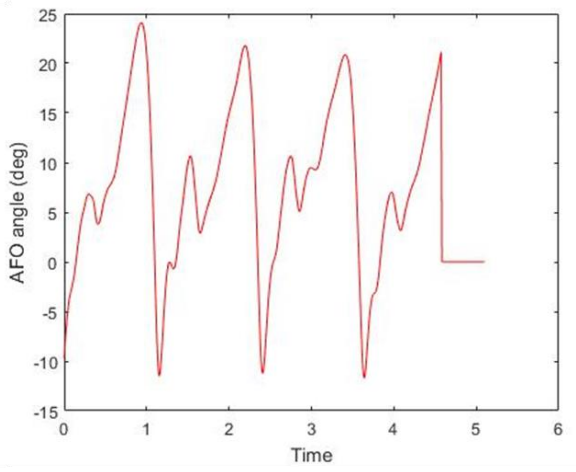
AFO angle (deg)
Time

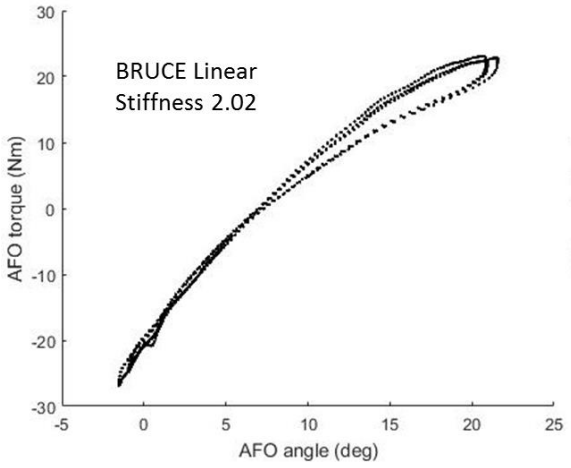
BRUCE Linear
Stiffness 2.02
AFO torque (Nm)
AFO angle (deg)

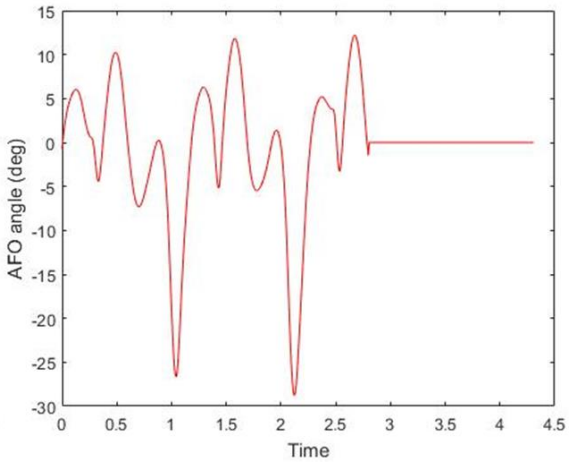
AFO angle (deg)
Time

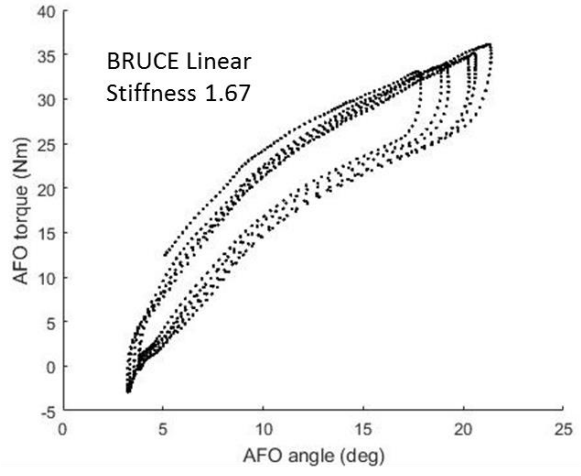
BRUCE Linear
Stiffness 1.67
AFO torque (Nm)
AFO angle (deg)

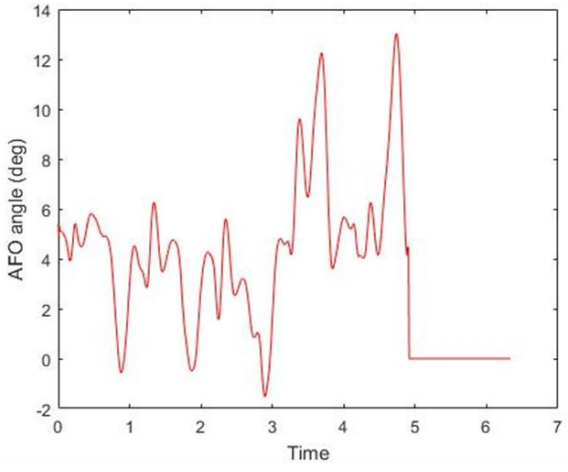
AFO angle (deg)
Time

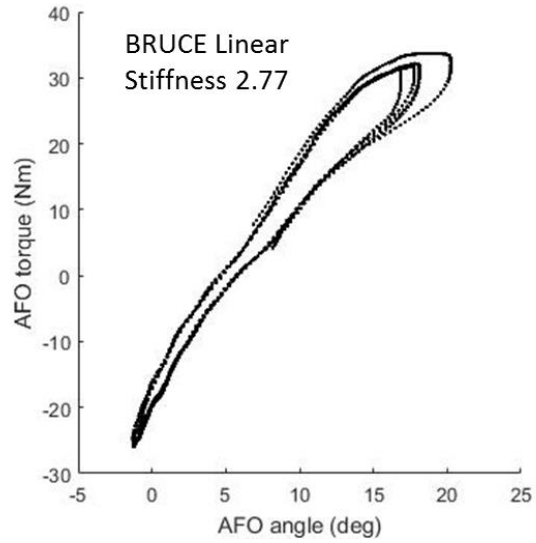
BRUCE Linear
Stiffness 2.77
AFO torque (Nm)
AFO angle (deg)

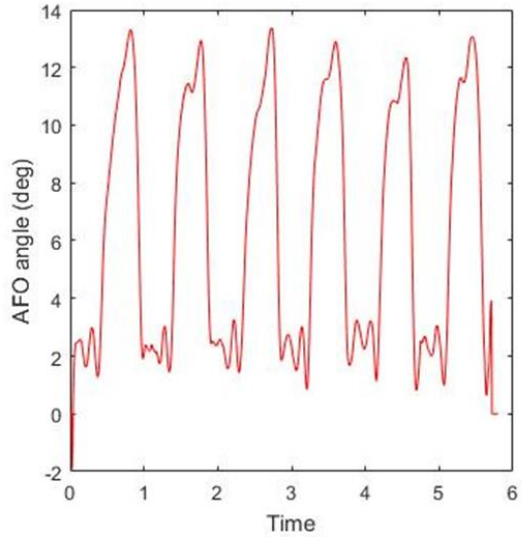
AFO angle (deg)
Time

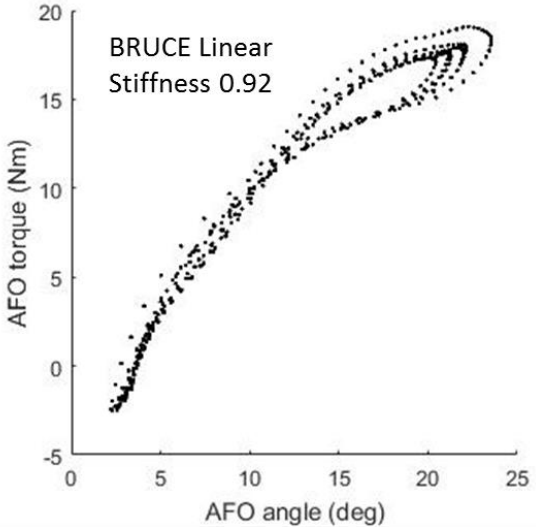
BRUCE Linear
Stiffness 0.92
AFO torque (Nm)
AFO angle (deg)

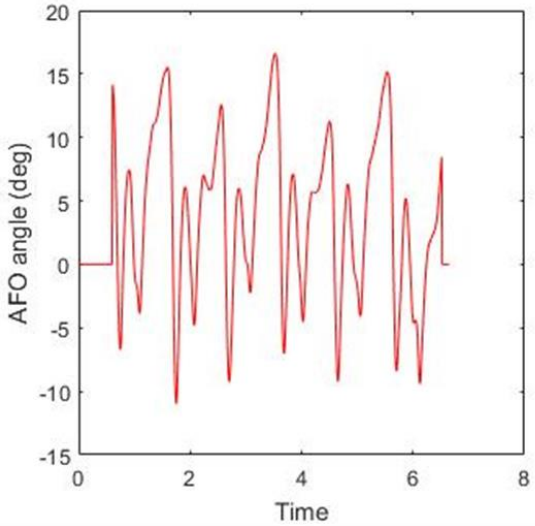
AFO angle (deg)
Time

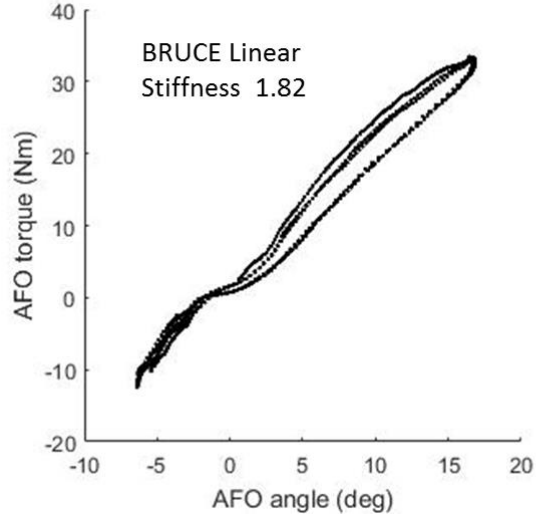
BRUCE Linear
Stiffness 1.82
AFO torque (Nm)
AFO angle (deg)

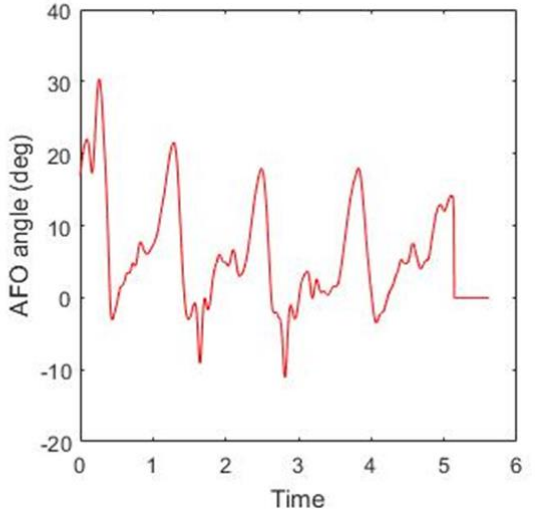
AFO angle (deg)
Time

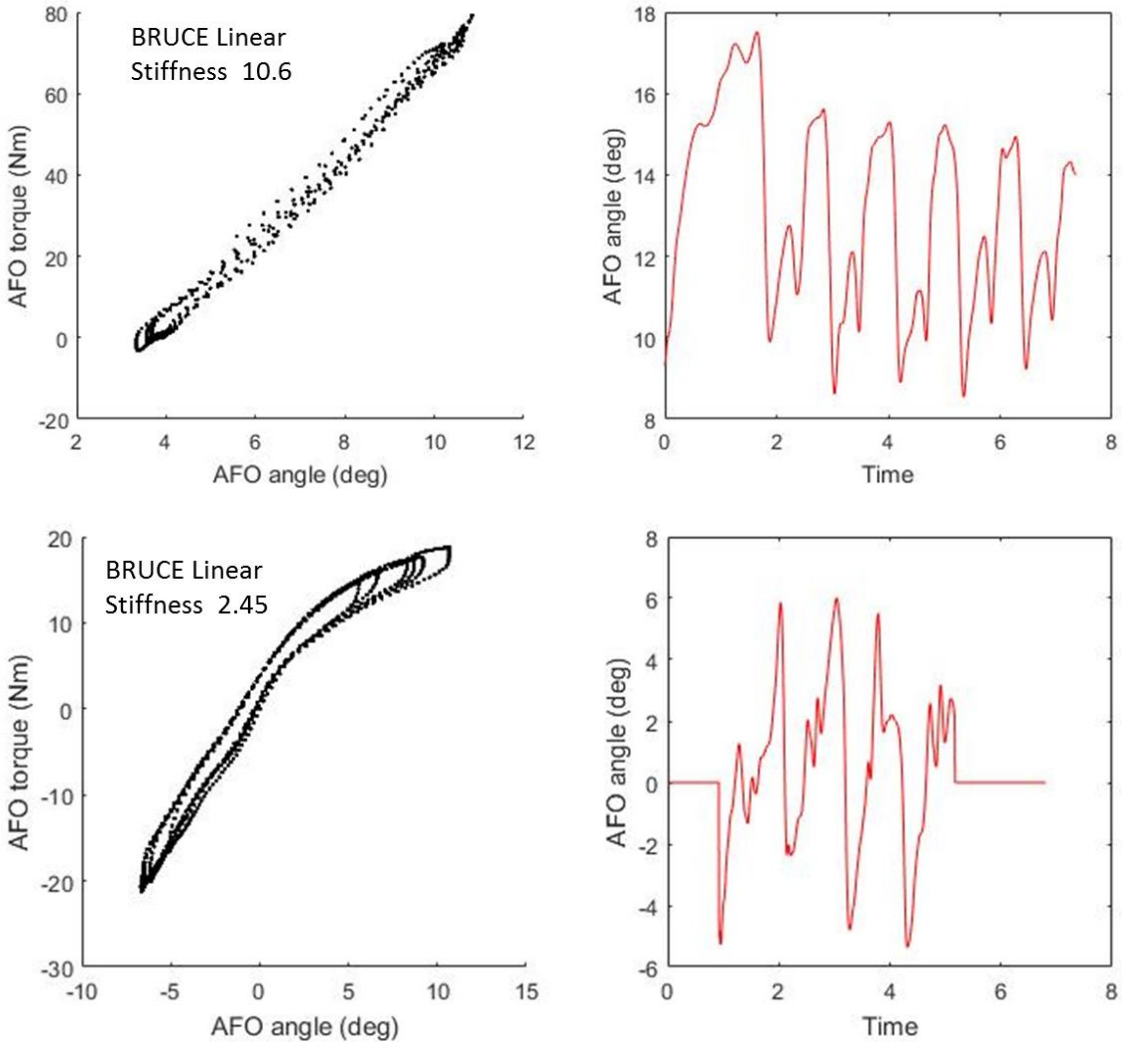

Figure A.31 Additional BRUCE and motion capture data sets